Designing Advanced Nanomaterials for Next Generation in vitro Diagnostics: Development ofOptical and Electrochemical Biosensors for Determination of Viral and Bacterial Infections based on Hollow AuAg Nanoparticles

Lorenzo Russo

PhD Thesis

Designing Advanced Nanomaterials for Next Generation in vitro Diagnostics:

Development of Optical and Electrochemical Biosensors for Determination of Viral and Bacterial Infections based on Hollow AuAg Nanoparticles

Lorenzo Russo

Prof. Dr. Arben Merkoçi Hyka
Nanobiosensors & Bioelectronics group

Prof. Dr. Victor Franco Puntes
Inorganic Nanoparticles group

ICN2
Institut Català de Nanociència i Nanotecnologia
EXCELENCIA SEVERO OCHOA

ICN2 – Catalan Institute of Nanoscience and Nanotechnology

Chemistry PhD Program

UAB
Universitat Autònoma de Barcelona

UAB – Universitat Autonoma de Barcelona

January 2019

Acknowledgements

This section of this PhD thesis is the only one where no mistakes have been made. While there is much to learn from a dissertation, these pages are typically the only glimpse into the human side of the dissertation writer, and it is always interesting to discover who helped the writer achieve his goal. Earning this degree is a test of fortitude and resilience that should not be overlooked, and it is something that cannot be accomplished alone.

I would like to first acknowledge both my thesis directors, Prof. Arben Merkoçi and Prof. Victor Puntes, for they have taken the responsibility of guiding me through my first true journey into scientific research. I deeply appreciate their engagement in fostering students to look critically into problems with level-headed, thoughtful and systematic approach, and their generosity in granting their expertise and know-how. A particularly warm and sincere "Gracias!" goes to Prof. Victor Puntes for the great effort he puts in sharing all his profound knowledge of nanotechnology to his students, no matter how busy his schedule is. Tirelessly distributing his enthusiasm and "out-of-the-box" thinking, so inspiring and destabilizing, he also reminds us constantly the important connection between our scientific work and the real-world challenges outside the lab. I am grateful to him for what I consider one of the most valuable gifts I received during my thesis. I would like also to thank Prof. Kimberly Hamad-Schifferli for welcoming me in her group and share her attention, trust and knowledge during such a short time. With her gentle and sound help this PhD thesis acquired the fundamental piece it was missing. Finally, a special acknowledgement goes to Dr. Neus Bastus, who taught me the rational and systematic method which, although initially intended for the synthesis of nanoparticles, became so precious and crucial in shaping the entire work described in this dissertation. Also, I want to thank her for helping me navigating the sometimes complicated political obstacles I encountered during these years.

Next, I would like to thank all the members of the three research groups where I spent the last four years here at ICN2 in Barcelona, the Nanobioelectronics and Biosensors group and the Inorganic Nanoparticles group, as well as the NanoBioInterfaces Lab at UMass in Boston. They all were instrumental to my success and helped me keep up with the difficulties I encountered during my journey. Though I was surrounded by many great people, a list too long to fit in these pages, life would have been much tougher without having the following people around. Francesco Barbero, my new friend. Juan Leva, probably the person that most of all helped me during the toughest part of this PhD. I owe him a lot. Luz Agueda Pérez Toma, who so joyfully shared with me all her know-how about ELISA and antibodies. All the questions and the friendliness of Xavier Castellvi. Daniel Quesada, the soft cornerstone of the Nanobioelectronics & Biosensors group. Florind Merkoçi, who taught me the magic of galvanic replacement and brought a happy mood in the lab every day. Maria Sanchez-Purrà, for her patience with me and my shape-less spots. All the beers, chats and movies shared with Delyan Hristov. Leticia Manen, who brought some brightness into a lab without windows. Alfredo de la Escosura-Muñiz for his kindness in listening to everyone's problems. Niloufar Amin and Mireya Borrajo for believing in my ideas and working so hard. And also, Rocio Rodriguez and her wise advices about almost everything. Alba Mignorance with who I shared the suffering of a PhD. Jose Manuel Roque because he is the only happy person in ICN2.

Although the life of a PhD student consists in tackling daily complex technical challenges, "paperwork" remains one of the scariest tasks we have to take care of. I would like to greet sincerely Marta Gonzalez and Andres Ballesteros from the Competitive Funding department at ICN2. Even if they might not know it, their help in making my life easier with forms, procedures and funding was extremely important for completing this PhD thesis.

Finally, I am grateful to my family for all the support I received during these last 6 years as I have pursued this degree. My parents Luciano and Antonella, my sister Marta, my grandparents Enrica, Luigi and Maria, and aunts and uncle Luisa, Sandra and Behzad, who have all sustained me with love, listening and understanding. Though I know they still are not sure why I pursued this PhD, the true value of my family's support lies in their belief and trust in both me and my goals. They have and always will help keep me grounded.

Another family grew around me during these last 6 years in Barcelona, they were all the ones that helped me remaining sane during this PhD. Thank you, Grazie, Gracies, Gracias, Nandree, Eskerrik, to Francesco, Lucia, Greta, Dimitri, Azzurra, Roberto, Maider, Daniele, Jorge y el tango, Ezhil, Ram, David, Omeila, Elisa, Elia, Ihlenia, Emma, Rocio, Andrea, Anna, and Caterina, thank you for bringing me home. A very warm thanks to Mary and Andy for hosting and taking care of me while staying in their house in Savin Hill.

A special thought is for Carme and all her kindness. I am sure I would not have completed this difficult challenge without her. I will always be grateful to her and her beautiful family for making me feel at home in Catalunya. Bona sort!

This work was carried out within the “Doctorat en Química” Ph.D. programme of Universitat Autònoma de Barcelona, supported by the Spanish MINECO (MAT2015-70725-R) and from the Catalan Agència de Gestió d’Ajuts Universitaris i de Recerca (AGAUR) (2017-SGR-143). Financial support from the HISENTS (685817) Project financed by the European Community under H20202 Capacities Programme is gratefully acknowledged. It was also funded by the CERCA Program/Generalitat de Catalunya. ICN2 acknowledges the support of the Spanish MINECO through the Severo Ochoa Centers of Excellence Program under Grant SEV-2013-0295.

A goal without a plan is just a wish.

Antoine de Saint-Exupéry

Table of Contents

Preface

Antimicrobial resistance, a set of adaptations that make bacteria grow in the presence of antibiotics, is considered the major medical threat to the global public health system in the years to come.[1] The development of resistance is linked to the systematic misuse and overuse of these drugs in human medicine and food production. This unfortunate habit, together with the few antibacterial agents currently in development (no major new class of antibiotics has been discovered since 1987), has worsened the problem not only in lower-income countries, where life-saving antibiotics that can effectively treat diseases or blood infections are not always accessible, but is also affecting "first-world", industrialized societies, where even routine surgical operations as well as cancer chemotherapy are becoming less safe due to the lack of protection against infections.

While the discovery of new antimicrobial drugs is fundamental for curative measures, the use of antibiotics must also be supplemented by affordable, point-of-care (PoC) diagnostic tools to help health practitioners and veterinarians identify the type of infection they are treating and thus avoid inappropriate prescribing and dispensing. Effective, rapid, low-cost biosensors are needed for guiding optimal use of antibiotics in human and animal medicine, and such tools should be easily integrated into clinical, pharmacy and veterinary practices. While nowadays the choice to prescribe antibiotics is rarely based on definitive diagnoses, which generally require laboratory-based analytical tests often consisting of costly, days-long procedures and requiring highly trained and skilled personnel, new concepts are needed for fostering innovation in academia and the pharmaceutical industry towards better technologies.[2]

In this context, nanotechnology has proven to be extremely successful in pioneering innovative and advantageous solutions to overcome the conventional *in vitro* diagnostic (IVD) intrinsic limitations.[3] Among others, moderate detection sensitivities for clinically relevant biomarkers, complex test procedures based on fragile and expensive biological molecules as well as need for expensive and bulky instrumentations are issues that have been tackled with several strategies aimed at pushing the development of highly sensitive and convenient biosensors. Although few of these innovations have reached the pharmaceutical market yet, a vast number of examples populate the scientific literature, confirming the elevate potential of nanotechnology in this field. These applications rely generally on the use of nanometer-sized materials (nanomaterials) which hold unique physicochemical properties compared to their macroscale counterparts, and offer desirable and unmatched characteristics for chemical and biological detection, such as high surface-to-volume ratio, strong signal intensities, and finely tunable surface chemistries.[4–6]

This work emphasizes this point by exploring the field of nanomaterials-based biosensors with the goal of developing innovative PoC diagnostic tools able to contribute to the challenge against bacterial resistance. The advancements presented herein can be of interest to the whole IVD community involved in overcoming many of the technological barriers normally encountered with traditional molecular biology techniques, as well as providing two *proof-of-concept* diagnostic applications for the discrimination between viral and bacterial infections. A precise work paradigm has been chosen for the development of this project, consisting in systematically study and understand the parameters governing the synthesis of the nanomaterial chosen, hollow AuAg nanoparticles, in order to be able to precisely tailor its optical and electrochemical properties. This strategy revealed to be crucial for rationally designing the working principles of both biosensors presented, namely a SERS-based lateral flow assay for the quantitative detection of human myxovirus resistance protein A (MxA) and an electrochemical test for semi-quantitative determination of *E.coli*.

References

1. World Health Organization. Global action plan on antimicrobial resistance. *WHO Press* 1–28 (2015). doi:ISBN 978 92 4 150976 3

2. Drain, P. K. *et al.* Diagnostic point-of-care tests in resource-limited settings. *Lancet Infect. Dis.* **14,** 239–249 (2014).

3. Zhou, W., Gao, X., Liu, D. & Chen, X. Gold Nanoparticles for in Vitro Diagnostics. *Chem. Rev.* **115,** 10575–10636 (2015).

4. Howes, P. D., Chandrawati, R. & Stevens, M. M. Colloidal nanoparticles as advanced biological sensors. *Science* **346,** 1247390 (2014).

5. Quesada-González, D. & Merkoçi, A. Nanomaterial-based devices for point-of-care diagnostic applications. *Chem. Soc. Rev.* **47,** 4697–4709 (2018).

6. Chen, J., Andler, S. M., Goddard, J. M., Nugen, S. R. & Rotello, V. M. Integrating recognition elements with nanomaterials for bacteria sensing. *Chem. Soc. Rev.* **46,** 1272–1283 (2017).

Chapter I

Introduction

Rational Design of Inorganic Nanoparticles for Optical and Electrochemical Sensing

Inorganic Nanoparticles

The term "Inorganic nanoparticles" (INPs) generally refers to a wide class of nanomaterials composed of metals, semiconductors, their oxides and/or a mixture of any of these, existing in the form of colloidal dispersions of discrete atomic aggregates, whose size ranges between 1 and 100 nm. Compared to their macroscale counterparts, these nano-sized materials exhibit unique physical and chemical properties which are the result of a concerted synergy between their morphology (i.e. size and shape), chemical composition and surface effects.[1] Firstly, due to their small size, quantum confinement effects induce great diversity in the optical properties of noble metal NPs with the emergence of localized surface plasmon resonance (LSPR) modes which, depending on their morphology, determine their absorption spectra in the ultra-violet (UV), visible and near infrared (NIR), as well as a number of other optical features.[2] Secondly, the elemental composition of both mono- and multi-metallic INPs is also determining the material electronic configurations and valence states, which in turn allow to tune the material's band gap, trigger luminescence emission and produce versatile redox behaviors.[3] Lastly, given the high surface-to-volume ratio, INPs display a variety of surface effects and interactions with their surrounding environment, since a large percentage of their atoms are located on their surface. This corresponds to outstanding chemical reactivities and enhanced catalytic properties, which contribute to explain the reportedly game-changing potential INPs demonstrate in more traditional chemical catalysis[4] as well as energy production[5,6] and storage[7]. INPs can be prepared through a plethora of methodologies, developed and improved significantly in the recent years, including solution-based synthesis in both aqueous and organic solvents, microemulsions and biphasic templated protocols, laser-, ultrasound- and microwave-assisted processes as well as electrochemical deposition. Generally, the main scientific goal of modern synthetic recipes is to achieve the highest possible degree of control over INPs defining features, namely morphology, chemical composition and surface state.[1] The crucial importance of fulfilling this requirement resides in the intimate connection between these features and INPs physico-chemical properties, and therefore represents the key for obtaining high quality nanomaterials with elevate performances.

INPs-based (Bio)Sensors

Among all the different scientific and technological fields where INPs' properties revealed to be useful, such as catalysis[4], energy conversion[5], energy storage[7], nanomedicine[2] and biofuel production[6], the number of publications regarding the development of sensors and biosensors based on INPs has significantly grown during the last 2-3 decades (**Figure 1**).

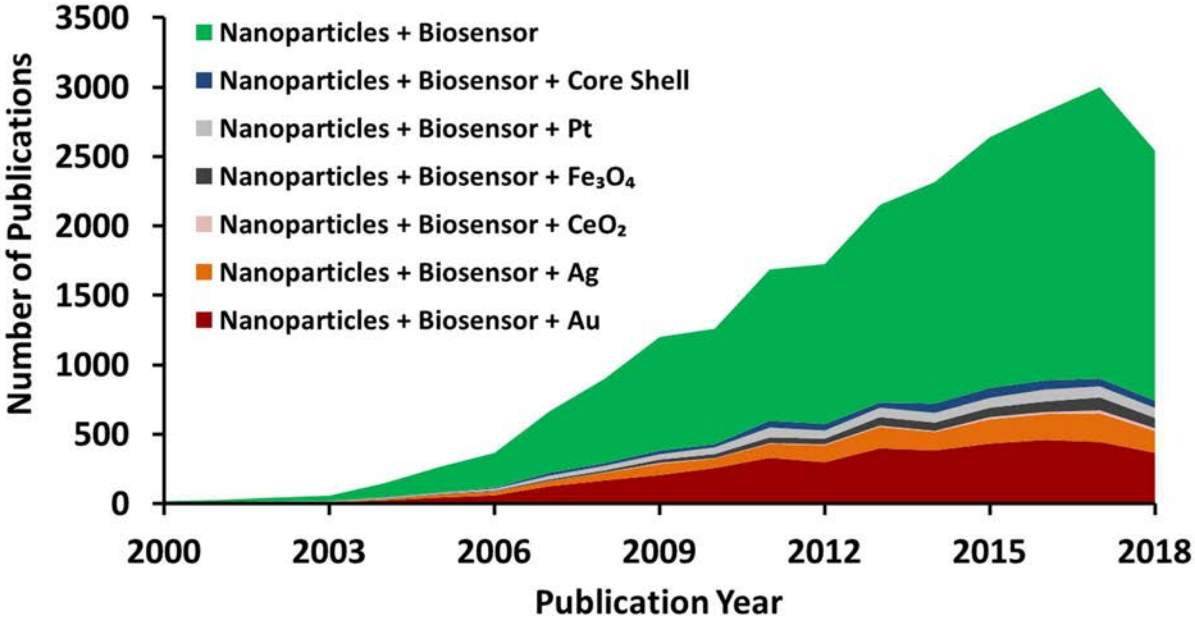

Figure 1 – Web of Science analytics regarding the number of publications related to the development of biosensors and nanoparticles during the last 18 years. Various combination of keywords are shown in order to confirm the growing trend.

This trend confirms how the use of INPs in (bio)sensing can effectively bring new detection technologies or improve analytic performances of established molecular biology and electroanalytical methods, such as enzyme-linked immunosorbent assay (ELISA), lateral flow assay (LFA), Immunoagglutination, heavy metals and glucose detection, by introducing new amplification strategies able to enhance their sensitivities, as well as increase their robustness substituting costly enzymes and bleachable fluorophores.[3] Moreover, a similar interest in INPs-based (bio)sensing has been also recognized in the biomedical and pharmaceutical industries, flourishing with a growing number of *in vitro* diagnostics applications, which are nowadays beginning to reach the market with their innovative products.[8]

In this context, although different working principles have been applied in both direct and indirect INPs-based (bio)sensing, the vast majority of these techniques takes advantage of INPs astounding optical and electrochemical properties in order to employ them either as signal reporters, transducers or amplifiers (**Scheme 1**). The use of INPs as reporters consist in exploiting one or more of their attributes for generating an easily detectable optical or electrochemical signal. Transducers involve a change in INPs' properties induced by a chemical event in their proximity, which represents the signal itself. Amplifiers take advantage of INPs' optical or catalytic properties for intensifying an analytical signal. In all these cases the enhanced sensing capabilities offered by INPs rely on the precise understanding of the origin and dependence of their properties on their morphological, compositional and surface features. Achieving a precise and tunable synthetic control over those features becomes therefore the key for the production of advanced INPs with finely tailored optical and electrochemical properties.

The potential of applying the different classes of nanomaterials, including that of INPs, in biosensing platforms has been object of various reviews by our group and others.[9,10] While these reviews focused mainly on the different strategies employed within the specific diagnostic platforms described, we herein report a selection of recent and particularly inspiring examples of INPs-based (bio)sensors whose common trait is the *ad hoc* synthetic tuning of INPs' properties, enabling the development of innovative (bio)analytical techniques and devices. Although many of the reported works do not rely solely on one INPs' property for enhancing the analytical performance of their specific application, but rather on a combination of more than one mechanism, our attempted taxonomy hopes to delineate a representative set of strategies for the rational design of advanced INPs for next generation sensing and biosensing.

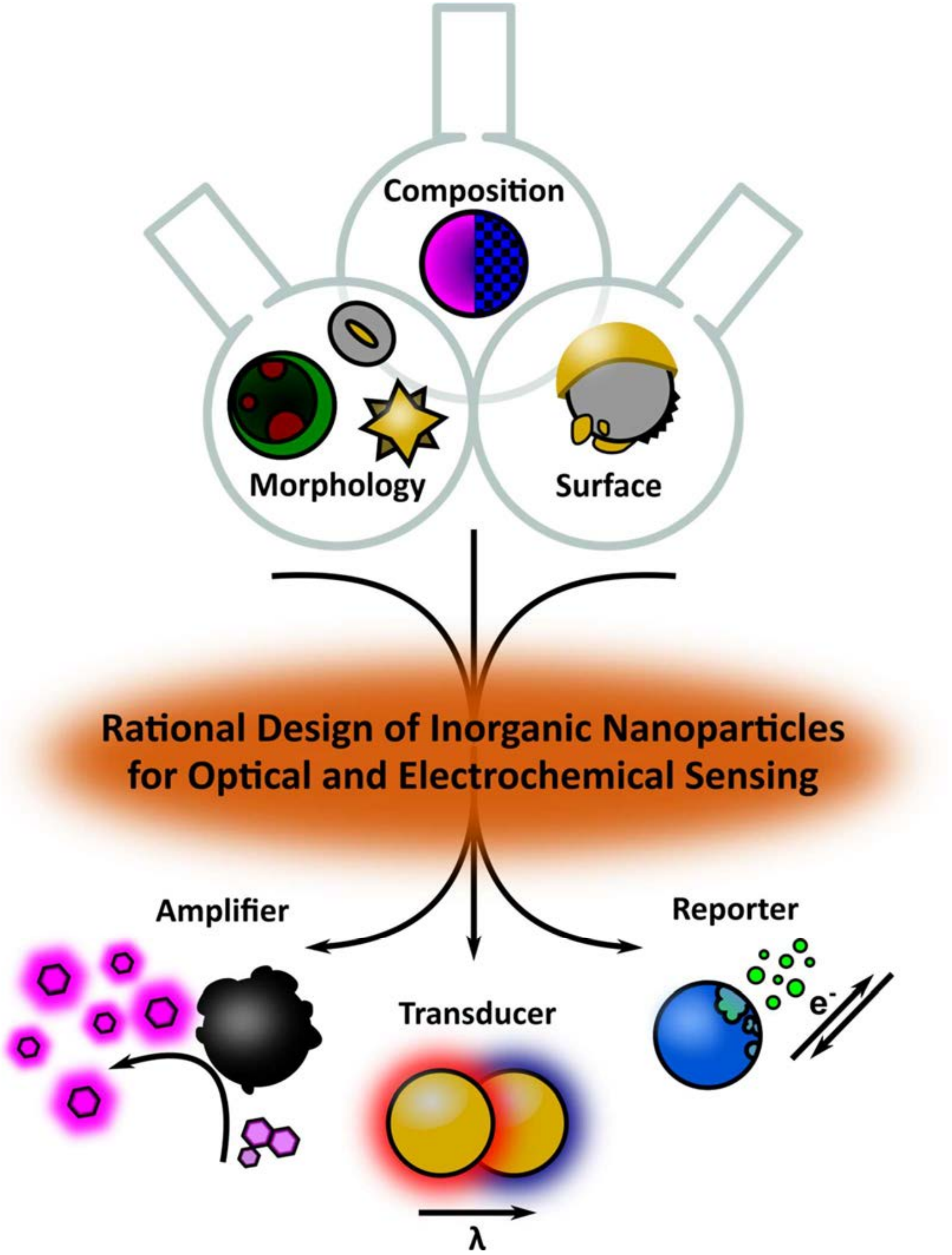

Scheme 1 – Inorganic Nanoparticles possess versatile and tunable properties that depend on their main defining features, morphology, chemical composition and surface state. Through their controlled modification and interplay, these features determine the role played by advanced nanomaterials when applied in (bio)sensing technologies, be it of amplifiers, transducers or reporters.

Rational Design of INPs for (Bio)Sensing

Morphology

Since the first reports about Au NPs, the main focus of synthetic recipes has been to achieve the highest possible control over INPs morphology (i.e. size and shape) through the reasoned interplay of stoichiometry, co-reagents (i.e. acids, metal precursors) and auxiliary molecules (i.e. polymers, surfactants). This effort is explained in the first place by the well-known correlation between surface plasmons, that is light-induced oscillations of electrons at the surface of plasmonic noble metal NPs, and their optical properties. These are in turn the origin of these metallic nanostructures' performances in many optical sensing applications, such as plasmonic antennas and surface-enhanced Raman scattering (SERS) probes. Additionally, the control over INPs morphology enables as well the spatial localization of different functionalities and properties along the nanostructure, providing a better control over their interface with the surrounding chemical environment.

Plasmonic Sensors

A large number of examples in (bio)sensing literature focuses on tuning of noble metal NPs' plasmonic properties as a pathway for enhancing their optical properties. As a matter of fact, the electromagnetic field generated at Au and Ag NPs surface is known to be highly susceptible to changes in surrounding refractive index, thus any chemical event taking place at the close proximity of the particles' surface corresponds to a detectable shift in particles' LSPR wavelength.

Following this approach, Chiu et al. prepared Au@Pd core@shell nanocrystals (NCs) with different morphologies in order to evaluate their hydrogen-sensing ability (**Figure 2 – A**).[11] In their system they exploited the LSPR of the Au cores as plasmonic transducers, together with the known ability of Pd nanostructures to interact with hydrogen through surface adsorption as well as incorporate the gaseous molecule forming palladium hydride (PdH). When exposed to H_2 in solution, the immediate formation of PdH caused a change in the refractive index of the Pd shell, and the absorption spectrum of the particles reported this change. In their design, the Au cores serve as plasmonic antennae to detect changes in the refractive index of the Pd shells after the diffusion of atomic hydrogen into the shell layer. Since the LSPR position is modulated by the thickness of the Pd shell, they evaluated the effect of shell thickness on the extent of spectral shifts upon hydrogen absorption in solution, revealing that the use of smaller Au@Pd octahedra with thinner Pd shells resulted in a visually detectable change in the color of the solution within 1 min upon hydrogen absorption. The system's selectivity was also proved when no spectral changes were recorded when the particles were exposed to oxygen or CO.

Among plasmonic nanostructures, hollow ones are known to display enhanced optical susceptibilities to changes in refractive index in the proximity of their surfaces.[12] Compared to their solid counterparts, in fact, the hybridization of the surface and cavities plasmonic resonance modes generate more intense and homogeneous electromagnetic fields, resulting in larger absorption cross-sections allowing to sense chemical transformations further from their surface. In a recent work reported by our group, we showed a highly reproducible and robust methodology based on galvanic replacement reaction (GRR) for the synthesis of monodisperse AuAg nanoshells (NSs) with tunable shells thicknesses and voids size (**Figure 2 – B**).[13] Through the systematic identification of the role played by each different synthetic parameter an unprecedented control over the material's morphological and optical properties was obtained. The study of the time- and size-resolved evolution of AuAg NSs LSPR band, which spans almost through the whole visible spectrum and beyond NIR wavelengths, combined with simulations based on Mie's theory, allowed building a transferable and scalable synthetic tool for the development of an advanced plasmonic nanomaterials.

Figure 2 (*next page*) – Controlling the morphology of plasmonic INPs allows achieving enhanced optical performances and improved sensing. **A: a)** Schematics and SEM images of Au@Pd core–shell of different morphologies. **b)** UV/Vis absorption spectra of Au–Pd core–shell NCs before (blue) and after (green) the hydrogen-absorption experiment. **c)** Photographs of the solutions before (left) and after (right) the hydrogen-absorption experiment. **B: a)** Time-resolved absorption spectra evolution of 80 nm-sized solution of Ag NCs into hollow AuAg NSs. During GRR the LSPR shifts gradually through the whole visible spectrum toward NIR wavelengths (background color corresponding to the color of the solution). **b)** HAADF-STEM micrographs of highly monodisperse 80 nm AuAg NSs. **C:** LSPR *red-shift* comparison between spherical Au NPs and single-walled AuAg nanoboxes after the first NP−protein interaction and secondary protein−antibody interaction. **D:** CD spectra of citrate-capped, chiral Al NP (inset schematic) dispersions (solid curve) showing a ≈5.5 nm *red-shift* upon electrostatic adsorption of 14×10^{-9} M lysozyme (dashed curve). **E:** Calculated scatter plots of polarization-averaged absorption against aspect ratio (AR) tuned by varying branch height while keeping the base width, core and tip diameters and branch number constant (their corresponding 3D geometry is on top). (Inset) The linear relationship between the plasmon peak position and AR, which is tuned by varying branch height or base width while keeping all other parameters constant. **F: a)** TEM images of spiky Au nanostars. **b)** Temperatures of the solutions containing different spiky Au nanostars as a function of irradiation time. (Inset) 3D reconstruction by TEM tomography of single spiky Au nanostar. **c)** Schematic for the *in vivo* photothermal therapy experiment demonstrating complete tumor ablation upon NIR light irradiation. Reproduced with permission from: **A:** ref. 11. *Copyright © 2013 WILEY-VCH Verlag GmbH & Co. KGaA, Weinheim*. **B:** ref. 13. *Copyright 2018, American Chemical Society*. **C:** ref. 14. *Copyright 2016 American Chemical Society*. **D:** ref. 15. *Copyright © 2015 WILEY-VCH Verlag GmbH & Co. KGaA, Weinheim*. **E:** ref. 16. *Copyright 2015, Elsevier B.V*. **F:** ref. 17. *Copyright 2018, American Chemical Society*.

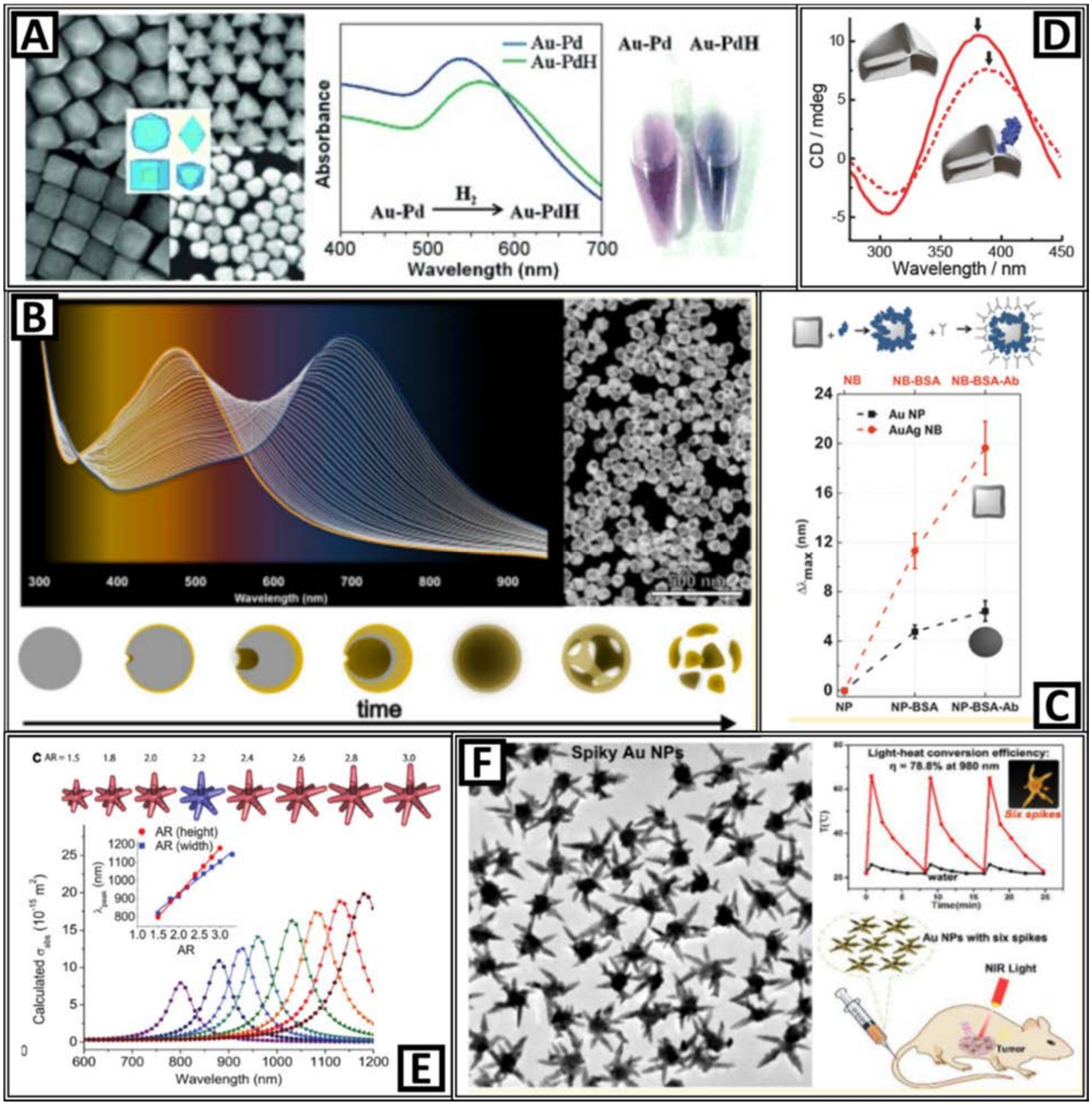

The same strategy was also applied in our group by Genç and coworkers, who showed the rational nanoengineering of improved plasmonic nanoprobes based on hollow AuAg nanocubes, and their application as optical label-free transducers (**Figure 2 – C**).[14] By coupling boundary element method (BEM) simulations of LSPR modes of nanocubes of different morphologies (i.e. walls thickness and pores sizes) with their spatially resolved plasmonic mapping through electron energy loss spectroscopy (EELS), two main effects directing the wavelength position and intensities of LSPRs were individuated. On one hand, and in a substantially predominant manner, morphological effects due to void formation and pores opening are responsible for the large *red-shifts* observed in the LSPR of AuAg nancubes with respect with their silver precursors. Besides, compositional effects due to AuAg alloying also contribute to define the optical properties of the material. With these results AuAg nanocubes LSPRs with the highest possible spatial accuracy were exactly located, revealing how the surface of such hollow nanostructures acts like a continuous "hot-spot" with intense plasmon excitations. Thus, the plasmonic response of 50 nm AuAg nanocubes with spherical Au NPs of the same size for the label-free homogeneous immunoassay for a model antigen. Thanks to the enhancement of the localized electromagnetic field around the hollow nanoboxes, 4-fold stronger shifts were observed compared to Au NPs, allowing easy and direct detection of binding events in their vicinity.

When the shape of INPs is chiral, that is not superimposable on its mirror image, the resulting asymmetric LSPR modes cause strong chiral optical effects when circular dichroism (CD), the differential extinction between left- and right-handed light, is used to probe the particles' optical properties. McPeak et al. reported recently[15] that chiral colloidal aluminum NPs provide strong UV plasmonic CD signals characterized by high-energy superchiral near-fields (**Figure 2 – D**). These plasmonic features were exploited for optically probing the electrostatic-driven adsorption of differently charged proteins onto a colloidal solution of these particles. While biomolecules typically exhibit a chiral optical response in the UV, traditional plasmonic metals such as Au and Ag cannot be used for their optical transduction since their CD signals occur only in the visible or NIR regime. The use instead of citrate-stabilized Al chiral NCs allowed to tune the chiral LSPR modes into the UV wavelengths and to achieve the selective detection of lysozyme at the nanomolar concentration range. Despite the high sensitivity displayed, the synthesis of Al chiral NCs required complex clean-room techniques and costly materials for directing their final morphology, an experimental aspect that could forbid their application in real-world diagnostic tools.

Au NPs have been employed extensively for *in vivo* theranostics applications, given the great advantage represented by their high biocompatibility and chemical stability.[2] On the other hand, their strong absorption and light scattering in the second NIR window, also known as 'tissue diagnostic window' being the most suitable for *in vivo* imaging, is a crucial technical challenge to overcome in order to apply Au NPs as efficient optical reporters for both NIR imaging and photothermal therapy. Tackling this issue, Yuan et al. presented a new, surfactant-free synthesis method of biocompatible Au nanostars with controllable geometry enabling to tune the LSPR band into the NIR region (**Figure 2 – E**). The plasmon band shift, which was firstly simulated with theoretical modelling for multiple-branched 3D nanostars, was attributed to variations in branch aspect-ratio, with the LSPR band intensifying with increasing branch number, branch length, and overall star size.[16] Similarly, Bi et al.[17] explored how the judicious adjustment of Au nanostars' sharp tips number, length and width could precisely locate their LSPR peaks in the second NIR window as well as achieve a higher absorption-to-extinction ratio (**Figure 2 – F**). Through numerical simulations they found *the* optimal relationship between number of spikes and particles' extinction spectra, allowing them to accordingly design Au nanostars exhibiting a record light-to-heat conversion efficiency (78.8%) under irradiation by 980 nm light.

SERS-based Sensors

The dependence between surface plasmons and noble metal NPs' morphology has been clearly highlighted by the significant effort made to expand SERS analytical applications. Plasmonic nanomaterials are exploited as Raman signal amplifiers because of the electric field enhancement generated at their surface when illuminated with light that is in resonance with their LSPR frequency. To further strengthen this effect, the strategy generally applied relies on the creation of *hot-spots*, additional localized enhancements of electromagnetic field, between the plasmonic nanostructures used as substrate for this technique. These *hot-spots* are generated in correspondence of tips, pores and other morphological features of plasmonic NPs, and are responsible for amplifying the Raman spectra of small organic molecules adsorbed on them.

In a recent report by Liu et al.,[18] SiO_2-encapsulated porous AuAg alloy NPs were produced with a controlled dealloying process of their core-shell precursors (**Figure 3 – A**). The obtained plasmonic nanostructure contains abundant inherent *hot-spots*, showing excellent SERS activity with an enhancement factor of $\sim 1.3 \times 10^7$ on a single particle basis. Besides, being encased in ultrathin hollow silica shell, not only the need of conventional organic capping ligands for stabilization is eliminated, but a chemically clean surface and a high accessibility of the *hot-spots* are guaranteed. While this nanoporosity constitutes a significant advantage from an application-oriented perspective, given that SiO_2-encapsulated AuAg alloy NPs can be enriched with the molecules of interest from an aqueous solution where they can be directly detected, adding magnetic properties to these nanomaterials would allow also the possibility to achieve analyte pre-concentration and obtain stronger SERS signals. In a similar and particularly inspiring work, Sanz-Ortiz et al. developed a method for synthetizing Au NPs protected by radial mesoporous silica (SiO_2) shells (**Figure 3 – B**).[19] Through a post-synthesis modification, using the radial mesoporous channels as templates, gold tips were grown and allowed to branch out from the cores: the resulting morphology improved significantly the particles' SERS analytical performance in solution by favoring the localization of diffusing analyte molecules at high electric field regions, found close to the tips and inside the pores.

Recently, the group of Hamad-Schifferli explored the use of SERS-active nanotags as efficient signal amplifiers in the commonly used LFA diagnostic platform. In two different works they used different plasmonic NCs morphologies, namely Au nanostars and AuAg NSs, for the sensitive and quantitative detection of Zika and Dengue biomarkers, and human myxovirus resistance protein A (MxA), respectively (**Figure 3 – C**).[20] In both cases the SERS amplification originated by the intrinsic surface plasmon enhancement provided by *hot-spots* distribution, located specifically on tips of Au nanostars, whilst homogeneously distributed on the whole AuAg NSs surface in a "continuous hot-spot" fashion. The use of plasmonically-engineered SERS nanotags provides one useful strategy for improving significantly the sensitivity and versatility of the LF assay format, which generally gives "yes-*vs*-no" answers and possesses limited dynamic ranges, but at the same time represents a technological requirement for a diagnostic platform known for its low cost and ease of use, an issue that could be however solved by the recent advancements in portable instrumentation and mobile phone technologies.

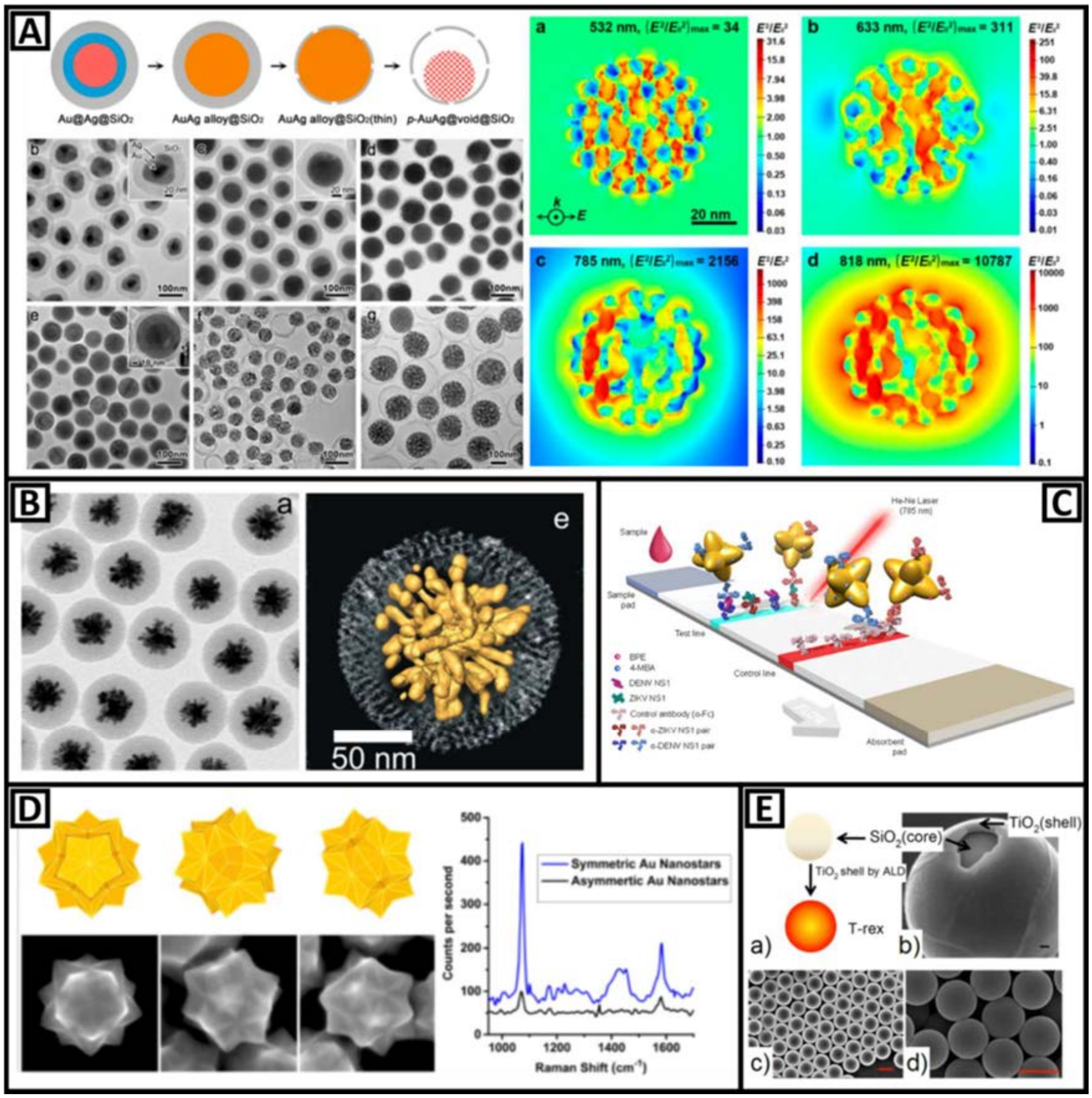

Figure 3 – Tuning plasmonic INPs for enhancing SERS sensitivity. **A: a)** Scheme illustrating the synthesis route for SiO_2-encapsulated porous AuAg alloy NPs. **b)** TEM images of the intermediates of the synthesis. **c)** Simulated FDTDs of SiO_2-encapsulated porous AuAg alloy NPs irradiated with different wavelengths (on-resonance condition). **B:** 2D (left) and 3D (right) TEM characterization of hybrid nanostructures containing nanospheres coated with mesoporous silica, after growing gold tips through the silica channels. **C:** Schematic representation of the SERS-LF strip based on the multiplexed immunoassay for the sensitive discrimination between Zika and Dengue biomarkers. **D: a)** SEM images and corresponding geometric models of Au nanostars viewed from their 5-fold, 3-fold, and 2-fold axes, respectively. **b)** SERS spectra of Raman reporter from symmetric (blue) and asymmetric (black) Au nanostars. **E: a)** Scheme of preparation of TiO_2 spherical resonators. **b)** SEM image showing a surface fracture, allowing to see the SiO_2 core and evaluate the thickness of the titania layer (scale bar: 100 nm). **c)** Low- and **d)** high-magnification SEM images of spherical resonators of different thicknesses (scale bars: 2 μm). Reproduced with permission from: **A:** ref. 18. *Copyright 2016, American Chemical Society*. **B:** ref. 19. *Copyright 2015, American Chemical Society*. **C:** ref. 20. *Copyright 2017, American Chemical Society*. **D:** ref. 21. *Copyright 2015, American Chemical Society*. **E:** ref. 22. *Copyright 2013, American Chemical Society*.

In another example (**Figure 3 – D**), Niu et al reported the synthesis of Au nanostars with unprecedented degree of symmetry control in high yield and with remarkable monodispersity.[21] Current synthetic methods of Au nanostars have limited control over their symmetry, generally resulting in uncertain number of arms with different lengths and random spatial arrangement, which in turn lead to poor reproducibility in their plasmonic and SERS applications. By using instead icosahedral seeds to dictate the growth of 3D evenly distributed arms in an I_h symmetric manner, highly symmetrical Au nanostars were synthetized, exhibiting superior single-particle SERS performance compared to asymmetric ones both in terms of intensity and reproducibility.

Finally, Alessandri demonstrated for the first time that a remarkable enhancement of Raman sensitivity can be obtained in the absence of plasmonic materials by means of titania (TiO_2) shell- based spherical resonators (**Figure 3 – E**).[22] The TiO_2 resonators used in this work consist of monodisperse core@shell SiO_2@TiO_2 microspheres, prepared by coating the silica cores with different conformal shell layers of amorphous TiO_2 with thicknesses of 5, 10, 20, 50, and 100 nm by atomic layer deposition, followed by its conversion into fully crystalline anatase by annealing. The physical principle allowing the SERS amplification observed relies on the high difference between the chosen materials' refractive indexes. By placing the TiO_2 high-refractive-index shell ($n \approx 2.5$ for the anatase) between two lower refractive index media (air, $n = 1$ and SiO_2, $n \approx 1.45$) total internal reflection of light within the titania shell layer can be achieved, giving rise to evanescent electromagnetic fields that can generate local surface "hot spots". This particular SERS substrate morphology allows therefore the investigation of analytes interacting with the TiO_2 surface as well as its recycle, thanks to the self-cleaning properties of anatase under UV irradiation.

Gas Sensors

Coupling mono-metallic NPs with metal oxides in complex nanoarchitectures has been shown to be a valuable approach to generate novel INPs with controlled topologies and structures, able to provide improved sensing performances through a diverse set of mechanisms.

Rai et al. reported the use of Ag@SnO_2 core-shell NPs to improve both sensitivity and specificity of *p*-xylene sensing (**Figure 4 – A**).[23] In order to detect this toxic volatile organic compound (VOC) they combined the already known sensing ability of tin oxide with the catalytic activity of silver NPs, finding out that Ag@SnO_2 NPs sensitivity for *p*-xylene was approximately 7 times higher than that of bare SnO_2 NPs. The improved gas sensing performance was attributed both to electronic and morphological features of the nanostructured transducer. Firstly, the increase in air resistance of Ag@SnO_2 core@shell NPs compared to bare SnO_2 NPs originates from a transfer of electrons from SnO_2 conduction band to Ag NPs due to the latter higher work function (4.7 eV) compared to the former one (4.5 eV). However, the increase of selectivity observed for *p*-xylene cannot be explained only with Ag NPs catalytic activity towards *p*-xylene gas, but also to the effective inwards diffusion of the VOC through the SnO_2 shell and its subsequent catalytic dissociation into smaller and more active species in the inner part of the nanoreactor.

Similarly, Tripathy et al. investigated Au@SnO_2 core-shell NPs for the carcinogenic VOC acetaldehyde photocatalytic sensing, revealing a higher sensitivity and selectivity with respect to Au/SnO_2 nanocomposites without the core–shell structure (**Figure 4 – B**).[24] In their synthetic design, the photoactive SnO_2 outer shells play an important role in absorption of incident photons and injection of electrons into the noble metal surfaces of Au NPs, which provide in turn a more efficient surface catalysis for acetaldehyde. However, given the high working temperatures required for this class of gas sensors, materials without a core–shell structure undergo a rapid grain growth and agglomeration, resulting in a loss in sensitivity. Thus, the core-shell morphology of Au@SnO_2 NPs not only allows the analyte gas adsorption on their porous surface and then react on the gold–tin dioxide interface, but also maintains the particles size at the high operating temperatures.

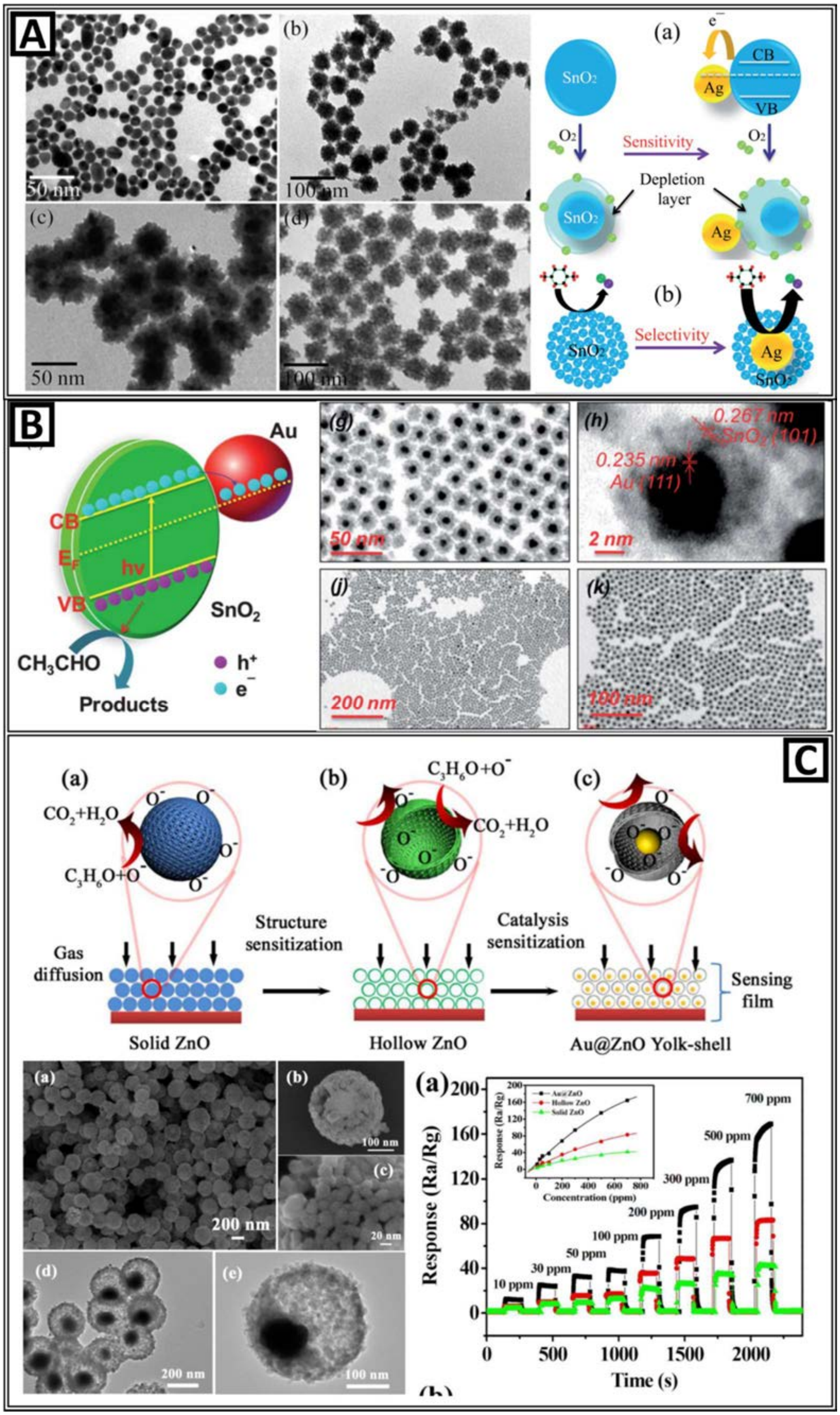
A
(b)
50 nm
100 nm
(c)
(d)
50 nm
100 nm
(a)
e⁻
SnO2
CB
Ag
VB
O2
Sensitivity
O2
Depletion
layer
SnO2
Ag
(b)
SnO2
Selectivity
Ag
SnO2
B
Au
CB
EF
hv
VB
SnO2
CH3CHO
Products
h⁺
e⁻
(g)
50 nm
(h)
0.267 nm
SnO2 (101)
0.235 nm
Au (111)
2 nm
(j)
200 nm
(k)
100 nm
C
(a)
(b)
(c)
CO2+H2O
C3H6O+O⁻
O⁻
Structure
sensitization
Catalysis
sensitization
Gas
diffusion
Sensing
film
Solid ZnO
Hollow ZnO
Au@ZnO Yolk-shell
(a)
(b)
100 nm
(c)
20 nm
200 nm
(d)
200 nm
(e)
100 nm
(a)
Response (Ra/Rg)
Time (s)
10 ppm
30 ppm
50 ppm
100 ppm
200 ppm
300 ppm
500 ppm
700 ppm
Au@ZnO
Hollow ZnO
Solid ZnO
Concentration (ppm)
(b)

Figure 4 (*previous page*) – Through the controlled synthesis of hybrid nanostructures containing both metallic and metal oxides materials, innovative nanoreactors function as sensitivie and selective substrates for gas sensing. **A: a)** TEM images of Ag and Ag@SnO$_2$ core@shell and bare SnO$_2$ NPs **b), c)** Schematic presentation of depletion layer formation and diffusion of p-xylene, respectively, in bare SnO$_2$ and Ag@SnO$_2$ core-shell NPs. **B: a)** Mechanism of photo- catalytic degradation of acetaldehyde over Au@SnO$_2$ NPs. **b)** TEM images showing the formation of monodisperse Au@SnO$_2$ core@shell nanostructures NPs. **C: a)** Typical SEM and TEM images of Au@ZnO yolk-shell nanospheres and Au@ZnO composites. **b)** Responses of pure (solid and hollow) ZnO nanospheres and Au@ZnO composites versus acetone concentration in the range of 10–700 ppm. **c)** Gas sensing principles of solid ZnO nanospheres, hollow ZnO nanospheres, and Au@ZnO nanospheres. Reproduced with permission from: **A:** ref. 23. *from the Royal Society of Chemistry*. **B:** ref. 24. *from the Royal Society of Chemistry*. **C:** ref. 25. *Copyright 2012, American Chemical Society* **D:** ref. 26. *Copyright 2014, American Chemical Society*.

In another notable example by Li et al., Au@ZnO yolk-shell nanospheres with a distinctive core@void@shell configuration have been successfully synthesized and applied as highly sensitive and selective acetone sensing substrate (**Figure 4 – C**).[25] The reported improvement in transducing performance, exhibiting an ultra-low detection limit of 200 ppb, was ascribed to the catalytic effect of Au particles and the unique structure of Au@ZnO yolk–shell nanospheres. The distinctive configuration (hollow interiors and porous shells) endows hollow Au@ZnO composite plenty of pores and facilitates the diffusion of the test gas. At the same time, the introduction of the Au core provides a larger degree of electron extractions from the conduction band of ZnO, corresponding to an increase in air resistance, as well as generating more reactive radical at the gold surface.

Composition

Multi-metallic and metal oxide NPs can be synthetized in a variety of conditions which allow to adjust their chemical composition through the formation of alloys, domains and core-shell structures. Different synthetic strategies for controlling INPs composition can be applied (i.e. cation exchange, galvanic replacement, co-precipitation), which in turn result in modifying their chemical reactivity, tuning their band-gap and affecting their redox behaviour.

Colorimetric Sensors

The possibility to tune the elemental composition of multi-metallic NPs has shown great promise for the production of inorganic catalysts.[4] Among the wide range of technological applications reported, catalytic INPs have been employed as advantageous inorganic substitutes for expensive and fragile natural enzymes due to their robustness in harsh experimental conditions and the easier production and engineering for *ad-hoc* properties. In the field of (bio)sensing, many reports exploit so-called *nanozymes* to catalyze the oxidation of small chromogenic molecules and dyes commonly used as indicator in colorimetric assays.

Wu et al. provided an insightful example of how the fine control over INPs metal composition allows to develop artificial peroxidase-like *nanozymes* able to function as signal amplifiers in a colorimetric H_2O_2 assay (**Figure 5 – A**).[26] They synthetized Pt-decorated Au branched (Au@Pt) nanostars, combining the strong electric field generated from the Au core for SERS enhancement, together with Pt catalysis towards the oxidation of 3,3',5,5'-tetramethylbenzidine (TMB) with H_2O_2 into oxidized TMB (TMBox). Finite difference time domain (FDTD) simulations were performed to reveal how different Pt contents would affect the electromagnetic field of the Au core, showing that Au@Pt nanostars with 2.5% Pt produced the highest Raman enhancement. Besides, kinetic studies on TMB oxidation lead to the optimization of the *nanozymes* Pt-based catalysis, since TMBox provided a characteristic SERS signal. With their clever design the authors showed how Au@Pt nanostars can act as amplifiers for both the SERS detection of TMB and its catalytic oxidation, and could apply the Au@$Pt_{2.5\%}$ nanozyme successfully in a colorimetric H_2O_2 assay. Unfortunately, the authors only run this assay in buffer media and do not attempt it in more complex matrixes, such as serum or cellular media, where the real-time monitoring of H_2O_2 could realistically be of more interest.

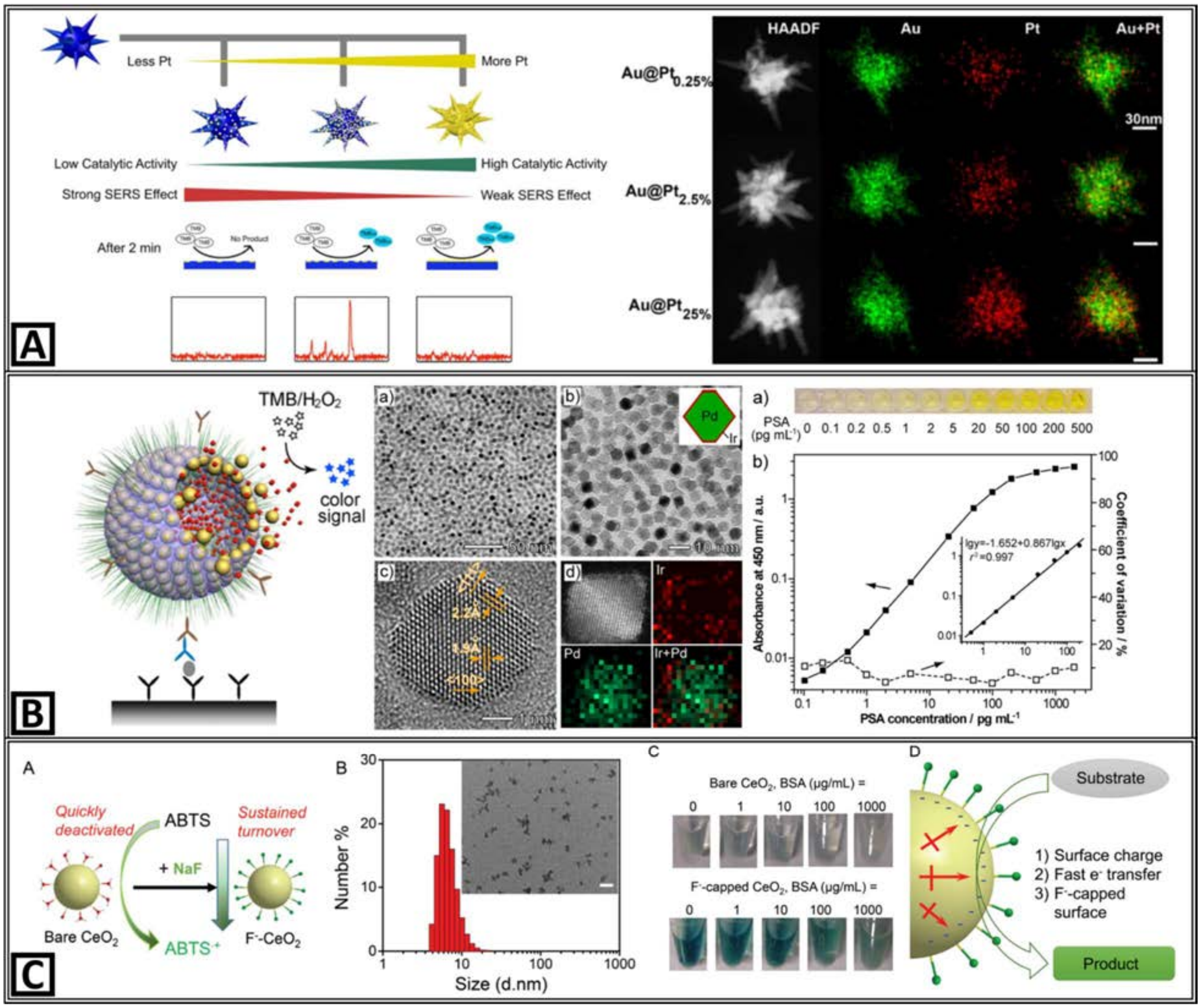

Figure 5 – Catalytic INPs as tunable nanozymes for colorimetric sensing. **A:** Schematics of branched Au@Pt NPs: various amounts of Pt precursor led to Au@Pt NPs with different shapes and LSPR features. The prepared Au@Pt NPs acted not only as peroxidase mimics for catalytically converting Raman-inactive reporters into active ones but also as the SERS-active substrates to enhance the activated reporters' Raman signals. **b)** High-angle annular dark field STEM images of Au@Pt NPs with different Pt contents and their corresponding elemental mapping. **B: a)** Schematic illustration of utilizing Pd@Ir NPs loaded into gold vescicles for ELISA detection of disease biomarkers. The Pd−Ir NPs released from captured gold vescicles act as effective peroxidase mimics to catalyze chromogenic substrates. **b)** Structural (low and high magnification TEM and HRTEM images) and compositional (HAADF-STEM image and EDX mapping) analyses of Pd@Ir NPs prepared by depositing Ir atoms on 5.6 nm Pd truncated octahedral seeds. **c)** Representative photographs taken from the Pd@Ir NPs based ELISA of PSA standards and corresponding calibration curve. **C: a)** Scheme showing F$^-$-capped nanoceria with improved oxidase turnovers. **b)** DLS size distribution and a TEM image of nanoceria. **c)** Photographs of ABTS oxidation by bare and F$^-$-capped CeO_2 in the presence of various concentrations of BSA protein. **d)** Proposed effects of F$^-$ as a promoter for the CeO_2 nanozyme. Reproduced with permission from: **A:** ref. 27. *Copyright 2018, American Chemical Society*. **B:** ref. 28. *Copyright 2017, American Chemical Society*. **C:** ref. 29. *from the Royal Society of Chemistry*.

Exploring the same TMB-directed catalysis, Ye et al. took advantage in a recent report of novel Pd@Ir NPs as peroxidase mimics (**Figure 5 – B**).[27] Compared to natural enzymes, Pd−Ir NPs possess much higher catalytic efficiency thanks to the coating of Ir monolayer on Pd seeds produced during their synthesis. In addition, Pd−Ir NPs consist of inert noble metals with excellent stabilities, enabling them to survive harsh environments (up to 200 °C and in strong acidic/basic conditions) while still retaining the peroxidase-like activity. Thanks to these features, they developed an enzyme-free signal amplification technique for traditional ELISAs based on the encapsulation of Pd-Ir NPs into gold vesicles. The significantly enhanced sensitivity obtained, achieving a limit of detection at the femtogram/mL level, was also made possible by the peculiar assay design chosen. The use of gold vesicles as carriers for the *nanozymes* maximized the loading capacity of Pd-Ir NPs, avoided the loss of catalytic efficiency caused by chemical conjugation with antibodies and favored their ready dispersion upon release, making them more active than immobilized catalysts on solid surfaces.

Generally, apart from their intrinsic low selectivity, the application of *nanozymes* can also be limited by their low catalytic activity and low turnover numbers. In their study, Liu and coworkers engineered CeO_2 NPs (nanoceria) obtaining a robust oxidase mimic, able to compete with its natural counterpart both in terms of catalytic rates and stability (**Figure 5 – C**).[28] The improved performances with respect to bare nanoceria was attributed to highly electron negative F- strong adsorption on CeO_2 surface, which can modulate the intrinsic energy bands of the nanomaterial. This in turn allowed altering nanoceria surface charge for tuning substrate adsorption affinity as well as preventing inhibition due to adsorption of the oxidation product, while at the same time facilitating electron transfer between substrates, oxygen, and the particle surface, all involved in the dye oxidation catalysis. These results allowed the development of a colorimetric, selective assay for F- detection in river water and commercial toothpastes, with LODs over 100-fold lower than the guideline recommended by the World Health Organization (WHO) for drinking water.

Photoluminescence Sensors

The unique photophysical properties of INPs have been deeply studied and applied in many optical sensing methodologies because of their intrinsic higher robustness to photo-bleaching compared to organic fluorescent dyes. In particular, the fluorescence in the visible range of quantum dots (QDs) and its dependence from their composition and size have made of them a versatile material for a number of optical sensing and imaging techniques.

Susumu et al. developed a whole palette of multishell ternary alloyed QDs for intracelular ratiometric pH sensing by synthetically controlling their elemental composition (**Figure 6 – A**).[29] Starting from monodisperse ZnSe cores, the fluorescence peak positions were precisely tuned by combining two synthetic strategies: cation exchange with Cd^{2+} ions and over-coating with CdZnS layers. Increasing the amount of Cd^{2+} ions used during cation exchange with ZnSe cores progressively causes a *red-shift* of the fluorescence band, allowing to adjust the fluorescence colors of ternary CdZnSe QDs from violet to blue and then green. Furthermore, an alloying process during the CdZnS overcoating steps lead not only to additional span the fluorescence wavelength, but also significantly improved the QYs (up to ~60%) and helped to protect the emitting cores from harsh biological environments (i.e. acidic or high in ionic content). These NCs were further conjugated with pH sensitive fluorescein derivatives and applied as ratiometric pH sensors, whose increased robustness and QYs allowed to monitor the pH changes localized in extracellular environments.

In a recent study, Pratsinis and coworkers rationally designed a label-free H_2O_2 biosensor based on CeO_2 NPs doped with Eu^{3+} in order to make them luminescent (**Figure 6 – B**).[30] Nanoceria is known to possess super oxide dismutase (SOD)-mimetic activity due to oxidation of Ce surface atoms (Ce^{3+} to Ce^{4+}) with concomitant catalytic decomposition of H_2O_2 adsorbed on the particle surface. This way, CeO_2 NPs act as electron sponges upon H_2O_2 decomposition with a delocalized charge density redistribution over the entire NP. In the luminescent $CeO_2{:}Eu^{3+}$ NPs described, any charge redistribution on the Ce−O bond resulting from H_2O_2 interaction markedly quenches their luminescence. Indeed, the results obtained showed how the emission intensity strongly depends on the average NP size, with higher intensities for larger crystal sizes, and that the smallest ones display the highest catalytic activity, confirmed the proposed mechanism. This intelligent transducer design represents a significant advantage compared to the organic dyes typically used in commercial H_2O_2 assays, which suffer from poor stability in ambient conditions (e.g., room lighting) and require tedious procedures. Instead, $CeO_2:Eu^{3+}$ NPs here demonstrated superior stability and reach low LODs, outperforming all reported optical, particle-based, enzyme-, conjugate- and label-free approaches for H_2O_2 detection in physiological, although protein-free, conditions.

Contrarily to *in vitro* measurements, the design of nanostructured reporters for *in vivo* fluorescence imaging has to consider the relatively high turbidity of tissues, which can damper photon penetration through scattering, absorption and auto-fluorescence of their components. The ability of lanthanide-based upconversion NPs (UCNPs) of converting lower energy photons into high-energy emissions represents a crucial advantage for achieving fluorescence bioimaging in the second NIR window (NIR-II, 1000-1700 nm), known to provide better spatial resolution and feature contrast at deeper imaging depth owing to reduced auto-fluorescence and photon scattering. In a remarkable recent work, Liu and coworkers developed a ratiometric, H_2O_2-sensitive microneedle patch sensor based on Er^{3+}-sensitized UCNPs for *in vivo* bioimaging of inflammation sites (**Figure 6 – C**).[31] They synthetized a new type of Er^{3+}/Ho^{3+}-doped UCNPs exhibiting both excitation (1530 nm) and emission (1180 nm) located in the NIR-II window.

Figure 6 (***next page***) **– A: a)** Schematic describing the multilayer synthesis of core@shell $Cd_xZn_{1-x}Se@Cd_yZn_{1-y}S@ZnS$ QDs. **b)** Fluorescence spectra and images of a series of $Cd_xZn_{1-x}Se/Cd_yZn_{1-y}S/ZnS$ and $ZnSe/Cd_yZn_{1-y}S/ZnS$ core@shell QDs synthesized in this study. **B: a)** Schematic representing biomimetic artificial enzymes based on antioxidant CeO_2 NPs that become luminescent upon their Eu^{3+} doping. **b)** Emission spectra of the smallest 4.4 nm $CeO_2:Eu^{3+}$ NPs in solutions before (red line) and after H_2O_2 addition (blue line). **C: a)** Illustration of ratiometric fluorescent sensor for H_2O_2 and kinetics studies of emission attenuation in the simulation tissue, absorption and upconversion emission spectra in presence of different concentrations of H_2O_2. **b)** Schematics, SEM and confocal laser scanning microscopy images of the fabrication process of microneedle patch of the microneedle patch. **c)** The *in vivo* bioimaging experimental setup and upconversion-luminescent images at 980, 1180 nm and ratiometric (I980/I1180) channels of microneedle patches taken at different time after lipopolysaccharide-induced inflammation. **D: a)** Luminescence decay curves of Er-doped NPs with energy relay shells of increasing thickness and incremental Er^{3+} doping concentration. **b)** Pseudocolour-mapped lifetime images of the Er-doped NPs. Reproduced with permission from: **A:** ref. 30. *Copyright 2017, American Chemical Society*. **B:** ref. 31. *Copyright 2017, American Chemical Society*. **C:** ref. 32. *Copyright © 2018 WILEY-VCH Verlag GmbH & Co. KGaA, Weinheim*. **D:** ref. 33. Springer: Nature. *Copyright 2018*.

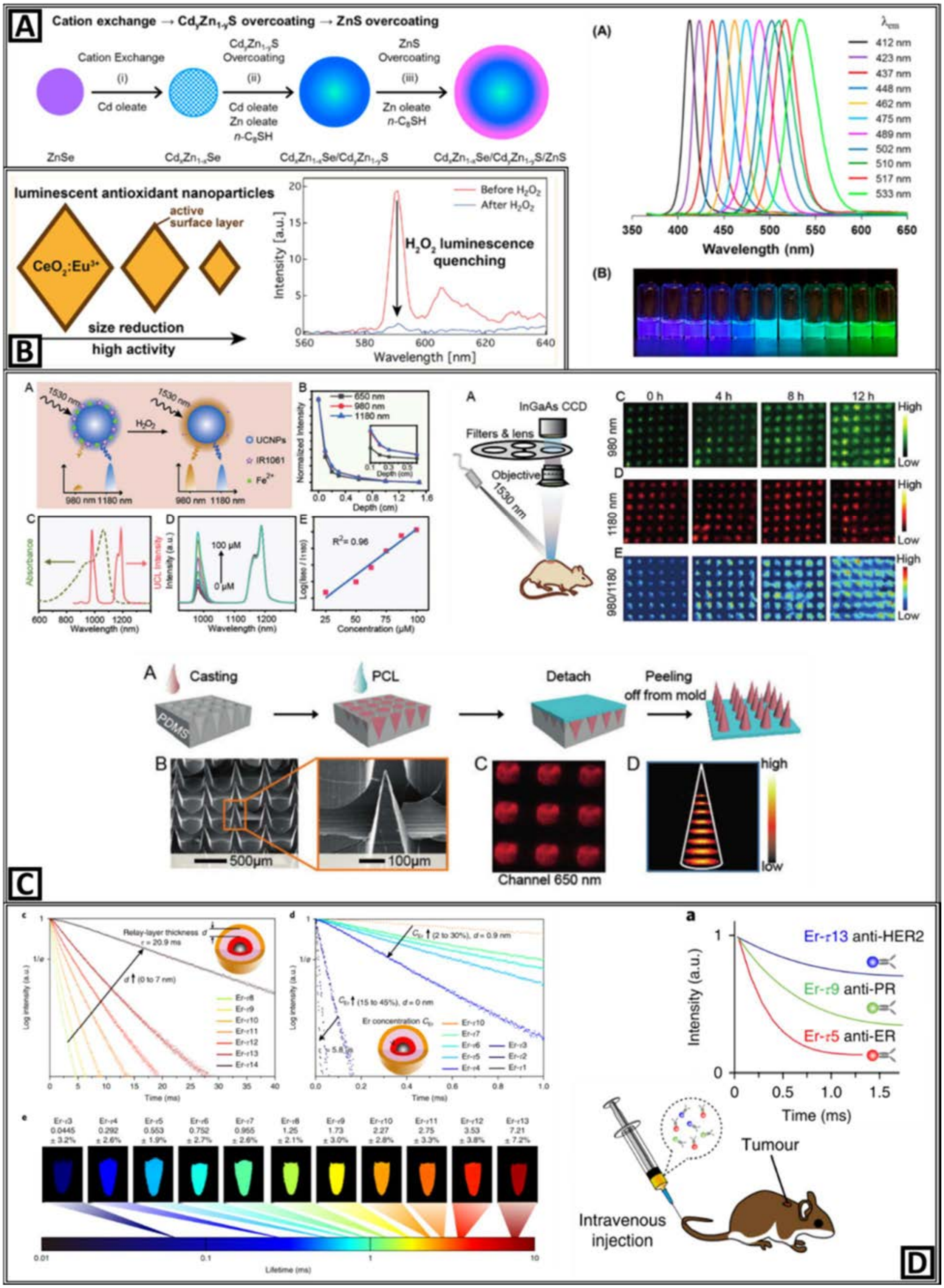
A
Cation exchange → $Cd_yZn_{1-y}S$ overcoating → ZnS overcoating
Cation Exchange
(i)
Cd oleate
$Cd_yZn_{1-y}S$ Overcoating
(ii)
Cd oleate
Zn oleate
n-C_8SH
ZnS Overcoating
(iii)
Zn oleate
n-C_8SH
ZnSe
$Cd_xZn_{1-x}Se$
$Cd_xZn_{1-x}Se/Cd_yZn_{1-y}S$
$Cd_xZn_{1-x}Se/Cd_yZn_{1-y}S/ZnS$
(A)
λ_{em}
412 nm
423 nm
437 nm
448 nm
462 nm
475 nm
489 nm
502 nm
510 nm
517 nm
533 nm
Wavelength (nm)
(B)
B
luminescent antioxidant nanoparticles
active surface layer
$CeO_2:Eu^{3+}$
size reduction
high activity
Before H_2O_2
After H_2O_2
H_2O_2 luminescence quenching
Intensity [a.u.]
Wavelength [nm]
A
1530 nm
H_2O_2
UCNPs
IR1061
Fe^{2+}
980 nm 1180 nm
B
650 nm
980 nm
1180 nm
Normalized intensity
Depth (cm)
C
Absorbance
UCL intensity
Wavelength (nm)
D
100 μM
0 μM
Intensity (a.u.)
Wavelength (nm)
E
$R^2 = 0.96$
Log(I_{980} / I_{1180})
Concentration (μM)
A
InGaAs CCD
Filters & lens
Objective
1530 nm
C
0 h
4 h
8 h
12 h
980 nm
High
Low
D
1180 nm
E
980/1180
A
Casting
PCL
Detach
Peeling off from mold
PDMS
B
500μm
100μm
C
Channel 650 nm
D
high
low
C
c
Relay-layer thickness d
τ = 20.9 ms
d ↑ (0 to 7 nm)
Er-τ8
Er-τ9
Er-τ10
Er-τ11
Er-τ12
Er-τ13
Er-τ14
Log intensity (a.u.)
Time (ms)
d
C_{Er} ↑ (2 to 30%), d = 0.9 nm
C_{Er} ↑ (15 to 45%), d = 0 nm
Er concentration C_{Er}
τ = 5.8 μs
Er-τ10
Er-τ7
Er-τ6
Er-τ5
Er-τ4
Er-τ3
Er-τ2
Er-τ1
e
Er-τ3 0.0445 ± 3.2%
Er-τ4 0.292 ± 2.6%
Er-τ5 0.553 ± 1.9%
Er-τ6 0.752 ± 2.7%
Er-τ7 0.955 ± 2.6%
Er-τ8 1.25 ± 2.1%
Er-τ9 1.73 ± 3.0%
Er-τ10 2.27 ± 2.8%
Er-τ11 2.75 ± 3.3%
Er-τ12 3.53 ± 3.8%
Er-τ13 7.21 ± 7.2%
Lifetime (ms)
a
Er-τ13 anti-HER2
Er-τ9 anti-PR
Er-τ5 anti-ER
Intensity (a.u.)
Time (ms)
Tumour
Intravenous injection
D

Thanks to the controlled lanthanide doping, Er^{3+} are acting as both sensitizer and emitter to harvest pump photons at 1530 nm and subsequently promote the 980 nm emission, while the Ho^{3+} dopants can also serve as emitter to generate an efficient upconversion emission at 1180 nm. The microneedle patch sensor for *in vivo* inflammation dynamic detection is developed based on the ratiometric fluorescence by combining the effective NIR-II emission of these novel Er^{3+}-doped UCNPs and H_2O_2 sensing organic probes under the Fenton catalysis of Fe^{2+}. Owing to the large anti-Stokes shifting, low auto-fluorescence and tissue scattering of the NIR-II upconversion luminescence, the inflammation can be imaged and evaluated *in vivo* at very high resolution.

Using a similar approach, Fan et al. tackled the challenge of achieving *in vivo* NIR-II multiplexing imaging through lanthanide-doped NIR-II NPs with engineered luminescence lifetimes (**Figure 6 – D**).[32] They were able to synthetize core@multi-shell nanostructures composed of an outer layer co-doped with Nd^{3+} and Yb^{3+}, an intermediate layer doped with Yb^{3+} only, and an inner layer co-doped with Yb^{3+} and Er^{3+}. Through a systematic tuning the lanthanide doping and thicknesses each external shell, they were able to finely tailor the luminescence lifetime over a dynamic range as large as three orders of magnitude (spanning from the microsecond to millisecond region). As clearly shown by their results, increasing the thickness of the energy relay layer prolongs the average process from absorption to emission, leading to a longer lifetime. On the other hand, an increase in the Er^{3+} concentration accelerates the conversion of stored energy into luminescence emission, which shortens the lifetime. Moreover, they demonstrated the enabling capabilities for *in vivo* multiplexed imaging of life-time-engineered NPs by conjugating them with antibodies against 3 different biomarkers for breast cancer and injecting them in mice, showing how these emission-encoded reporters could effectively distinguish the positive group from control one.

Electrochemical Sensors

Electrochemical sensing, especially when PoC, relies quite often on the use of redox enzymes, either as catalysts or reporters, for generating a number of successful technological solutions (i.e. glucose sensors in diabetes care). Nevertheless, natural enzymes suffer from their intrinsic susceptibility to non-optimal operating conditions and require costly processes for their modification/engineering. From this point of view, substituting them with catalytic of metallic and oxides NPs represents a great advantage for (bio)sensors development, given the possibility of controlling synthetically their chemical composition, adjusting their redox properties, as well as manipulating their electronic configurations resulting by their combination.

Wan et al. reported a novel strategy for electrochemical cancer cell identification and multi-marker analysis based on the use of a family of mono-metallic NPs, namely Cu, Ag and Pd NPs, selected depending on the reported oxidation potentials of their composing metals (**Figure 7 – A**).[33] Given that the simultaneous electrochemical readout of several markers requires redox-active probes with well-separated potentials, they confirmed that the redox chemistry of the chosen metallic NPs could be resolved using linear-sweep voltammetry. In a typical assay, Cu, Ag and Pd nano-reporters modified respectively with antibodies or aptamers for the specific recognition of different biomarkers expressed on cancer cells, were incubated with cells captured on an array of nanostructured gold electrodes. Electrochemical scans, which required only 10 seconds per scan, then oxidize the attached NPs directly, with different levels of current corresponding to the number of cells present on the sensor. This interesting strategy, extremely cheaper and simpler than typical immunostaining methods, allows to detect as few as two cancer cells per sensor and simultaneously analyze three different surface biomarkers in whole blood. However, the assay described requires the use of a HNO_3 solution for oxidizing the metallic particles and produce their respective cations, which are the actual redox-active species detected. This corrosive reagent becomes therefore an obstacle for the commercial application of this system.

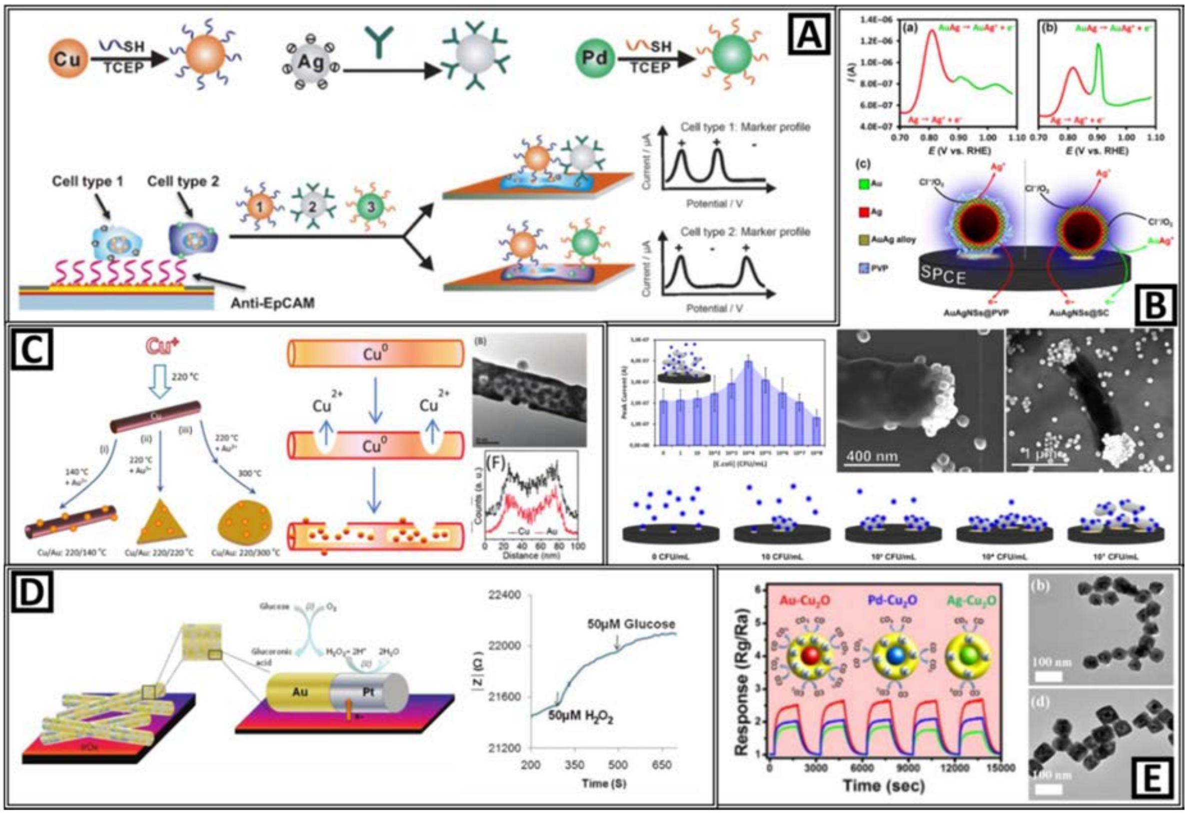

Figure 7 – Multimetallic INPs can act as inorganic catalytic substrates for electrochemical sensing. **A: a)** Monometallic NPs labels are made specific for cell surface markers with DNA aptamers attached using a thiol/metal bond to Cu or Pd NPs or antibodies attached to Ag NPs by electrostatic binding. **b)** Cancer cells are first captured on an electrode, then a mixture of modified Cu, Pd or Ag NPs is introduced and an electrochemical profile is generated using linear-sweep voltammetry. **B: a)** Electrochemical behavior of hollow AuAg NSs triggered by chlorides in PBS for different organic coatings. **b)** Schematization of the proposed electrochemical mechanism through controlled corrosion of Ag contained in the nanostructures. **c)** Detection of E.coli through non-specific adsorption and electrochemical oxidation of AuAg NSs: concentration profile, SEM images of bacterial cells-AuAg NSs complexes, and schematization of the sensing mechanism. **C: a)** Schematic fabrication of bimetallic Cu/Au nanostructures controlled with the temperature of synthesis**. b)** Schematic of the formation, TEM and line scanning of bimetallic Cu/Au nanotubes with gold-incorporated NPs. **D: a)** Proposed mechanism for glucose electrocatalytic detection using Au–Pt NWs: glucose is transported by convection to the gold surface, where it is oxidized to glucuronic acid by reducing O_2 to H_2O_2, after which H_2O_2 decomposes into H_2O on the platinum surface. **b)** Real-time impedancimetric response of the Au–Pt NWs-based electrode. **E: a)** Responses of pure Cu_2O and metal–Cu_2O NCs to 200 ppm of CO recorded at 200 °C and schematic of the sensing principle. **b)** TEM images of Au–Cu_2O and Pd–Cu_2O NCs. Reproduced with permission from: **A:** ref. 34. *Copyright © 2014 WILEY-VCH Verlag GmbH & Co. KGaA, Weinheim*. **B:** ref. 35 and 36. *Copyright © 2018 WILEY-VCH Verlag GmbH & Co. KGaA, Weinheim and Copyright 2019, American Chemical Society*. **D:** ref. 38. *from the Royal Society of Chemistry*. **E:** ref. 39. *Copyright 2014, Elsevier B.V.*

Recently, our group described for the first time the electrochemical properties of hollow AuAg NSs and their dependence on relative metal composition (**Figure 7 - B**).[34] In order to effectively make use of INPs as electrochemical reporters in real world applications, thus substituting expensive natural enzymes, their redox behaviour has to be activated *in situ* without the use of any secondary reagent. As shown previously, the general rout for "extracting" redox moieties from INPs is their acidic corrosion, which liberates metal cations that can be detected with voltammetric techniques but at the same time renders unfeasible its commercialization. The metal composition of AuAg NSs, instead, can be finely tuned to make them structurally robust, thanks to the thin Au shell, but at the same time corrodible in the mild oxidizing biological matrixes, given Ag well-known susceptibility to chlorides. Exploiting this versatile features, AuAg NSs were employed as redox reporter in the development of a simple and low-cost electrochemical assay for E.coli detection.[35]

In this context, Tee et al. fabricated an innovative, non-enzymatic glucose electrochemical sensor based on hollow Cu/Au nanowires (NWs), where the controlled tuning of relative composition of Au and Cu were obtained by adjusting the reduction temperature during synthesis (**Figure 7 – C**).[36] The glucose sensor demonstrates high sensitivity (down to a low detection limit of 2 μM), selectivity, with no significant response from the potential interfering species, and stability, exhibiting also a highly reproducible current response (more than 95% of its initial value) after 3 months. This great sensing capability was attributed firstly to the synergistic effect coming from the incorporation of Au into Cu nanostructures, which promoted faster electron transfers as well as significant electrocatalytic enhancement starting from 1 mol% gold relative composition. Besides, the porous Cu/Au@1% NWs exposed more electroactive sites and higher surface area and facilitate mass transport with higher current density. Despite the chemical and electrochemical inertness of Cu/Au NWs claimed by the authors, though, this innovative non-enzymmatic sensor was tested only on a rigid FTO-glass substrate, while it could be significantly improved if built onto flexible and biocompatible substrates.

In an analogous work aimed to substitute the conventionally used enzymes for glucose amperometric detection, namely glucose oxidase (GOx) or glucose dehydrogenase (GDH), Mayorga-Martinez reported the development of a non-enzymatic, impedimetric glucose sensor based on alloyed Au-Pt NWs (**Figure 7 – D**).[37] Generally, non-enzymatic noble metal-based electrodes used in glucose sensing quickly lose their activity due to accumulation of chemisorbed intermediates, which block the electrocatalytic surface. The use of bimetallic Au-Pt NWs favors the non-competitive occurring of two coupled reactions: the oxidation of glucose to gluconic acid and H_2O_2, catalyzed at the Au surface, and the reduction of hydrogen peroxide, catalyzed at the Pt surface. This sensor can therefore detect glucose through this mechanism because both metals are present at the electrode surface, while at the same time avoid surface passivation thanks to the polishing effect of catalytic H_2O_2 degradation.

Finally, the strategy of controlling INPs composition for tuning their electronic properties has proven to be effective also in the field of gas sensing, as shown by the work of Lin et al., who synthetized metal@Cu_2O core@shell NCs with different metal cores, namely Au, Ag and Pd (**Figure 7 – E**).[38] Cu_2O is a typical p-type semiconductor which displays changes in resistance when exposed to specific gas molecules through an electron–hole recombination mechanism promoted by chemisorbed reactive oxygen anions. The introduction of a metal in the semiconductor matrix alters holes mobility of the latter, which will then affect the electric response upon gas adsorption. In the report described, the influence of metal composition on the sensor response of metal@Cu_2O NCs was investigated, revealing their superior gas sensing performance in comparison with pure Cu_2O. Among them, Au–Cu_2O displayed the highest performance, followed by Pd and then Ag. This behavior depends on the work functions difference between the three noble metals and Cu_2O, whose reasoned combination can direct electron mobility towards the metal core, leaving abundant holes in Cu_2O and thus making it more susceptible to gases. An interesting and particularly advantageous aspect of this work resides in the mild conditions used for the synthesis of these composite NPs, which can be obtained in aqueous solution at 35 °C. Thanks to the use of citrate as only capping agent, Cu_2O can nucleate and grow easily and exclusively on the noble metal cores.

Surface

The great potential nanostructures show in many technological applications comes from the fact that many of their chemical reactivities and catalytic activities are surface-generated. The extremely high surface-to-volume ratio contributes to amplify significantly all surface-mediated processes and their effect on INPs' optical catalytic and electrochemical properties. Being able to modify these surface effects through the controlled synthesis of these materials opens to novel sensing pathways and mechanisms both in optical and electrochemical sensing.

Plasmonic Sensors

Rodriguez-Lorenzo et al. designed an ELISA with inverse sensitivity where Au nanostars act as plasmonic transducers upon Ag crystal growth on their surface (**Figure 8 – A**).[39] The largest LSPR variations in noble metal nanostructures are generally observed when they interact in close proximity with other metallic bodies. Thus, in their system the LSPR shift is tuned by programming *in situ* Ag crystal growth onto Au nanostars' surfaces proportional to the analyte concentration. In order to control crystal growth they used the enzyme glucose oxidase (GOx), which generates hydrogen peroxide that reduces silver ions and favors the formation of a silver coating around the transducer. The susceptibility of Au nanostars surfaces for a change in dielectric constant is so high that it provides the greatest sensitivity for the lowest concentrations of analyte: since GOx determines the rate of silver crystallization, directing it either towards free-standing Ag NPs nucleation, or towards Ag growth on Au nanostars' surface, when the enzyme is present at low concentrations, the short supply of reducing agent dictates slow crystal growth conditions. These favor in turn the deposition of a thin Ag coating using Au nanostars as seeding points, yielding a large blue-shift in the LSPR of the nanosensors even for enzyme concentrations as low as 10^{-20} gmL^{-1}. Despite this astounding sensitivity, this intelligent design do not solve any of the issues related to the fragility and shelf-life of natural enzymes, adding instead a further reagent ($AgNO_3$) for the assay revelation with its inherent more complex manipulation.

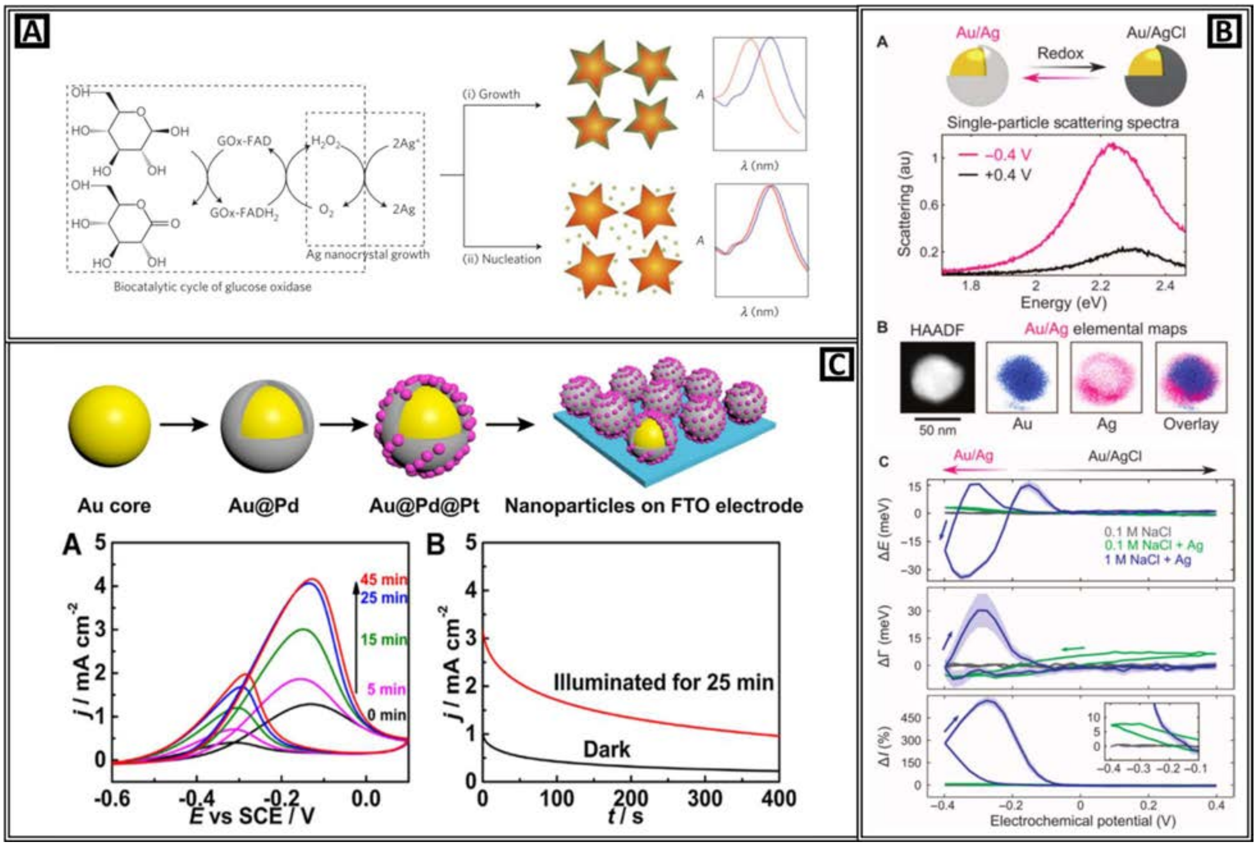

Figure 8 – The controlled modification of INPs' surfaces reflects on their plasmonic properties. **A:** Scheme of the proposed signal-generation mechanism by means of enzyme-guided crystal growth. GOx generates hydrogen peroxide, which reduces silver ions to grow a silver coating around plasmonic Au nanostars. **B: a)** Reversible redox tuning and optical response of Au@Ag NPs, whose shells were reversibly switched between Ag and AgCl using redox electrochemistry. **b)** HAADF- STEM and EDS elemental maps of a single Au@Ag NP. **c)** Mean response of changes in resonance energy (DE), full width at half maximum (DG), and intensity (DI) as a function of applied potential under different electrolyte conditions. **C: a)** Schematic illustration for the preparation of Au@Pd@Pt NPs. **b)** Cyclic voltammograms and i–t curves Au@Pd@Pt NPs under different illumination times. Reproduced with permission from: **A:** ref. 40. Springer: Nature. *Copyright 2012*. **C:** ref. 42. Copyright 2016, Elsevier B.V.

In a recent and particularly enlightening work, although not directly applied to the (bio)sensors field, Byers and coworkers show for the first time the active plasmon control of Au@Ag core@shell NPs through electrochemical reduction and chloridation of Ag on their surface (**Figure 8 – B**).[40] Through well-known Ag-AgCl redox chemistry, they were able to form and reversibly interconvert the shells between Ag and AgCl by electrochemical potential cycling, thus tuning the optical and electronic properties on both isolated Au NPs and strongly coupled

Au NP dimers. While in the AgCl shell case the local refractive index seen by the NP plasmon is that of the AgCl dielectric shell, a large change in NP optical properties occurs as the dielectric AgCl is replaced by Ag metal that supports plasmon resonances in the visible, since the refractive index is now that of the surrounding electrolyte. These reversible changes in NP optical properties, triggered by induced variations in the surface oxidation state, were even more pronounced for Au dimers with interparticle gap widths ranging from 1 to 5 nm. As the gap between Au NPs surfaces approached contact due to the metallic, highly conducting Ag shell formation, a charge transfer pathway through electron tunneling between NPs was observed. By then applying a positive potential, conductive coupling was broken as the shell composition was switched to semiconducting AgCl. This demonstrated that, under electrochemical potential control of NPs surfaces, the plasmonic coupling mechanism for NPs dimers was reversibly switched between capacitive and conductive coupling.

Finally, Yang et al. evaluated the potential of exploiting differences in noble metals work functions, that is their ability to gain or lose electrons, for directing electron transfers and therefore tailoring photoelectrocatalytic activities (**Figure 8 – C**).[41] They smartly designed trimetallic NPs composed by plasmonic Au cores whose surfaces were finely engineered with thin Pd shells decorated with Pt clusters through a systematic stoichiometric control during synthesis, and they probed its ability to promote the photoelectrocatalysis of methanol oxidation. The voltammetric investigation of the catalyzed reaction during different illumination times revealed how Au@Pd@Pt NPs provided enhanced catalytic performances compared to bimetallic systems, as well as observing an additional increase under illumination. This effect was strongly dependent on Pt coverage due to two parallel mechanisms: on one hand, synergistic surface effects occurring between Pt clusters grown on Pd surface can make the adsorption of poisoning CO decrease, and thus enhance the catalytic activity; on the other hand, an excess of Pt coverage could completely quench Au plasmon, blocking hot electrons generated from its LSPR from being transferred to Pd sites and enhance the electrocatalytic reduction of methanol. Furthermore, the trimetallic system displayed a secondary amplification mechanism caused by the LSPR-induced photothermal conversion under illumination, which caused an overall catalytic enhancement thanks to a local increase in temperature. Although not intended strictly for sensing applications, this system could be potentially applied as a sensitive methanol sensor thanks to its tunable, light-powered catalytic properties.

Colorimetric Sensors

A number of reports have shown how various chemical processes can be catalyzed by INPs' surfaces. Indeed, the exposition of different crystallographic facets and surface atoms with varying coordination number affects strongly the catalytic performance, often independently of the specific catalytic reaction. These phenomena have been studied and used for designing enzyme-mimicking INPs able to substitute their natural counterparts in colorimetric sensing.

Colloidal Au NPs are known to exhibit glucose oxidase (GOx)-like activity, that is to be able to catalytically oxidize glucose with the co-substrate oxygen (O_2) producing gluconate and hydrogen peroxide (H_2O_2). Luo and coworkers designed a GOx-like, self-limiting system in which the catalytic activity could be regulated by surface passivation and re-growth of Au NPs (**Figure 9 – A**).[42] Au NPs first catalyzed the glucose oxidation reaction, and the *in situ* generated product H_2O_2 reduced further $HAuCl_4$ added to Au^0, which deposited on the seeds surface as a nano-islands, leading to gradually enlarged and passivated NCs. Their results showed how Au atoms at the surface were responsible for the observed negative feedback, given the known tendency of NCs to minimize overall Gibb's free energy and surface tension through surface atom lattice rearrangement. In a following work by the same group, Zheng et al. demonstrated that the GOx-like catalytic activity of Au NPs could be finely regulated also by DNA hybridization, and that these catalytic Au NPs can be employed as a nanoprobes for a variety of biomolecular assays.[43] Given the GOx-like Au NPs high sensitivity to surface passivation, they showed that the relatively strong non-covalent interaction of single-stranded DNA with their surface could attenuate their catalysis, while, upon hybridization of complementary DNA probes, they would recover GOx-like activity.

Among the many *in vitro* diagnostic applications, multimetallic catalytic NPs have emerged as promising signal amplifiers in colorimetric immunoassays due to their high catalytic efficiency and extraordinary stability in harsh environments (i.e high temperature, extreme pH). In an admirable piece of applied research, Loynachan and coworkers incorporated peroxidase-mimicking porous platinum core@shell nanocatalysts (PtNCs) into LFA for the naked-eye detection of p24, the viral capsid protein of HIV (**Figure 9 – B**).[44] The extremely low LOD (down to femtomolar concentrations) and the broad dynamic range of the test obtained relied on the strong amplification mechanism through which PtNCs catalytic activity increases the signal intensity through local deposition of dyes at the test line. In order to produce this efficient amplification, PtNCs synthesis required careful optimization, focusing in particular on obtaining highly porous, polycrystalline platinum shells. This internal catalytic surface area is accessible through nanometer-scale pores to smaller molecules such as the peroxidase substrate H_2O_2, while inaccessible to larger molecules (i.e. antibodies and serum proteins), making PtNCs well suited for use in protein-rich serum environments. Moreover, these artificial *nanozymes* could retain their catalytic activity for over 6 months aging at room temperature, and only minimal change in test line intensity when incubated at 44 °C for 6 weeks, while HRP labels were found to lose 90% of signal intensity after 2 weeks in the same conditions.

The peroxidase-like activity of another class of multimetallic NPs, Au@Fe_3O_4 NPs, was effectively employed in the development of an aptasensor for ochratoxin (OTA) colorimetric detection by Wang et al., taking advantage of the intrinsic dual functionality of the Au@Fe_3O_4 NPs as magnetic separators and signal indicators (**Figure 9 – C**).[45] Surface-doping of Fe_3O_4 NPs with Au NPs enhanced the catalytic performance of the system thanks to the synergetic effect occurring at interface of the two components, effectively improving the affinity toward H_2O_2. However, the authors do not explore the dependence between the peroxidase-like activity of the composite material and its degree of surface Au doping, which could have potentially resulted in improved catalytic properties. Besides, even though a decrease in saturation magnetization, due to the diamagnetic contribution of the Au surface “wrapping”, was observed, Au@Fe_3O_4 NPs could be completely accumulated within 2 s upon placement of a magnet, behaving very similarly to super-paramagnetic particles. Thus, in a typical assay, capture-DNA (cDNA) probes were immobilized onto Au@Fe_3O_4 NPs, and the complex further attached to aptamer-functionalized glass beads through cDNA-aptamer hybridization. With the introduction of OTA (10 $ngmL^{-1}$), the cDNA-Au@Fe_3O_4 NPs linked on the glass beads were released in solution, due to the formation of the OTA-aptamer complex. After supernatant removal, Au@Fe_3O_4 NPs were collected through magnetic separation and then exposed to TMB in presence of H_2O_2 to produce a blue colored solution.

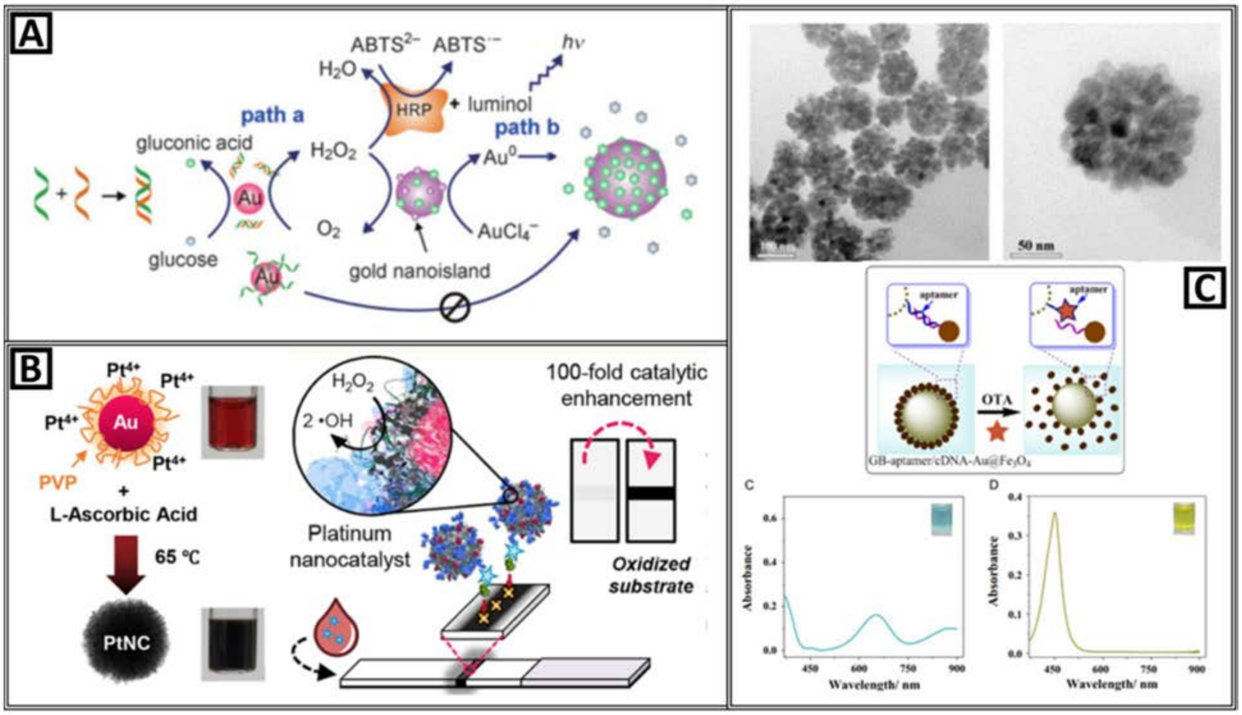

Figure 9 – Colorimetric sensing strategies based on catalytic INPs. **A:** Illustration of the GOx-like catalytic activity of AuNPs regulated by DNA hybridization, which can be either amplified by HRP- cascaded color or chemiluminescence variations (path a), or lead to nanoplasmonic changes owing to size enlargement (path b). **B: a)** Scheme showing synthesis of Au@Pt core@shell structure (PtNC), where 15 nm gold NPs are used as seeds for subsequent platinum overgrowth in the presence of polyvinylpyrrolidone (PVP) as a stabilizer and L-ascorbic acid as a reducing agent. **b)** Scheme showing amplified LFA where functionalized PtNCs and biotinylated nanobody fragments are mixed with a plasma or serum sample. In the presence of a target, PtNCs' [target]-dependent deposition at the test line catalyzes the production of an insoluble black product which is clearly visible with the naked eye. **C: a)** TEM images of Au@Fe_3O_4 NPs at low and high magnification. **b)** Schematic diagram of the basic principle for OTA aptasensing. **c)** Absorption spectra and corresponding photographs of the reaction solution before and after the colorimetric revelation of TMB. Reproduced with permission from **A:** ref. 44, *Copyright 2010, American Chemical Society*. **B:** ref. 45, *Copyright © 2011 WILEY-VCH Verlag GmbH & Co. KGaA, Weinheim*. **C:** ref. 46, Copyright 2016, Elsevier B.V.

Electrochemical Sensors

The interaction of INPs' surface with molecular species in solution or in any surrounding environment often results in a perturbation/modification of the electronic structure and/or band gap of the nanomaterial. This effect is the basis for building sensitive electrical and electrochemical sensors based on INPs with controlled surface chemistries and reactivities.

Following this strategy, Wang et al. prepared cobalt phosphate nanorods ($Co_3(PO_4)_2$ NRs) through a simple and effective micro-emulsion method which allowed fine control over surface area and porosity, exploring their potential as superoxide anions electrochemical sensors (**Figure 10 – A**).[46] Given the recognized importance of measuring reactive oxygen species (ROS) in living cells and tissues, phosphates and cobalt complexes were chosen as composing materials because of the widely recognized biocompatibility of the formers, and superoxide dismutase-like catalytic activity of the latters. The micro-emulsion synthetic method provided complete control over not only size and shape, but also surface area and pore size distribution, spanning between lamellar morphologies to homogeneous, ≈70 nm-long $Co_3(PO_4)_2$ NRs composed of a large number of ≈16 nm-sized NPs. Thanks to this engineered surface characterized by large specific surface area, rich porous network, and lower reaction and diffusion resistance, the nanostructure transducer exhibited ultrasensitive *in situ* detection of $O_2^{\bullet-}$ released from living normal and cancer cells, demonstrating superior electrocatalytic activity and sensitivity compared to the bulk analogous. The sharp oxidative peak and reductive waves observed in presence of $O_2^{\bullet-}$, corresponding to the electrochemical switching between Co^{II} and Co^{III}, received no interference from a series of ions (i.e. K^+, Na^+, Cl^-, SO^{4-}, NO^{3-}) as well as H_2O_2, presumably due to the highly specific catalytic effect of the biomimetic superoxide dismutase $Co_3(PO_4)_2$ NRs.

Maltez-da Costa et al. reported a simple and fast detection of cancer circulating cells (CTCs) using electrocatalytic Au NPs (**Figure 10 – B**).[47] They exploited the previously reported H_2 formation from solvated protons (hydrogen evolution reaction, HER) electrocatalyzed on the surface of 20 nm, citrate-coated Au NPs. CTCs detection was achieved after immunomagnetic capture and enrichment onto an electrode surface, were they were incubated with specific anti-CTCs antibodies labelled with Au NPs. Chronoamperometry was then applied and the current recorded, generated by the catalytic HER, corresponded to the number of Au NPs-CTC complexes. To improve the electrochemical signal, careful optimization of AuNPs/anti-CTC ratio was performed, so to avoid the catalytic surface blocking caused by an excess of antibody which could lead to a loss in current intensity. As already envisioned by the authors, due especially to the intrinsically digital output of the electrochemical assay, this strategy appears extremely promising for being applied in an automatized system, where the simple magnetic separation could be carried out inside a microfluidic chip.

A widely used strategy for electrochemical signal amplification is to maximize the loading of natural redox enzymes onto electrodes or nanocarriers. In a particularly interesting work, Zheng and coworkers reported a non-enzymatic nanoelectrocatalysts for ultrasensitive electrochemical cytosensing (**Figure 10 – C**).[48] They successfully combined the intrinsic surface-catalyzed activity of Fe_3O_4 submicrometer NCs toward the electrochemical reduction of small dye molecules with an original amplification strategy based on Ag-Pd nanocages. These bimetallic nanostructures were synthesized through galvanic replacement reactions using Ag nanocubes as the sacrificial templates, allowing the systematic adjustment of shell thickness and porosity, and then assembled onto Fe_3O_4 NCs electrostatically.

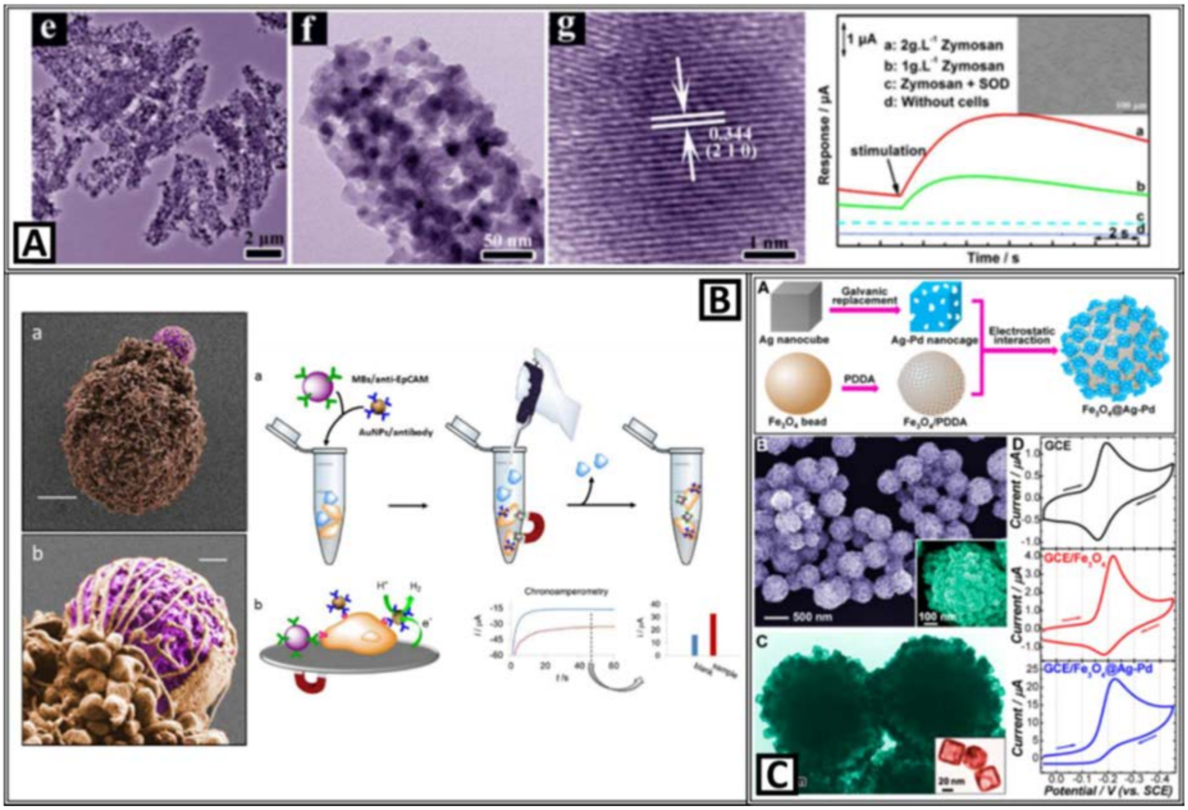

Figure 10 – Electrochemical sensors are built by tailoring different reactivities of INPs surfaces. **A: a)** TEM and HRTEM of $Co_3(PO_4)_2$ nanorods. **b)** Real time monitoring of $O_2^{\bullet-}$ released from living cells stimulated by different amount of drug in cell culture medium. **B: a)** SEM images of cancer cells captured with magnetic beads and labeled with AuNPs. **b)** Scheme describing cells capture and simultaneous labeling with AuNPs@specific antibodies in the presence of control cells, followed by detection of labeled ones through the HER electrocatalyzed by the AuNPs labels. **C: a)** Schematics of the fabrication of Fe_3O_4@Ag−Pd hybrid NPs. **b)** SEM and TEM images of Fe_3O_4@Ag−Pd hybrid NPs. **c)** CVs of a bare electrode, with Fe_3O_4 NPs and Fe_3O_4@Ag−Pd for thionine electrochemical detection. Reproduced with permission from **A:** ref. 47, Copyright 2017, Elsevier B.V. **B:** ref. 48, *Copyright 2012, American Chemical Society.* **C:** ref. 49, *Copyright 2014, American Chemical Society.*

The highest current amplification effect was observed for cages with thin shells and greater shell porosity, suggesting that high electron conductivity and large specific surface area could be synergistically responsible for the ∼5-fold enhancement of the cathodic current. Interestingly, while the current increased with the coverage density of the homogeneous Ag−Pd nanocages monolayer formed, no significant shift in potential was observed, indicating their role as a current amplifier rather than an electrocatalysts. Finally, using thiolated aptamers against CTCs, they were able to electrochemically detect as few as 4−5 cells captured on each electrode.

Conclusions and Future Perspectives

Inorganic nanomaterials have proven in a variety of examples to constitute useful and precious tools for improving the analytical performances of many different sensing and biosensing platforms. Reaching the fine control of their synthesis is the key for tuning their defining features, morphology, composition and surface, and for precisely tailoring their optical and electrochemical properties. Through these advancements in INPs synthesis, nanotechnology can provide valuable solutions to many practical issues often encountered by traditional biomolecular diagnostic techniques, such as proteins stability and shelf-life, need for secondary reagents and instrumentation, robustness in harsh environments lacking of technical resources and trained personnel. The exploration of cheaper and more abundant metallic nanomaterials (i.e. Cu, Al, Ni, Fe among others) as alternative to noble metal NPs can open the pathway for mass production of affordable diagnostic platforms without compromising their enhanced properties.[49] Through the reasoned tailoring of their optical and electrochemical properties, these systems can be used without costly and delicate benchtop instrumentation by integrating them with ubiquitous mobile phones[50] as well as develop smart and simple strategies for minimum manipulation.[51] These features are strongly and urgently needed for truly translating the potential of nanotechnology to the diverse array of diagnostic technologies devoted to PoC applications in resources-poor settings and developing countries.

References

1. Wang, Y., He, J., Liu, C., Chong, W. H. & Chen, H. Thermodynamics versus kinetics in Nanosynthesis. *Angew. Chemie - Int. Ed.* **54,** 2022–2051 (2015).
2. Xin, H., Namgung, B. & Lee, L. P. Nanoplasmonic optical antennas for life sciences and medicine. *Nat. Rev. Mater.* **3,** 228–243 (2018).
3. Zhang, S., Geryak, R., Geldmeier, J., Kim, S. & Tsukruk, V. V. Synthesis, Assembly, and Applications of Hybrid Nanostructures for Biosensing. *Chem. Rev.* **117,** 12942–13038 (2017).
4. Prieto, G. *et al.* Hollow Nano- and Microstructures as Catalysts. *Chem. Rev.* **116,** 14056–14119 (2016).
5. Erwin, W. R., Zarick, H. F., Talbert, E. M. & Bardhan, R. Light trapping in mesoporous solar cells with plasmonic nanostructures. *Energy Environ. Sci.* **9,** 1577–1601 (2016).
6. Casals, E. *et al.* Programmed iron oxide nanoparticles disintegration in anaerobic digesters boosts biogas production. *Small* **10,** 2801–2808 (2014).
7. Lu, J. *et al.* The role of nanotechnology in the development of battery materials for electric vehicles. *Nat. Nanotechnol.* **11,** 1031–1038 (2016).
8. Sanne, J.-L. Horizon 2020 SME Instrument Topic : PHC12 - Clinical research for the validation of biomarkers and / or diagnostic medical devices. *Per. Med.* **15,** 303–309 (2018).
9. Perfézou, M., Turner, A. & Merkoçi, A. Cancer detection using nanoparticle-based sensors. *Chem. Soc. Rev.* **41,** 2606–2622 (2012).
10. Aragay, G., Pino, F. & Merkoçi, A. Nanomaterials for sensing and destroying pesticides. *Chem. Rev.* **112,** 5317–5338 (2012).
11. Chiu, C. Y. & Huang, M. H. Polyhedral Au-Pd core-shell nanocrystals as highly spectrally responsive and reusable hydrogen sensors in aqueous solution. *Angew. Chemie - Int. Ed.* **52,** 12709–12713 (2013).
12. Genç, A. *et al.* Hollow metal nanostructures for enhanced plasmonics: Synthesis, local plasmonic properties and applications. *Nanophotonics* **6,** 193–213 (2017).
13. Russo, L. *et al.* SuppInfo - Time- and Size-Resolved Plasmonic Evolution with nm Resolution of Galvanic Replacement Reaction in AuAg Nanoshells Synthesis. *Chem. Mater.* **30,** 5098–

5107 (2018).

14. Genç, A. *et al.* Tuning the plasmonic response up: Hollow cuboid metal nanostructures. *ACS Photonics* **3,** 770–779 (2016).

15. McPeak, K. M. *et al.* Ultraviolet Plasmonic Chirality from Colloidal Aluminum Nanoparticles Exhibiting Charge-Selective Protein Detection. *Adv. Mater.* **27,** 6244–6250 (2015).

16. Yuan, H. *et al.* Gold nanostars: Surfactant-free synthesis, 3D modelling, and two-photon photoluminescence imaging. *Nanotechnology* **23,** 075102 (2012).

17. Bi, C. *et al.* Realizing a Record Photothermal Conversion Efficiency of Spiky Gold Nanoparticles in the Second Near-Infrared Window by Structure-Based Rational Design. *Chem. Mater.* **30,** 2709–2718 (2018).

18. Liu, K. *et al.* Porous Au-Ag nanospheres with high-density and highly accessible hotspots for SERS analysis. *Nano Lett.* **16,** 3675–3681 (2016).

19. Sanz-Ortiz, M. N., Sentosun, K., Bals, S. & Liz-Marzán, L. M. Templated Growth of Surface Enhanced Raman Scattering-Active Branched Gold Nanoparticles within Radial Mesoporous Silica Shells. *ACS Nano* **9,** 10489–10497 (2015).

20. Sánchez-Purrà, M. *et al.* Surface-Enhanced Raman Spectroscopy-Based Sandwich Immunoassays for Multiplexed Detection of Zika and Dengue Viral Biomarkers. *ACS Infect. Dis.* **3,** 767–776 (2017).

21. Niu, W., Chua, Y. A. A., Zhang, W., Huang, H. & Lu, X. Highly Symmetric Gold Nanostars: Crystallographic Control and Surface-Enhanced Raman Scattering Property. *J. Am. Chem. Soc.* **137,** 10460–10463 (2015).

22. Alessandri, I. Enhancing raman scattering without plasmons: Unprecedented sensitivity achieved by TiO2 shell-based resonators. *J. Am. Chem. Soc.* **135,** 5541–5544 (2013).

23. Rai, P., Majhi, S. M., Yu, Y. T. & Lee, J. H. Synthesis of plasmonic Ag@SnO2 core-shell nanoreactors for xylene detection. *RSC Adv.* **5,** 17653–17659 (2015).

24. Tripathy, S. K., Mishra, A., Jha, S. K., Wahab, R. & Al-Khedhairy, A. A. Synthesis of thermally stable monodispersed Au@SnO2 core-shell structure nanoparticles by a sonochemical technique for detection and degradation of acetaldehyde. *Anal. Methods* **5,** 1456–1462 (2013).

25. Li, X. *et al.* Design of Au@ZnO yolk-shell nanospheres with enhanced gas sensing properties. *ACS Appl. Mater. Interfaces* **6,** 18661–18667 (2014).

26. Wu, J. *et al.* Rational Design of Au@Pt Multibranched Nanostructures as Bifunctional Nanozymes. *ACS Appl. Mater. Interfaces* **10,** 12954–12959 (2018).

27. Ye, H. *et al.* An Enzyme-Free Signal Amplification Technique for Ultrasensitive Colorimetric Assay of Disease Biomarkers. *ACS Nano* **11,** 2052–2059 (2017).

28. Liu, B., Huang, Z. & Liu, J. Boosting the oxidase mimicking activity of nanoceria by fluoride capping: Rivaling protein enzymes and ultrasensitive F^- detection. *Nanoscale* **8,** 13562–13567 (2016).

29. Susumu, K. *et al.* Purple-, Blue-, and Green-Emitting Multishell Alloyed Quantum Dots: Synthesis, Characterization, and Application for Ratiometric Extracellular pH Sensing. *Chem. Mater.* **29,** 7330–7344 (2017).

30. Pratsinis, A. *et al.* Enzyme-Mimetic Antioxidant Luminescent Nanoparticles for Highly Sensitive Hydrogen Peroxide Biosensing. *ACS Nano* **11,** 12210–12218 (2017).

31. Liu, L. *et al.* Er^{3+} Sensitized 1530 nm to 1180 nm Second Near-Infrared Window Upconversion Nanocrystals for In Vivo Biosensing. *Angew. Chemie - Int. Ed.* **57,** 7518–7522 (2018).

32. Fan, Y. *et al.* Lifetime engineered NIR-II nanoparticles unlock multiplexed in vivo imaging. *Nat. Nanotechnol.* **13,** 941–946 (2018).

33. Wan, Y. *et al.* Highly Specific Electrochemical Analysis of Cancer Cells using Multi-Nanoparticle Labeling. *Angew. Chemie - Int. Ed.* **53,** 13145–13149 (2014).

34. Russo, L., Puntes, V. & Merkoçi, A. Tunable Electrochemistry of Gold-Silver Alloy Nanoshells. *Nano Res.* **11,** 6336 (2018).

35. Russo, L. *et al.* A low-cost strategy for the development of a rapid electrochemical assay for bacteria detection based on AuAg nanoshells. *ACS Omega* in press (2019).

36. Tee, S. Y. *et al.* Fabrication of bimetallic Cu/Au nanotubes and their sensitive, selective, reproducible and reusable electrochemical sensing of glucose. *Nanoscale* **7,** 11190–11198 (2015).

37. Mayorga-Martinez, C. C., Guix, M., Madrid, R. E. & Merkoi, A. Bimetallic nanowires as electrocatalysts for nonenzymatic real-time impedancimetric detection of glucose. *Chem. Commun.* **48,** 1686–1688 (2012).

38. Lin, Y. K., Chiang, Y. J. & Hsu, Y. J. Metal-Cu2O core-shell nanocrystals for gas sensing applications: Effect of metal composition. *Sensors Actuators, B Chem.* **204,** 190–196 (2014).

39. Rodríguez-Lorenzo, L., de la Rica, R., Álvarez-Puebla, R. a., Liz-Marzán, L. M. & Stevens, M. M. Plasmonic nanosensors with inverse sensitivity by means of enzyme-guided crystal growth. *Nat. Mater.* **11,** 604–607 (2012).

40. Byers, C. P. *et al.* From tunable core-shell nanoparticles to plasmonic drawbridges: Active control of nanoparticle optical properties. *Sci. Adv.* **1,** e1500988 (2015).

41. Yang, H. *et al.* Surface plasmon resonance promoted photoelectrocatalyst by visible light from Au core Pd shell Pt cluster nanoparticles. *Electrochim. Acta* **209,** 591–598 (2016).

42. Luo, W. *et al.* Self-catalyzed, self-limiting growth of glucose oxidase-mimicking gold nanoparticles. *ACS Nano* **4,** 7451–7458 (2010).

43. Zheng, X. *et al.* Catalytic gold nanoparticles for nanoplasmonic detection of DNA hybridization. *Angew. Chemie - Int. Ed.* **50,** 11994–11998 (2011).

44. Loynachan, C. N. *et al.* Platinum Nanocatalyst Amplification: Redefining the Gold Standard for Lateral Flow Immunoassays with Ultrabroad Dynamic Range. *ACS Nano* **12,** 279–288 (2018).

45. Wang, C. *et al.* Colorimetric aptasensing of ochratoxin A using Au@Fe3O4nanoparticles as signal indicator and magnetic separator. *Biosens. Bioelectron.* **77,** 1183–1191 (2016).

46. Wang, M. Q. *et al.* Nanostructured cobalt phosphates as excellent biomimetic enzymes to sensitively detect superoxide anions released from living cells. *Biosens. Bioelectron.* **87,** 998–1004 (2017).

47. Maltez-Da Costa, M. *et al.* Simple monitoring of cancer cells using nanoparticles. *Nano Lett.* **12,** 4164–4171 (2012).

48. Zheng, T. *et al.* Robust nonenzymatic hybrid nanoelectrocatalysts for signal amplification toward ultrasensitive electrochemical cytosensing. *J. Am. Chem. Soc.* **136,** 2288–2291 (2014).

49. Kim, S., Kim, J. M., Park, J. E. & Nam, J. M. Nonnoble-Metal-Based Plasmonic Nanomaterials: Recent Advances and Future Perspectives. *Adv. Mater.* **1704528,** 1–24 (2018).

50. Quesada-González, D. & Merkoçi, A. Nanomaterial-based devices for point-of-care diagnostic applications. *Chem. Soc. Rev.* **47,** 4697–4709 (2018).

51. Huang, X., Liu, Y., Yung, B., Xiong, Y. & Chen, X. Nanotechnology-Enhanced No-Wash Biosensors for In Vitro Diagnostics of Cancer. *ACS Nano* **11,** 5238–5292 (2017).

The mechanisms of protein adsorption onto nanoparticles

As introduced in the previous section, large surface area and low coordination of the atoms located at the surface determines the high energy potential of INPs and consequently their catalytic behaviors and reactivity profiles. This explains the successful use of many inorganic NPs as catalyst (such as small Pt for fuel cells)[1,2] or as a reagent (such as zero-valent iron for environmental remediation).[3] The application of INPs in biosensing, though, has revealed how their *in vivo* and *in vitro* behavior changes substantially in comparison with other systems.[4] In fact, when exposed to biological fluids the surface of INPs interacts strongly and dynamically with the complex mixture of ions, small molecules and proteins contained in complex biological matrixes, undergoing a set of alterations in structure and reactivity. For this reason, the potential impact of engineered INPs in biosensing is not only determined by the physicochemical properties of the NPs *per se*, but also on the interactions of these NPs with the immediate surrounding biological environments. On the other hand, in order to use INPs as optical or electrochemical labels to detect specific target analytes in complex matrixes, the intentional and therefore controlled immobilization of biological receptors such as antibodies onto their surfaces is necessary for providing them with specific recognition capabilities.

Homo- vs Hetero-aggregation

Due to their high percentage of surface atoms and their colloidal nature, once being brought into contact with a physiological medium INPs experience processes that lead them towards more stable thermodynamic states,[4,5] including aggregation, corrosion, dissolution and interaction with media proteins. Interestingly, while the high ionic strengths of biological media can destabilize INPs through aggregation and corrosion, at the same time they can be coated by proteins, which in turn stabilize them against aggregation and sedimentation (**Figure 1**).[6] When salinity is increased, the screening of electrostatic repulsion by adsorbed salt ions causes fast *homo*-aggregation between NPs (**Figure 1a**). When proteins are present in the medium (**Figure 1b**), they provide instead a stabilizing electro-steric (electrostatic and steric) effect upon adsorption (*hetero*-aggregation) on NPs surfaces, an effect that can prevent NPs from precipitation only if a sufficient concentration of proteins is available. Later on, NPs may undergo chemicals transformations that lead to their dissolution, the third mechanism able to further lower NP colloidal stability, where electrolyte ions (together with dissolved oxygen and/or helped by acidic environments) start oxidizing surface atoms (**Figure 1c**). The kinetics of these three separate but often co-existing processes are strongly influenced by the respective concentrations of the causing chemical agents. Indeed, proteins in solution have to be at much higher concentration than NPs in order to avoid NP aggregation when dispersed in media of high ionic strength as physiological media, indicating the stronger tendency of NPs for *homo*-aggregation than *hetero*-aggregation.[7] These coupled processes are mediated by the different interactions between the NPs and components of the biological medium in which they are exposed, and ultimately determine the nature of the nano-bio interface.[5,8–13]

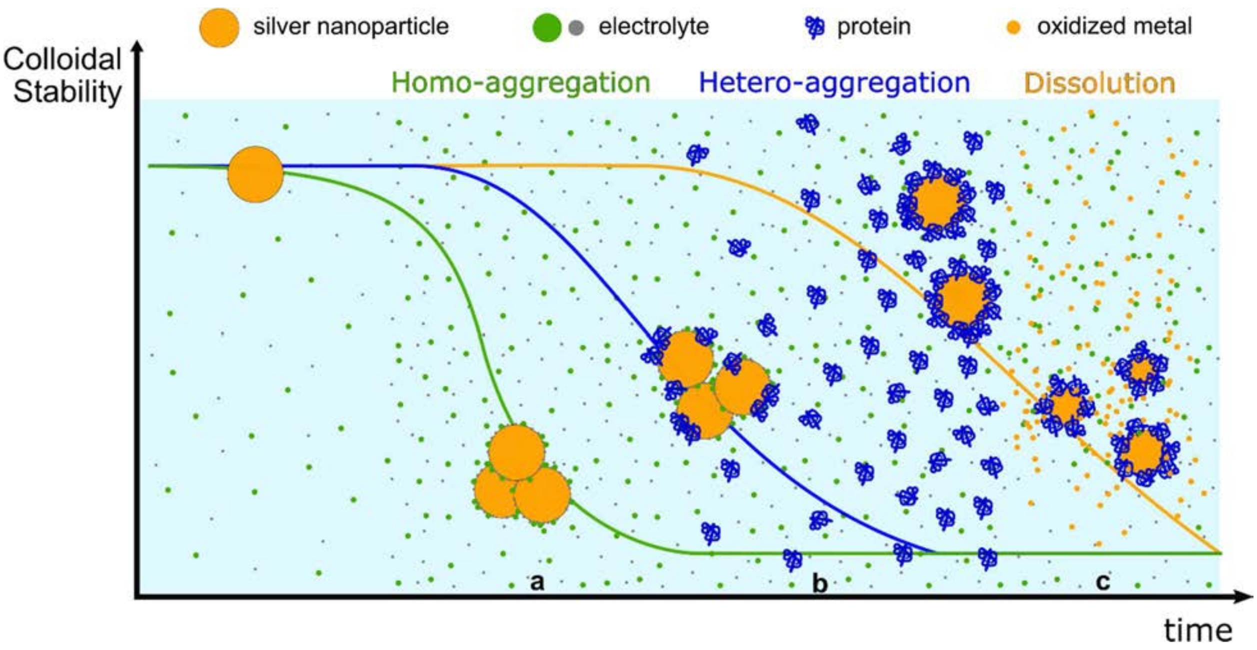

Figure 1 – Colloidal and Chemical Stability of NPs. **a)** Homo-aggregation induced by high ionic concentration; **b)** Hetero-aggregation between NPs and proteins at different concentration rates; **c)** chemical degradation, corrosion and dissolution of NPs incubated longer incubation times in physiological media.

Remarkably, small modifications on the nature of the conjugate and the dispersing media have a strong influence on conjugate interactions and consequently different biological behavior and fate.[14] Since NPs can be produced with different functional groups on their surface, by modifications of NP's surface coating, charge and hydrophobicity, their reactivity can be modified altering its interactions with the biological surroundings.[15] From the NP point of view, the different interactions can cause phase transformations, particle aggregation, surface reconstruction and dissolution, all processes that can have a significant influence on their reactivity.[4] From the biomolecules point of view, these interactions may lead to their physical adsorption onto NPs' surface and thus to the formation of Protein Coronas (PCs) of a different nature.[7,16–18]

Physical Adsorption of Proteins

In order to understand the interaction between INPs and biological fluids, it is worth to study the most important factors that define the relationships between biological fluids and inorganic solid surfaces. Hydrophobicity and surface charge have historically been the factors taken into account to describe the process of protein adsorption to surfaces. This was illustrated in the work of Prime and Whitesides using self-assembled monolayers (SAMs) supported onto gold films.[19] Those SAMs consisted on alkane chains with different terminal groups, that provided different hydrophobicity, and the more hydrophobic the conjugate the greater the degree of adsorption. Also the net charge of the protein can drive its adsorption. A higher adsorption of positively charged proteins onto negatively charged polystyrene surfaces and vice versa was observed by Norde and Lyklema.[20] Several examples of the role of surface charge and hydrophobicity on the protein adsorption process to surfaces and NPs can be found in the literature.[21,22] Undoubtedly, the set of interactions by which proteins stick to surfaces are principally weak interactions, namely hydrophobic interactions, electrostatic interactions and hydrogen bonds.

Over recent decades, many studies of interface phenomena involving proteins have identified their adsorption to surfaces as an irreversible process (hence, the failure in fitting protein adsorption data to the Langmuir equation).[23] At first, that proteins are provided with multiple, although weak, anchor points was the strongest argument for this irreversibility. Different studies aimed to describe the hardening of the protein adsorption process through different mechanisms. Norde and Anusiem,[24] for example, reported that Bovine Serum Albumin

(BSA) that adsorbed to silica surface and later desorbed had more affinity for silica surfaces than BSA that had not undergone this process. In a further work,[25] they suggested that the attachment BSA-silica surface caused an increase in the internal entropy of BSA, perhaps a slight modification of its structure, resulting in desorbed BSA being more stable on silica surface than "fresh" BSA. The work of Nygren and Aleadine[26] showed that, contrary to what might be suspected, proteins do not distribute on surfaces randomly. Instead, once the first proteins are attached, an initial cluster of proteins forms around, stabilizing them (a positive cooperative tendency also called "crowding" effect), and this mechanism is repeated until the entire surface is filled. These and other attempts to explain the irreversibility of this process seem to have in common that the initial attachment of a protein to a surface is followed by a series of movements and/or rearrangements to make this attachment more stable and ultimately irreversible. Therefore, not only affinities but also mechanisms such as conformational rearrangements and time- and concentration-dependent surface distribution have been identified as determining factor in making the adsorption as definitive.

Hard and Soft Protein Corona

The fact that adsorption of proteins turns irreversible through these time-dependent mechanisms has important implications in the case of complex mixtures of proteins such as blood serum, plasma, etc. According to the Vroman Effect,[27] initially proteins with low affinity (i.e. proteins that when adsorbed are rapidly desorbed) establish a fast equilibrium exchange between surface and solution, failing in generating strong attachment to the surface and therefore stabilize onto it. Later on, proteins possessing a higher affinity for the surface are able to adsorb and stabilize onto it despite the delayed occupation of the attachment sites. Thus, the "Soft" corona is formed initially, with more abundant and mobile proteins coating the NPs surface, but with weak and dynamic interactions, setting an equilibrium between bound and unbound proteins in solution. As time goes by, the adsorption equilibrium shifts towards the attachment of proteins with higher affinities for NPs surface, modifying the initial corona composition resulting into a "Hard" corona. At the same time, an ensemble of thermodynamic stabilizations mechanisms (i.e. conformational rearrangements, crowding effects) hardens the proteins layer bringing it to a steady, irreversible minimum energy state.[7] This process can be followed through a set of common techniques, namely UV–vis Absorption Spectroscopy (UV–

vis) and measurements of hydrodynamic radii by Dynamic Light Scattering (DLS) and surface charge by ζ-potential.

Initially (**Figure 2a**), only a weakly bound layer of proteins (*grey*) adsorb on the particle surface, stabilizing the colloid in the saline medium but being in dynamic equilibrium with the unbound ones in solution. When the incubation is extended for longer times, the corona stabilizes progressively through the different mechanisms described, leading to the stronger attachment of proteins onto the particles surface (*black*). If purified through centrifugation and re-suspension in protein-free physiological media (**Figure 2b**), protein-coated NPs display different colloidal stabilities depending on the duration of the incubation time. After short ones, loosely bound proteins readily detach from NP surfaces causing them to irreversibly aggregate in the saline medium. Colloidal stability increases gradually with longer expositions to proteins, which become more and more tightly adsorbed onto NP surfaces and do not get lost with purification. Besides the evident time dependency, PC hardening kinetics strongly depend as well on each experimental parameter involved (i.e. NP material, size and concentration, protein type and concentration, pH and ionic strength of biological media). The immobilization of biological receptors onto micro- and nanoparticles, a process often referred as bioconjugation, represents possibly the most widespread and explored strategy used for the preparation of nanobiosensors.[28] Thus, understanding of the physico-chemical parameters governing the immobilization of proteins, and in particular of antibodies, onto NPs becomes of crucial importance for the application of INPs in biological sensing. For a gas-like adsorption process, proteins will attach randomly on the surface showing no cooperative behavior or surface organization; if cooperativity is present (either positive or negative), proteins will reorganize on the particle surface through conformational rearrangements and crowding effects, leading to the formations of domains. In the context of bioconjugations intended for biosesensing, it is important not only the adsorption of proteins themselves but also the implications that this adsorption entails for the adsorbed proteins, especially the maintenance of their tertiary structure, since biological function depends largely on it. Consequently, these effects could reasonably influence strongly the accessibility of functional proteins such as antibodies and enzymes, hindering/enhancing their activity.[29]

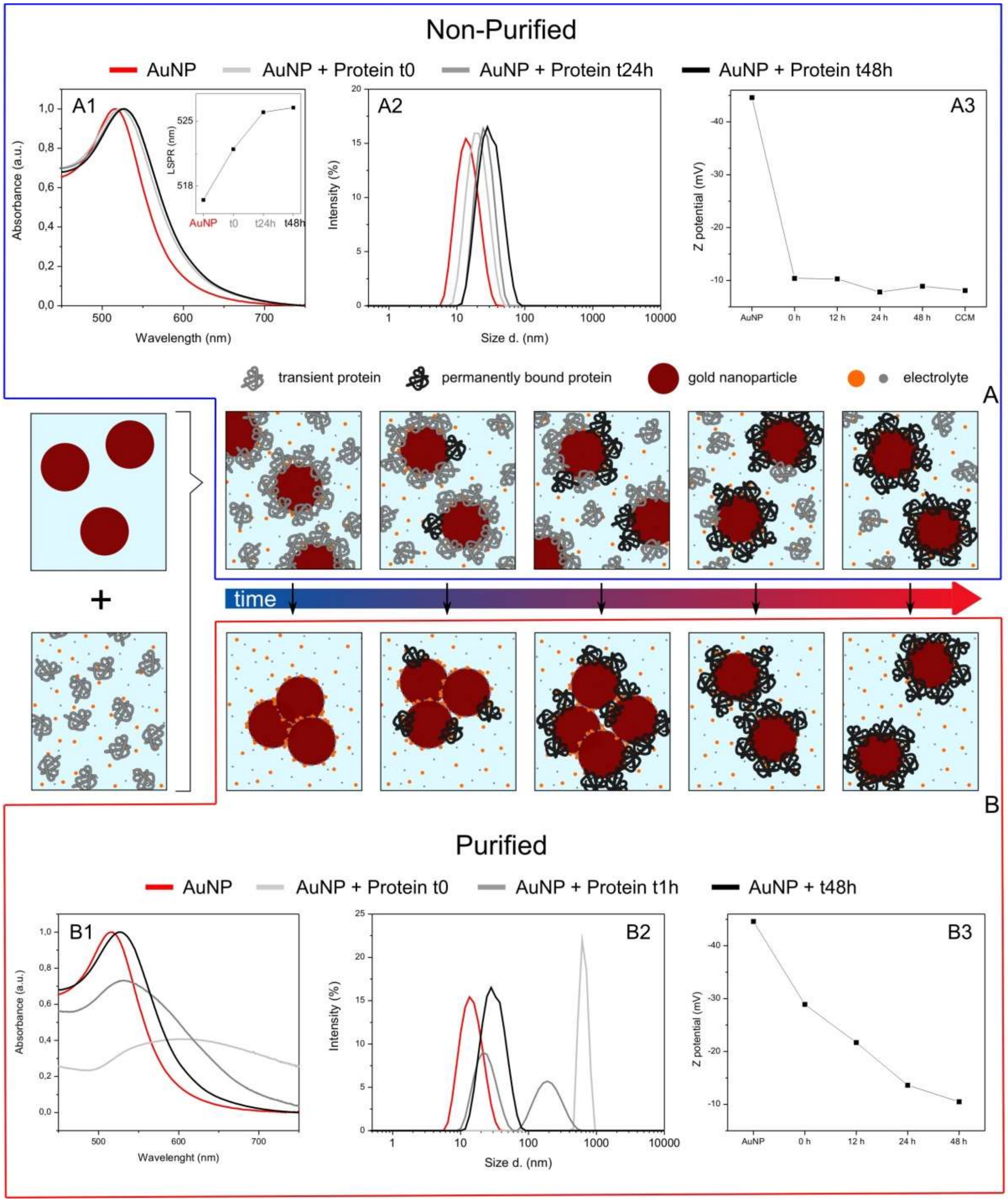

Figure 2 – The hardening of the Nanoparticle-Protein Corona. **A1)** UV–vis, **A2)** Dynamic Light Scattering (distribution by Intensity), **A3)** ζ-potential characterizations of 10 nm AuNP@SC before (*red*) and after the exposition to complete culture media (CCM + FBS) at time 0 (*light grey*), 24 h (*grey*) and 48 h (*black*). **B1)** UV–vis, **B2)** Dynamic Light Scattering (distribution by Intensity), **B3)** ζ-potential characterization of the same 10 nm Au NPs solution after purification procedure at different time of exposition to the complete CCM. 10 nm AuNP@SC before (*red*) and after the exposition to complete CCM at time 0 (*light grey*), 1 h (*grey*) and 48 h (*black*).

Indeed, crowding effects seem to facilitate the maintenance of the native, functional state of proteins, as noted in the works of Norde,[30] where the size of the adsorbed protein layer was closer to the size of the native protein. This, together with the success demonstrated widely in many immunoassay applications based on "nano-bioconjugates",[31–33] is an indication that at least a part of adsorbed proteins preserve their active structure. On the contrary, other studies observe an unfolding of the proteins when adsorbed on a surface but not always followed by aggregation.[34] It may happen that the closest model to reality is the one depicting proteins coating surfaces in a mixture of states. The first ones undergoing physical adsorption are likely more prone to lose their original conformation, or even denature, given the higher degree of freedom, while the ones adsorbing later have less or no room for denaturation and more easily maintain their native structure. These modification may have important effects, as induction of exposure of hydrophobic residues and consequent aggregation, as well as modifications in how proteins are recognized, employed and processed.[35–37] The various characteristic of the NP (morphology, that is size and shape, composition, surface charge and energy), the different nature of the protein involved (primary/secondary/tertiary structure, molecular weight, hydrophobicity, number and exposition of disulfide bridge) and the several exposure conditions seem to highly influence the possible protein conformational changes. Goy et al.,[34] after studying the interaction between sodium citrate-coated Au NP of different diameters and Human Serum Albumin (HSA), suggested a decrease of the bio-molecule mobility due to a small change in its secondary and tertiary structure. Interestingly, this effect was found to increase as the NP curvature decreases. In addition, studying the thermal protein unfolding profile, they observed an enhancement of the unfolding temperature when the HSA is adsorbed onto the Au NPs, revealing that the observed conformational changes brought a higher resistance to the complete thermal denaturation. Under fibrillation conditions they did not observe an increase in the HSA amyloid-like fibrils formation when NPs were present, seeming instead that Au NP smaller than 40 nm reduced the fibrils formation, and this effect was ascribed to the enhanced stability of the bound proteins. Conversely, Zhang et al.,[38] investigating the interaction of sodium citrate-coated 90 nm Au NP with lysozyme, showed that the protein forming the PC were partially unfolded with a partial dissociation of the disulfide bonds bringing to an Au-S coordinate covalent bonding, not detected in previous works. In here, in the presence of NPs and in a not fibrillation conditions, they observed a formation of extended, amorphous protein-NP assemblies and also large protein aggregates not containing NPs. This process was attributed to the NP colloidal destabilization and aggregation. The comparison of these two studies shows how several NP-protein exposure conditions with different proteins (Lysozyme, 15 kDa protein with only 4 S-S bonds, and the large HSA 67 kDa with over 17 disulfide bonds) can bring to distinct proteins conformational changes and consequently modify the NP properties and functional behaviors.

References

1. González, E. *et al.* Enhanced reactivity of high-index surface platinum hollow nanocrystals. *J. Mater. Chem. A* **4,** 200–208 (2016).
2. Reyes, C. Platinum-based nanocages with subnanometer-thickwalls and well-defined, controllable facets. *Science (80-.).* **106,** 1379–1383 (1999).
3. Crane, R. A. & Scott, T. B. Nanoscale zero-valent iron: Future prospects for an emerging water treatment technology. *J. Hazard. Mater.* **211–212,** 112–125 (2012).
4. Casals, E., Gonzalez, E. & Puntes, V. F. Reactivity of inorganic nanoparticles in biological environments: Insights into nanotoxicity mechanisms. *J. Phys. D. Appl. Phys.* **45,** (2012).
5. Bastús, N. G., Casals, E., Ojea, I., Varon, M. & Puntes, V. F. The Reactivity of Colloidal Inorganic Nanoparticles. in *The Delivery of Nanoparticles* (2012). doi:10.5772/2647
6. Casals, E., Vázquez-Campos, S., Bastús, N. G. & Puntes, V. Reactivity of engineered inorganic nanoparticles and carbon nanostructures in biological media. *TrAC - Trends Anal. Chem.* **27,** 672–683 (2008).
7. Piella, J., Bastús, N. G. & Puntes, V. F. Size-Dependent Protein-Nanoparticle Interactions in Citrate-Stabilized Gold Nanoparticles: The Emergence of the Protein Corona. *Bioconjug. Chem.* **28,** 88–97 (2017).
8. Mudunkotuwa, I. A. & Grassian, V. H. The devil is in the details (or the surface): Impact of surface structure and surface energetics on understanding the behavior of nanomaterials in the environment. *J. Environ. Monit.* **13,** 1135–1144 (2011).
9. Liu, J. & Hurt, R. H. Ion release kinetics and particle persistence in aqueous nano-silver colloids. *Environ. Sci. Technol.* **44,** 2169–2175 (2010).

10. Reidy, B., Haase, A., Luch, A., Dawson, K. A. & Lynch, I. Mechanisms of silver nanoparticle release, transformation and toxicity: A critical review of current knowledge and recommendations for future studies and applications. *Materials (Basel).* **6,** 2295–2350 (2013).

11. Stebounova, L. V., Guio, E. & Grassian, V. H. Silver nanoparticles in simulated biological media: A study of aggregation, sedimentation, and dissolution. *J. Nanoparticle Res.* **13,** 233–244 (2011).

12. Wang, X. *et al.* Use of coated silver nanoparticles to understand the relationship of particle dissolution and bioavailability to cell and lung toxicological potential. *Small* **10,** 385–398 (2014).

13. Nel, A. E. *et al.* Understanding biophysicochemical interactions at the nano-bio interface. *Nat. Mater.* **8,** 543–557 (2009).

14. Izak-Nau, E., Voetz, M., Eiden, S., Duschl, A. & Puntes, V. F. Altered characteristics of silica nanoparticles in bovine and human serum: The importance of nanomaterial characterization prior to its toxicological evaluation. *Part. Fibre Toxicol.* **10,** 2–13 (2013).

15. Blanco, E., Shen, H. & Ferrari, M. Principles of nanoparticle design for overcoming biological barriers to drug delivery. *Nat. Biotechnol.* **33,** 941–951 (2015).

16. Casals, E., Pfaller, T., Duschl, A., Oostingh, G. J. & Puntes, V. F. Time evolution of the nanoparticle protein corona. *ACS Nano* **4,** 3623–3632 (2010).

17. Casals, E., Pfaller, T., Duschl, A., Oostingh, G. J. & Puntes, V. F. Hardening of the nanoparticle-protein corona in metal (Au, Ag) and oxide (Fe 3O 4, CoO, and CeO 2) nanoparticles. *Small* **7,** 3479–3486 (2011).

18. Lo Giudice, M. C., Herda, L. M., Polo, E. & Dawson, K. A. In situ characterization of nanoparticle biomolecular interactions in complex biological media by flow cytometry. *Nat. Commun.* **7,** 1–10 (2016).

19. Prime, K. L. . & Whitesides, G. M. . Self-Assembled Organic Monolayers: Model Systems for Studying Adsorption of Proteins at Surfaces. *Science.* **252,** 1164–1167 (2016).

20. Norde, W. & Lyklema, J. Why proteins prefer interfaces. *J Biomater Sci Polym Ed* **2,** 183–202 (1991).

21. Madura, J. D. & Haymet, A. D. J. Proteins at interfaces. *Abstr. Pap. Am. Chem. Soc.* **222,**

U344–U344 (2001).

22. Mahmoudi, M. *et al.* Protein-nanoparticle interactions: Opportunities and challenges. *Chem. Rev.* **111,** 5610–5637 (2011).

23. Latour, R. A. The Langmuir isotherm: A commonly applied but misleading approach for the analysis of protein adsorption behavior. *J. Biomed. Mater. Res. - Part A* **103,** 949–958 (2015).

24. Norde, W. & Anusiem, A. C. I. Adsorption, desorption and re-adsorption of proteins on solid surfaces. *Colloids and Surfaces* **66,** 73–80 (1992).

25. All, E. S. B. V. Globular proteins at solid / liquid interfaces. *Colloids Surfaces A Physicochem. Eng. Asp.* **2,** 517–566 (1994).

26. Alaeddine, S. & Nygren, H. Logarithmic growth of protein films. *Proteins Interfaces II* 41–51 (1995). doi:10.1021/bk-1995-0602.ch003

27. Yamada, S., Sato, H. & Group, N. P. Effect of adsorbed proteins on the wettability of hydrophilic and hydrophobic solids. *Nature* **198,** 476–477 (1962).

28. Montenegro, J. M. *et al.* Controlled antibody/(bio-) conjugation of inorganic nanoparticles for targeted delivery. *Adv. Drug Deliv. Rev.* **65,** 677–688 (2013).

29. Ardao, I., Comenge, J., Benaiges, M. D., Álvaro, G. & Puntes, V. F. Rational nanoconjugation improves biocatalytic performance of enzymes: Aldol addition catalyzed by immobilized rhamnulose-1-phosphate aldolase. *Langmuir* **28,** 6461–6467 (2012).

30. Norde, W. Adsorption of proteins from solution at the solid-liquid interface. *Adv. Colloid Interface Sci.* **25,** 267–340 (1986).

31. Parolo, C., de la Escosura-Muñiz, A. & Merkoçi, A. Enhanced lateral flow immunoassay using gold nanoparticles loaded with enzymes. *Biosens. Bioelectron.* **40,** 412–6 (2013).

32. Parolo, C. *et al.* Design, preparation, and evaluation of a fixed-orientation antibody/gold-nanoparticle conjugate as an immunosensing label. *ACS Appl. Mater. Interfaces* **5,** 10753–10759 (2013).

33. de Puig, H., Bosch, I., Carré-Camps, M. & Hamad-Schifferli, K. Effect of the Protein Corona on Antibody–Antigen Binding in Nanoparticle Sandwich Immunoassays. *Bioconjug. Chem.* **28,** 230–238 (2017).

34. Goy-López, S. *et al.* Physicochemical characteristics of protein-NP bioconjugates: The role of particle curvature and solution conditions on human serum albumin conformation and fibrillogenesis inhibition. *Langmuir* **28,** 9113–9126 (2012).

35. Gagner, J. E., Lopez, M. D., Dordick, J. S. & Siegel, R. W. Effect of gold nanoparticle morphology on adsorbed protein structure and function. *Biomaterials* **32,** 7241–7252 (2011).

36. Gebauer, J. S. *et al.* Impact of the nanoparticle-protein corona on colloidal stability and protein structure. *Langmuir* **28,** 9673–9679 (2012).

37. Lundqvist, M., Sethson, I. & Jonsson, B. H. Protein adsorption onto silica nanoparticles: Conformational changes depend on the particles' curvature and the protein stability. *Langmuir* **20,** 10639–10647 (2004).

38. Zhang, D. *et al.* Gold nanoparticles can induce the formation of protein-based aggregates at physiological pH. *Nano Lett.* **9,** 666–671 (2009).

Chapter II

Objectives

This work focuses on the design of sensitive and affordable biosensors based on AuAg alloy nanoshells (NSs) for the determination of viral and bacterial infections. Two diagnostic formats will be explored: a LFA will be employed for the SERS-based detection of MxA, while the revelation of *E.coli* and *Salmonella* will be achieved with an electrochemical assay. Following **Chapter I,** dealing with state of the art of INPs-based sensing and biosensing applications, as well as the physico-chemical aspect of nano-bioconjugations, the next sections of this dissertation will explore all aspects of the applications described, from the nanomaterial design and characterization to the biosensors development and optimization, and will be organized in the following manner:

Chapter III will describe the synthesis of AuAg alloy nanoshells (NSs), the nanomaterial chosen for this project because of the high flexibility and tunability of its properties, and the study of their optical and electrochemical behavior.

Time- and Size-Resolved Plasmonic Evolution with nm Resolution of Galvanic Replacement Reaction in AuAg Nanoshells Synthesis

In the first section, a general, highly reproducible and robust protocol based on GRR for the quantitative production of monodisperse AuAg NSs will be presented, together with the systematic identification of the role played by each synthetic parameter in defining the nanomaterial's morphology, in terms of shell thicknesses and void sizes, the relative composition and topological distribution of their constituting noble metals, as well as their surface roughness and porosity. Particular emphasis will be dedicated to the study of the time-dependent evolution of AuAg NSs' plasmonic properties, whose precise control will be required for their application in the SERS-based LFA developed (*vide infra*). Moreover, simulations based on Mie's theory will also be provided as theoretical confirmation of the described mechanism.

Tunable electrochemistry of gold-silver alloy nanoshells

The second section of this chapter will explore the electrochemical behavior of AuAg NSs. A set of voltammetric studies of AuAg NSs will be discussed, highlighting the dependency of their electrochemical properties from their size, morphology and composition. Particular attention will be paid to the mechanism generating the discovered electrochemical behavior, as well as the emergence of electrocatalytic effects, in order to precisely understand how to adjust

AuAg NSs redox potentials and choose convenient working conditions. These findings will constitute the rational basis for developing AuAg NSs with desirable properties to be applied in the electrochemical assay described further on.

Chapter IV focuses on the application of AuAg NSs in two biosensing platforms:

Detection of myxovirus resistance protein A (MxA) in paper-based immunoassays with surface enhanced Raman spectroscopy

The first section of this chapter will cover the whole process undertaken for the preparation of a SERS-based LFA for the sensitive and quantitative detection of MxA, a biomarker commonly associated to viral infections. This part will include the construction of the immunochromatographic strip, the conjugation of AuAg NSs to the antibodies used in the LFA, the optimization of all working conditions and experimental parameters necessary for the test correct functioning, and finally the analytical performance of the assay. In addition, this chapter will also evaluate the amplification efficiency of three different nanomaterials (namely: Ag NPs, AuAg NSs, Au nanostars) used in the SERS detection system as well as their technical drawbacks, comparing the effect of different morphologies and compositions on the overall suitability for this particular diagnostic platform.

A low-cost strategy for the development of a rapid electrochemical assay for bacteria detection based on AuAg nanoshells

The second section of this chapter will treat the development of a *proof-of-concept* electrochemical assay for the rapid detection of two model bacterial strains, *Escherichia coli* and *Salmonella typhimurium*. The capability of precisely modulate AuAg NSs elemental composition during their synthesis, and therefore to tune their electrochemical properties, will be exploited for applying them as electrochemical reporters in this test. Moreover, aiming at truly satisfying the PoC requirements of low-cost and simple diagnostic technologies, the chapter will explore the possibility of using neither dangerous and manipulation-intensive co-reagents, nor expensive and fragile bioreceptors for the construction of this assay.

Chapter III

AuAg Nanoshells: Synthesis and Properties

Time- and Size-Resolved Plasmonic Evolution with nm Resolution of Galvanic Replacement Reaction in AuAg Nanoshells Synthesis

The emerging physical and chemical properties materials display when down-sized to the nanoscale outstand their macroscale counterparts and confer them unique behavior, otherwise unreachable with more traditional ones. Achieving the highest degree of control and understanding of the processes employed in their crafting is key for obtaining the best performances and highest added value from the technologies in which they find application, such as highly sensitive (bio)diagnostics and imaging as well as efficient and selective catalysis.[1,2,3,4,5,6]

Galvanic Replacement Reaction

In this context, the process of Galvanic Replacement Reaction (GRR) represents an extremely versatile chemical tool for designing and producing high quality materials with customized features, combining the effect of both chemical conversion and structural transformation to obtain enhanced optical and catalytic properties.[7] GRR is a heterogeneous redox reaction which happens at the solid-liquid interface between a solid metal and a cation of a nobler one in solution. This process, very well-known at the macro- and micro-scale for its numerous applications in metallurgy and engineering, is used at the nanoscale as a very convenient and flexible synthetic tool for obtaining complex hollow morphologies, which represent a new class of materials with enhanced properties in the field of catalysis[8,9] drug delivery[10] and optics.[11] In a typical reaction, the surface atoms of a colloidal suspension of pre-synthetized metal nanocrystals (NCs) (typically Ag[12] but also Cu and Co[13]) are used as sacrificial templates and undergo oxidative dissolution caused by the redox reaction with a more noble metal ion in solution (mainly Au and Pt).[14]

Despite all these advantages, few are the examples found in literature providing reproducible and reliable methods for synthetizing hollow nanomaterials through GRR with highly controlled reproducibility, morphologies and properties.[12,15,16,17] The majority provides instead spurious and limited recipes whose lack of reproducibility has been attributed to a poor understanding of the reaction mechanism.[18,19,20,21] Given the fundamental importance of correlating synthesis recipes and NCs atomic distribution with the strict determination of the material properties, it is crucial to deeply understand the role of each governing parameter of the hollowing process. With this strategy it is possible to produce a larger palette of materials whose properties are precisely tailored for the specific application for which they are required. In addition, the variation in the optical properties of the material, while often considered merely as a secondary effect of the reaction, has to be considered instead a direct projection of the undergoing modification in its structure and composition.

Thus, in this work we report the time- and size- resolved plasmonic evolution of the synthesis of AuAg hollow nanoshells (NSs) through GRR at room temperature (RT). We focus our efforts in achieving a precise morphology among all the thermodynamically possible ones[22], composed by a thin gold shell with homogeneous and smooth surface and a large internal void. These features have been shown to possess the most desirable enhanced optical properties for application in plasmonic sensing thanks to the resonant cavity effect,[11] the possibility to tune their absorption spectra into NIR wavelenght in order to take advantage of the biological window,[23] and an improved stability towards corrosion of alloyed Ag given by the "nobleing" effect of gold.[24] This improved and extremely reproducible synthetic process allows the quantitative production of large amounts of monodisperse, high quality AuAg NSs of different sizes and degrees of conversion of Ag to Au, while working at RT permits the easy monitoring of the process and avoids temperature gradients, adding the possibility to scale-up the methodology towards its use in real-world applications.

General Synthetic Protocol

The synthesis of AuAg NSs through GRR consists in mixing a solution of silver nanoparticles in a variety of conditions with a solution of a gold salt in a controlled reacting medium: thanks to the difference in reduction potentials between the two noble metals (standard reduction potentials of Ag^+ and Au^{III} are 0.7996 V and 1.498 V, respectively[25,26]), Au^{III} cations oxidize Ag atoms from the bulk of the particle and get reduced at the particle surface, resulting in a hollow shell of a varying degree of AuAg alloy. Initially, the reduction of Au causes the passivation of the Ag templates surface through the formation of a thin metallic shell, forcing the oxidation of the bulk NC atoms to take place through a pinhole, kept unclogged thanks to the continuous cations outflow from its interior (**Figure 1 - a**).[14] This process establishes a galvanic pair where, as the deposited metal protects the template, the surface ratio between the galvanic electrodes increases, directing the flow of electrons through the NC body and favoring the interdiffusion and alloying of the two metals at their interface.[27] **Figure 1 – b** shows the morphological evolution of nearly monodispersed 80 nm-sized quasi-spherical Ag NCs upon titration with $HAuCl_4$ (thorough templates characterization is reported in **Figure S1**). We use spheres instead of the commonly used nanocubes to avoid surface atomic heterogeneity (flat surface, edges and corners) what improved homogeneity and reproducibility. At short reaction times, a tiny cavity appears into the Ag templates body at the initial stages of GRR, caused by Ag oxidation and dissolution, which grows progressively as Au deposition proceeds. This chemical and structural transformation, which occurs without significant loss in monodispersity, as shown by histograms, ends up in the formation of a hollow structure enclosed by a metal alloy outer shell (**Figure 1 – d**), which can further evolve into a porous one with the de-alloying of its less noble component.[7] Conversely, the pinhole ends up closed when oxidizers are the limiting reagents in the reaction, as it is clearly visible from SEM micrographs of final GRR stages (**Figure 1 – e**), where only few hollow NCs still display a hole in their surfaces. Following the change in morphology, a radical transformation in the material's optical properties takes place, visibly indicated by clear color changes as the localized surface plasmon resonance (LSPR) band shifts through the whole visible spectrum (**Figure 1 – c**). In order to study the time-dependent evolution of Ag NCs into hollow AuAg NSs by stopping the reaction at different times, different precursor amounts were carefully dosed using a syringe pump. After the addition of 100-150 μL of the $HAuCl_4$ aqueous solution, the typical dipole plasmon resonance mode of 80 nm Ag templates (λ_{MAX} ≈ 450 nm) starts decreasing in absorbance intensity together with a slow but constant red-shift, indicating the progressive Ag plasmon suppression operated by the deposited Au thin shell. This trend continues throughout the wavelengths range typical of AuAg alloy NCs[24,28], until reaching an absorbance minimum (λ_{MAX} ≈ 570 nm). Then, as the process advances, a larger red-shift is accompanied by a steep increase in absorbance intensity: a plasmonic enhancement typical of hollow nanostructures caused by plasmon "hybridization"[29], in which the presence of cavities allows the dipole plasmon mode to extend up to the beginning of the near infrared (NIR) range (λ_{MAX} ≈ 700 nm).[11] During this process, the entire added gold precursor was converted into gold hollow NCs. Since GRR can also be described as a progressive corrosion of the silver scaffold, which will be sacrificed as a source of electrons for the Au deposition, the two half reactions can be to some extent independently controlled by introducing surfactants, co-etchers, halides and species able to modify the reactivity of the template surfaces and the intermediates stability.[18] In order to control the production of high quality AuAg NSs, the systematic identification of the role played by the different synthetic parameters involved in the process (such as template polydispersity, surfactants, co-oxidizers, complexing agents, time and T) has to be investigated.

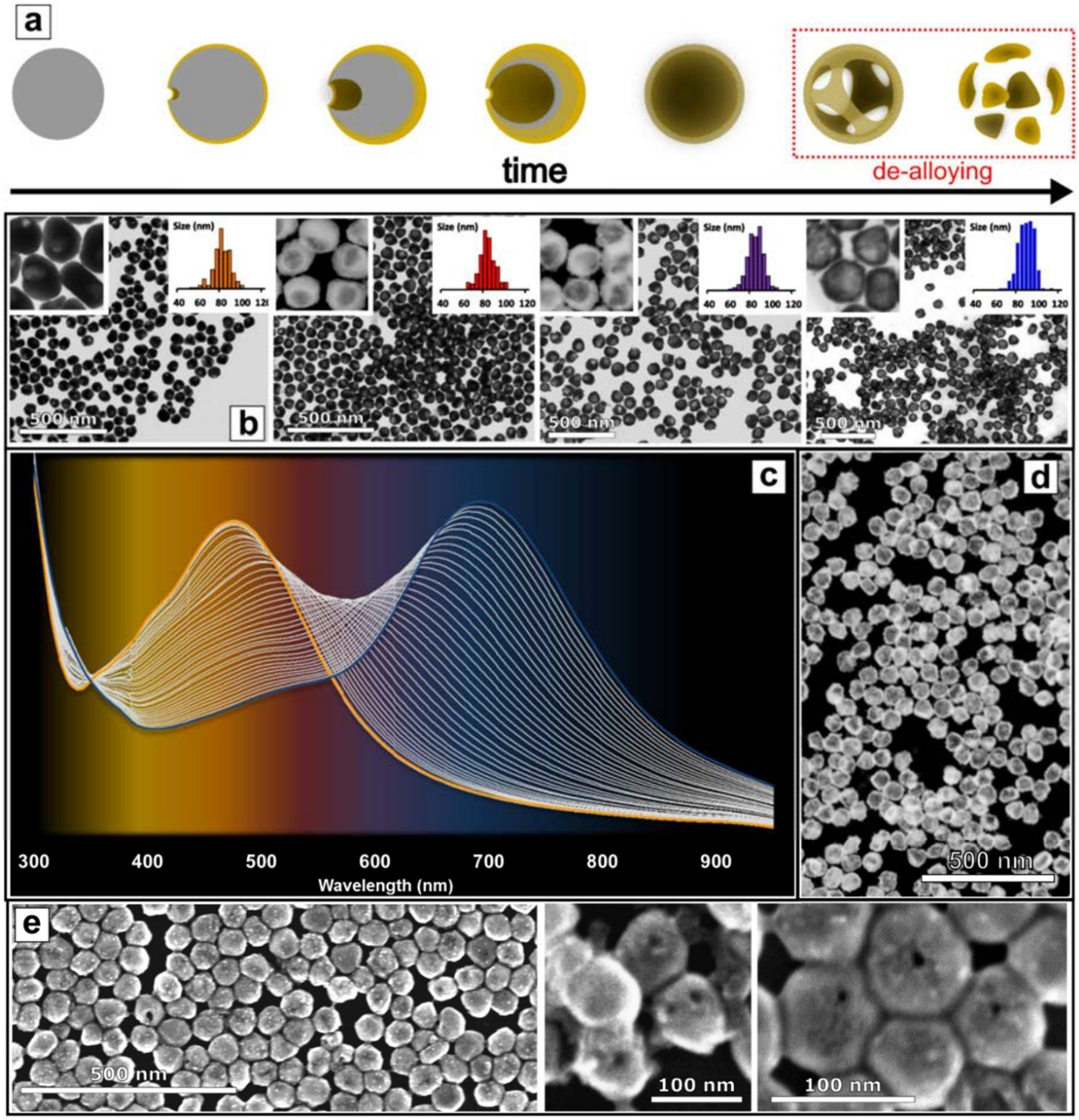

Figure 1 – a: Schematic representation of the structural evolution of AuAg nanostructures during GRR upon addition of $HAuCl_4$. **b:** TEM and HAADF-STEM micrographs showing four different phases of GRR (from left to right, images corresponding to the addition of c.a 100, 550, 900 and 1500 uL of $HAuCl_4$ 1 mM, corresponding at 10 min, 55 min, 1h30 and 2h30 of GRR respectively): the morphological transformation starts with small cavity which grows together with the thickening of the outer shell, resulting in a hollow structure. This modification affects slightly the monodispersity of the initial templates. **c:** Time-resolved absorption spectra evolution of 80 nm-sized solution of Ag NCs titrated with increasing volumes of $HAuCl_4$ (each absorption spectrum corresponding to 25 µL of a 1 mM HAuCl4 aqueous solution upon titration at 10 µL/min): LSPR shifts gradually through the whole visible spectrum towards NIR wavelengths (background color corresponding to the color of the solution). **d:** HAADF-STEM micrographs of highly monodisperse 80 nm AuAg NSs. **e:** SEM micrographs of PVP-coated AuAg NSs with a clearly visible single pinhole (depending on the orientation).

Synthetic Parameters

The key feature for obtaining this smooth evolution of AuAg NSs optical properties relies, among other, on the use of highly monodisperse quasi-spherical Ag NCs, obtained following a recently developed synthetic methodology (**Figure S1**)[30], as colloidal scaffolds onto which gold will be deposited and from which the resulting material will inherit its shape. Otherwise, templates of different sizes, that is with a dissimilar chemical potential, will introduce polydispersity in the hollowing process.[31] Additionally, due to the high difference in reduction potentials of the Au^{III} - Ag^0 redox couple, the process often results extremely fast, meaning that surface nucleation and growth of the Au shell are limited only by thermodynamics, allowing only a poor control over morphology. Thus, the passivation of the Ag NCs surface plays a critical role controlling the kinetics of the heterogeneous redox process. Furthermore, the molar ratio of Au^{III} precursor with respect to Ag^0 content in the templates solution (Au/Ag ratio from now on) is known to affect strongly the final morphology of the material.[25] As shown in **Figure 2 – i**, the initial nucleation of small Au domains in correspondence of the templates surface defects is observed when low concentrations of $HAuCl_4$ are used, not providing the system with enough material to build a complete and stable gold shell; an excess of metal precursor instead leads first to the depletion of the bulk silver reservoir in the particle core, then triggering an energetically less convenient de-alloying process (the selective removal of the less noble metal from a binary alloy), and in the end to the formation of a porous frame or to the complete breakdown of the nanostructure into smaller (< 5 nm) Au NCs (**Figure 2 – iii**). Unfortunately, Au/Ag ratio sole adjustment does not provide the desired control on shell thickness, void size and surface porosity of the AuAg NSs. Indeed, irregular, half broken structures presenting granular and rough surfaces are obtained even when the Au/Ag ratio seems to be the optimal one (**Figure 2 – ii**). Thus, carrying out the reaction in presence of a high concentration of PVP protects the Ag templates surface, lowering the reaction rate, while at the same time forming a complex with Au^{III}, decreasing its reactivity and reducing it to Au^{I} (as control experiments did show[27]), whose deposition has been shown to produce smoother and more uniform surface morphologies.[32,18,20] Thus, gradually augmenting the amount of PVP leads to an increasingly recognizable hollow morphology with more integral shells (**Figure 2 – iv, v, vi**), while in its absence a loss in monodispersity with broader ranges of void sizes and shell thicknesses is observed, which in turn leads to a flat absorbance spectrum of a black colored particles solution (**Figure S2**). Besides, the introduction of co-etchers such as HCl increases the oxidizing character of the reaction media, making protons compete with Au^{III} for the oxidative etching of silver atoms from the particles core and therefore participate in determining the extent of wavelength shift for equivalent Au/Ag ratios (**Figure 2 – vii, vii, ix**; **Figure S3**).

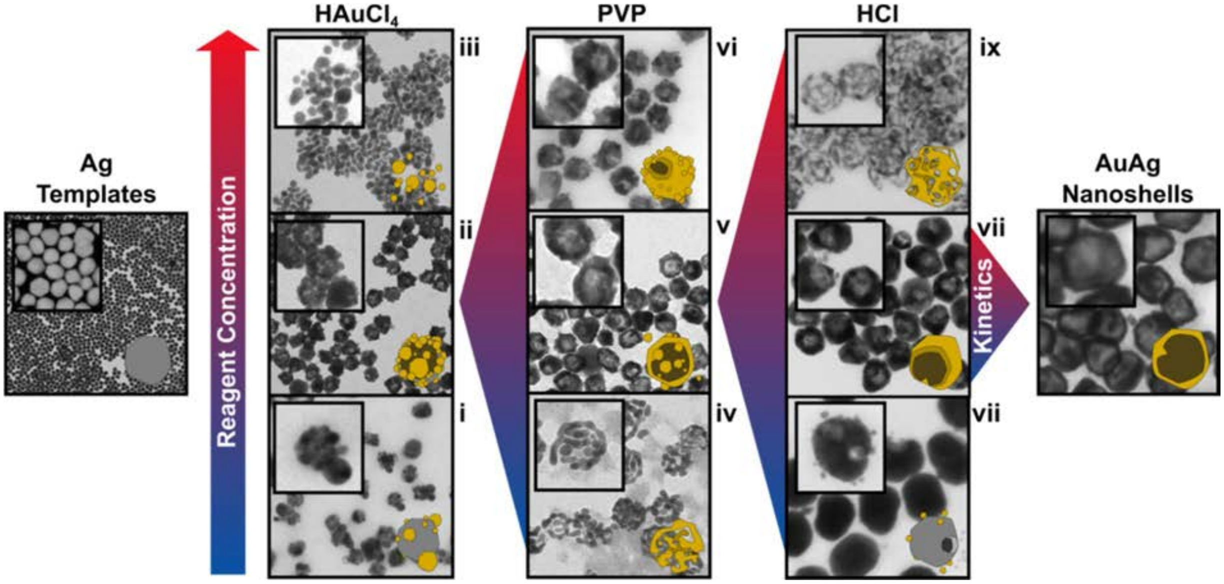

Figure 2 – Rational synthetic design of the hollow AuAg NSs morphology starting from nearly monodisperse 80 nm-sized Ag NCs (TEM micrographs recorded at different magnifications). The effect of each co-reagent (HAuCl$_4$, PVP and HCl) is explored and balanced in order to define the optimal synthetic strategy. Once the best synthetic conditions are found, a further kinetic optimization allows focusing the synthetic control on the precise and unique morphology (i.e. thin, smooth shells and large voids).

Remarkably, the addition of protons to the system appears to be crucial for speeding up the GRR: TEM micrographs of morphologies resulting from GRR without HCl show that in these conditions the process initiation appears greatly delayed (1-2 hours of reaction compared to few minutes), since only untouched or slightly “bitten” templates by “soft-etching” of the surface low coordination atoms are observed (**Figure S4**). The plasmonic band does not change significantly either, apart from a relatively small quenching of the plasmon intensity due to some minor gold deposition on the surface of the template. Interestingly, chlorides well known affinity for Ag atoms[33] seems to lower templates surface energy by removing some degree of passivation due to the presence of a native Ag_2O layer, favoring Au epitaxial deposition.[12] Indeed, when

GRR was carried out with HNO_3 instead of HCl (**Figure S5**), that is in presence of protons but absence of halides, small gold domains where observed on the surface of the hollow structure, indicating a poorer surface homogeneity.[15,18] Finally, the precise, diffusion-controlled dosage obtained using a syringe-pump helps slowing down Au^{III} deposition rate, allowing a better NC surface reorganization through interdiffusion and alloying of the two metals (whose typical diffusion rates at the nanoscale are about $10^{-11}cm^2s^{-1}$)[34], kinetically favoring its hetero-nucleation onto Ag surface[22] without compromising the thin shell stability. Thus, through the concerted interplay of all the synthetic parameters it is possible to selectively reach the desired particles morphology of a thin golden shell with homogeneous and smooth surface and a large void.

Time-resolved Evolution of GRR

The time-dependent evolution of GRR can be precisely followed by monitoring the optical properties of the system. The evolution of both LSPR maximum wavelength and intensity of a solution of 80 nm-sized Ag NCs was analyzed upon titration with 1 mM $HAuCl_4$ at a constant flux of 10 uL/min (**Figure 3 – b**). Remarkably, the process is highly reproducible as shown in **Figure S6**, where the evolution of the LSPR position after the addition of controlled volumes of $HAuCl_4$ is plotted for three independent synthesis.

The study of the kinetics of AuAg NSs structural and chemical conversion through GRR, associated with the elemental distribution analysis and EDS line scan (**Figure 4 – a, b, c**), led to the proposal of a general GRR mechanism divided in 4 phases, corresponding to the 4 different plasmonic regimes observed. In the first GRR phase, Au^{III} reaches the particle's surface, is reduced by reacting with Ag surface atoms and it is then deposited on the nearby surface while the oxidized silver ions are transferred into solution (eventually precipitating as insoluble AgCl and resuspended by PVP[14]) (**Figure 4 – a, Phase I**). At this early GRR stage almost no red-shift of the LSPR band is observed (**Figure 3 – b, Phase I**), which may indicate the amount of Au deposited does not have a detectable impact in the optical properties of the Ag templates. This induction time could correspond to the critical size needed by the vacancies created with the pitting corrosion to coalesce and form the pinhole, together with the formation of a continuous Au shell. Interestingly, TEM and SEM micrographs show that AuAg NSs present always a single pinhole (**Figure 1 – D**), even though pitting corrosion should start at the multiple asperities and defects at the NCs surfaces.

While this kinetic barrier, described also by Smith et al.[35], is easily overcome in presence of HCl, GRR ignition significantly slows down without the catalysis of a small excess of protons, which enhance the templates' initial pit corrosion and favours a faster pinhole formation (Figure S4). With the completion of a thin Au shell and the formation of a single pinhole begins the second GRR phase (**Figure 3 – b, Phase II**), dominated by a red-shift restricted between 400 and 520 nm, typical of Au-Ag alloy NCs.[24,28] At the same time the two noble metals initiate their alloying by inter-diffusing at their interface, thermodynamically driven by their bonding stabilization (Au-Au (226 kJmol-1) vs Au-Ag (229 kJmol-1)).[25] The gradual LSPR wavelength increase accompanied by a steep decrease in absorbance, which suggests a probable overlap in time and stoichiometry of gold deposition and alloy formation, marks a radical change compared to the previous phase. This transformation can be readily followed both with the increasing Au/Ag ratio (**Table 1**), showing good agreement between calculated and experimental data) as well as the rapidly evolving elemental profile displayed in the EDS line scan (**Figure 4 – c**).

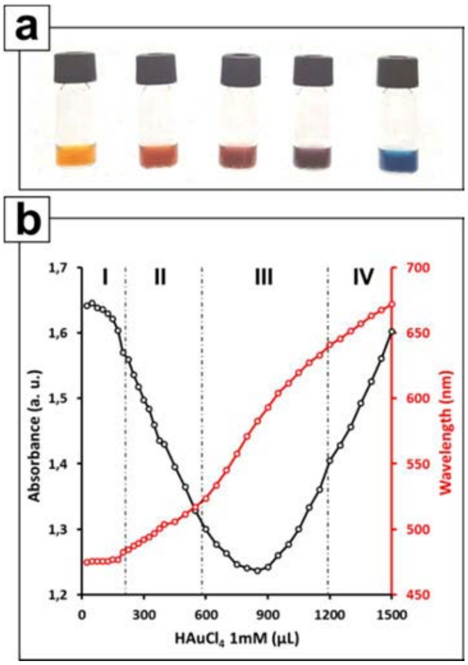

Figure 3 – a: AuAg NSs solution color change during GRR. **b:** Maximum LSPR wavelength (red) and intensity (black) vary with increasing amount of Au^{III} added (at a constant flux): four rates of variation in both features are observed in all GRR, accompanying the color transformation (above).

The third GRR phase is characterized by a minimum in absorbance followed by a steepening in the LSPR wavelength red-shift and an increase of the absorbance intensity. (**Figure 3 – b, Phase III**). This new plasmonic regime is determined not only by an enrichment in Au composition, provided with its continued deposition on the surface, but also by the appearance of a plasmonic void as the Ag core is emptied.

The growth of the alloy interface causes the Ag outwards migration and the accumulation of vacancies in the core, which eventually coalesce and add up to the internal void.[25,36] The impact of the void on the optical properties of the system, well-described by El-Sayed et al.[37], starts with the absorbance minimum and is translated into the attenuation of the NCs scattering contribution. When the AuAg NSs aspect-ratio reaches certain threshold values (**Table 1**) the contribution of the void starts to be dominant which results into a further red-shift of the SPR position towards the NIR region characteristic of thin NSs.[38] Finally, in the last proposed GRR phase the further LSPR band red-shift at NIR wavelengths and the absorbance increase correspond to the construction of a smooth and thin AuAg shell and a large internal void (**Figure 4 – a), b), Phase IV**). At this point, the continuation of the reaction would cause the nearly complete depletion of the core Ag, forcing its migration towards the outer shell and its oxidative de-alloying forming porous structures.[24,26] Indeed, in order to balance the solidity loss of the Au-rich scaffold with the lattice tension and surface curvature, the hollow morphology undergoes a structural reorganization that opens large pores through the AuAg shell (**Figure 2 – iv, ix**), a commonly observed behavior also in ligamented nanoporous gold.[39]

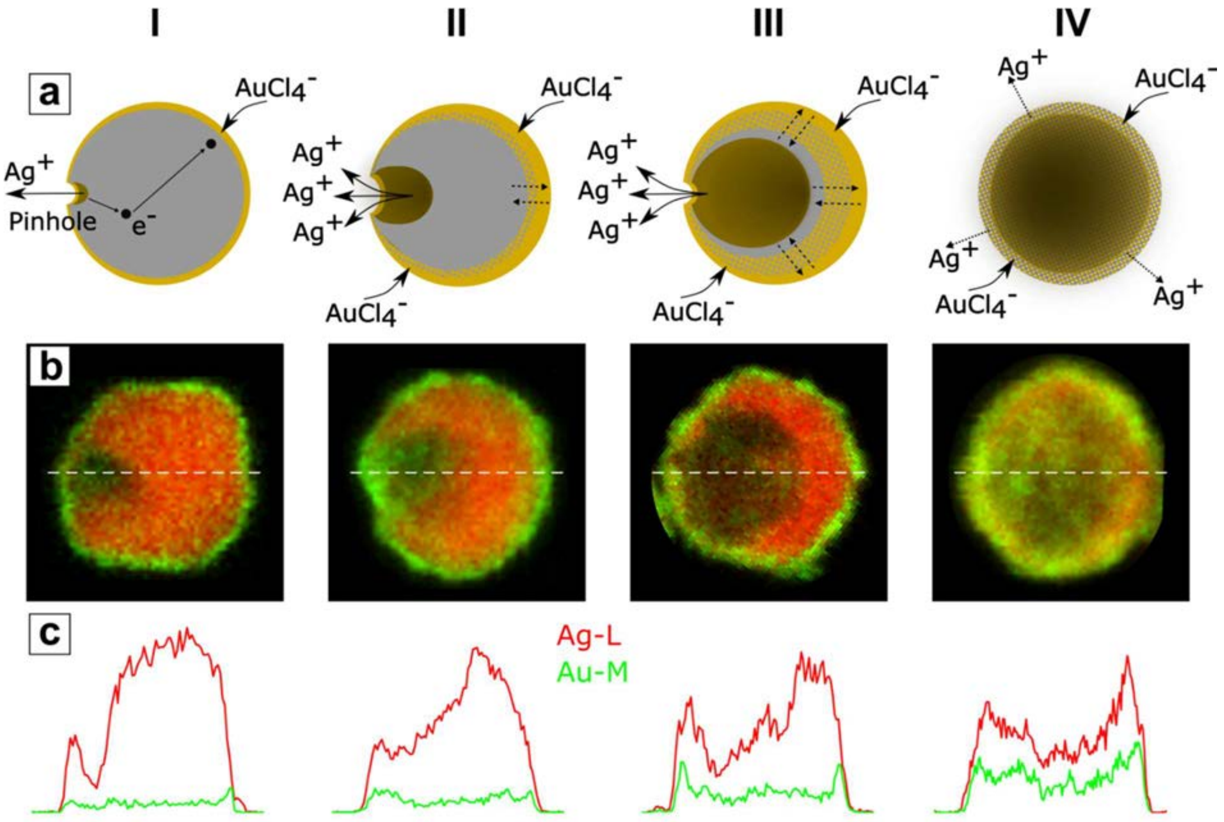

Figure 4 – a) GRR mechanism hypothesis with four phases, modelled correspondingly to the four different plasmonic regimes observed; **b), c)**: HAADF-STEM elemental distribution micrographs and EDS line scan elemental analysis of individual AuAg NSs corresponding to each GRR phase, confirming the proposed mechanism.

Phase (80 nm)	**Au/Ag$_{\mathbf{EDS}}$ (%)**	**Void size (nm)**	**Shell Thick. (nm)**	**Aspect ratio (nm)**
I	1.01 ± 0.08	23.0 ± 6.1	20.8 ± 4.1	**1.0** ± 0.4
II	3.38 ± 0.16	31.5 ± 6.0	16.4 ± 3.3	**0.5** ± 0.2
III	5.89 ± 0.35	39.9 ± 5.8	14.5 ± 2.8	**0.4** ± 0.1
IV	5.61 ± 0.31	63.8 ± 7.5	12.4 ± 2.6	**0.2** ± 0.1

Table 1: calculated and experimental (EDS) Au/Ag- and aspect-ratios evolution during GRR.

Effect of Size

We extended the analysis of the plasmonic evolution of GRR onto Ag templates solutions of different sizes (namely: 15, 30, 60, 80, 100, 150 nm, **Figure 5 – a), Figure S7**). To the extent of our knowledge, a systematic study of the effect of Ag templates size in GRR has not been reported in literature yet, probably due to the intrinsic difficulty in preparing highly monodisperse Ag NCs with controlled size.[30] By following the dipole plasmon resonance mode of all sizes it appears clearly that an analogous trend is followed both by the LSPR maximum wavelength and intensity, as shown in **Figure 5 – a)** and **Figure S7**. For GRR carried out onto templates of 60, 80, 100 and 150 nm, the presence of an initial induction time is clearly evidenced (for smaller templates (15, 30 and 60 nm) this stage is too fast to be observed spectroscopically). Later during the process, an intensity minimum is reached, followed by a gradual and constant increase caused by the cavity effect, a common feature for AuAg NSs of 60, 80, 100 and 150 nm which appears to be related to a common aspect ratio (**Table 2**).[31] In addition to the dipole mode, particles larger than 60 nm exhibited quadrupole plasmon resonance modes. The quadrupole and dipole peaks both shifted to longer wavelengths with increased Au content in AuAg NSs. Experimental (from EDS) Au/Ag ratios, void size and shell thickness distributions and aspect ratio (calculated as (D-d)/d), reported in **Table 2** for 4 different sizes, show how the elemental composition and morphology are the two main parameters governing the evolution of AuAg NSs plasmonic properties, and that a crucial feature needed for reaching absorption in NIR wavelength seems to be a precise aspect-ratio. When using smaller templates (15, 30 nm), keeping constant the (Au^{III} + H^+)/Ag ratio used for bigger ones does not apparently allow to observe either the formation of the hollow morphology or an analogous plasmonic progression towards NIR wavelengths. Rather, **Figure 5 – A** and **Figure S6** show that in these cases LSPR shift stops in correspondence with the typical Au NCs peak (c.a 500 nm), indicating the complete templates corrosion and conversion into Au NCs. The higher surface atoms mobility as well as lower atomic coordination at the surface of small NCs, given by their increased curvature, impede the formation of a stable homogeneous shell and favor the segregation of gold atoms into discrete domains.

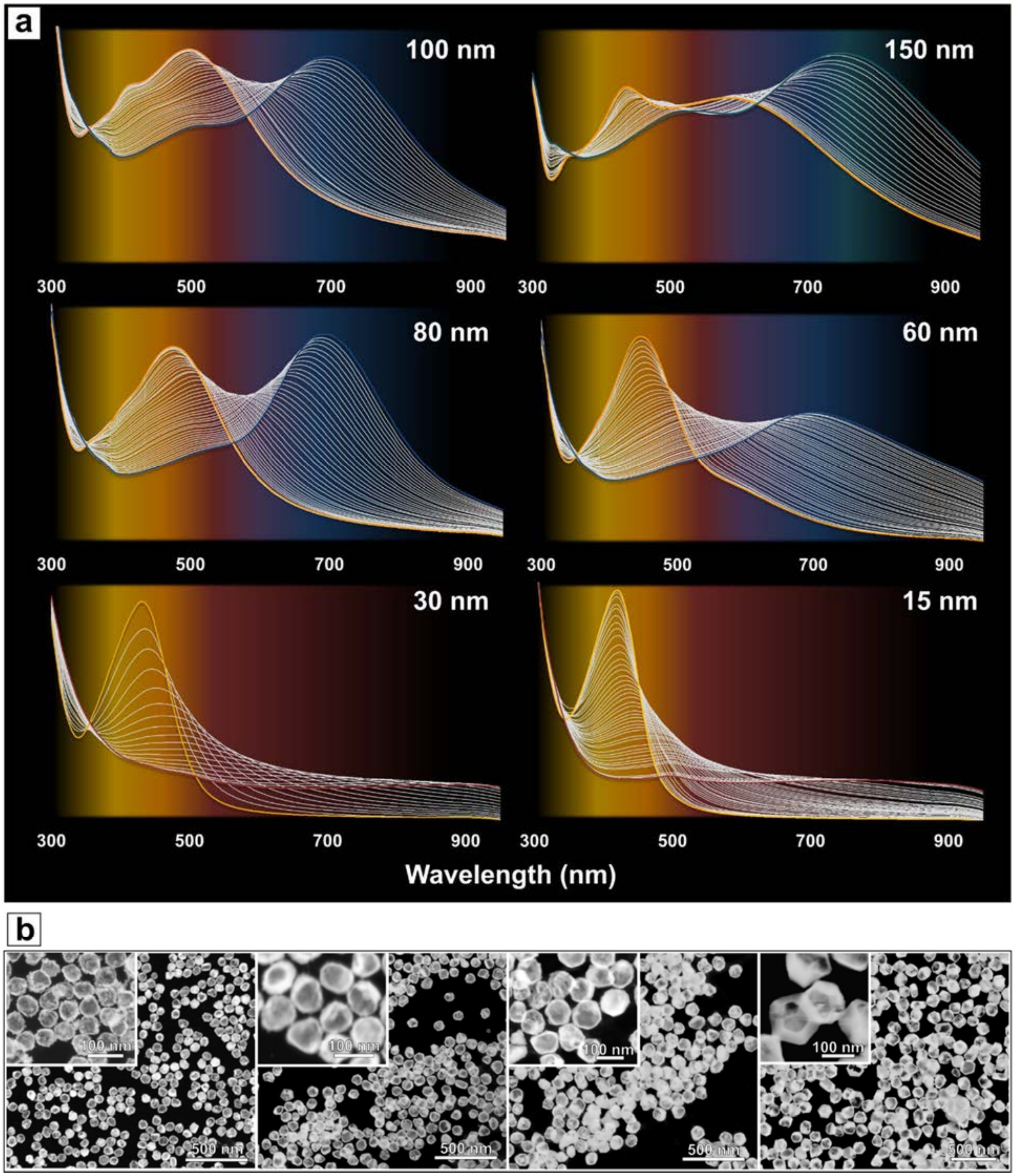

Figure 5 – a) Time-resolved absorption spectra evolution of Ag templates solutions of different sizes titrated with increasing volumes of $HAuCl_4$ (each absorption spectrum corresponding to 25 μL of a 1 mM $HAuCl_4$ aqueous solution upon titration at 10 μL/min). Starting from c.a 60 nm, the Au-Ag stoichiometry allows to obtain the hollow morphology and to reach NIR wavelengths. **b)** HAADF-STEM micrographs of AuAg NSs with thin shells and large voids (aspect ratio ≈ 0.2) of different diameters: from the left, 60, 80, 100, 150 nm.

Size (nm)	Concentration (NPs/mL)	Au/Ag$_{EDX}$ (%)	Void size (nm)	Shell Thick. (nm)	Aspect ratio (nm)
60	2.5 x 10^{11}	22.91 ± 0.20	41.6 ± 5.4	9.1 ± 1.6	**0.1** ± 0.0
80	1.0 x 10^{11}	18.96 ± 0.20	63.8 ± 7.5	12.4 ± 2.6	**0.2** ± 0.1
100	5.2 x 10^{10}	14.14 ± 0.13	68.2 ± 9.3	16.1 ± 5.2	**0.2** ± 0.1
150	2.1 x 10^{10}	10.13 ± 0.12	98.9 ± 16.5	24.1 ± 8.8	**0.3** ± 0.1

Table 2: AuAg NSs plasmonic properties are strongly influenced by two main synthetic parameters: calculated and experimental Au/Ag ratios (from EDS mapping), as well as void size and shell thickness distributions (aspect ratio calculated as (D-d)/d, being D the outer and d the inner diameter respectively).

This behavior, together with the limited silver content, leads to the collapse of the forming structure and the conversion of the shell into a porous, ligamented Au-rich structure and, eventually, its fragmentation into small Au NCs, and it establishes a minimum size for hollow NCs. In the attempt to lower this limit, we also compared the use of $HAuCl_4$ as a gold precursor with a reduced Au^I salt in the GRR of 30 nm-sized Ag templates (**Figure S7**) in order to highlight the stoichiometric limit imposed by the amount of Ag atoms in small templates, modifying an existing protocol described elsewhere.[16,36] Only in the latter case the hollow morphology is achieved, conferring a pale blue color to the solution, while in the former the structure inevitably collapses into small Au NCs agglomerates. These are, to the extent of our knowledge, among the smallest ever reported AuAg NSs.[43]

When bigger particles are used instead, a higher amount of Au can be deposited thanks to the more relaxed crystal and a larger silver reservoir, and more robust shells with higher degree of alloy are obtained (**Figure 5 – b**). Indeed, the surface morphology comparison of AuAg NSs obtained using templates of bigger sizes present a gradual increase in smoothness and disappearance of pores/fractures. In these cases (60, 80, 100 and 150 nm) the dipole plasmon peak follows the stoichiometric-dependent evolution described before, confirming the undergoing morphological and chemical transformation (**Figure S6**).

Theoretical Calculations

In order to confirm the experimental observations, we carried out theoretical calculations based on the standard Mie theory of spherical particles[42]. The model system used in our calculations is based on a core/shell/shell structure. Morphological parameters that describe our system are the diameter of the original Ag template used, the core (void) size and the thickness of the shell layer (**Figure 6 – b, Figure S9**).

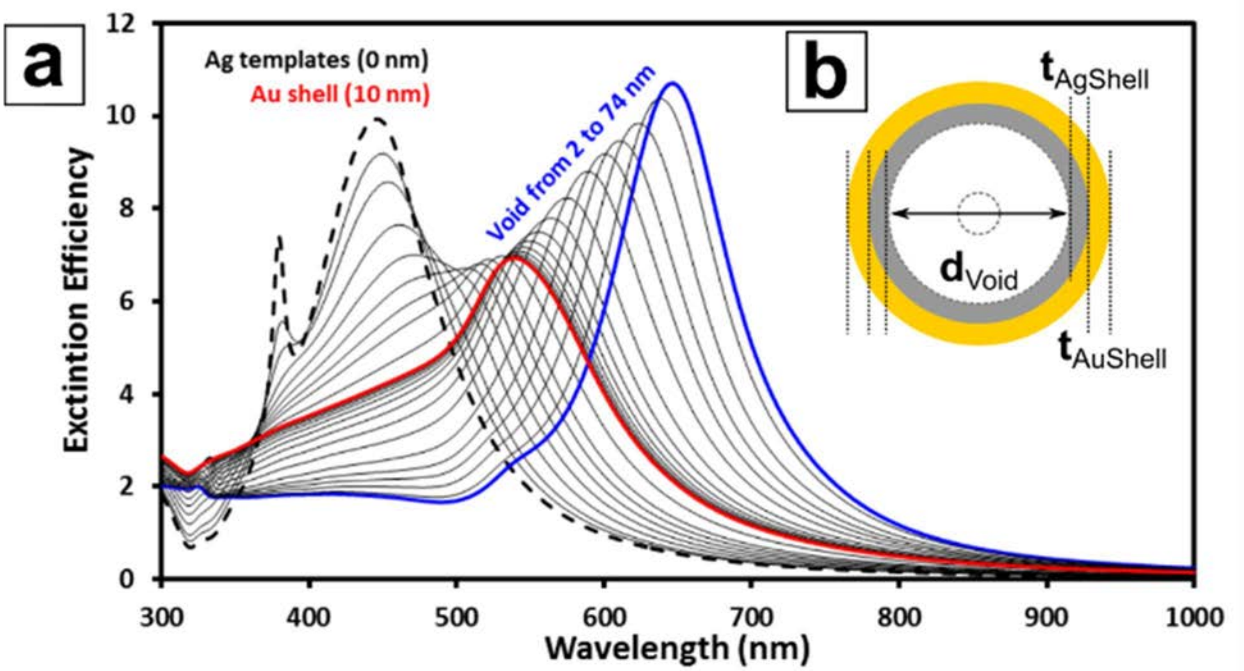

Figure 6 – a) Calculated extinction efficiency for 80 nm Ag spheres surrounded by a 10 nm-thick Au shell enclosing a void of growing diameter. **b)**: Scheme of the morphological parameters used to model the LSPR response of hollow AuAg systems (void/shell/shell configuration), including core-void- diameter ($\mathbf{d}_{\text{Void}}$), Ag shell thickness ($\mathbf{t}_{\text{AgShell}}$), Au shell thickness ($\mathbf{t}_{\text{AuShell}}$). The NCs are dispersed in an aqueous medium, and coated with a ligand shell that was not accounted for in the models.

For each NC system, the outer and inner diameters were measured from TEM micrographs obtained from the sample shown in **Figure 1 – c)**, and the measured values were used for the calculations. **Figure 6 – a)** represents the calculated spectra evolution for 80 nm AuAg NSs composed by an inner H_2O sphere of varying diameter surrounded by two shells: one of Ag, which corresponds to the original Ag template not dissolved, and one 10 nm-thick of Au, corresponding to the deposited outer shell. In general, although there is a slight mismatch in the peak positions, a good agreement with the experimental observation is obtained, allowing to estimate the dimensions of the Au shell deposited and therefore to develop a computational tool for precisely define the morphological architecture of plasmonic nanomaterials with tailored optical properties.

Conclusions

We report herein a robust, highly reproducible and quantitative synthetic method for the high yield production of monodisperse AuAg NSs at RT with extended control over surface morphology, wall thickness, void size and elemental composition. The process described allows to finely modulate the optical and structural properties of the material almost at will, enabling its employment in a variety of real-world applications. This unique optical tunability, resulting from the synergy between both the change in the outer shell chemical composition and the formation of the hollow architecture, is achieved through the reasoned and dosed use of halide co-etchers and complexating surfactants, which can change drastically not only stoichiometry but also both the precursor surface chemical potential and the diffusion of dissolved species towards it. We also propose a detailed mechanism for the GRR of silver quasi-spherical templates and HAuCl4 composed of four phases as an attempt to better describe this versatile synthetic strategy and increase the resolution of its underlying mechanism, richly corroborated by computational simulations displaying extremely good correspondence with experimental data. Remarkably, this process can be easily scaled up to thanks to the absence of temperature gradients (RT synthesis) and the slow precursor addition that avoids complicate mass gradients, both conditions necessary for an easy scale up of the reaction.

References

1. Qiu, H.-J., Li, X., Xu, H.-T., Zhang, H.-J. & Wang, Y. Nanoporous metal as a platform for electrochemical and optical sensing. *J. Mater. Chem. C* **2,** 9788–9799 (2014).
2. Prieto, G. *et al.* Hollow Nano- and Microstructures as Catalysts. *Chem. Rev.* **116,** 14056–14119 (2016).
3. Hembury, M. *et al.* Gold-silica quantum rattles for multimodal imaging and therapy. *Proc. Natl. Acad. Sci. U. S. A.* **112,** 1959–64 (2015).
4. Yang, X. F. *et al.* Hollow melon-seed-shaped lithium iron phosphate micro- and sub-micrometer plates for lithium-ion batteries. *ChemSusChem* **7,** 1618–1622 (2014).
5. Santos, L. *et al.* WO3 Nanoparticle-Based Conformable pH Sensor. *ACS Appl. Mater. Interfaces* **6,** 12226–12234 (2014).
6. Yazdi, A. *et al.* The influence of the MOF shell thickness on the catalytic performance of composites made of inorganic (hollow) nanoparticles encapsulated into MOFs. *Catal. Sci. Technol.* **6,** 8388–8391 (2016).
7. Cobley, C. M. & Xia, Y. Engineering the properties of metal nanostructures via galvanic replacement reactions. *Mater. Sci. Eng. R Reports* **70,** 44–62 (2010).
8. Nafria, R. *et al.* Co-Cu Nanoparticles: Synthesis by Galvanic Replacement and Phase Rearrangement during Catalytic Activation. *Langmuir* **32,** 2267–2276 (2016).
9. Liu, R. *et al.* Alloyed Crystalline Au–Ag Hollow Nanostructures with High Chemical Stability and Catalytic Performance. *ACS Appl. Mater. Interfaces* **8,** 16833–16844 (2016).
10. Yavuz, M. S. *et al.* Gold nanocages covered by smart polymers for controlled release with near-infrared light. *Nat. Mater.* **8,** 935–939 (2009).
11. Genç, A. *et al.* Hollow metal nanostructures for enhanced plasmonics: Synthesis, local plasmonic properties and applications. *Nanophotonics* **6,** 193–213 (2017).
12. Sun, X. *et al.* Gold-Based Cubic Nanoboxes with Well-Defined Openings at the Corners and Ultrathin Walls Less Than Two Nanometers Thick. *ACS Nano* **10,** 8019–8025 (2016).
13. Gilroy, K. D., Farzinpour, P., Sundar, A., Hughes, R. A. & Neretina, S. Sacrificial templates

for galvanic replacement reactions: Design criteria for the synthesis of pure pt nanoshells with a smooth surface morphology. *Chem. Mater.* **26,** 3340–3347 (2014).

14. Gonzalez, E. *et al.* Carving at the Nanoscale: Sequential Galvanic Exchange and Kirkendall Growth at Room Temperature. *Science* **334,** 1377–1380 (2011).

15. Jing, H. & Wang, H. Structural Evolution of Ag–Pd Bimetallic Nanoparticles through Controlled Galvanic Replacement: Effects of Mild Reducing Agents. *Chem. Mater.* **27,** 2172–2180 (2015).

16. Bai, T. *et al.* AuBr 2 – -Engaged Galvanic Replacement for Citrate-Capped Au–Ag Alloy Nanostructures and Their Solution-Based Surface-Enhanced Raman Scattering Activity. *J. Phys. Chem. C* **119,** 28597–28604 (2015).

17. Wan, D., Xia, X., Wang, Y. & Xia, Y. Robust synthesis of gold cubic nanoframes through a combination of galvanic replacement, gold deposition, and silver dealloying. *Small* **9,** 3111–3117 (2013).

18. Zhang, W., Yang, J. & Lu, X. Tailoring galvanic replacement reaction for the preparation of Pt/Ag bimetallic hollow nanostructures with controlled number of voids. *ACS Nano* **6,** 7397–7405 (2012).

19. Xie, H. *et al.* Synthesis and NIR optical properties of hollow gold nanospheres with LSPR greater than one micrometer. *Nanoscale* **5,** 765–71 (2013).

20. Preciado-Flores, S. *et al.* Highly reproducible synthesis of hollow gold nanospheres with near infrared surface plasmon absorption using PVP as stabilizing agent. *J. Mater. Chem.* **21,** 2344–2350 (2011).

21. Jang, H. & Min, D. H. Spherically-clustered porous Au-Ag alloy nanoparticle prepared by partial inhibition of galvanic replacement and its application for efficient multimodal therapy. *ACS Nano* **9,** 2696–2703 (2015).

22. Wang, Y., He, J., Liu, C., Chong, W. H. & Chen, H. Thermodynamics versus kinetics in Nanosynthesis. *Angew. Chemie - Int. Ed.* **54,** 2022–2051 (2015).

23. Pansare, V. J., Hejazi, S., Faenza, W. J. & Prud'Homme, R. K. Review of long-wavelength optical and NIR imaging materials: Contrast agents, fluorophores, and multifunctional nano

carriers. *Chem. Mater.* **24,** 812–827 (2012).

24. Gomes, J. F. *et al.* Impact of the AuAg NPs composition on their structure and properties: A theoretical and experimental investigation. *J. Phys. Chem. C* **118,** 28868–28875 (2014).

25. Xia, X., Wang, Y., Ruditskiy, A. & Xia, Y. 25Th Anniversary Article: Galvanic Replacement: a Simple and Versatile Route To Hollow Nanostructures With Tunable and Well-Controlled Properties. *Adv. Mater.* **25,** 6313–33 (2013).

26. Lewis, E. a. *et al.* Real-time imaging and elemental mapping of AgAu nanoparticle transformations. *Nanoscale* **6,** 13598–13605 (2014).

27. González, E. *et al.* Enhanced reactivity of high-index surface platinum hollow nanocrystals. *J. Mater. Chem. A* **4,** 200–208 (2016).

28. Link, S., Wang, Z. L. & El-Sayed, M. a. Alloy Formation of Gold-Silver Nanoparticles and the Dependence of the Plasmon Absorption on Their Composition. *J. Phys. Chem. B* **103,** 3529–3533 (1999).

29. Prodan, E. A Hybridization Model for the Plasmon Response of Complex Nanostructures. *Science* **302,** 419–422 (2003).

30. Bastús, N. G., Merkoçi, F., Piella, J. & Puntes, V. F. Synthesis of Highly Monodisperse Citrate-Stabilized Silver Nanoparticles of up to 200 nm: Kinetic Control and Catalytic Properties. *Chem. Mater.* **26,** 2836–2846 (2014).

31. Varón, M. *et al.* Spontaneous formation of hollow cobalt oxide nanoparticles by the Kirkendall effect at room temperature at the water–air interface. *Nanoscale* **5,** 2429–2436 (2013).

32. Nakazato, Y., Taniguchi, K., Ono, S., Eitoku, T. & Katayama, K. Formation dynamics of gold nanoparticles in poly(vinylpyrrolidone) and other protective agent solutions. *Phys. Chem. Chem. Phys.* **11,** 10064–10072 (2009).

33. Zelyanskii, A. V, Zhukova, L. V & Kitaev, G. A. Solubility of AgCl and AgBr in HCl and HBr. *Inorg. Mater.* **37,** 622–625 (2001).

34. Hodak, J. H., Henglein, a, Giersig, M. & Hartland, G. V. Laser-induced inter-diffusion in AuAg core-shell nanoparticles. *J. Phys. Chem. B* **104,** 11708–11718 (2000).

35. Smith, J. G., Yang, Q. & Jain, P. K. Identification of a critical intermediate in galvanic exchange reactions by single-nanoparticle-resolved kinetics. *Angew. Chemie - Int. Ed.* **53,** 2867–2872 (2014).

36. Au, L., Lu, X. & Xia, Y. A comparative study of galvanic replacement reactions involving Ag nanocubes and AuCl2- or AuCl4-. *Adv. Mater.* **20,** 2517–2522 (2008).

37. Jain, P. K., Lee, K. S., El-Sayed, I. H. & El-Sayed, M. A. Calculated absorption and scattering properties of gold nanoparticles of different size, shape, and composition: Applications in biological imaging and biomedicine. *J. Phys. Chem. B* **110,** 7238–7248 (2006).

38. Genç, A. *et al.* Tuning the plasmonic response up: Hollow cuboid metal nanostructures. *ACS Photonics* **3,** 770–779 (2016).

39. Erlebacher, J., Aziz, M. J., Karma, a, Dimitrov, N. & Sieradzki, K. Evolution of nanoporosity in dealloying. *Nature* **410,** 450–453 (2001).

Tunable electrochemistry of gold-silver alloy nanoshells

The rational design of advanced metallic nanoparticles (MNPs) with unique properties and functionalities has proven to be an extremely successful strategy in providing innovative and advantageous solutions to overcome the conventional intrinsic limitations of macro/micro size materials applied in *in vitro* diagnostic technologies[1,2], among other industrial uses. In particular, the profound understanding of the relationship between noble MNPs' localized surface plasmon resonance (LSPR) and their atomic structure, morphology and composition has led to the successful development of a number of optical biosensors, whose enhanced sensitivity and flexibility outdo their more conventional predecessors.[3] In spite of that, a comparable ability in predicting and designing MNPs' electrochemical properties through their controlled synthesis hasn't been reached yet (with only few exceptions available in literature)[4], probably due to the lack of reliable and reproducible synthetic methodologies for complex nanomaterials. Interestingly though, the introduction of electroactive MNPs as signal amplification carriers or direct signal generating elements provided increased sensitivities and enhanced performances in many biosensing applications thanks to their unique redox and electrocatalytic properties,[5,6,7] which in turn emerge from their shape, surface morphology and chemical composition.[4,8,9] Indeed, electroactive MNPs represent a promising alternative to redox enzymes as electrochemical transducers since they are significantly more affordable in production and engineering, while their robustness allows easy storage (i.e. temperature, pH) and longer half-lives.[10]

Au and Ag NPs in Biosensing

Gold and silver nanoparticles (Au and Ag NPs) are probably the most widely studied and applied nanomaterials in sensing thanks to well-established understanding of their optical properties, highly susceptible to their chemical environment and easily tunable by controlling their shape, morphology and composition, as well as the electrochemical behaviour they show in certain working conditions.[11,12] Unfortunately, monometallic Ag NPs have found limited practical use because of a severe susceptibility to oxidation[13], resulting in a low durability and reproducibility in many bio-related applications. On the other hand, obtaining a direct electrochemical response from monometallic Au NPs requires secondary reagents or strong oxidizers able to activate catalytic effects or to generate redox active species, making extremely impractical to translate the use of this nanomaterial into electrochemical diagnostic platforms for commercial use.[8] As a result, significant effort has been put into combining Au and Ag into a single functional nanoprobe possessing both the former's high biocompatibility and stability to oxidation and the readily accessible electrochemical activity of the latter.[11,14] In this context, the two most explored morphologies, core shell Au@Ag NPs and AuAg alloy NPs, both exhibit an enhanced resistance to Ag oxidation thanks to an electronic density redistribution between the two noble metals, which enriches Ag orbitals with *d*-charge from Au.[15,16] However, no previous studies have focused on controlling the amount of this effect in order to trigger the electrochemical activity of silver without compromising the structural integrity of the system. This is in part due to the inherent immiscibility of Au and Ag at the nanoscale which, despite their perfect bulk miscibility, promotes the latter's spontaneous segregation in polycrystalline heterogeneous mixtures given its higher surface energy.[17]

Herein, hollow AuAg nanoshells (NSs) are proposed as a novel class of electroactive nanomaterial with highly promising applicability and flexibility as electrochemical labels. Their electrochemical characterization reveals the features of catalytic Ag underpotential deposition (UPD) at their surface, which has been found to depend directly on the combination of their morphology and relative chemical composition. This work provides the base for a better understanding of hollow AuAg NSs electrochemistry as well as a successful example of how the rational design of nanomaterials with controlled properties can provide suitable tools for electrochemical sensing.

Controlled Composition of AuAg NSs

Hollow AuAg Nanoshells were synthetized following a protocol developed recently by our group.[18] Briefly, starting from an aqueous 5 mM polyvinyl pyrrolidone (PVP) solution containing Ag NPs of the desired size, a galvanic replacement reaction (GRR) was carried out by adding gradually a 1 mM $HAuCl_4$ solution through a syringe pump. Thanks to the difference in reduction potentials of the two noble metals (standard reduction potentials of Ag^+ and Au^{3+} are 0.7996 V and 1.498 V, respectively[19]), Au^{III} is progressively reduced onto the silver sacrificial templates surface while metallic Ag is oxidized forming a gold shell which encloses a growing inner cavity. **Figure 1 – A** shows TEM micrographs of the final stage of the reaction displaying highly monodisperse hollow AuAg NSs of c.a 60 nm in diameter, with a thin and smooth outer shell of c.a 10 nm thickness. The presence of PVP in the reaction mixture is crucial to slow down reaction kinetics and obtain thin and smooth surfaces, while at the same time provides them with increased stability towards aggregation.[20]

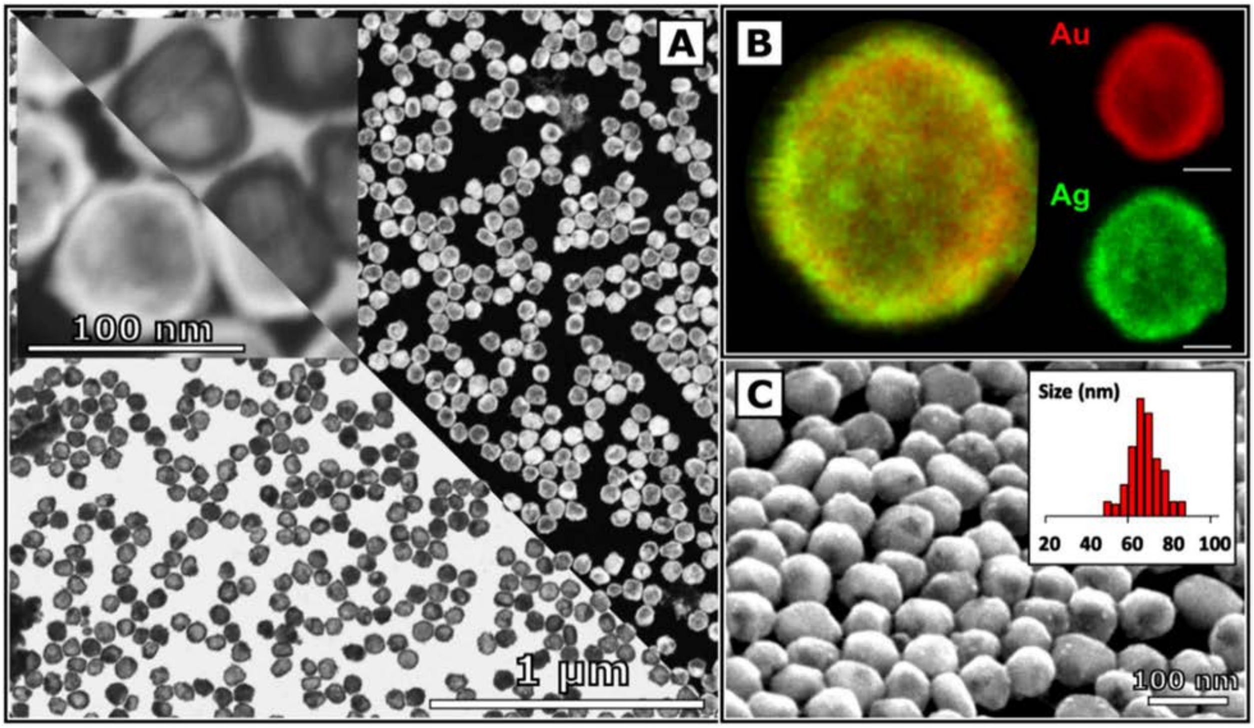

Figure 1 - A: TEM and HAADF-STEM micrographs of highly monodispersed 60.0 ± 4.4 nm AuAg NSs composed by a thin (≈10 nm) shell with a smooth surface and a large (≈40 nm) internal void. **B:** HAADF-STEM elemental distribution micrographs of a single AuAg NS (white bar corresponding to 20 nm). At the final stage of GRR Ag is found both in the Au-rich alloy outer thin shell as well as in the inner particle surface in its metallic form. **C:** SEM AuAg NSs surface characterization and size distribution.

During GRR, the difference in interdiffusion rates between the two noble metals favours the formation of a stable alloy at the interface between the particle's Ag dissolving core and the forming Au-rich shell.[21] **Figure 1 – B** shows the elemental distribution of hollow AuAg NSs by EDS mapping: while Au (*green*) is located only in the outer particle surface together with alloyed Ag (*red*), some "bulk" silver remaining from the original core is still present at the interface. Indeed, co-etchers such as HCl are needed during the hollowing process in order to vary the internal void size by corroding the "bulk", not alloyed core Ag remaining during the reaction. Thin hollow AuAg NSs with smooth integral surfaces are then obtained in high conversion yields and precisely controlled morphologies and chemical composition (**Figure 1 – C**), thanks also to the high monodispersity of the templates solution.[22]

Electrochemistry of AuAg NSs

The exposure of metallic silver to ambient atmosphere as well as nucleophilic species (such as halide anions) at pH lower than 8 is known to lead to its oxidative dissolution.[15,23] In order to generate the electrochemical signal necessary for AuAg NSs to be used as redox reporters, the controlled corrosion of their "bulk" Ag core needs to be achieved through the use of a suitable medium.[24] Phosphate buffer saline (PBS) at pH 7.4 was therefore chosen as electrolyte not only to provide this necessary oxidizing character, given by its relatively high chlorides concentration, but also to better reproduce the typical pH and salinity of biological matrixes. **Figure 2 – A, B** show DPVs of AuAg NSs performed onto SPCEs in PBS 10 mM pH 7.5. When performing DPVs of PVP-coated AuAg NSs (**Figure 2 – A,** "**AuAgNSs@PVP"**), two well-defined anodic current peaks were observed: the first and more intense one (+0.8 V vs RHE, *red curve segment*), corresponding to oxidation of the metallic, "*bulk*" silver contained in the partially emptied particle core, accompanied by a weaker signal at higher oxidation potentials (+0.9 V vs RHE, *green curve segment*), given by the "*more noble*" alloyed silver. It is known that the driving force for the formation of energetically favourable alloys, such as the gold-silver one, is the thermodynamic gain obtained by the interdiffusion of the two metals favoured by the rather small difference observed in the lattice parameters of both metals (408.53 pm for Ag and 407.82 pm for Au).[19]

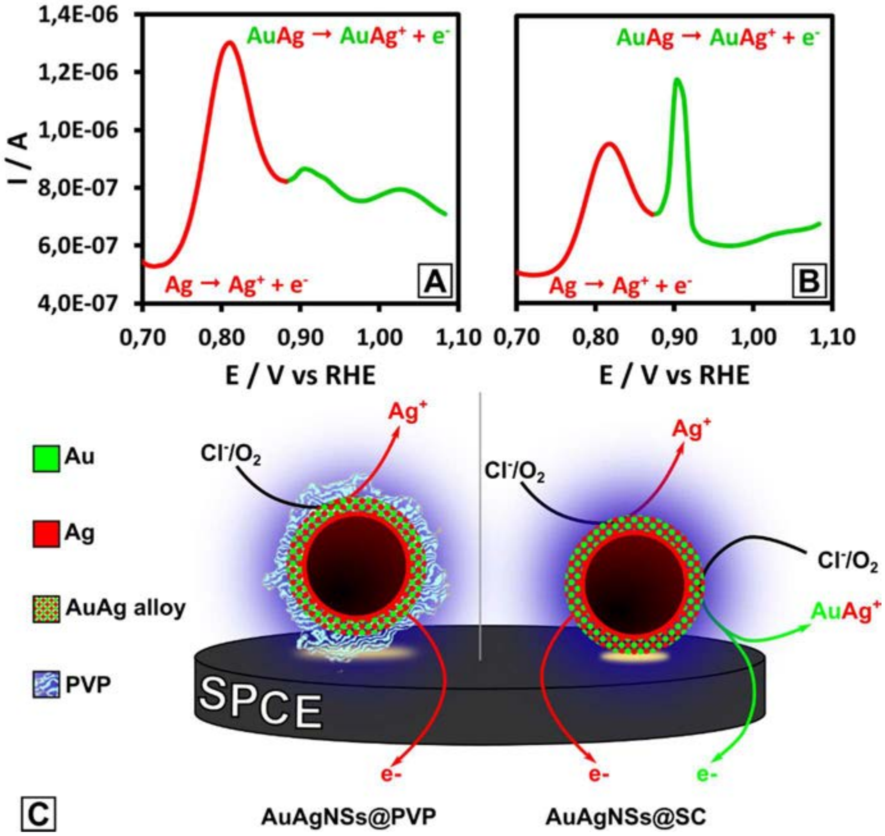

Figure 2 – A, B: DPVs in PBS 10 mM pH 7.5 of AuAg NSs coated with PVP and SC respectively. The analytical peak, found at +0.8 vs RHE, corresponds to the stripping oxidation of metallic silver, while the secondary one recorded at +0.9 vs RHE derives from the concurrent oxidation of the alloyed silver. **C:** proposed electrochemical mechanism for the AuAg NSs voltammetric profile. *Left*: PVP-coated AuAg NSs. The presence of chlorides and dissolved oxygen promotes the partial corrosion of metallic Ag from the particle's core, allowing for its detection through anodic stripping voltammetry. Only a weak signal for the oxidation of alloyed silver is observed. *Right*: SC-coated AuAg NSs. No insulating layer prevents the particle direct contact with the electrode surface, resulting in an increased current intensity in correspondence with the anodic stripping peak of alloyed silver.

Compared to metallic silver, Ag atoms composing the alloy possess a higher stability towards oxidation thanks to the proximity effect[15,16,14], causing their characteristic anodic stripping peak to be observed at higher oxidation potentials. This behaviour is coherent with the unique electronic configuration of bimetallic AuAg systems, described also by Nishimura *et al.*, where a unique charge transfer from Au 4*f* and 5*d* levels increases electron density within Ag *d*-levels, yielding to a negative Ag oxidation state which suppresses its chemical oxidation when exposed to surrounding environments.[15,16,25] The description of the system is further corroborated when sodium citrate (SC)-coated hollow AuAg NSs are characterized (**Figure 2 – B, "AuAgNSs@SC"**): in this case the material does not have any polymeric coating preventing the direct contact between the thin alloy shell and the electrode surface[26] and, even if an analogous current profile is observed in term of peak potentials, their relative intensities change. In particular, the signal of the alloyed Ag, localized only in the 10 nm-thick AuAg shell, increases relevantly because of a better contact with the electrode. **Figure 2 – C** provides a schematization of the electrochemical signal's generation mechanism for AuAg NSs with each type of coatings. Moreover, the same measurement performed on a PVP-coated monometallic Ag NPs solution (**Figure S1**) shows correspondence between the $Ag^0 \rightarrow Ag^+$ oxidation peak at +0.80 - +0.82 vs RHE[23] for the three kinds of NPs studied (only sodium citrate-coated Ag NPs (**Figure S1**) cannot be measured due to their instant aggregation in PBS[27]). Interestingly, no electrochemical signal appears when using equimolar PB instead of its saline formulation (**Figure S1**). As expected, without chlorides no Ag^+ ions are generated from the particles' residual silver core for its cathodic reduction during DPV initial deposition step, and therefore no anodic stripping current can be observed, showing how crucial the presence of the corroding O_2/Cl^- solvated couple is in promoting silver oxidation. This aspect acquires notable importance since conventionally the use of metal and semiconductor NPs as electrochemical labels requires strong acids in order to generate the corresponding cations through particles corrosion.[2] The need for these impractical but necessary components precludes completely the possibility for the commercialization of such a system or their application in biological environments. Exploiting instead the mild oxidizing character of biological matrixes as the only trigger for activating the electrochemical properties of AuAg NSs represents a game-changing step forward for the development of electrochemical transducers in real-world diagnostic applications.

Au Electrocatalytic Effect

As it is widely known and reported, the elemental composition of AuAg NSs, together with their aspect-ratio (understood as the ratio between the shell thickness and the void radius), determines the localized surface plasmon resonance (LSPR) band position.[18] These two parameters depend on the extent of GRR and can be controlled by tuning the amount of Au^{III}

added to the reaction mixture: depending on the stoichiometry of the process, the silver core of the particle is progressively depleted, both by the redox reaction driven by the difference in reduction potentials between the two noble metals and by the alloying process, which "extracts" metallic silver from the particle core and favours its migration towards the surface.[17] Additionally, core Ag is dissolved by the combined action of protons, dissolved oxygen and nucleophiles present in solution.[18] **Figure 3 – A** shows high magnification TEM micrographs of the different phases of the GRR, where 60 nm-sized Ag NPs are progressively converted into hollow NSs through the formation of a thin Au shell on their surface while a growing inner void is corroded from their core. During this process the relative amount of the two noble metals (Au/Ag ratio) grows accordingly: **Table 1** reports the calculated and experimental values of Au/Ag ratio, which are in good agreement with each other, for the different phases of GRR. Less reported is the effect of the nanoalloys composition on their electrochemical behaviour, explored only to our knowledge for "*bulk*" AuAg NPs[28,29] and macroscopic AuAg micro/nano-porous electrodes.[30,31] Thus, Cyclic Voltammetries (CVs) of AuAg NSs at different degrees of galvanic replacement conversion were carried out (**Figure 3 – B**) and revealed an increasing trend in the Ag oxidation current intensity. At the initial and intermediate stages of GRR (**Figure 3 – B**, *yellow, orange, red and purple curves*), characterized by a relatively low Au/Ag relative composition as well as a small void and an incomplete Au shell, the hollow nanocrystals display a weak anodic signal, with peak currents not overcoming the ≈ 3 μA value (**Figure 2 – B,** *inset*; **Table 1**). The higher amount of Au deposited at the later GRR stages together with the continued enlargement of the internal cavity greatly enhances the oxidation current intensity, reaching a maximum for particles with Au-rich alloyed outer shells and large internal voids (**Figure 3 – B**, *blue curve*, **Table 1**). The reason for this electrochemical signal amplification resides probably in two synergic effects caused by the transformations in AuAg NSs morphology and chemical composition. Firstly, the increased surface-to-volume ratio obtained with the void enlargement (**Figure 3 – A**) would correspond to a higher degree of chlorides corrosion and therefore a larger amount of Ag^+ generated at the electrode surface, which in turn brings to higher oxidation currents. Secondly, when analysing the CVs of the different phases of GRR, a weak but clearly defined reduction peak appears at +0.44 vs RHE only in the case of the latest GRR stages (**Figure 3 – B**, *blue curve*): this well-known and studied feature corresponds to the UPD of Ag^+ ions onto the NSs' surface[32,33] exploited successfully in the electrochemical silver-enhanced method with Au NPs.[34,35,36] The metal cations electrodeposition mechanism onto other metallic surfaces has been largely investigated at the macro-scale, while few examples of metal UPD over MNPs are found in literature.[37,38] During the UPD process metal ions in solution can adsorb onto the MNPs surface altering the local surface charge density of the metal. Upon application of a cathodic potential the *ad*-atoms undergo a partial discharge, which corresponds to a negative partial charge transfer from the NPs excess electron density.

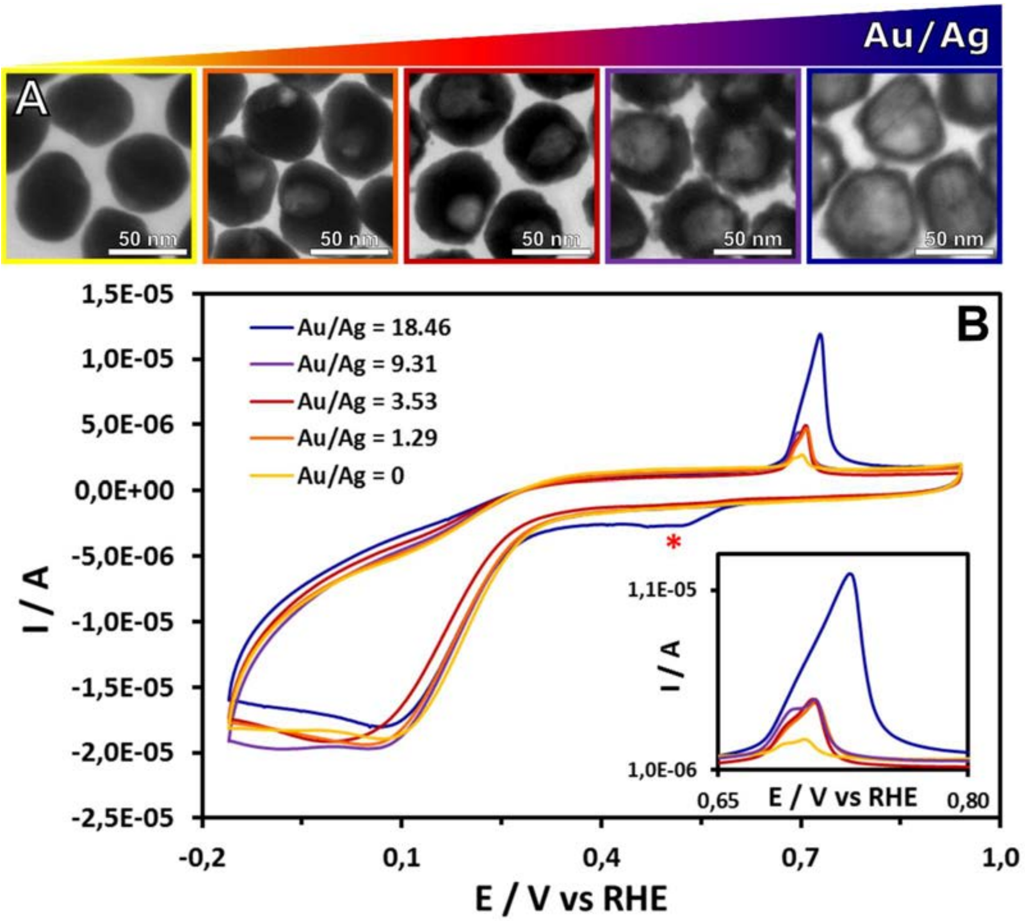

Figure 3 - A: TEM images showing the morphological evolution of silver templates during GRR. Starting from ≈ 60 nm monodispersed Ag NPs (*left*), titration with $HAuCl_4$ triggers the structural and chemical transformation leading gradually to the formation of a thin AuAg alloy shell enclosing an empty internal cavity (*right*). **B**: CVs of AuAg NSs at different GRR stages (inset showing peak currents for Ag oxidation at ≈ +0.76 vs RHE normalized over concentration). While the voltammetric profile maintains the same features in term of peaks position and shape, the current intensity increases once the GRR is started. At the latest phase, corresponding to a thin Au-rich shell enclosing a large void (*right*), the electrocatalytic $Ag^+ + e^- \rightarrow Ag^0$ reduction peak appears at +0.44 V vs RHE (*).

This cathodic current is observed at reducing potentials less negative than the metal's standard reduction one. As shown by the CVs of hollow AuAg NSs bearing a Au-rich outer shell and a large internal void (**Figure 3 – B,** *blue curve*), during the cathodic scan the peak observed at -0.2 V vs Ag/AgCl represents the first deposition stage, attributed to the partial discharge of solvated Ag^+ *ad*-atoms, followed by bulk deposition of Ag only at -0.16 V vs RHE (the broad nature of the UPD peak compared to macroscale metals surfaces is attributed to AuAg NSs small sizes and faceted surface). This catalytic effect is observed only for AuAg NSs obtained at the final stages of the GRR, suggesting a correlation between morphology, surface chemical composition and the Ag UPD reaction. Indeed, variations in morphology and degree of alloying in bimetallic systems are known to influence their catalytic activity through a modulation of the electronic structure of the constituting metals.[12,14,39,40] Hollow AuAg NSs at the latest GRR stages possess the highest content of Au atoms (**Table 1**), which are concentrated in the thin outer shell due to their synthesis mechanism.[18] As explained previously, the injection of Au *d*-charge into Ag electronic levels results in an increased electron density localized on the particles surface.[16] Hollow AuAg NSs will therefore display higher surface potential, given its direct dependence form the metal surface excess charge[41], causing the adsorbed Ag ions to interact with a more intense generated electromagnetic field. As a consequence, Au-rich NSs will then catalyse the reduction of Ag^+ produced by PBS, generating a more intense anodic stripping current.

Peak Current [μA] [a]	Au/Ag % (Theor.)	Au/Ag % (EDS)
0.66 ± 0.5	0.00	0.00
2.88 ± 0.5	1.87	1.29
2.92 ± 0.1	3.38	3.53
3.25 ± 0.2	10.77	9.31
7.76 ± 0.4	22.91	18.46

[a] Anodic current measured at +0.12 mV vs Ag/AgCl.

Table 1. Calculated and experimental values of Au/Ag ratio for the different phases of GRR and their corresponding anodic current. For low Au/Ag ratios, only a slight increase in peak current is observable compared with the sacrificial Ag NPs (Au/Ag = 0). At the latest stages of GRR, corresponding to the higher amount of Au deposited (Au/Ag ≈ 20), a greater signal enhancement appears.

Following a different but agreeing description of the catalytic mechanism, hollow nanostructures are known to display better plasmonic properties than their solid counterparts thanks to the plasmon hybridization mechanism, in which the presence of cavities induce an enhancement and more homogeneous distribution of the generated electromagnetic fields.[42,43] The adsorption and partial discharge of metal ions during the UPD, which takes place at the closest proximity to the MNPs surface, will therefore be affected by the enhanced field intensities showed by the hollowed particles, resulting in an increased Ag catalytic reduction.

Size Effect

We extended the study of the electronic effect on AuAg NSs electrocatalytic UPD to hollow nanoalloys of different sizes (namely 60, 80, 100, 150 nm), all having in common the final SPR maximum wavelength, found at 700 nm. As it is synthetically extremely difficult to precisely control the final relative amount of Au and Ag using templates whose silver content and total surface area vary with size at different proportionalities, fixing a common final wavelength provides a direct correlation between both the Au/Ag composition and the relative morphological aspect ratio.[18] **Figure 4 – A** shows low and high magnifications TEM dark field micrographs of 60, 80, 100, 150 nm AuAg NSs (*from top-left, clockwise*), all possessing the common hollow morphology characterized by a relatively thin outer shell and a large internal void, summarized in **Table 2**. EDS elemental mapping of these particles (**Figure 4 – B**) reveals that, while the topological distribution of Au (*green*) and Ag (*red*) is analogous among all the different sizes, their relative amount differs from size to size. Calculated and experimental Au/Ag ratios for all sizes, reported with significantly good agreement in **Table 2**, show how bigger hollow AuAg NCs possess a higher Ag content compared to smaller ones, regardless of the quite constant aspect ratio between shell thickness and void size. As shown in **Figure 4 – C**, DPVs of AuAg NSs of different sizes show large current intensity variations depending on their relative noble metal content. The most intense oxidation current is observed for 80 nm-sized NSs which seem to provide the higher signal enhancement. Both 60 nm and 100 nm AuAg NSs display a lower current amplification while for 150 nm hollow nanocrystals no peak appears. By comparing these results with the Au/Ag content of each case (**Table 2**) it is clearly visible how 80 nm-sized AuAg NSs possess a high-enough Au content to trigger the electrocatalytic silver reduction through the mechanism described above. In contrast bigger particles do not possess such high-enough Au content since their alloy composition is still too rich in silver (an effect that cannot be explained by the morphological aspect ratio alone). Interestingly, even though 60 nm particles possess a sufficient Au/Ag ratio for triggering the catalysed Ag UPD, their lower anodic current intensity is a consequence of the almost complete depletion of the core metallic silver, responsible for generating the actual electrochemical signal.

Size (nm)	**60**	**80**	**100**	**150**
Au/Ag % (Theor.)	18.46	17.17	16.73	9.74
Au/Ag % (EDS)	22.91 ± 0.20	18.96 ± 0.20	14.14 ± 0.13	10.13 ± 0.12
Void size (nm)	41.6 ± 5.4	63.8 ± 7.5	68.2 ± 9.3	98.9 ± 16.5
Shell thick. (nm)	9.1 ± 1.6	12.4 ± 2.6	16.1 ± 5.2	24.1 ± 8.8
Aspect ratio[a]	**0.1** ± 0.0	**0.2** ± 0.1	**0.2** ± 0.1	**0.3** ± 0.1

[a] Aspect ratio calculated as (D-d)/d, being D the outer and d the inner diameter respectively.

Table 2. Au/Ag ratio calculated and measured by EDS, morphological features and aspect ratio of AuAg NSs of different sizes (60, 80, 100, 150 nm): a gold-rich alloy shell, together with a low aspect ratio, are necessary in order to obtain a strong oxidation signal

Conclusions

Hollow AuAg (NSs) are presented as promising electroactive nanomaterials showing high potential and flexibility for future use as electrochemical labels for diagnostics (biosensing), beside other applications. The AuAg surface-catalysed Ag underpotential deposition is discovered and its mechanism described in detail. Thanks to it, DPV anodic oxidation signals are enhanced up to almost one order of magnitude compared to Ag NPs, depending on AuAg NSs morphology and relative chemical composition. This behaviour, previously unreported for AuAg NSs, is likely connected to the increase in surface charge density obtained with the Au enrichment of the outer shell, which seems to favour Ag^+ UPD onto it. A precise modulation of this electrocatalytic effect can be obtained by carefully design and control of the synthesis of these advanced materials, allowing the construction of efficient and robust electrochemical transducers ready for substituting enzymes in electrochemical diagnostic technologies beside other uses. This approach could be extended to other types of multimetallic nanomaterials whose diverse and selective electrocatalytic properties could be exploited as labels in immuno- and in enzymatic assays.

References

1. Genç, A. *et al.* Hollow metal nanostructures for enhanced plasmonics: Synthesis, local plasmonic properties and applications. *Nanophotonics* **6,** 193–213 (2017).
2. Merkoçi, A. Nanoparticles-based strategies for DNA, protein and cell sensors. *Biosens. Bioelectron.* **26,** 1164–1177 (2010).
3. Kumar, A., Kim, S. & Nam, J. M. Plasmonically Engineered Nanoprobes for Biomedical Applications. *J. Am. Chem. Soc.* **138,** 14509–14525 (2016).
4. Qiu, H.-J., Li, X., Xu, H.-T., Zhang, H.-J. & Wang, Y. Nanoporous metal as a platform for electrochemical and optical sensing. *J. Mater. Chem. C* **2,** 9788–9799 (2014).
5. Costa, M. M. *et al.* Simple monitoring of cancer cells using nanoparticles. *Nano Lett.* **12,** 4164–4171 (2012).
6. Perfézou, M., Turner, A. & Merkoçi, A. Cancer detection using nanoparticle-based sensors. *Chem. Soc. Rev.* **41,** 2606–2622 (2012).
7. Merkoçi, A. Nanoparticles Based Electroanalysis in Diagnostics Applications. *Electroanalysis* **25,** 15–27 (2013).
8. Ambrosi, A., Merkoçi, A. & de la Escosura-Muñiz, A. Electrochemical analysis with nanoparticle-based biosystems. *TrAC - Trends Anal. Chem.* **27,** 568–584 (2008).
9. Kelley, S. O. *et al.* Advancing the speed, sensitivity and accuracy of biomolecular detection using multi-length-scale engineering. *Nat. Publ. Gr.* **9,** 969–980 (2014).
10. Wang, X., Hu, Y. & Wei, H. Nanozymes in bionanotechnology: from sensing to therapeutics and beyond. *Inorg. Chem. Front.* **3,** 41–60 (2016).
11. Byers, C. P. *et al.* From tunable core-shell nanoparticles to plasmonic drawbridges: Active control of nanoparticle optical properties. *Sci. Adv.* **1,** e1500988 (2015).

12. Zugic, B. *et al.* Dynamic restructuring drives catalytic activity on nanoporous gold-silver alloy catalysts. *Nat. Mater.* **16,** 558–564 (2017).

13. Zheng, Y., Zeng, J., Ruditskiy, A., Liu, M. & Xia, Y. Oxidative etching and its role in manipulating the nucleation and growth of noble-metal nanocrystals. *Chem. Mater.* **26,** 22–33 (2014).

14. Slater, T. J. a *et al.* Correlating catalytic activity of Ag-Au nanoparticles with 3D compositional variations. *Nano Lett.* **14,** 1921–1926 (2014).

15. Shankar, C. *et al.* Chemical stabilization of gold coated by silver core-shell nanoparticles via electron transfer. *Nanotechnology* **23,** (2012).

16. Nishimura, S., Dao, A. T. N., Mott, D., Ebitani, K. & Maenosono, S. X-ray Absorption Near-Edge Structure and X-ray Photoelectron Spectroscopy Studies of Interfacial Charge Transfer in Gold–Silver–Gold Double-Shell Nanoparticles. *J. Phys. Chem. C* **116,** 4511–4516 (2012).

17. Lewis, E. a. *et al.* Real-time imaging and elemental mapping of AgAu nanoparticle transformations. *Nanoscale* **6,** 13598–13605 (2014).

18. Russo, L. *et al.* Time- and Size-Resolved Plasmonic Evolution with nm Resolution of Galvanic Replacement Reaction in AuAg Nanoshells Synthesis. *Chem. Mater.* **30,** 5098–5107 (2018).

19. Xia, X., Wang, Y., Ruditskiy, A. & Xia, Y. 25Th Anniversary Article: Galvanic Replacement: a Simple and Versatile Route To Hollow Nanostructures With Tunable and Well-Controlled Properties. *Adv. Mater.* **25,** 6313–33 (2013).

20. Gonzalez, E. *et al.* Carving at the Nanoscale: Sequential Galvanic Exchange and Kirkendall Growth at Room Temperature. *Science* **334,** 1377–1380 (2011).

21. Cobley, C. M. & Xia, Y. Engineering the properties of metal nanostructures via galvanic replacement reactions. *Mater. Sci. Eng. R* **70,** 44–62 (2010).

22. Bastús, N. G., Merkoçi, F., Piella, J. & Puntes, V. F. Synthesis of Highly Monodisperse Citrate-Stabilized Silver Nanoparticles of up to 200 nm: Kinetic Control and Catalytic Properties. *Chem. Mater.* **26,** 2836–2846 (2014).

23. Toh, H. S., Batchelor-McAuley, C., Tschulik, K. & Compton, R. G. Electrochemical detection of chloride levels in sweat using silver nanoparticles: a basis for the preliminary

screening for cystic fibrosis. *Analyst* **138,** 4292–4297 (2013).

24. Tschulik, K., Batchelor-McAuley, C., Toh, H.-S., Stuart, E. J. E. & Compton, R. G. Electrochemical studies of silver nanoparticles: a guide for experimentalists and a perspective. *Phys. Chem. Chem. Phys.* **16,** 616–623 (2014).

25. Liu, R. *et al.* Alloyed Crystalline Au–Ag Hollow Nanostructures with High Chemical Stability and Catalytic Performance. *ACS Appl. Mater. Interfaces* **8,** 16833–16844 (2016).

26. Kleijn, S. E. F., Lai, S. C. S., Koper, M. T. M. & Unwin, P. R. Electrochemistry of Nanoparticles. *Angew. Chemie - Int. Ed.* **53,** 3558–3586 (2014).

27. Cloake, S. J. *et al.* Anodic stripping voltammetry of silver nanoparticles: Aggregation leads to incomplete stripping. *ChemistryOpen* **4,** 22–26 (2015).

28. Holt, L. R., Plowman, B. J., Young, N. P., Tschulik, K. & Compton, R. G. The Electrochemical Characterization of Single Core-Shell Nanoparticles. *Angew. Chemie - Int. Ed.* **55,** 397–400 (2016).

29. Saw, E. N., Grasmik, V., Rurainsky, C., Epple, M. & Tschulik, K. Electrochemistry at single bimetallic nanoparticles – using nano impacts for sizing and compositional analysis of individual AgAu alloy nanoparticles. *Faraday Discuss.* **157,** 243–284 (2016).

30. Liu, Z., Huang, L., Zhang, L., Ma, H. & Ding, Y. Electrocatalytic oxidation of d-glucose at nanoporous Au and Au-Ag alloy electrodes in alkaline aqueous solutions. *Electrochim. Acta* **54,** 7286–7293 (2009).

31. Xu, C. *et al.* Low temperature CO oxidation over unsupported nanoporous gold. *J. Am. Chem. Soc.* **129,** 42–43 (2007).

32. Herrero, E., Buller, L. J. & Abruña, H. D. Underpotential deposition at single crystal surfaces of Au, Pt, Ag and other materials. *Chem. Rev.* **101,** 1897–1930 (2001).

33. Rogers, L. B., Krause, J. C., Griess, J. & Ehrlinger, D. B. The electrodeposition behavior of traces of silver. *J. Electrochem. Soc.* **95,** 33–46 (1949).

34. Lai, G., Wang, L., Wu, J., Ju, H. & Yan, F. Electrochemical stripping analysis of nanogold label-induced silver deposition for ultrasensitive multiplexed detection of tumor markers. *Anal. Chim. Acta* **721,** 1–6 (2012).

35. Chu, X. *et al.* Silver-enhanced colloidal gold metalloimmunoassay for Schistosoma japonicum antibody detection. *J. Immunol. Methods* **301,** 77–88 (2005).

36. Zhang, J., Xiong, Z. & Chen, Z. Ultrasensitive electrochemical microcystin-LR immunosensor using gold nanoparticle functional polypyrrole microsphere catalyzed silver deposition for signal amplification. *Sensors Actuators, B Chem.* **246,** 623–630 (2017).

37. Price, S. W. T., Speed, J. M. R. J. D., Calvillo, L., Kannan, P. & Russell, a E. Exploring the First Steps in Core-Shell Electrocatalyst Preparation: In Situ Characterization of Cu and Pd shells on Supported Au Nanoparticles. *J. Am. Chem. Soc.* 19448–19458 (2011).

38. Mulvaney, P., Linnert, T. & Henglein, A. Surface chemistry of colloidal silver in aqueous solution: Observations on chemisorption and reactivity. *J. Phys. Chem.* **95,** 7843–7846 (1991).

39. He, W. *et al.* Design of AgM bimetallic alloy nanostructures (M = Au, Pd, Pt) with tunable morphology and peroxidase-like activity. *Chem. Mater.* **22,** 2988–2994 (2010).

40. Tominaga, M. *et al.* Electrocatalytic oxidation of glucose at gold-silver alloy, silver and gold nanoparticles in an alkaline solution. *J. Electroanal. Chem.* **590,** 37–46 (2006).

41. Scanlon, M., Peljo, P., Mendez, M. a, Smirnov, E. a. & Girault, H. Charging and Discharging at the Nanoscale: Fermi Level Equilibration of Metallic Nanoparticles. *Chem. Sci.* **6,** 2705–2720 (2015).

42. Prodan, E. & Nordlander, P. Plasmon hybridization in spherical nanoparticles. *J. Chem. Phys.* **120,** 5444–5454 (2004).

43. Mahmoud, M. A. & El-Sayed, M. A. Gold nanoframes: Very high surface plasmon fields and excellent near-infrared sensors. *J. Am. Chem. Soc.* **132,** 12704–12710 (2010).

Chapter IV

AuAg Nanoshells: Sensing Applications

SERS Detection of Myxovirus Resistance Protein A in Paper-based Immunoassays with AgAu Nanoshells

The ability to differentially detect viral vs. bacterial infections is essential for infection management. Both viral and bacterial infections share similar non-specific symptoms, especially for respiratory diseases. Fever, congestion, respiratory symptoms, and headaches can be attributed to either viral or bacterial infections. When antibiotics are prescribed for viral infections, they will not treat the disease, and the unnecessary antibiotic therapy could ultimately contribute to the growing problem of drug-resistant bacteria.

Myxovirus Resistance Protein A – MxA

Interferons (IFN) are released upon viral infection due to the innate immune response, and while their presence is correlated with viral infections, they are not viable as a biomarker due to their short half-life. However, studies have shown that the 76 kDa protein myxovirus resistance protein A (MxA) is linked with elevated type I IFN levels upon viral infection.[1] Furthermore, it has been shown that MxA is induced quickly, has a longer lifetime of 2-3 days, and is present in blood at high levels, and thus can serve as a good biomarker of acute viral infection and distinguish them from bacterial infections. MxA has broad antiviral activity against a wide range of viruses. Thus, MxA detection can be used to provide guidance for antimicrobial therapy and thus prevent antibiotic resistance. Clinical studies have confirmed the utility of MxA for diagnosing viral infections in a routine clinical setting for respiratory diseases.[2]

Others have demonstrated MxA detection via flow cytometry and ELISA.[3] However, the lateral flow assay (LFA) format used in commercial pregnancy tests is more convenient as a diagnostic, as it can be used PoC and does not require technical expertise to operate. Although commercial lateral flow diagnostic tests for MxA do exist, such as FebriDx (Rapid Pathogen Screening, Inc.),[4] in order to distinguish between viral vs. bacterial infections the MxA assay needs to be used in conjunction with one for C-reactive protein (CRP), which is a biomarker bacterial infections.[5] This assay has been used successfully for distinguishing viral vs. bacterial infections in children.

However, the levels of MxA vary with the age of the patient. MxA levels tend to be higher in infected children, in the 880-1250 ng/ml range.[2,6] On the other hand, in infected adults the reported cut-off value is >40 ng/ml. Thus, being able to quantify MxA levels, particularly in the 40-100 ng/ml range, is important for diagnosis in adults as well as children. Unfortunately, one of the drawbacks of traditional LFAs is that their sensitivity is weak, due to the fact that they are read out by eye, and are used predominantly to provide only yes/no answers. Traditional LFAs[7–9] cannot detect MxA at significant levels for adults, and more importantly cannot quantify the amount of biomarker present due to the lack of sufficient sensitivity. There have been approaches to increase LFA sensitivity include evaporation, utilization of photothermal effects[10] or fluorescent up converting nanoparticles (UCNPs).[4] However, outside of using UCNP, there are no studies of techniques to increase LFA sensitivity for MxA detection.

SERS Nanotags

One attractive approach for increasing the sensitivity of paper based immunoassay detection is surface enhanced Raman spectroscopy (SERS). When a species is in proximity of a gold or silver nanoparticle, the Raman spectrum of the species can be enhanced by as high as 9 orders of magnitude due to the electric field enhancement by the metal nanoparticle.[11–14] This has enabled detection of trace amounts of analytes down to attomol levels.[15,16]

One format of SERS that has facilitated biological detection is the "nanotag" format, where the nanoparticle is decorated with an antibody, peptide, or DNA strand that can bind specifically to a target of interest. The nanoparticle is also decorated with a Raman reporter, which provides the signal.[17–22] This format has been used successfully to enable SERS readouts of immunoassays.

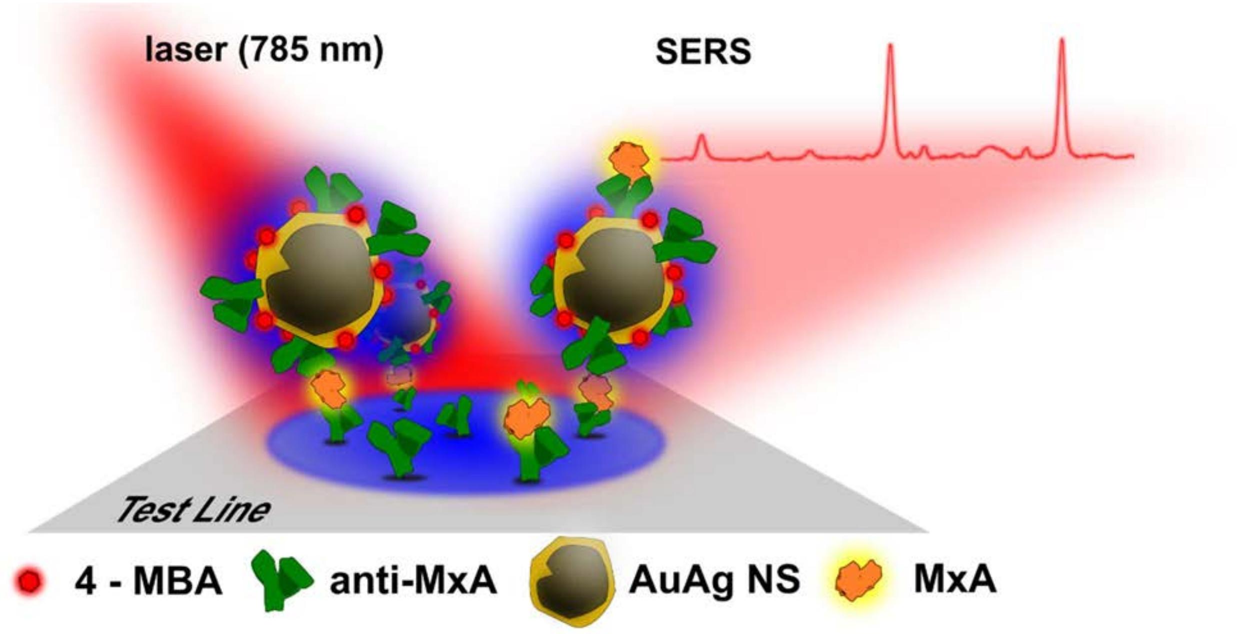

Figure 1 - Schematic representation of the SERS-based LFA immunoassay.

Recently, it has been shown that SERS can enhance the sensitivity of lateral flow immunoassays over a visual readout by 4 orders of magnitude,[23] and 10-15 fold in detecting dengue and zika nonstructural protein 1 (NS1) using star-shaped gold nanoparticles in a dipstick immunoassay.[24] In addition, SERS nanotags can be multiplexed to allow investigation of multiple biomarkers simultaneously.[19,25,261] Consequently, this combination of SERS with paper immunoassays has shown great promise for boosting assay sensitivity.[27,28] Recent advances in SERS instrumentation has resulted in handheld instruments which are more fieldable than traditional spectrometers. Thus, application of SERS readout of paper based immunoassays has the potential to detect MxA at clinically relevant levels, in the 40-100 ng/ml range that is relevant.

Here, we investigate the use of SERS for detection of the viral biomarker MxA in a paper-based immunoassay. As the enhancer, we used hollow AuAg NSs in order to take advantage of their reported strong SERS enhancement.[29] While Ag is known to provide higher amplifications due to its plasmonic properties, its rapid oxidation in biological media can detract from its utility in SERS. Leveraging instead its combination with Au reduces their propensity to be oxidized. At the same time, the use of Au in the nanostructure, despite its lower SERS enhancement, allows to attach covalently Raman reporters through Sulphur bonds. Thus AuAg NSs were conjugated to the Raman reporter mercaptobenzoic acid (4-MBA) for SERS readout and also to anti-MxA antibodies, which enable detection of MxA protein in a nitrocellulose dipstick immunoassay (**Figure 1**). We characterize the NP-Ab conjugates first for optimal stability, reporter coverage and conjugation ratio. Then, we demonstrate the ability to detect MxA at clinical relevant levels for adults in both buffer and human serum with an LOD of 123.5 ng/ml and 51.8 ng/ml respectively. These results could aid the development of assays for distinguishing bacterial vs. viral infections.

Bioconjugate Preparation

NPs have been extensively investigated for use as SERS nanotags, predominantly of Au. SERS enhancement is highest for Ag NPs due to its plasmonic properties. However, Ag oxidation can be a limiting factor for biological applications of Ag NPs. Recent investigation of alloys or composites of Ag and Au have shown that the presence of Au can increase NP stability with respect to oxidation while retaining the strong enhancement properties of the Ag. Furthermore, AuAg composite NPs have been successfully used for detection by SERS.[27,30,31]

We synthesized hollow water soluble AuAg NPs using a method previously developed, which involves the galvanic replacement of Ag in a pre-synthesized Ag NP with Au, resulting in a hollow NP (**Figure 2a**, Methods).[29] TEM bright field and HAADF micrographs of monodisperse hollow AuAg NSs measured a mean diameter of 75 nm ± 7 nm, and showed evidence of a hollow structure (**Figure 2b, Figure S1**). DLS measurements measured a NP hydrodynamic diameter (D_H) of 77 ± 34 nm (**Figure 2e**). NPs of Ag and also Au that were star shaped were compared, which have both been used in the literature as SERS enhancement applications. [32,33]

Figure 2 (*next page*) - Nanoparticle synthesis and conjugation. **A:** Schematic of the process of nanotag preparation. Hollow AuAg NSs are first functionalized with the Raman reporter (4-MBA), then conjugated to the antibody. **B:** TEM bright field and HAADF micrographs of monodisperse hollow AuAg NSs with a mean diameter of ~75 nm. **C:** Functionalization of AuAg NSs with the Raman reporter was monitored by UV-vis spectroscopy at increasing concentrations of 4-MBA. **D:** Characterization of antibody conjugation to AuAg NSs by UV-vis spectroscopy at increasing concentrations of anti-HuIgG. Inset: spectra of SPR peak with increasing anti-HuIgG concentration. **E:** DH and F: ζ-potential of of AuAg NSs-antibody conjugates for increasing concentrations of anti-HuIgG antibody.

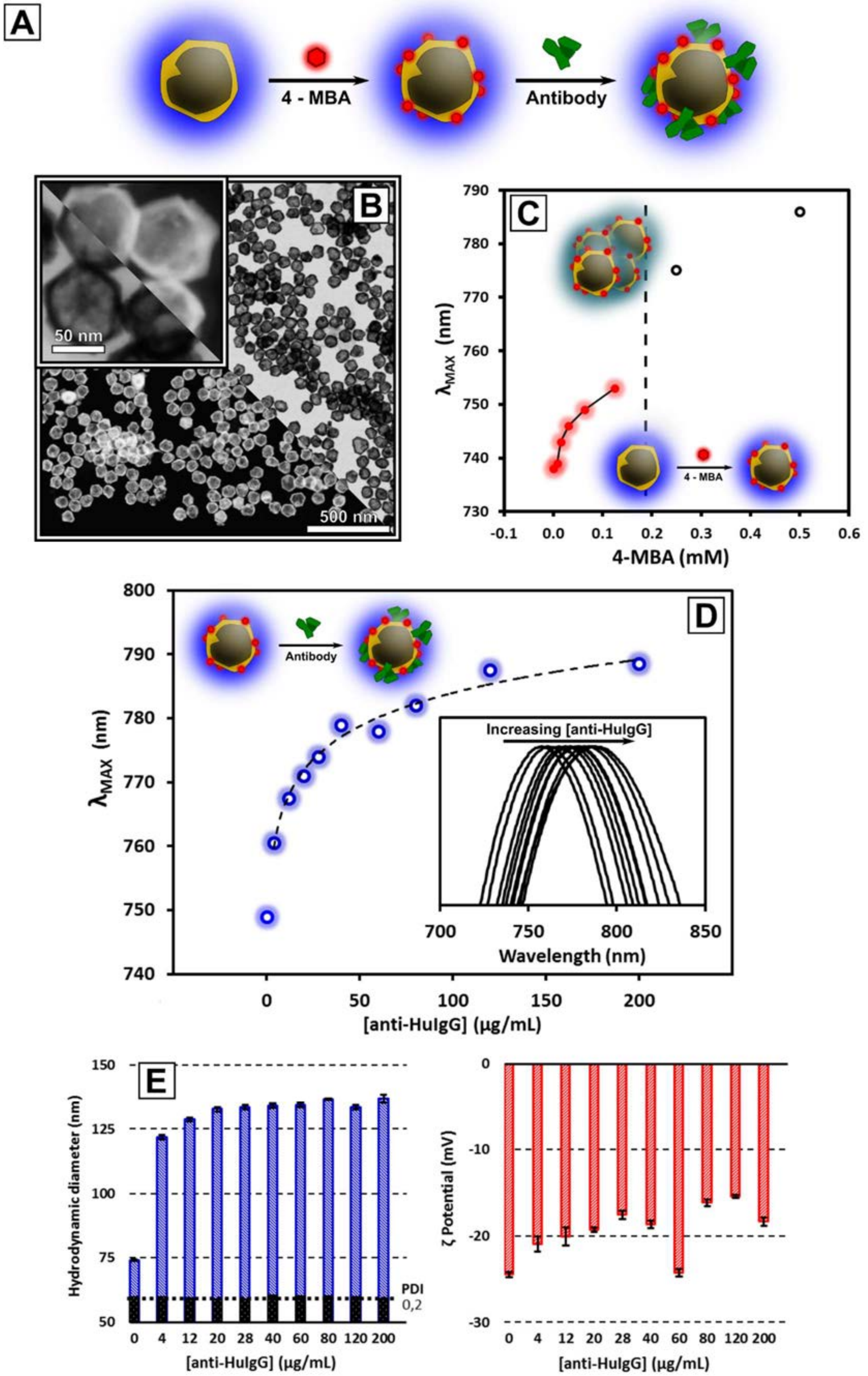
A
4 - MBA
Antibody
B
50 nm
500 nm
C
790
780
770
760
750
740
730
λ_{MAX} (nm)
-0.1
0.0
0.1
0.2
0.3
0.4
0.5
0.6
4-MBA (mM)
4 - MBA
D
800
790
780
770
760
750
740
λ_{MAX} (nm)
Antibody
Increasing [anti-HuIgG]
700
750
800
850
Wavelength (nm)
0
50
100
150
200
[anti-HuIgG] (µg/mL)
E
150
125
100
75
50
Hydrodynamic diameter (nm)
PDI
0,2
0
4
12
20
28
40
60
80
120
200
[anti-HuIgG] (µg/mL)
0
-10
-20
-30
ζ Potential (mV)
0
4
12
20
28
40
60
80
120
200
[anti-HuIgG] (µg/mL)

The NPs were first conjugated to 4-MBA, which is commonly used as a Raman reporter for SERS due to its narrow spectral features.[30] 4-MBA has a thiol group which can bind to Au surfaces, enabling simple incubation for NP functionalization. We measured the optical absorption spectra of the AuAg NPs as a function of the NP:(4-MBA) incubation ratio (**Figure 2c**). Increasing the concentration of 4-MBA relative to the AuAg NPs resulted in a red-shift of the LSPR band, which initially followed an adsorption-like trend towards a saturation plateau. For 4-MBA concentrations greater than 0.2 mM, the red-shift increased more drastically. The initial SPR red shift could be attributed to the change in the index of refraction around the NP upon 4-MBA functionalization. The latter spectral change could be attributed to NP aggregation, where the thiolated MBA affected AuAg NSs colloidal stability. Based on the LSPR red-shift results, we chose an optimal incubation ratio of 4-MBA on the AuAg NPs of ≈3000:1, which maximized the conjugation with the NP, but did not induce NP aggregation.

LFA Optimization

For the dipstick immunoassay, we first explored the use of a model antibody-antigen system. We used anti-human IgG as the binding species on the AuAg NPs and human IgG as its corresponding antigen, which allowed systematic variation of synthesis conditions. This enabled tuning of the sandwich immunoassay response curve to optimally overlap with the relevant MxA concentration window. Anti-human IgG was conjugated to the 4-MBA AuAg NP conjugates by adsorption, where NPs were incubated together with anti-IgG in solution. We varied the NP:Ab incubation ratio, which varied the Ab coverage on the NP The change in AuAg NSs refractive index upon attachment of increasing concentrations of anti-IgG resulted in a Langmuir-like saturation profile for the LSPR maximum wavelength (**Figure 2d**). An antibody concentration of 40 μg/ml was chosen as sufficient for building a monolayer onto the NP surface. AuAg NSs antibody conjugates were characterized by DLS, which revealed an increase in D_H with the addition of antibodies at low concentrations, and increased until it reached a plateau at a value of ~130 nm (**Figure 2e**). Taking into account that AuAg NSs are coated with a layer of PVP, this value is consistent with the adsorption of a monolayer of antibodies. The ζ-potential AuAg NSs varied with increased antibody concentration. The initial value of ~-25 mV stabilizes around a less charged value (~-15 mV) due to antibody adsorption on the particles (**Figure 2f**).

We characterized the SERS signal upon conjugation to the AuAg NSs when spotted down onto nitrocellulose membranes. Multiple (25) SERS spectra were taken over the entire test area. The SERS spectra exhibited a peak at 1584 cm^{-1} which could be assigned to the $\nu_{(C=C)}$ vibrational mode of phenyl ring-stretching motion of the 4-MBA.[30] 25 scans were taken over a grid of the test area (Supporting Information, **Figure S2**) and the average intensity of the 4-MBA peak at 1590 cm^{-1} was plotted as a function of the coverage (inset, **Figure 3a**). The 4-MBA Raman signal increased with increasing 4-MBA concentration in the conjugation reaction, as expected. Furthermore, there was negligible Raman signal from the nitrocellulose background. However, for concentrations higher than 0.04 mM, the 4-MBA induced NPs aggregation, which resulted in a decrease of the SERS signal. Thus, we determined an optimal ~3000:1 incubation ratio between 4-MBA and AuAg NSs for obtaining a sufficient signal.

We measured the SERS signal as a function of nanotag (AuAgNSs@4-MBA@Ab) concentration (**Figure 3b**). A linear trend was observed when spotting increasing amounts of functionalized NPs on the nitrocellulose strip (**Figure 3b, inset**). Dipstick immunoassays using the nanotags were constructed. Anti-IgG was immobilized on the test area and anti-Fc on the control area by spotting. An absorbent pad was attached to the top of the strip, and then the bottom of the strip was immersed in a 2 % bovine serum albumin (BSA) solution with nanotags and IgG antigen. The fluid wicked up the strip to the absorbent pad due to capillary action. If binding of the IgG occurred to both the immobilized antibody and also the conjugated one, a blue color appeared at the test area due to the accumulation of AuAg NSs. In addition, a colorimetric signal appears at the control area as well, resulted from the immobilized anti-Fc binding to the antibodies on the nanotag. This verified that proper flow in the strip occurred. First, the impact of varying Ab coverage on the NPs was investigated. Nanotags were synthesized using antibody solutions at increasing concentration (0 to 200 μg/ml), and then used in the LFA (**Figure 3c**). The visual image of the strips showed increasing colorimetric intensity with Ab coverage. SERS spectra of the resulting test areas were measured (*green*, **Figure 3c**). The 4-MBA SERS intensity at 1590 cm^{-1} (inset, **Figure 3c**) increased in intensity with Ab coverage, but then reached a maximum for AuAg NSs incubated with anti-IgG at 40 μg/ml. This value corresponds to the formation of a monolayer of physically adsorbed antibodies, as supported by the optical monitoring of anti-IgG adsorption (**Figure 2D**).

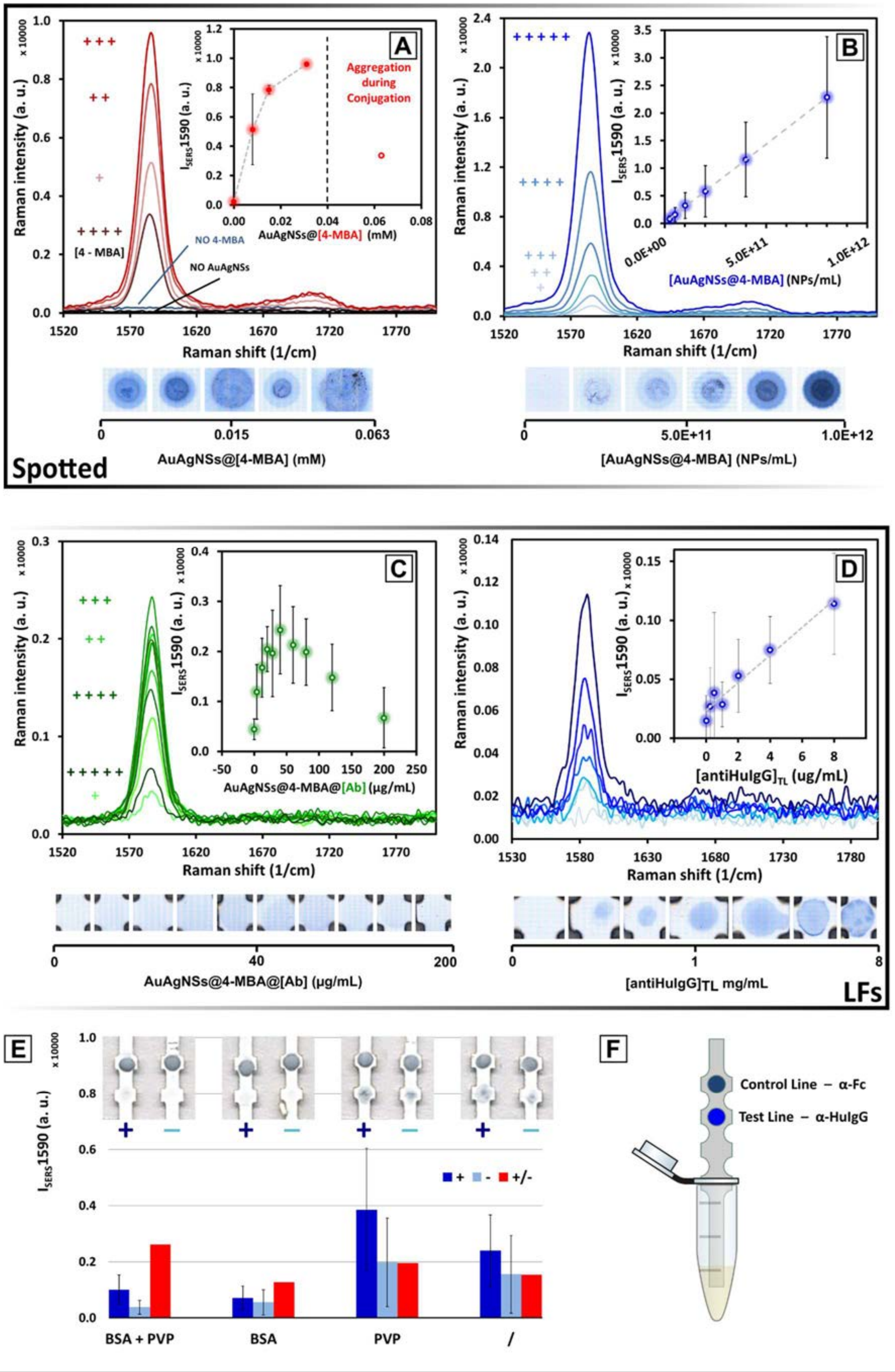
A
Raman intensity (a. u.)
x 10000
+++
++
+
++++
[4 - MBA]
NO 4-MBA
NO AuAgNSs
Raman shift (1/cm)
I$_{SERS}$1590 (a. u.)
Aggregation during Conjugation
AuAgNSs@[4-MBA] (mM)
0
0.015
0.063
Spotted
B
+++++
++++
+++
++
+
[AuAgNSs@4-MBA] (NPs/mL)
0.0E+00
5.0E+11
1.0E+12
C
AuAgNSs@4-MBA@[Ab] (µg/mL)
0
40
200
D
[antiHuIgG]$_{TL}$ (ug/mL)
[antiHuIgG]$_{TL}$ mg/mL
0
1
8
LFs
E
+
−
+/-
BSA + PVP
BSA
PVP
/
F
Control Line – α-Fc
Test Line – α-HuIgG

Figure 3 (*previous page*) - Immunoassay optimization for SERS. **A:** SERS spectra of AuAg NSs as a function of 4-MBA concentration in the conjugation reaction. Inset: SERS intensity at 1590 cm^{-1} as a function of 4-MBA concentration. **B:** SERS spectra as a function of conjugate (AuAgNSs@4-MBA@Ab) concentration. Inset: SERS intensity at 1590 cm^{-1} as a function of AuAgNS@4-MBA concentration. **C:** SERS intensity as a function of antibody concentration incubated with the AuAg NSs during the conjugation reaction. Inset: SERS intensity at 1590 cm^{-1}. Image: immunoassay test line visual signal. **D:** Dependence of SERS intensity on the concentration of capture antibodies immobilized on the test line. Inset: SERS intensity at 1590 cm^{-1}. Image: immunoassay test line visual signal. **E:** Effect of blocking the strips, showing the comparison between positive (*dark blue*) and negative (*light blue*) tests and their ratio (*red*, scaled for better graphic visualization) by blocking of the strips by BSA or by using PVP in the running buffer (dynamic blocking). Inset: image of test strips.

For higher antibody concentrations, where an excess of anti-IgG was used in conjugation process, the measured SERS signals decreased. This could be due to the formation of multilayers of loosely bound antibodies, which could detach during LFA flow and compete with the conjugates for antigen binding. From this, we were able to determine the optimal Ab:NP incubation ratio, which was 200:1, calculated from the typical IgG footprint[34] and assuming a maximized packing on the NP surface. Then, the effect of the concentration of the immobilized antibody on the strip was investigated. Images of the strips (**Figure 3d**) show that the spot at the test area increased in colorimetric intensity with increasing immobilized Ab as it was varied from 0 mg/ml to 8 mg/ml. In addition, the SERS intensity (blue, **Figure 3d**) increased with increasing antibody concentration. This could be attributed to a higher amount of nanotag-antigen complex captured on the test line, and therefore result in more intense SERS signals.

Paper-based immunoassays often suffer from non-specific adsorption, which can detract from their specificity and result in false positives.[35] One strategy to minimize non-specific adsorption is to use blocking agents. Two different strategies were investigated: 1) using 1% bovine serum albumin (BSA) to block the nitrocellulose and 2) adding 0.02% PVP to the running buffer, or dynamic blocking (**Figure 3e**). To quantify the effect of the blocking agents, we compared the intensity for a positive test (+IgG, dark blue) and negative (-IgG, light blue) tests and their ratio (red, scaled for better graphic visualization). While either strategy alone was not able to completely remove the non-specific signal, the combination of both strategies was the most effective, yielding the higher positive-to-negative intensity ratio.

We also compared the signal of the AuAg NS to AgNPs and Au nanostars[36] in SERS as these are commonly used in SERS LFAs. In comparison to the Au nanostars and Ag NPs, the enhancement factor of the 4-MBA by the AuAg NPs was 1.6×10^5, whereas it was lower for the Au nanostars (1.0×10^4), but higher for the AgNPs (1.76×10^6) as Ag is known to be a superior Raman enhancer (**Supporting Info: Figure S3**). In an immunoassay, this resulted in a higher SERS intensity at the test line for the Ag NPs (**Supporting Info. Figure S4**) which actually increased after 75 days due to oxidation. However, despite the higher intensity, it also resulted in a higher variability in the signal at the test line.

Human IgG Detection: Visual vs SERS

Once we determined optimal parameters for the NP-Ab, we ran a dose response curve to quantify the sensitivity of the assay with the IgG antigen. Strips were run with increasing IgG concentration ranging from 2.5 ng/ml to 2.5 μg/ml and the visual intensity of the test line also increased (**Figure 4C**). Increasing the amount of nanotag (0.5, 1 and 2 μl) incubated with the antigen-containing sample resulted in a higher SERS signal measured at the test line (**Figure 4A**). The highest amount, 2 μl, was therefore chosen as the optimal amount of conjugate for the assay for obtaining an analytical dynamic range covering the reported MxA levels (background colors corresponding to healthy (*green*), bacterial (*yellow*) and viral (*red*) infection respectively).

Then, a dose response curve for IgG using 2 μl of nanotag was measured for both the visual test (inset, blue data points) and SERs (red data points, **Figure 4b**) of IgG at concentrations ranging from 2.5 ng/ml to 2.5 μg/ml. Both the SERS and visual intensities of the test line increased with increasing IgG, as expected, and then reached a plateau at higher concentrations.

A fit to the concentration dependence for the SERS intensity (red dotted line, left axis, **Figure 4b**) resulted in an affinity constant of K_d = 100.9 nM[37,38] and an IgG LOD of 72.2 ng/ml. For the colorimetric readout (blue dotted line, right axis, **Figure 4b**), the K_d = 98.3 nM and LOD was 9.9 ng/ml. K_d values provided by both detection methods are in good agreement with each other and in range with the usual ones for high binding affinity antibodies ($\leq 10^{-7}$ M). The LOD of the nanotag by SERS was confirmed to be in the range of the clinically relevant values for adult infections (yellow).

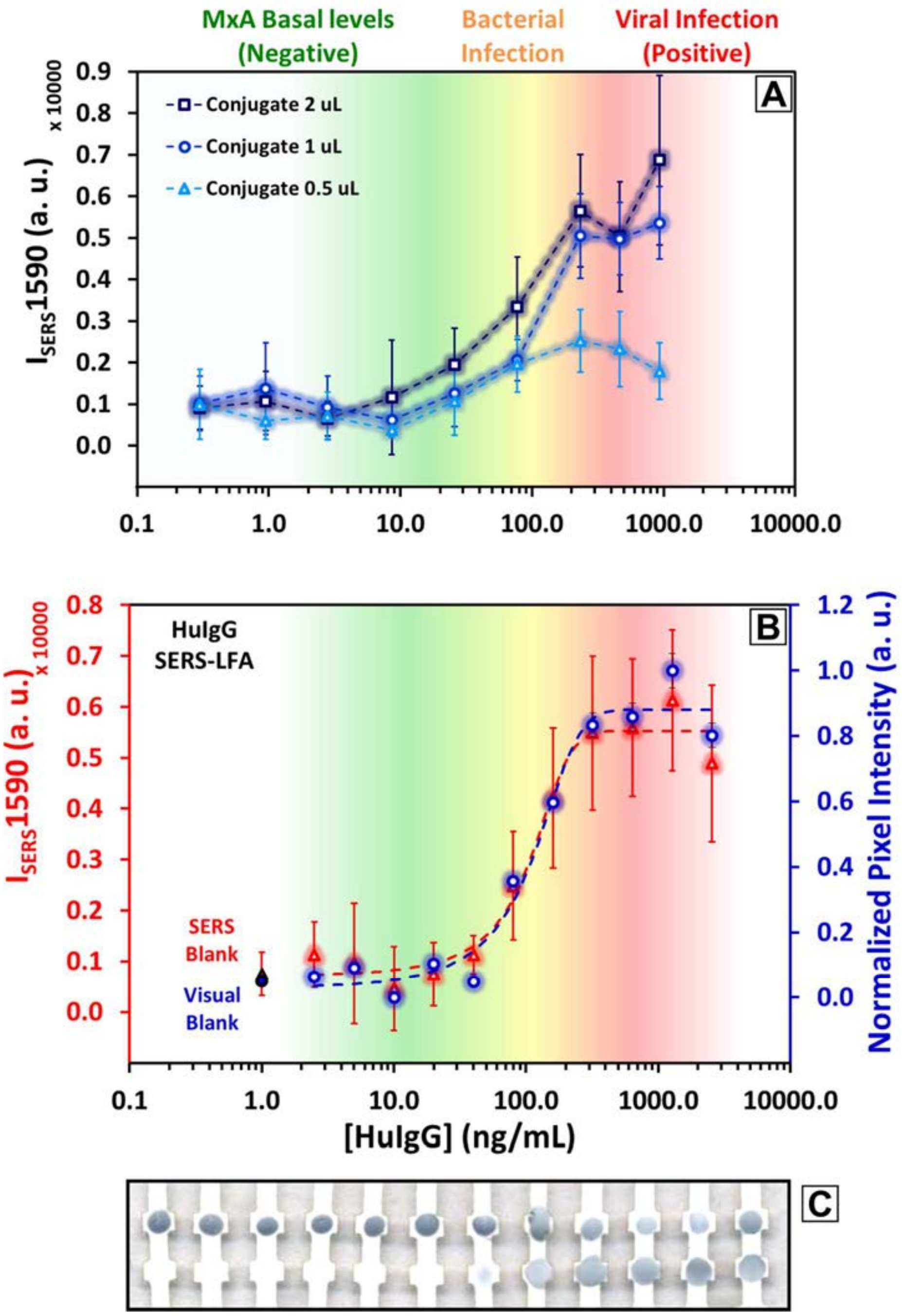

Figure 4 - SERS vs. visual detection of IgG. **A:** Dose response curve measured by SERS of immunoassays run with three different concentrations of nanotags over an IgG concentration range covering the reported MxA levels (background colors corresponding to healthy (*green*), bacterial (*yellow*) and viral (*red*) infection respectively). **B:** Comparison between SERS (*red*) and visual (*blue*) detection of HuIgG with LFA (HuIgG concentrations ranging from 2.5 ng/ml to 2.5 µg/ml; "Dose-Response" fitting curves for SERS (*red*, $R^2 = 0.96$, $K_d = 100.9$ nM; calculated LOD = 72.2 ng/ml) and visual (*blue*, $R^2 = 0.94$, $K_d = 98.3$ nM; calculated LOD = 9.9 ng/ml). **C:** Bright field image of dipstick nitrocellulose strips of the HuIgG immunoassay.

MxA Detection: Visual vs SERS

Finally, the nanotag-anti-MxA conjugates were synthesized using the optimized parameters from the nanotag-anti IgG experiments as a guide. The antibody was polyclonal anti-MxA (rabbit). We adsorbed the anti-MxA onto the AuAg NSs conjugated to 4-MBA (**Figure 5**) using an anti-MxA:NP incubation ratio of 200:1 determined from the synthesis of the anti-IgG nanotags. We characterized the anti-MxA AuAg NPs by optical absorption. The AuAg NPs showed a SPR peak shift to the red by ~15 nm upon conjugation.

Immunoassay strips were then run with the anti-MxA nanotags against MxA at concentrations ranging from 2.5 ng/ml to 2.5 μg/ml in a 2 % BSA solution and PVP as a dynamic blocking buffer. The anti-MxA antibody was immobilized onto the test area by spotting, similar to the anti-IgG strips. Visual readout of the strips showed that the color at the test area increased with increasing MxA concentration (**Figure 5b**), indicating successful binding of the MxA to the immobilized anti-MxA and the anti-MxA on the AuAg NSs. No color appeared at the test line for when no MxA was present, indicating that there was no non-specific adsorption to the test area.

Then, SERS measurements of the test areas showed an increase in SERS intensity with increasing MxA, until reaching a plateau at higher concentrations. A fit of the MxA dose response curves as measured by SERS was K_d = 64.2 nM and a LOD of 123.5 ng/ml. A fit of the visual dose response curve resulted in a K_d = 77.9 nM and an MxA LOD of 30.9 ng/ml. Even though the visual readout had a lower LOD, it was less amenable for quantifying MxA levels in the relevant range for diagnosis (yellow area), where the visual readout had a sharper intensity threshold. This shows that SERS has the potential to better quantify MxA in concentration ranges relevant for distinguishing viral vs. bacterial infections. Again, obtained K_d values for both visual and SERS detection were in good agreement with each other, and in the range typical of high binding affinity antibodies ($\leq 10^{-7}$ M).

Fits of the dose response curves to a Hill plot (**Supporting Information, Figure S6**) resulted in a Hill coefficients of $n > 1$, indicating cooperative binding. This could be due to the fact that the nanotag is multivalent from having multiple antibodies on its surface. This could in turn favor binding to multiple immobilized antibodies on the test area.

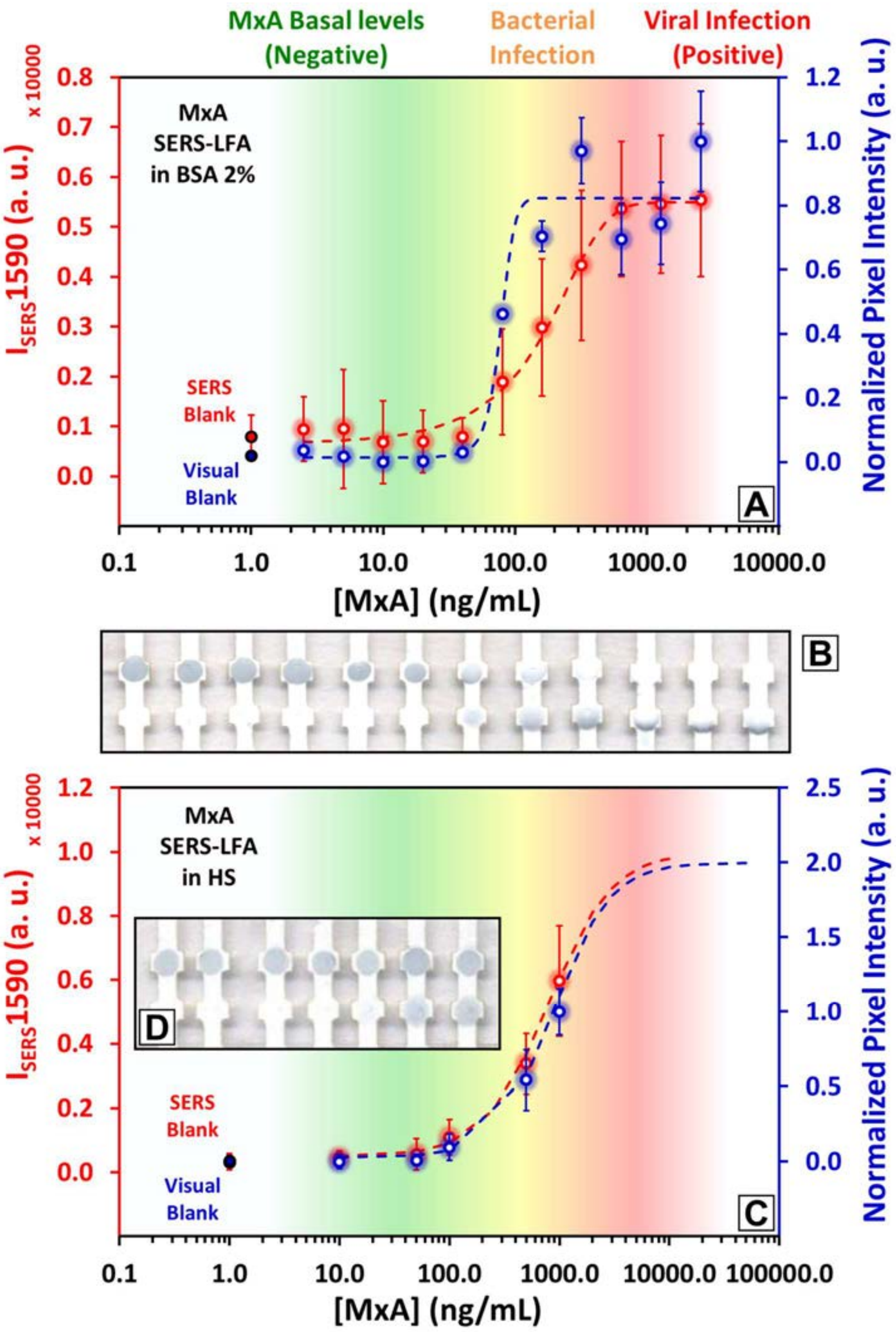

Figure 5 - MxA detection in the immunoassay by SERS and visual readouts and effect of sample matrix. **A:** Comparison between SERS (*red*) and visual (*blue*) detection of MxA in BSA 2%, where [MxA] = 2.5 ng/ml to 2.5 µg/ml. Fits to the dose-response curves for SERS (*red*, $R^2 = 0.99$, $K_d = 64.2$ nM; calculated LOD = 123.5 ng/ml) and visual (*blue,* $R^2 = 0.94$, $K_d = 77.9$ nM; LOD = 30.9 ng/ml). **B:** Bright field image of MxA immunoassay run on dipstick nitrocellulose strips. **C:** Comparison between SERS (*red*) and visual (*blue*) detection of MxA in HS, where [MxA] = 10 ng/ml to 1 µg/ml. Fits to the dose-response curves for SERS (*red*, calculated LOD = 51.8 ng/ml) and visual (*blue,* LOD = 135.8 ng/ml). **D:** Bright field image of MxA immunoassay in HS run onto dipstick nitrocellulose strips.

We finally tested the functionality of the MxA immunoassay in human serum (HS) because MxA is picked up in HS at values of 75-100 ng/ml. MxA nanotags were run in solutions of HS spiked with MxA at 0, 10, 50, 100, and 500 ng/ml. As with the titration curve in buffer, both the visual (**Figure 5b**, *blue*) and SERS intensity (**Figure 5b**, *red*) started low and increased in intensity with increasing MxA concentration. Fits of the titration curve yielded an LOD in HS of 51.8 ng/ml. This increase in LOD could be due to the effects of HS on immunoassay performance, where the proteins in the HS form a protein corona around the nanotag and/or passivation of the strip surface [37].

Conclusions

In summary, we demonstrate that SERS can be used to detect the MxA antigen in a paper based dipstick immunoassay. We find that SERS can increase assay sensitivity, and thus enable quantification of clinically relevant MxA levels in a simple paper immunoassay format. We demonstrate successful use of hollow AuAg NSs in a nanotag reporter format for SERS. These results could aid in differential diagnosis of viral vs. bacterial infections. Furthermore, quantitative measurement of MxA could potentially obviate the need for adding a CRP assay in a multiplexed test.

References

1. Haller, O., Frese, M. & Kochs, G. Mx proteins: Mediators of inmate resistance to RNA viruses. *OIE Rev. Sci. Tech.* **17,** 220–230 (1998).
2. Engelmann, I. *et al.* Diagnosis of Viral Infections Using Myxovirus Resistance Protein A (MxA). *Pediatrics* **135,** e985–e993 (2015).
3. Kawamura, M. *et al.* New Sandwich-Type Enzyme-Linked Immunosorbent Assay for Human MxA Protein in a Whole Blood Using Monoclonal Antibodies Against GTP-Binding Domain for Recognition of Viral Infection. *J. Clin. Lab. Anal.* **26,** 174–183 (2012).
4. Juntunen, E. *et al.* Lateral Flow Immunoassay With Upconverting Nanoparticle-Based Detection for Indirect Measurement of Interferon Response by the Level of MxA. *J. Med. Virol.* **89,** 598–605 (2017).
5. Kimberlin, D. W. & Poole, C. L. Assessing the Febrile Child for Serious Infection: A Step Closer to Meaningful Rapid Results. *Pediatrics* **140,** e20171210 (2017).
6. Ivaska, L. *et al.* Aetiology of febrile pharyngitis in children: Potential of myxovirus resistance protein A (MxA) as a biomarker of viral infection. *J. Infect.* **74,** 385–392 (2017).
7. Davidson, M. FebriDx Point-of-Care Testing to Guide Antibiotic Therapy for Acute Respiratory Tract Infection in UK Primary Care: A Retrospective Outcome Analysis. *J Infect Dis Preve Med* **5,** 1000165 (2017).
8. Self, W. *et al.* Diagnostic Accuracy of FebriDx: A Rapid Test to Detect Immune Responses to Viral and Bacterial Upper Respiratory Infections. *J. Clin. Med.* **6,** 94 (2017).
9. Kapasi, A. J., Dittrich, S., González, I. J. & Rodwell, T. C. Host biomarkers for distinguishing bacterial from non-bacterial causes of acute febrile illness: A comprehensive review. *PLoS One* **11,** 1–29 (2016).
10. Qin, Z. *et al.* Significantly improved analytical sensitivity of lateral flow immunoassays by using thermal contrast. *Angew. Chemie - Int. Ed.* **51,** 4358–4361 (2012).
11. Fabris, L. Gold-based SERS tags for biomedical imaging. *J. Opt.* **17,** 114002 (2015).
12. He, S., Chua, J., Tan, E. K. M. & Kah, J. C. Y. Optimizing the SERS enhancement of a facile gold nanostar immobilized paper-based SERS substrate. *RSC Adv.* **7,** 16264–16272 (2017).

13. Kearns, H., Shand, N. C., Smith, W. E., Faulds, K. & Graham, D. 1064 nm SERS of NIR active hollow gold nanotags. *Phys. Chem. Chem. Phys.* **17,** 1980–1986 (2015).

14. Xie, J., Zhang, Q., Lee, J. Y. & Wang, D. I. C. The Synthesis of SERS-Active Gold Nanoflower Tags for In Vivo Applications. **2,** 2473–2480 (2008).

15. Cao, Y. W. C., Jin, R. & Mirkin, C. A. Nanoparticles with Raman spectroscopic fingerprints for DNA and RNA detection. *Science* **297,** 1536–1540 (2002).

16. Karabel Ocal, S. *et al.* Plasmonic assemblies of gold nanorods on nanoscale patterns of poly(ethylene glycol): Application in surface-enhanced Raman spectroscopy. *J. Colloid Interface Sci.* **532,** 449–455 (2018).

17. Zavaleta, C. L. *et al.* Multiplexed imaging of surface enhanced Raman scattering nanotags in living mice using noninvasive Raman spectroscopy. *Proc. Natl. Acad. Sci.* **106,** 13511–13516 (2009).

18. Wang, Y., Yan, B. & Chen, L. SERS Tags: Novel optical nanoprobes for bioanalysis. *Chem. Rev.* **113,** 1391–1428 (2013).

19. Guerrini, L., Pazos-Perez, N., Garcia-Rico, E. & Alvarez-Puebla, R. Cancer characterization and diagnosis with SERS-encoded particles. *Cancer Nanotechnol.* **8,** (2017).

20. Vo-Dinh, T. *et al.* SERS Nanosensors and Nanoreporters: Golden Opportunities in Biomedical Applications. *Wiley Interdiscip. Rev. Nanomedicine Nanobiotechnology* **7,** 17–33 (2015).

21. Bodelõn, G. *et al.* Au@pNIPAM SERRS Tags for Multiplex Immunophenotyping Cellular Receptors and Imaging Tumor Cells. *Small* **11,** 4149–4157 (2015).

22. Porter, M. D., Lipert, R. J., Siperko, L. M., Wang, G. & Narayanan, R. SERS as a bioassay platform: Fundamentals, design, and applications. *Chem. Soc. Rev.* **37,** 1001–1011 (2008).

23. Hwang, J., Lee, S. & Choo, J. Application of a SERS-based lateral flow immunoassay strip for the rapid and sensitive detection of staphylococcal enterotoxin B. *Nanoscale* **8,** 11418–11425 (2016).

24. Sánchez-Purrà, M. *et al.* Surface-Enhanced Raman Spectroscopy-Based Sandwich Immunoassays for Multiplexed Detection of Zika and Dengue Viral Biomarkers. *ACS Infect. Dis.* **3,** 767–776 (2017).

25. Jimenez De Aberasturi, D. *et al.* Surface Enhanced Raman Scattering Encoded Gold Nanostars for Multiplexed Cell Discrimination. *Chem. Mater.* **28,** 6779–6790 (2016).

26. Mir-Simon, B., Reche-Perez, I., Guerrini, L., Pazos-Perez, N. & Alvarez-Puebla, R. A. Universal one-pot and scalable synthesis of SERS encoded nanoparticles. *Chem. Mater.* **27,** 950–958 (2015).

27. Kang, H. *et al.* Near-infrared SERS nanoprobes with plasmonic Au/Ag hollow-shell assemblies for in vivo multiplex detection. *Adv. Funct. Mater.* **23,** 3719–3727 (2013).

28. Lee, S., Kim, G. & Moon, J. Performance improvement of the one-dot lateral flow immunoassay for aflatoxin b1 by using a smartphone-based reading system. *Sensors (Switzerland)* **13,** 5109–5116 (2013).

29. Russo, L. *et al.* Time- and Size-Resolved Plasmonic Evolution with nm Resolution of Galvanic Replacement Reaction in AuAg Nanoshells Synthesis. *Chem. Mater.* **30,** 5098–5107 (2018).

30. Liu, Y. *et al.* Au@Ag core-shell nanocubes: Epitaxial growth synthesis and surface-enhanced Raman scattering performance. *Phys. Chem. Chem. Phys.* **17,** 6819–6826 (2015).

31. Chang, H. *et al.* Ag shell-Au satellite hetero-nanostructure for ultra-sensitive, reproducible, and homogeneous NIR SERS activity. *ACS Appl. Mater. Interfaces* **6,** 11859–11863 (2014).

32. Osinkina, L., Lohmüller, T., Jäckel, F. & Feldmann, J. Synthesis of gold nanostar arrays as reliable, large-scale, homogeneous substrates for surface-enhanced Raman scattering imaging and spectroscopy. *J. Phys. Chem. C* **117,** 22198–22202 (2013).

33. Atta, S., Tsoulos, T. V. & Fabris, L. Shaping Gold Nanostar Electric Fields for Surface-Enhanced Raman Spectroscopy Enhancement via Silica Coating and Selective Etching. *J. Phys. Chem. C* **120,** 20749–20758 (2016).

34. Tan, Y. H. *et al.* A Nanoengineering Approach for Immobilization. *ACS Nano* **2,** (2008).

35. de Puig, H., Bosch, I., Gehrke, L. & Hamad-Schifferli, K. Challenges of the Nano–Bio Interface in Lateral Flow and Dipstick Immunoassays. *Trends Biotechnol.* **35,** 1169–1180 (2017).

36. De Puig, H., Tam, J. O., Yen, C. W., Gehrke, L. & Hamad-Schifferli, K. Extinction Coefficient of Gold Nanostars. *J. Phys. Chem. C* **119,** 17408–17415 (2015).

37. de Puig, H., Bosch, I., Carré-Camps, M. & Hamad-Schifferli, K. Effect of the Protein Corona on Antibody–Antigen Binding in Nanoparticle Sandwich Immunoassays. *Bioconjug. Chem.* **28,** 230–238 (2017).

38. Huaman, M. A. *et al.* A Comparison of Nanoparticle-Antibody Conjugation Strategy in Sandwich Immunoassay. *J. Immunoass. Immunochem.* **38,** 355–377 (2017).

A low-cost strategy for the development of a rapid electrochemical assay for bacteria detection based on AuAg nanoshells

Bacterial resistance to antimicrobials is considered widely the most urgent health issue the world is facing in the coming years.[1] Nowadays the choice to prescribe antibiotics is rarely based on definitive diagnoses, which generally require laboratory-based analytical test (i.e. polymerase chain reaction (PCR), traditional plate counting), often consisting of days-long procedure characterized by high costs and the need for highly trained and skilled personnel. Effective, rapid, low-cost diagnostic tools are needed for guiding optimal use of antibiotics in human and animal medicine and, also in the form of Point-of-Care (PoC) devices. Such tools should be easily integrated into clinical, pharmacy and veterinary practices as high-throughput screening methods for the early discrimination between bacterial and viral infections.[2] In this context, nanotechnology has proven to be extremely successful in providing innovative and advantageous solutions to overcome the conventional *in vitro* diagnostic intrinsic limitations through the rational design of advanced nanomaterials with suitable properties and functionalities.[3,4,5,6] Among them, nanomaterials with unique electrochemical and electrocatalytic properties have been introduced as signal amplification carriers or direct signal generating elements in order to increase sensitivities and enhance analytic performances.[7,8,9]

Properties Design for PoC Sensing

The cost of diagnostics technologies is on the other hand one of the fundamental global health aspects to be considered for accessing the market with competitive and sustainable products.[10] Indeed recognition elements found on the few POC electrochemical biosensors available consist fundamentally of biomolecules (i.e. enzymes, nucleic acids, antibodies), which represent one of the largest fraction of the total production cost.[11] Besides their unmatched specificity and selectivity, several drawbacks, such as high production cost and high susceptibility to environmental conditions (i.e pH, temperature, metal cations, fouling agents, metabolites) can limit their applicability, especially when integrated into PoC devices.[12] Exploiting instead the catalytic properties of electroactive nanomaterials presents a number of advantages, such as a lower production cost and engineering, ease of mass production as well as a higher stability both in working conditions and long-term storage.[13,14,15]

The aim of this work is therefore to employ the unique electrocatalytic properties of AuAg nanoshells (NSs)[16] for the quantitative detection of two model bacteria, *Escherichia coli* (*E. coli*) and *Salmonella typhimurium* (*Salmonella*). The ability to tune precisely their morphology and metal composition grants AuAg NSs with increased resistance to chemical oxidation, while at the same time allows them to generate a strong electrochemical signal. These unique features, together with high colloidal stability and large surface area, make AuAg NSs extremely promising materials to be employed as electrochemical labels in biosensors applications. While AuAg NSs have been applied previously as nanostructured carriers for intracellular drug delivery and as SERS labels for optical detection,[17,18] to the best of our knowledge no similar reports of the use of this class of particles as electrochemical reporters have been published yet. Moreover, in our system the detection of bacterial cells is achieved without the use of any biological receptor, basing it instead on non-specific interactions between the AuAg NSs and the intrinsically highly differentiated bacterial cell surfaces. This approach, also experimented elsewhere[19,20], provides a promising *proof-of-concept* for the development of a low-cost, robust electrochemical assay reaching high sensitivities (down to 10^2 CFU/mL) in very short times (within 10 min) compared to available commercial *E.coli* PoC assays and recently reported nanoparticles-based electrochemical detection techniques.[21]

AuAg NSs as Electrochemical Reporters

AuAg Nanoshells consist of a hollow structure composed by a gold-silver alloy shell which encloses an inner cavity. Their synthesis, based on a modified Galvanic Replacement Reaction (GRR) reported previously by our group,[22] allows to precisely control both the morphology and the relative amount of the two noble metals. **Figure 1 – A** shows TEM micrographs of the product of the GRR displaying highly monodisperse hollow AuAg NSs of c.a 60 nm in diameter, with a thin outer shell of c.a 10 nm thickness. The hollow particles bear a PVP layer adsorbed on their surface during their synthesis, a hydrosoluble polymer which provides enhanced colloidal stability without compromising their electrochemical properties.

Conventionally, noble metal and semiconductor nanoparticles applied so far as electrochemical labels require strong oxidants or acids in order to generate their corresponding cationic species through corrosion, which can then be detected electrochemically through common voltammetric techniques.[23] Translating these technologies into electrochemical diagnostic platforms for commercial use becomes therefore extremely difficult due to the danger implied in handling these corrosive reagents. Although Ag NPs are instead prone to corrosion, they have found limited practical use due to a severe susceptibility to oxidation[24], resulting in limited durability and reproducibility in many bio-related applications. Thus, AuAg NSs were chosen as electrochemical signalling tool thanks to their ability to generate an electrochemical signal in presence of mildly oxidizing agents, as demonstrated recently by our group.[16] The exposure of AuAg NSs to relatively high concentrations of nucleophilic halides and dissolved oxygen, typically found in most biological matrixes, is sufficient for activating their electrochemical properties: thanks to the residual Ag atoms contained in AuAg NSs cores, whose amount can be precisely controlled during synthesis[22] (**Figure 1 – B**), Ag^+ cations are generated by corrosion without compromising the particles structural stability, and anodic stripping analysis can be carried out for their detection.[16] **Figure 1 – C** shows DPVs of AuAg NSs in PBS (*red curve*), showing a relatively strong and defined anodic peak at +0.16 V vs Ag/AgCl, completely absent instead when the same measurement is performed in PB (*black dashed curve*), that is without chlorides in solution. A secondary oxidation peak is also observed at more positive potentials (+0.28 V vs ag/AgCl), corresponding to the oxidation of alloyed Ag found in the outer shell of the particles.[16] These findings not only confirm the electrochemical mechanism of current generation described above, but also make AuAg NSs a promising substitute of natural redox enzymes as electrochemical labels for sensing applications.

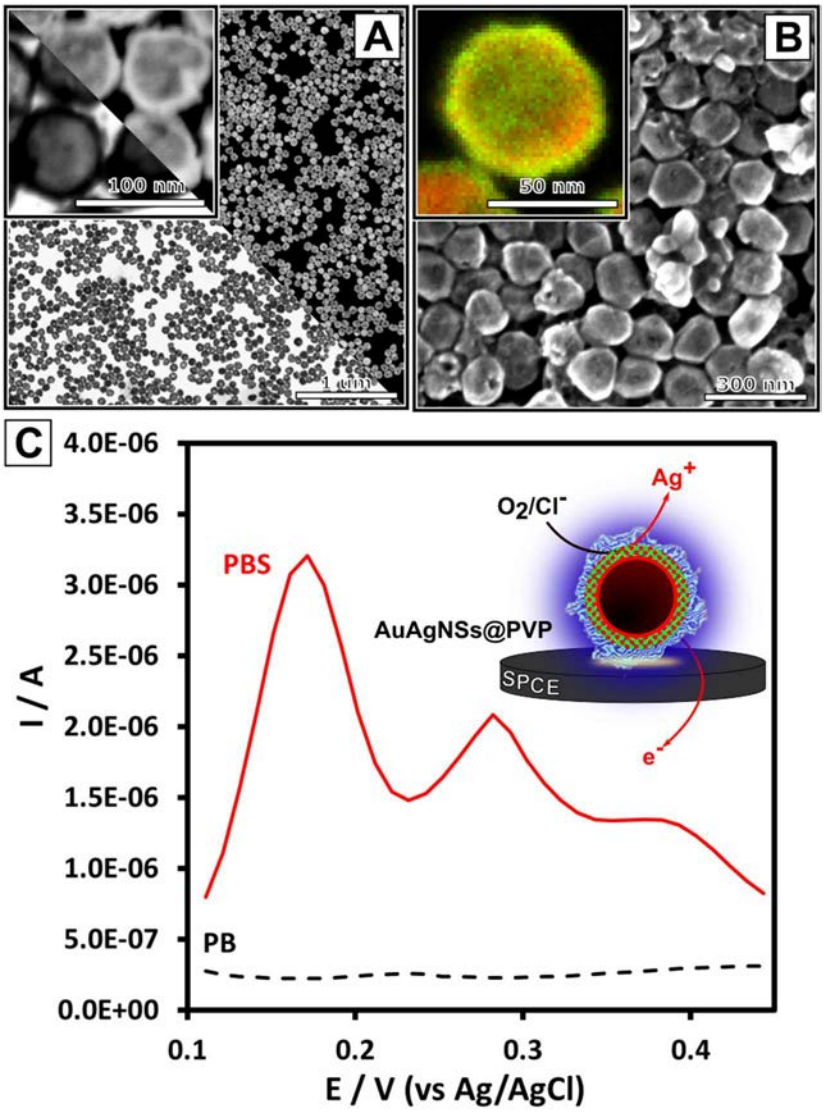

Figure 1 – A: TEM and HAADF-STEM micrographs of highly monodisperse 60.0 ± 4.4 nm AuAg NSs composed by a thin (≈10 nm) shell with a smooth surface and a large (≈40 nm) internal void. **B**: SEM AuAg NSs surface characterization and HAADF-STEM elemental distribution micrographs of a single AuAg NS (inset; Au: green, Ag: red). At the final stage of GRR Ag is found both in the Au-rich alloy outer thin shell as well as in the inner particle surface in its metallic form. **C:** Comparison of DPVs of AuAg NSs in different buffers. The potential scan run in PBS (*red curve*) causes the anodic stripping signal of Ag to appear at +0.16 V vs Ag/AgCl. When instead AuAg NSs are measured in PB 10 mM pH 7.5 (*black dashed curve*) no relevant anodic current is observed. In absence of chlorides in the matrix no Ag corrosion is possible and therefore no stripping detection can be carried out.

Electrochemical Assay Optimization

We investigated systematically the different experimental parameters involved in the DPV measurement for optimizing the sensitivity of the system. Firstly, Ag corrosion was monitored during time in order to maximize the amount of Ag^+ cations generated and therefore the corresponding anodic stripping current produced for a fixed amount of AuAg NSs (**Figure 2 – A**).

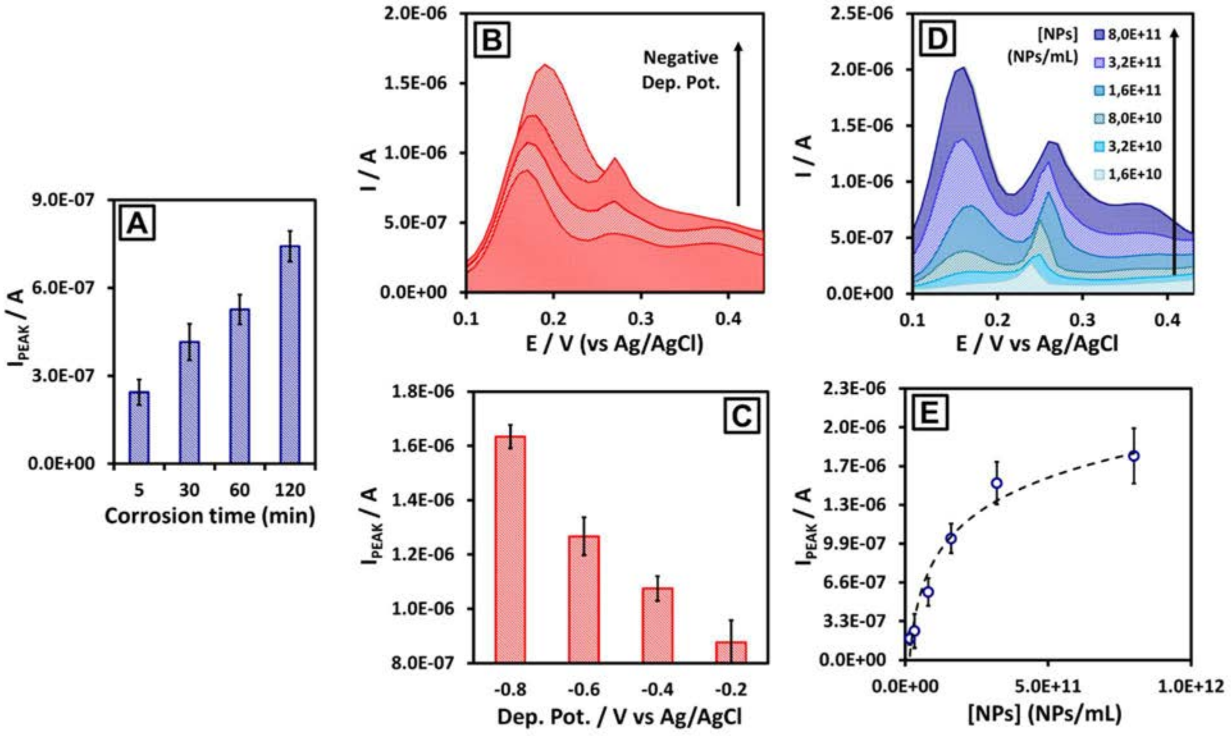

Figure 2 – A: The time of residence of AuAg NSs in the oxidant matrix affects the anodic stripping current of Ag. 5 min after mixing the hollow nanocrystal solution with PBS 10 mM pH 7.5 a relatively intense DPV current is obtained. Higher corrosion times allow to further enhance the current signal up to a 4-fold increase for 120 min. **B, C:** Effect of DPVs initial deposition potential on the anodic stripping wave of Ag on SPCEs. **D, E:** The dependency of the anodic stripping current on AuAg NSs concentration is analyzed by running DPVs of solution of increasing particles concentrations. The analytic peak (+0.16 V vs Ag/AgCl) intensity correlates positively with the increasing particles concentration (ranging from 1.6 x 10^{10} to 8.0 x 10^{11} NPs/mL), showing a logarithmic trend due to diffusion towards the electrode surface.

As expected, a higher residence time of the particles in the saline buffer prior to measurement causes a greater degree of Ag corrosion and therefore produces a stronger anodic current. Although the strongest signal was obtained for longer times (2h), a 5 min-long corrosion in the sample matrix was considered enough for generating the necessary signal intensity for the development of a rapid assay able to compete with traditional ones. This parameter could in theory be further optimized by increasing the total surface area available for chlorides corrosion, for instance by tuning the particles synthesis so to obtain a porous alloys shell.[22] It is worth mentioning that, despite the high salinity of the medium, no AuAg NSs aggregation is observed thanks to the steric stabilization provided by the PVP coating (study of AuAg NSs colloidal stability can be found in **Figure S1**).

Secondly, the effect of the deposition potential, that is the negative potential applied at the beginning of the measurement needed for reducing Ag^+ onto the electrode surface,[25] was also analyzed. DPVs of AuAg NSs solutions at a fixed concentration were therefore run applying different deposition potentials prior to measurement, namely -0.2, -0.4, -0.6 and -0.8 V vs Ag/AgCl.

As shown in **Figure 2 – B**, varying the applied reduction potential doesn't seem to affect relevantly the oxidation peak's shape, apart from a slight shift in the peak position. On the contrary, a clear positive correlation between the applied deposition potential and the anodic current recorded at 0.16 V vs Ag/AgCl is observed (**Figure 2 – C**), resulting in increased current intensities up to a 2-fold enhancement for -0.8 V vs Ag/AgCl. Remarkably, the possibility to reduce Ag^+ applying more positive deposition potentials than silver's formal reduction one (Ag^+ reduction potentials = 0.7996 V)[26] depends on the ability of AuAg NSs to catalyze the underpotential deposition of Ag^+ on their surfaces, as recently discovered by our group.[16] This electrocatalytic effect is directly dependent on the particles composition and morphology and can be tuned by modifying their synthesis.[22] Even though the highest signal obtained through this mechanism was found when using a deposition potential of -0.8 V vs Ag/AgCl, using less negative ones led to an improvement in the overall reproducibility of the measurement. In these conditions in fact Ag/AgCl pseudo-references electrodes, known to display stability issues in electrolytes containing high chlorides concentrations,[27] showed a higher reproducibility. **Figure S2** shows the behavior of the pseudo-reference Ag/AgCl electrode vs the initial deposition potentials used. Besides the expected reference oxidation peak (≈0.0 V vs Ag/AgCl), the appearance of a satellite one when applying more negative deposition potentials (-0.4, -0.6, -0.8 and -1.0 V vs Ag/AgCl) was considered a probable cause of the reproducibility problems encountered. Using milder reduction potentials during the DPV measurement (-0.2 V vs Ag/AgCl) allows instead to completely avoid this effect. Moreover, the possibility to use AuAg NSs as electrochemical labels without the need to apply highly negative reduction potentials during the deposition step represents a further advantage, since it eliminates the risk of interference from redox-active species easily found in biological matrixes.

Finally, the correlation between AuAg NSs concentration and the measured electrochemical signal was studied by recording the anodic stripping peak intensity at +0.16 V while varying particles concentration up to a 5-fold increase. As shown in **Figure 2 – D, E**, the electrochemical signal follows an increasing trend for the lower range of concentrations after which reaches a saturation plateau. This behaviour is reasonably compatible with the electrochemical mechanism described above, keeping into account that since no NSs immobilization over the electrode surface is carried out prior to measurement, the diffusion rate of NSs towards the electrode surface will set an upper limit for the electron transfer and only the fraction of particles found in close proximity of the electrode surface will provide a detectable signal.[28] This setup allows detecting AuAg NSs down to a L.O.D. of 5.6 x 10^{10} NPs/mL, but further improvement of sensitivity could be achieved by implementing longer deposition or corrosion steps.

Bacteria Detection

Conventional methods for specific quantification and differentiation of microbial cells use either selective culturing media, which can take up to several days to distinguish a positive from a negative sample, or molecular biology techniques, which instead target mainly intracellular biomarkers (i.e. proteins, nucleic acids) and therefore require complex and time-consuming procedures for extraction, amplification and revelation (i.e. immunolabeling, PCR).[29] A less explored strategy for cell sensing focuses instead on the extracellular complex array of macro/biomolecules expressed on bacterial cell walls (i.e. phospholipids, lipopolysaccharides). Such sensing strategy takes advantage of the chemical fingerprint of these complex moieties to generate a non-specific but selective response relying on the differential binding affinities between different nanoprobes and bacterial cells, thus without the need of costly biological receptors (i.e. antibodies, peptides and nucleic acids).[20,30,31] This approach has been shown already to be a viable and promising one for their rapid detection and identification with minimal processing.[19,32]

The general protocol herein adopted for bacteria detection consists in mixing a solution of a model bacterial strain of *E.coli* at a given concentration (ranging from 10^1 to 10^8 CFU/mL) with PVP-coated AuAg NSs at a final concentration of 1.6 x 10^{11} NPs/mL, incubating the mixture for 5 min in PBS 10 mM pH7.4 and then rapidly depositing it onto SPCEs to run a DPV, as described in Methods. The variation in anodic stripping current at +0.16 V, generated by the controlled corrosion of AuAg NPs in PBS, was then correlated with the concentration of *E.coli* cells (**Figure 3 – A**), revealing an initial increase in intensity up to a concentration of 10^4 CFU/mL, followed by a steep decrease in the peak current for higher ones. For *E.coli* concentrations higher than 10^6 CFU/mL the voltammetric signal displays values lower than the blank ones. This peculiar current profile, encountered also in a previous work,[33] can be explained considering the bacteria's ability to "capture" the electroactive NPs in solution through the non-specific affinity interactions between PVP-coated AuAg NSs and the microorganisms' cell walls. As confirmed by the ζ-potential measured at 3 different pHs (**Figure S3**), AuAg NSs colloidal stabilization is *electrosteric*, that is caused both by the electrostatic repulsion due to the negative surface charge (-24.5 ± 0.31 mV at pH = 7.5) and by the steric interaction provided by the PVP adsorbed layer. Interestingly, this same layer appears to be also responsible for the non-specific interaction between AuAg NSs in solution and *E.coli* cell wall: as shown in STEM micrographs of *E.coli* cells incubated with PVP-coated AuAg NSs (**Figure 3 – B**), the hollow nanocrystals seem to stick and accumulate on the bacterial cell wall extremities, probably thanks to the weak but additive interactions between the coating polymer and the extracellular macromolecules (i.e. phospholipids, lipopolysaccharides and flagellar proteins). This kind of non-specific interactions has been showed to be favored by the relatively hydrophobic character of both the extracellular macromolecules expressed and PVP, which is somehow able to screen the electrostatic repulsion between the negatively charged objects.[34,35,36] This attachment is not permanent, given the reversible nature of the weak interactions involved, but it is sufficient to label the bacterial cells with electrochemical reporters: after incubation of bacteria suspension with AuAg NSs, all samples were purified through differential centrifugation[37] in order to separate the bacteria-particles complexes formed from the unattached ones (the presence in **Figure 3 - B** STEM images of free particles is likely caused by the later detachment during solvent evaporation upon sample preparation).

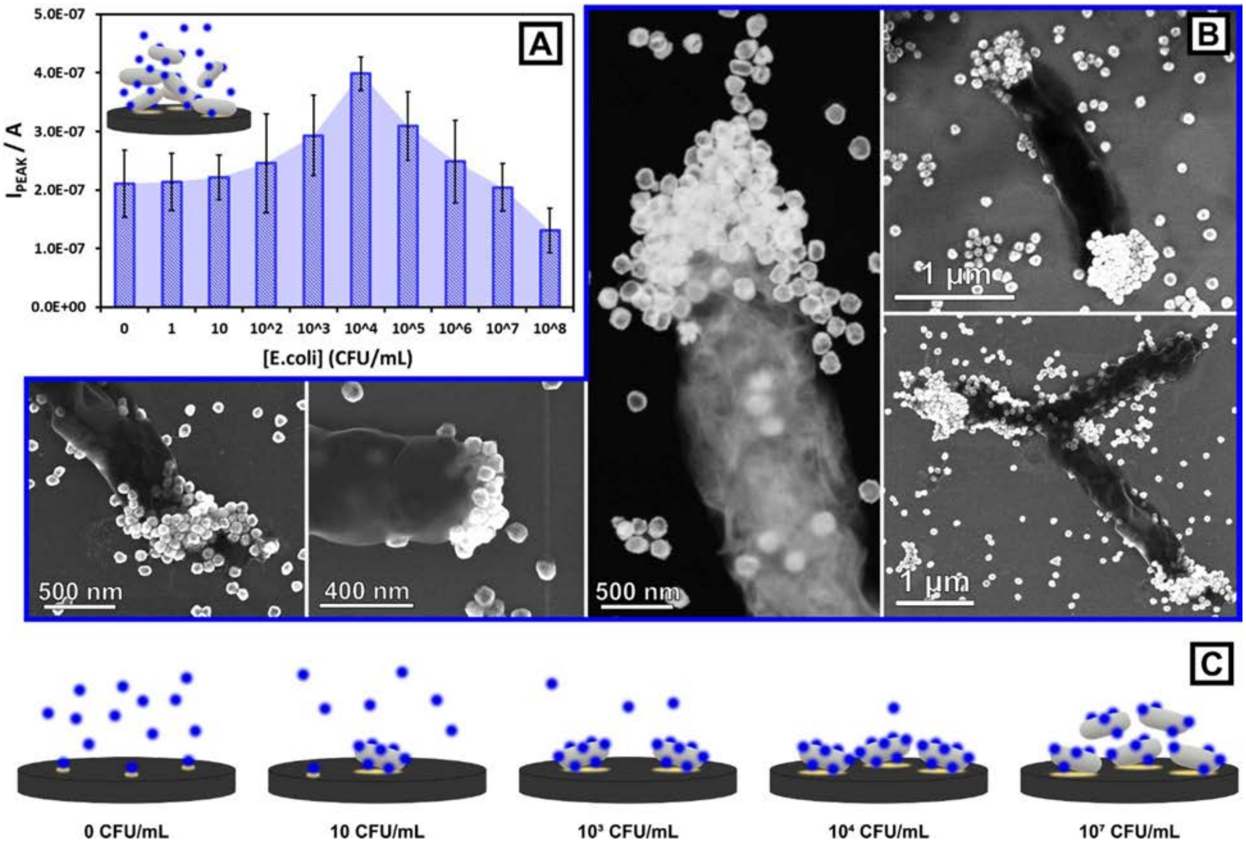

Figure 3 – A: *E.coli* detection through incubation with AuAg NSs and DPV measurement (bacteria cells concentration ranging from 10^1 to 10^8 CFU/mL). Error bars represent measurement standard deviation (n = 5), whose relatively high value are a result of the bacteria quantification (OD600) high error. **B:** STEM images (dark field and SEM) of *E.coli* cells decorated with AuAg NSs after incubation and differential centrifugation. **C:** Affinity-based detection mechanism, depicting AuAg NSs (blue) and *E.coli* cells (grey) coming into contact with the electrode surface.

During the electrochemical assay, once the suspension of AuAg NSs-decorated bacteria in PBS is deposited on the electrode, cells quickly start to sediment, bringing the captured particles in contact with the electrode surface. For bacterial concentration ranging from 10^1 to 10^4 CFU/mL, the number of active electrochemical reporters found at the electrode surface is increased compared to the blank sample (**Figure 3 – C**, **"0 CFU/mL"**) (in the absence of any cell, only the NPs in close proximity or contact with the electrode surface are able to provide an electrochemical signal). By increasing the concentration of cells, more particles can attach to the bacteria cell walls and thus reach the vicinity of the electrode surface, increasing the anodic stripping current of silver generated from the NSs (**Figure 3 – C**, **“10^1-10^4 CFU/mL”**). The electrochemical signal though reaches a maximum and then starts to decrease again for higher *E.coli* concentrations due to the depletion of free NPs in solution. In this second regime bacterial cells compete for capturing the limited amount of AuAg NSs, which are now distributed over a larger surface area, and hinder this way the electron transfers to the electrode surface (**Figure 3 – C, “10^7 CFU/mL”**). This particular electroanalytical response could be further improved for developing a more robust and reliable method for bacteria detection by performing a set of serial dilutions of the sample, where observing an increase rather than a decrease in current would correspond to a precise range of microbial concentrations, as demonstrated in **Figure S4**.

Selectivity Study

In order to test the selectivity of this detection strategy a second model bacterial strain, *Salmonella typhimurium*, was submitted to the same detection methodology. The current-vs-concentration profile obtained by incubating *Salmonella* cells with AuAg NSs (**Figure 4,** *red bars*) resulted substantially similar to the one observed with *E.coli* (**Figure 4,** *blue bars)*, although reaching the maximum current intensity for lower bacteria concentrations. This differentiation between the two electrochemical responses can be explained by taking into account that the two bacterial species possess analogous but dissimilar variety and type of surface functional macromolecules expressed on their cell walls.[20] Their distinct functionalities will determine the degree of interaction with the functional macromolecules present on the particles surface, depending for instance by the intrinsic availability of hydrogen bonds donors or their hydrophobic character. As a consequence, the average ratio between the number of electrochemical reporters per bacterial cell will vary between different species. When incubating *Salmonella* cells with AuAg NSs*,* the overall sum of weak, non-specific affinity interactions with the PVP-coated NPs corresponds to a distinct capture efficiency and NPs/bacteria ratio compared to the *E.coli* characteristic one, shifting in other words the bacteria concentration at which the capture effect reaches its maximum. This behaviour, already reported previously for PVP-coated AgNPs,[33,36,32] not only confirms the signal modulation mechanism proposed (**Figure 3 – A,C**), but also demonstrates the proof-of concept for the feasibility of a semi-specific assay able to discriminate between different pathogenic organisms without recurring to highly specific but also costly and fragile biological receptors. It is worth mentioning that this intrinsic affinity is obtained without the help (and notably the cost) of any kind of antibody or other bio-receptor, and that it could be in theory improved significantly by screening the non-specific affinity of different coating polymers towards a particular bacterial cell species.[30,38]

For further testing the capability of this assay to distinguish and quantify different bacterial strains in complex mixtures containing both *E.coli* and *Salmonella*, a set of experiments were run (**Figure S5**). The results obtained show clearly that the assay in its current proof-of-concept format is not able to distinguish univocally between different compositions of the two model bacterial strains without constructing the whole concentrations profile. Nevertheless, it seems that the influence of Salmonella on the current generation mechanism, that is the capture of AuAg NSs in solution through their non-specific adsorption onto bacterial cells, is stronger than the E.coli one. This behaviour gives additional clues about the different affinities of bacterial cell walls for AuAg NSs and could be used to further tune the hydrophobicity of the coating polymer towards a better selectivity of the assay.

In order to test the specificity in complex samples we performed the assay over a suspension of 10^4 CFU/mL E.coli in presence of 2 different kinds of interfering species. To check the specificity in presence of large bio-macromolecules, the assay was run firstly in a duplicate experiment in human serum (**Figure 4 – B, Human Serum**), given the potential applicability of this assay in biological samples, and in presence of humic acid (HA) (4 mg/L) (**Figure 4 – B, HA**), the major component of river waters' total organic carbon (TOC),[39] for application in environmental sensing. In the first case, the oxidation current peak at +0.16 V vs Ag/AgCl decreased in comparison to the control sample (**Figure 4 – B, AuAg NSs**), probably due to the formation of a protein corona around AuAg NSs,[40] which could either hinder the electron transfer to the electrode or directly lower the hollow nanocrystals' affinity for the macromolecules expressed onto the bacteria cell wall. Since the electrochemical quenching was not complete, this issue could be easily overcome by tuning the amount of AuAg NSs used in the assay to obtain a stronger current. In the case of humic acid instead, even though a slight decrease in the average intensity is observed, AuAg NSs seem to preserve their electrochemical properties, possibly because of the different chemical nature of humic substances, which makes them more stable in solution and less prone to adsorption.[39] A second set of experiment was run to test the resilience of the assay to the presence of heavy metals, a common contaminant in river waters. Copper and mercury (2 mg/L and 0.006 mg/L respectively)[41] salts were therefore chosen as interfering species because their oxidation potentials fall well within the potential window used in the assay. The electrochemical properties of AuAg NSs were this time completely quenched, both in presence of both metals and when either of them was used. Hg^{2+} showed to quench the redox behaviour completely, while Cu^{2+} resulted in a milder suppression. This effect can be easily explained taking into account the formation of amalgams between these cations and the noble metals, Au and Ag, constituting the hollow nanostructures, as well as other deposition effects.[42,43]

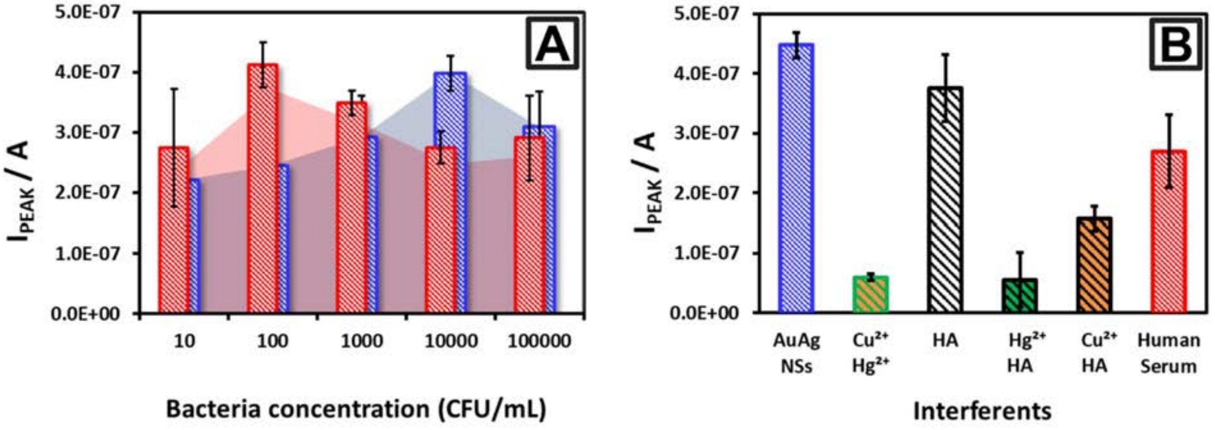

Figure 4 – A: Peak current profiles for different concentrations of *E.coli* (*blue*) and *Salmonella* (*red*): without the use of any specific receptor, affinity-based interactions between PVP-coated AuAg NSs and bacteria cell walls allow to selectively discriminate between the two species. **B:** Peak currents recorded for assays run on samples containing E.coli suspension of 10^4 CFU/mL in presence of different interfering species, namely humic acid (HA), mercury (Hg^{2+}) and copper (Cu^{2+}) ions and human serum.

Conclusions

In this work we propose a low-cost strategy for the simple and rapid detection of bacterial cells in biological matrixes based on the use of hollow AuAg NSs as novel electrochemical reporters. Through a rapid electrochemical test (<10 min), the model bacterial strain *E. coli* was quantified down to a concentration of 10^2 CFU/mL using low-cost, one-use SCPEs as the sensing platform. The protocol developed does not need any additional reagent, substrate or redox enzyme for generating the electrochemical signal, which is provided *in-situ* by the controlled corrosion of AuAg NSs caused by the matrix salinity. Moreover, discrimination between *E. coli* and *Salmonella* was achieved without the use of any biological receptor but through non-specific affinity interactions between the microorganism cell wall and AuAg NSs's surface, providing selectivity at a minimal operative and reagents cost. This work provides a promising proof-of-concept for the development of low-cost, rapid electrochemical assay for bacteria quantification able to compete with conventional costly and time-consuming laboratory analyses.

References

1. World Health Organization. Global action plan on antimicrobial resistance. *WHO Press* 1–28 (2015). doi:ISBN 978 92 4 150976 3
2. Drain, P. K. *et al.* Diagnostic point-of-care tests in resource-limited settings. *Lancet Infect. Dis.* **14,** 239–249 (2014).
3. Huang, X., Liu, Y., Yung, B., Xiong, Y. & Chen, X. Nanotechnology-Enhanced No-Wash Biosensors for In Vitro Diagnostics of Cancer. *ACS Nano* **11,** 5238–5292 (2017).
4. Lee, W. G., Kim, Y.-G., Chung, B. G., Demirci, U. & Khademhosseini, A. Nano/Microfluidics for diagnosis of infectious diseases in developing countries. *Adv. Drug Deliv. Rev.* **62,** 449–457 (2010).
5. Polavarapu, L. & Liz-Marzán, L. M. Towards low-cost flexible substrates for nanoplasmonic sensing. *Phys. Chem. Chem. Phys.* **15,** 5288–300 (2013).
6. Bülbül, G., Hayat, A. & Andreescu, S. Portable nanoparticle-based sensors for food safety assessment. *Sensors (Switzerland)* **15,** 30736–30758 (2015).

7. Qiu, H.-J., Li, X., Xu, H.-T., Zhang, H.-J. & Wang, Y. Nanoporous metal as a platform for electrochemical and optical sensing. *J. Mater. Chem. C* **2,** 9788–9799 (2014).

8. Ambrosi, A., Merkoçi, A. & de la Escosura-Muñiz, A. Electrochemical analysis with nanoparticle-based biosystems. *TrAC - Trends Anal. Chem.* **27,** 568–584 (2008).

9. Kelley, S. O. *et al.* Advancing the speed, sensitivity and accuracy of biomolecular detection using multi-length-scale engineering. *Nat. Publ. Gr.* **9,** 969–980 (2014).

10. Huckle, D. Point-of-care diagnostics: will the hurdles be overcome this time? *Expert Rev. Med. Devices* **3,** 421–426 (2006).

11. El Harrad, L., Bourais, I., Mohammadi, H. & Amine, A. Recent Advances in Electrochemical Biosensors Based on Enzyme Inhibition for Clinical and Pharmaceutical Applications. *Sensors* **18,** 164 (2018).

12. Rocchitta, G. *et al.* Enzyme biosensors for biomedical applications: Strategies for safeguarding analytical performances in biological fluids. *Sensors (Switzerland)* **16,** (2016).

13. Kotov, N. A. Inorganic Nanoparticles as Protein Mimics. *Science* **330,** 188–189 (2010).

14. Cheng, H., Lin, S., Muhammad, F. & Wei, H. Rationally modulate the oxidase-like activity of nanoceria for self-regulated bioassays. *ACS Sensors* **1,** 1336–1343 (2016).

15. Wang, C., Chen, W. & Chang, H. Enzyme Mimics of Au / Ag Nanoparticles for Fluorescent Detection of Acetylcholine. *Anal. Chem.* **84,** 9706–9712 (2012).

16. Russo, L., Puntes, V. & Merkoçi, A. Tunable Electrochemistry of Gold-Silver Alloy Nanoshells. *Nano Res.* **11,** 6336 (2018).

17. Wang, Y., Salehi, M., Schütz, M. & Schlücker, S. Femtogram detection of cytokines in a direct dot-blot assay using SERS microspectroscopy and hydrophilically stabilized Au-Ag nanoshells. *Chem. Commun.* **50,** 2711–2714 (2014).

18. Jang, H., Kim, D. E. & Min, D. H. Self-assembled Monolayer Mediated Surface Environment Modification of Poly(vinylpyrrolidone)-Coated Hollow Au-Ag Nanoshells for Enhanced Loading of Hydrophobic Drug and Efficient Multimodal Therapy. *ACS Appl. Mater. Interfaces* **7,** 12789–12796 (2015).

19. Miranda, O. R. *et al.* Colorimetric bacteria sensing using a supramolecular enzyme-

nanoparticle biosensor. *J. Am. Chem. Soc.* **133,** 9650–9653 (2011).

20. Chen, J., Andler, S. M., Goddard, J. M., Nugen, S. R. & Rotello, V. M. Integrating recognition elements with nanomaterials for bacteria sensing. *Chem. Soc. Rev.* **46,** 1272–1283 (2017).

21. Chen, J. *et al.* Electrochemical nanoparticle–enzyme sensors for screening bacterial contamination in drinking water. *Analyst* **140,** 4991–4996 (2015).

22. Russo, L. *et al.* Time- and Size-Resolved Plasmonic Evolution with nm Resolution of Galvanic Replacement Reaction in AuAg Nanoshells Synthesis. *Chem. Mater.* **30,** 5098–5107 (2018).

23. Wan, Y. *et al.* Highly Specific Electrochemical Analysis of Cancer Cells using Multi-Nanoparticle Labeling. *Angew. Chemie - Int. Ed.* **53,** 13145–13149 (2014).

24. Zheng, Y., Zeng, J., Ruditskiy, A., Liu, M. & Xia, Y. Oxidative etching and its role in manipulating the nucleation and growth of noble-metal nanocrystals. *Chem. Mater.* **26,** 22–33 (2014).

25. Cloake, S. J. *et al.* Anodic stripping voltammetry of silver nanoparticles: Aggregation leads to incomplete stripping. *ChemistryOpen* **4,** 22–26 (2015).

26. Douglas, F. *et al.* Silver, gold and the corresponding core shell nanoparticles: Synthesis and characterization. *J. Nanoparticle Res.* **10,** 97–106 (2008).

27. Toh, H. S., Batchelor-McAuley, C., Tschulik, K. & Compton, R. G. Electrochemical detection of chloride levels in sweat using silver nanoparticles: a basis for the preliminary screening for cystic fibrosis. *Analyst* **138,** 4292–4297 (2013).

28. Kleijn, S. E. F., Lai, S. C. S., Koper, M. T. M. & Unwin, P. R. Electrochemistry of Nanoparticles. *Angew. Chemie - Int. Ed.* **53,** 3558–3586 (2014).

29. Tamerat, N. & Muktar, Y. Application of Molecular Diagnostic Techniques for the Detection of E. coli O157:H7: A Review. *J. Vet. Sci. Technol.* **7,** 362 (2016).

30. Jiang, Z., Le, N. D. B., Gupta, A. & Rotello, V. M. Cell surface-based sensing with metallic nanoparticles. *Chem. Soc. Rev.* **44,** 4264–4274 (2015).

31. Feng, Z. V. *et al.* Impacts of gold nanoparticle charge and ligand type on surface binding and toxicity to Gram-negative and Gram-positive bacteria. *Chem. Sci.* **6,** 5186–5196 (2015).

32. Sepunaru, L., Tschulik, K., Batchelor-McAuley, C., Gavish, R. & Compton, R. G. Electrochemical detection of single E. coli bacteria labeled with silver nanoparticles. *Biomater. Sci.* **3,** 816–820 (2015).

33. Hassan, A. R. H. A. A., de la Escosura-Muñiz, A. & Merkoçi, A. Highly sensitive and rapid determination of Escherichia coli O157: H7 in minced beef and water using electrocatalytic gold nanoparticle tags. *Biosens. Bioelectron.* **67,** 511–515 (2015).

34. El Badawy, A. M. *et al.* Surface charge-dependent toxicity of silver nanoparticles. *Environ. Sci. Technol.* **45,** 283–287 (2011).

35. Song, J. E. *et al.* Hydrophobic interactions increase attachment of gum arabic- and PVP-coated Ag nanoparticles to hydrophobic surfaces. *Environ. Sci. Technol.* **45,** 5988–5995 (2011).

36. Bondarenko, O., Ivask, A., Käkinen, A., Kurvet, I. & Kahru, A. Particle-Cell Contact Enhances Antibacterial Activity of Silver Nanoparticles. *PLoS One* **8,** (2013).

37. Sousa, C., Sequeira, D., Kolen'Ko, Y. V., Pinto, I. M. & Petrovykh, D. Y. Analytical protocols for separation and electron microscopy of nanoparticles interacting with bacterial cells. *Anal. Chem.* **87,** 4641–4648 (2015).

38. MacKenzie, D. A., Sherratt, A. R., Chigrinova, M., Kell, A. J. & Pezacki, J. P. Bioorthogonal labelling of living bacteria using unnatural amino acids containing nitrones and a nitrone derivative of vancomycin. *Chem. Commun.* **51,** 12501–12504 (2015).

39. Frimmel, F. Aquatic Humic Substances. *Biopolymers* **1,** 301–310 (2001).

40. Barbero, F. *et al.* Formation of the Protein Corona: The Interface between Nanoparticles and the Immune System. *Semin. Immunol.* **34,** 52–60 (2017).

41. Gorchev, H. G. & Ozolins, G. WHO guidelines for drinking-water quality. *WHO Chron.* **38,** 104–108 (2011).

42. Li, L., Feng, D., Fang, X., Han, X. & Zhang, Y. Visual sensing of Hg2+ using unmodified Au@Ag core–shell nanoparticles. *J. Nanostructure Chem.* **4,** 117 (2014).

43. Price, S. W. T., Speed, J. M. R. J. D., Calvillo, L., Kannan, P. & Russell, a E. Exploring the First Steps in Core-Shell Electrocatalyst Preparation: In Situ Characterization of Cu and Pd shells on Supported Au Nanoparticles. *J. Am. Chem. Soc.* **133,** 19448–19458 (2011).

Chapter V

Conclusions

In this PhD thesis, the paradigm of rationally designing advanced nanomaterials with controlled properties for their *ad hoc* employment in the field of biosensing was successfully applied, leading to the development of two different diagnostic platforms for the determination of viral and bacterial infections.

Firstly, a highly reproducible and robust synthetic method for the production of monodisperse AuAg alloy NSs based on GRR was developed. The protocol described allows the precise control over the particles' morphology, in terms of shell thicknesses and void sizes, the relative composition and topological distribution of their constituting noble metals, as well as their surface roughness and porosity. This synthetic predictability, tested over a range of sizes, has been achieved through a systematic study of the convoluted interplay of each co-reagent, together with a detailed characterization of the material's composition and structure through an array of techniques. Moreover, the analysis of AuAg NSs' plasmonic properties evolution during their structural transformation, which spanned through almost the whole visible spectrum up to NIR wavelengths, revealed a tight dependence with their morphological and compositional features. These results, also confirmed by calculations based on Mie's theory, provided the basis for their application as signal enhancers in the SERS-based LFA developed.

Secondly, for the first time the electrochemical behavior of AuAg NSs was reported. Triggered by the controlled corrosion of Ag atoms contained in the particles' residual cores and thin alloy shells, the voltammetric study of these hollow nanocrystals has been found to be strongly dependent on their relative elemental composition and, partially, to their size and morphology. Indeed, a peculiar electrocatalytic effect appeared only for AuAg NSs possessing a high-enough Au/Ag ratio to let the catalytic electrodeposition of Ag^+ on the NSs' surfaces occur at potentials less negative than Ag standard reduction one. Interestingly, this unreported feature was shown to be triggered only by the mild oxidating character of the electrolyte used, without the need of any other co-reagent or oxidizer. These findings constituted the rational basis for developing AuAg NSs with desirable properties to be applied in the electrochemical assay described.

Taking advantage of the tunable plasmonic properties of AuAg NSs, the development of a SERS-based LFA for the sensitive and quantitative detection of MxA, a biomarker commonly associated to viral infections, was developed. Thanks to the enhanced plasmons intensities displayed by AuAg NSs, resulting from the plasmonic cavity effect commonly observed in hollow nanostructures, their surfaces acted as a continuous *hot-spot,* amplifying any Raman signal emitted by the reporters thereby attached. Moreover, the possibility to precisely adjust AuAg NSs' LSPR maximum wavelength to match the NIR excitation laser used during SERS measurements allowed to further improve the overall analytical performance. Thus, AuAg NSs were easily conjugated with anti-MxA antibodies and integrated in a LFA in order to reveal its presence in spiked serum samples. After careful optimization of the point-of-care platform parameters, MxA protein could be successfully detected down to the analytically-relevant LOD of few ng/mL.

Finally, the capability to precisely modulate AuAg NSs elemental composition lead to the design of a *proof-of-concept* electrochemical assay for the rapid detection of two model bacterial strains, *Escherichia coli* and *Salmonella typhimurium*. AuAg NSs were used as electrochemical reporters because of the ease of generation of the electrochemical signal, triggered by the sole mild oxidating character of the biological sample matrix. Besides, the polymeric coating of the hollow particles provided the non-specific, affinity-based interaction with bacterial cells in solution, avoiding the need for costly and fragile antibodies. With this low-cost strategy, *E.coli* could be detected in PBS down to 10^2 CFU/mL, while the semi-selective discrimination of the current-concentration profiles of the two model bacterial strains was also achieved.

Annex 1 – Experimental Section

Chapter 3

Time- and Size-Resolved Plasmonic Evolution with nm Resolution of Galvanic Replacement Reaction in AuAg Nanoshells Synthesis

Silver nitrate ($AgNO_3$), trisodium citrate ($Na_3C_6H_5O_7$), tannic acid ($C_{76}H_{52}O_{46}$), $HAuCl_4 \cdot 3H_2O$ (99%), polyvinylpyrrolidone (PVP) $(C_6H_9NO)_n$ Mw≈55,000 were purchased from Sigma-Aldrich. All chemicals were used as received without further purification. Distilled water passed through a Millipore system (ϱ = 18.2 MΩ) was used in all experiments. All glassware was first rinsed with acetone and then with Millipore water before use. Ag NCs of the desired size used as sacrificial templates for GRR were synthetized following a method developed by our group.[25] 10 mL of the prepared colloidal solution was centrifuged (8000 – 12000 rcf depending on particle size), the supernatant removed and the pellet re-suspended with 10 mL of a 5 mM (repeating unit) aqueous solution of PVP. The templates were then left conjugating with the polymer for about 1 hour. A syringe pump (Pump 11 Elite; Harvard Apparatus, USA) equipped with a plastic syringe (BD plastic, 5 mL) and a microfluidic silicon tube of 500 μm ending with a 0.1-10 μL plastic pipette tip was used to dose a $HAuCl_4$ 1 mM aqueous solution freshly prepared (10 μL/min). The approximate inner orifice diameter of the plastic pipette tip is 0.31 mm which corresponds to a needle of 24G. A 50 mL glass beaker containing Milli-Q water (10 mL), PVP 5 mM aqueous solution (20 mL) and 10 mL of the previously conjugated templates was prepared under vigorous stirring. The stirring rate was kept high enough (400/600 rpm) to ensure the homogeneity of the solution during the reaction, particularly to avoid mass gradients that often lead to the lack of control of the final NPs. Once homogenized, HCl 10 mM (10 mL) was added at once and let reacting with the mixture for 60 sec. Immediately after, the syringe pump injection was started and the reaction covered with parafilm® in order to avoid volume variations due to evaporation. When aliquots were collected to perform UV-Vis spectra, the injection was stopped, the sample measured quickly without any purification and re-added to the reaction mixture. Once the desired degree of conversion was reached, the reaction mixture was divided into 10 mL aliquots and transferred into 50 ml Falcon tubes, diluted with 10 mL Milli-Q water each and then centrifuged at 8000 rcf for 10 min. The supernatant was removed and the pellet resuspended in Milli-Q water (20 mL each aliquot), then sonicated for 5-10 min. This washing step was repeated for a total of 3 times and the last resuspension in Milli-Q water was performed into a total final volume of 10 mL, so to obtain the original particles concentration.

All nanoparticles were characterized by UV-vis spectroscopy (Perkin-Elmer "Lambda25"), Dynamic Light Scattering (DLS) Malvern Zetasizer, Transmission Electron Microscopy (TEM) and Scanning Electron Microscopy (SEM) with FEI Magellan XHR SEM, in transmission mode operated at 20 kV. HRTEM and HAADF-STEM micrographs and elemental distribution analysis by EDS line scan were obtained using a FEI Tecnai F20 field-emission gun microscope with a 0.19 nm point-to-point resolution operated at 200 keV. Localized Surface Plasmon Resonance (LSPR) extinction spectra of void/shell/shell NCs was modelled using the online platform "Extinction, Scattering and Absorption efficiencies of single and multilayer nanoparticles" based on the standard Mie theory[26]. Series of void/shell/shell NCs of varied core sizes, shell thicknesses and compositions, embedded in water at 25 °C were modelled. In all cases, the mean size measured by TEM was used for the calculations. Input parameters chosen were: the original Ag template's size, the core (void) diameter and the shell thickness. As a result, the extinction (Q_{ext}) efficiency was obtained and plotted using Origin software.

Chapter 3

Tunable electrochemistry of gold-silver alloy nanoshells

Silver nitrate ($AgNO_3$), trisodium citrate ($Na_3C_6H_5O_7$), tannic acid ($C_{76}H_{52}O_{46}$), $HAuCl_4 \cdot 3H_2O$ (99%), polyvinyl pyrrolidone $(C_6H_9NO)_n$ Mw ≈ 55,000 (PVP) were purchased from Sigma-Aldrich. All chemicals were used as received without further purification. Distilled water passed through a Millipore system (ϱ = 18.2 MΩ) was used in all experiments. All glassware was first rinsed with acetone and then with Millipore water before use. Buffers solutions were prepared in Milli-Q water obtained from a Millipore system Vent Filter MPK01. Both buffers, phosphate buffer (PB) and phosphate buffer saline (PBS), were prepared at a concentration of 0.01 M and at pH7.4. PB was prepared by mixing sodium-phosphate monobasic hydrogen along with sodium-phosphate dibasic hydrogen in the desired proportion; PBS was purchased from Sigma Aldrich in tablets. Screen Printed Carbon Electrodes (SPCEs) were fabricated with a semi-automatic screen-printing machine DEK248 (DEK International, Switzerland). Electrodes were printed over Autostat HT5 polyester sheets (McDermid Autotype, UK) using Carbon Sensor Paste C2030519P4 for working (WE) and counter (CE) electrodes, Grey Dielectric Paste D2070423P5 (Gwent, The Netherlands) to insulate the contacts and define the sample interaction area, and silver/silver chloride ink for reference electrode (RE) EDAG 6037E SS (Loctite).

All nanoparticles were characterized by UV-vis spectroscopy (Perkin-Elmer "Lambda25" Spectrophotometer), Dynamic Light Scattering (DLS) Malvern Zetasizer, Transmission Electron Microscopy (TEM) and Scanning Electron Microscopy (SEM) (FEI Magellan 400L). HRTEM images were obtained using a FEI Tecnai F20 field-emission gun microscope with a 0.19 nm point-to-point resolution operated at 200 keV. The electrochemical experiments were performed by an AUTOLAB PGSTAT302N (Echo Chemie, The Netherlands) potentiostat/galvanostat which was connected to a computer and monitored by Autolab GPES software. All experiments were performed at room temperature. SCPEs were connected with the potentiostat through a homemade connector. The general protocol for the electrochemical measurements of AuAg

NSs is the following: 10 μL of AuAg NSs solution (1.6x10^{11} NPs/mL) were transferred into a plastic 1.5 mL Eppendorf tube containing 50 μL of a PBS 10 mM pH7.4. After incubation in the saline matrix for a given time and under stirring at 600 rpm in a thermoshaker at 25 ˚C, 50 μL of the mixture were dropped onto the SPCE so that to cover the three electrodes. Differential Pulsed Voltammetry (DPV) was run: after applying a fixed deposition negative potential for 60 sec, voltage was scanned between +0.6 V and +1.04 V vs RHE with 0.01 V step potential. Cyclic voltammetries (CVs) were recorded in the same conditions scanning from -0.16 V to +0.94 V vs RHE at 100 mV/sec scan rate with 0.005 V step potential.

Chapter 4

Detection of myxovirus resistance protein A (MxA) in paper-based immunoassays with surface enhanced Raman spectroscopy with hollow AgAu nanoparticles

Chemicals. Silver nitrate ($AgNO_3$) (CAS: 7761-88-8), trisodium citrate ($Na_3C_6H_5O_7$) (CAS: 6132-04-3), tannic acid ($C_{76}H_{52}O_{46}$) (CAS: 1401-55-4), $HAuCl_4 \cdot 3H_2O$ (99%)(CAS: 27988-77-8), polyvinyl pyrrolidone $(C_6H_9NO)_n$ Mw ≈ 55,000 (PVP) (CAS: 9003-39-8), 4-mercaptobenzoic acid (MBA) (CAS: 1074-36-8), sucrose (CAS: 57-50-1), bovine serum albumin (BSA) (CAS: 9048-46-8), Tween-20 (CAS: 9005-64-5), anti-Human IgG (whole molecule, produced in goat, Catalog Number: I1886), IgG from goat serum (Catalog Number: I5256), anti-MxA (catalog Number: HPA049724) and Mx1 antigen (Catalog Number: APREST89598) were all purchased from Sigma-Aldrich. All chemicals were used as received without further purification. Hi-Flow Plus Nitrocellulose HF135 with plastic backing was purchased from EMD Millipore, US. All glassware was first rinsed with acetone and then with Millipore water before use. Buffers solutions were prepared in Milli-Q water obtained from a Millipore system Vent Filter MPK01 ($\varrho = 18.2$ MΩ). Phosphate buffer (PB) was prepared at a concentration of 0.01 M and at pH7.4 by mixing sodium-phosphate monobasic hydrogen along with sodium-phosphate dibasic hydrogen in the desired proportion. Hollow AuAg Nanoshells (AuAg NSs) were synthetized following a protocol developed recently[29] and characterized by UV-vis spectroscopy (Perkin-Elmer "Lambda25" Spectrophotometer), Dynamic Light Scattering (DLS) Malvern Zetasizer, Transmission Electron Microscopy (TEM) (FEI Magellan 400L).

Dipstick LFA. Antibodies were immobilized on the nitrocellulose strip by manually pipetting 0.3 µl of the antibody stock solution onto the nitrocellulose paper and allowed to dry. In the test line, polyclonal antibodies against human IgG were immobilized for LFA preliminary experiments and optimization, while polyclonal antibodies against MxA protein were immobilized for running the actual assay. The deposition step was repeated until the desired capture antibody concentration was reached. The control line was spotted with polyclonal antibodies against Fc fragment of the capture antibodies used. In order to run the test, the strip was submerged at its lower end in the test solution containing 4 µl of 50% w/v sucrose in water, 7 µL of 1% v/v Tween 80 in PB 10 mM pH7.5, 1 µl of 1% w/v PVP 55k in PB 10 mM pH7.5, 30 µl of 2% w/v BSA in PB 10 mM pH7.5, 2 µl of AuAgNSs@4-MBA@Ab conjugate and 1 µl of the analyte, rendering a total volume of 43 µl. Then, the solution was let migrating through the strip upward via capillary action towards the absorbent pad attached to the upper end of the strip. When all the solution had been absorbed, the strip was washed with 80 µl of 0.1% v/v Tween 80 in PB 10 mM pH 7.5 through the same procedure to eliminate unbound conjugates and allowed to dry.

Optical Analysis. Once the tests had dried, images of the tests were obtained by scanning the strips and quantified with ImageJ in 8-bit, color-inverted grayscale image by measuring 25 spots on the Test Line area of each strip (**Figure S5**, *red dots*). Each spot was obtained by tracing a circle with area = 1. The obtained pixel intensity values were then normalized using **Equation 1**:

$$Int_{NORM} = \frac{(Int_{SPOT} - In\ _{MAX})}{(Int_{MIN} - Int_{MAX})} \qquad \textbf{(1)}$$

being Int_{SPOT} the measured intensity, Int_{MAX} the maximum intensity measured over the range, Int_{MIN} the minimum intensity measured over the range and Int_{NORM} the resulting normalized value.

SERS Measurements. Raman and SERS spectra were acquired using a Raman Senterra II microscope (Bruker Optiks GmbH, Germany). A Ne laser with a power of 10 mW operating at λ = 785 nm was utilized as the excitation source. A thermoelectrically cooled CCD detector was coupled to a spectrograph. Raman spectra were obtained using a Raman point method with a 10× objective lens, with a total of 25 points per sample measured. The data integration time at each point was 5 s with 5 co-additions. The numerical aperture of the objective lens used in this work is 50 × 1000 µm. The spectrum acquired for each spot was decoded using OPUS software v 7.0 (Bruker Optiks GmbH, Germany). Baseline correction was performed by the concave Rubberband correction method using 15 iterations and 64 baseline points. Mathematical calculations on the spectra such as spectral averaging, intensity, area, or peak shift measurements were performed in Microsoft Excel.

Quantitative Analysis. The limit of detection (LOD) was defined as the minimum concentration that yielded an average test area intensity that exceeded by 3 times the standard deviation of the blank (test area intensity running sample without antigen) over the average intensity of the blank. To obtain K_D values, test line intensities (normalized grey values for colorimetric LFA and SERS intensities measured at 1590 cm^{-1} respectively) vs. analyte concentration were plotted and fitted to a sigmoidal dose-response equation using curve fitting toolbox in Origin.

Chapter 4

A low-cost strategy for the development of a rapid electrochemical assay for bacteria detection based on AuAg nanoshells

Silver nitrate ($AgNO_3$), trisodium citrate ($Na_3C_6H_5O_7$), tannic acid ($C_{76}H_{52}O_{46}$), $HAuCl_4 \cdot 3H_2O$ (99%), polyvinyl pyrrolidone $(C_6H_9NO)_n$ Mw≈55,000 (PVP), human serum and humic acid were purchased from Sigma-Aldrich. Copper nitrate tri-hydrate and mercury nitrate standard solutions were purchased from Panreac. All chemicals were used as received without further purification. Distilled water passed through a Millipore system (ϱ = 18.2 MΩ) was used in all experiments. All glassware was first rinsed with acetone and then with Millipore water before use. Buffers solutions were prepared in Milli-Q water obtained from a Millipore system Vent Filter MPK01. Both buffers, phosphate buffer (PB) and phosphate buffer saline (PBS), were prepared at a concentration of 0.01 M and at pH7.4. PB was prepared by mixing sodium-phosphate monobasic hydrogen along with sodium-phosphate dibasic hydrogen in the desired proportion; PBS was purchased from Sigma Aldrich in tablets.

Screen Printed Carbon Electrodes (SPCEs) were fabricated with a semi-automatic screen-printing machine DEK248 (DEK International, Switzerland). Electrodes were printed over Autostat HT5 polyester sheets (McDermid Autotype, UK) using Carbon Sensor Paste C2030519P4 for working (WE) and counter (CE) electrodes, Grey Dielectric Paste D2070423P5 silver/silver chloride ink for reference electrode (RE) and Minico 7000 Blue insulating ink (Acheson Industries, The Netherland) to insulate the contacts and define the sample interaction area.

All nanoparticles were characterized by UV-Vis spectroscopy (Perkin-Elmer "Lambda25"), Dynamic Light Scattering (DLS) (Malvern Zetasizer), Transmission Electron Microscopy (TEM) and Scanning Electron Microscopy (SEM) (FEI Magellan 400L). HRTEM images were obtained using a FEI Tecnai F20 field-emission gun microscope with a 0.19 nm point-to-point resolution operated at 200 keV.

The electrochemical experiments were performed by AUTOLAB PGSTAT302N (Echo Chemie, The Netherlands) potentiostat/galvanostat which was connected to a computer and monitored by GPES software. All experiments were performed at room temperature. SCPEs were connected with the potentiostat through a homemade connector. The general protocol for the electrochemical measurements of nanoparticles (NPs)-containing samples is the following: 10 uL of AuAg NSs suspension at a nominal concentration of $1.6x10^{11}$ NPs/mL, unless specified otherwise, were transferred into a plastic 1.5 mL Eppendorf tube containing 50 uL of a bacteria suspension in PBS 10 mM pH7.4 with a given bacteria colony forming units (CFU)/mL. After incubation in the saline matrix for a given time and under stirring at 600 rpm in a thermoshaker at 25 ^{o}C, 50 uL of the mixture were displaced onto the SPCE so that to cover the three electrodes. Differential Pulsed Voltammetry (DPV) was run: after applying a fixed deposition negative potential for 60 s, voltage was scanned between -0.05 V and +0.4 V with 0.01 V step potential. Cyclic voltammetries (CVs) were recorded in the same conditions scanning from -0.8 V to +0.3 V at 100 mV/s scan rate with 0.005 V step potential.

Escherichia coli O157:H7 (CECT 4783) *Salmonella enterica* subsp. *enterica serovar typhimurium* LT2 (CECT 722 T) strains were obtained from "Colección Española de Cultivos Tipo" (CECT). *E. coli* stock cultures were kept in TSA (Typticase Soy Agar) sloped tubes at 4 ^{o}C and stored in these conditions no longer than two months. To start up the culture, some *E. coli* colonies were transferred from TSA to TSB (Trypticase Soy Broth) tubes at 37 ^{o}C for 24 h for bacterial growth. Next day, a small fraction of the new grown bacterial culture was taken with a loop (≈ 1 μL) and carried to a TSA plate. Again, bacteria were allowed growing at 37 ^{o}C for 24 h. Finally, a glass tube was filled up with 0.01 M PBS and some colonies were introduced into the tube. Bacteria solution was vortexed and OD was measured using McFarland standards: a value of 0.5 indicated bacterial density is around $1.5x10^{8}$ cfu/mL. *E.coli* living cells were eventually subjected to a sharp temperature increase (80^{o}C) for 20 min in order to kill without compromising the outer cell wall structure. The same process was carried out for *Salmonella* strain.

Annex 2 – Supporting Information

Chapter III

Time- and Size-Resolved Plasmonic Evolution with nm Resolution of Galvanic Replacement Reaction in AuAg Nanoshells Synthesis

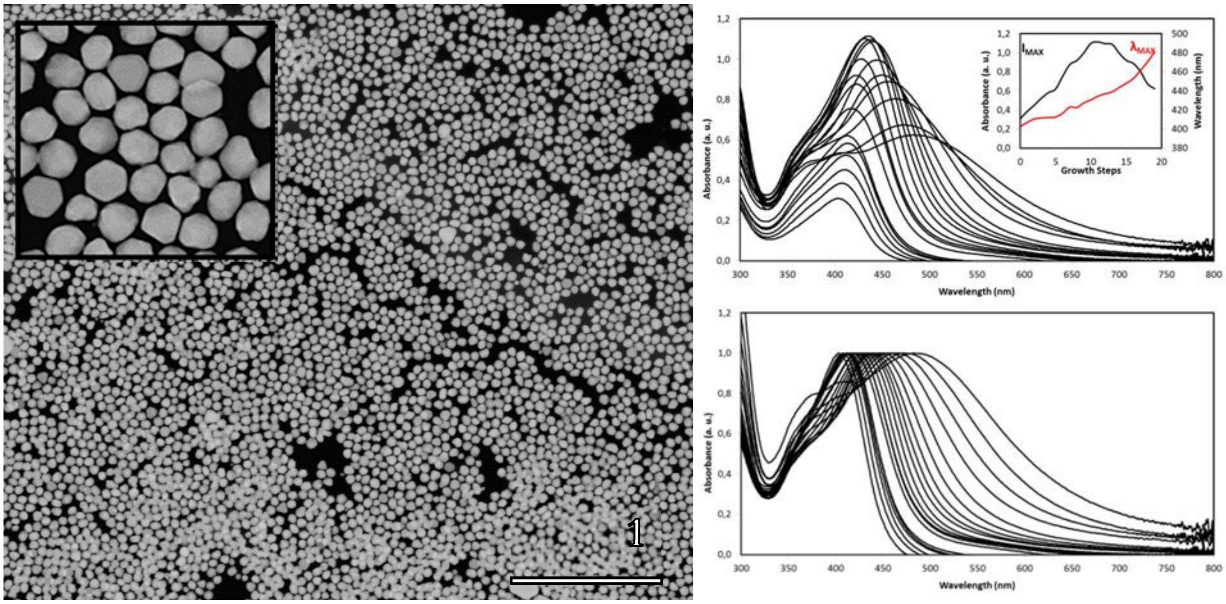

Figure S1 – Monodispersed and high quality silver pseudo-spherical NCs are used as sacrificial templates for the GRR. **Left**: TEM dark field images of silver templates of c.a 80 nm size (SD < 10%) showing high degree of crystallinity and multifaceted surface. **Right**: The seeded-growth synthesis of silver templates is followed by UV-Vis spectroscopy (*above*) and normalized (*below*). Inset shows LSPR intensity and maximum wavelength trends during synthesis.

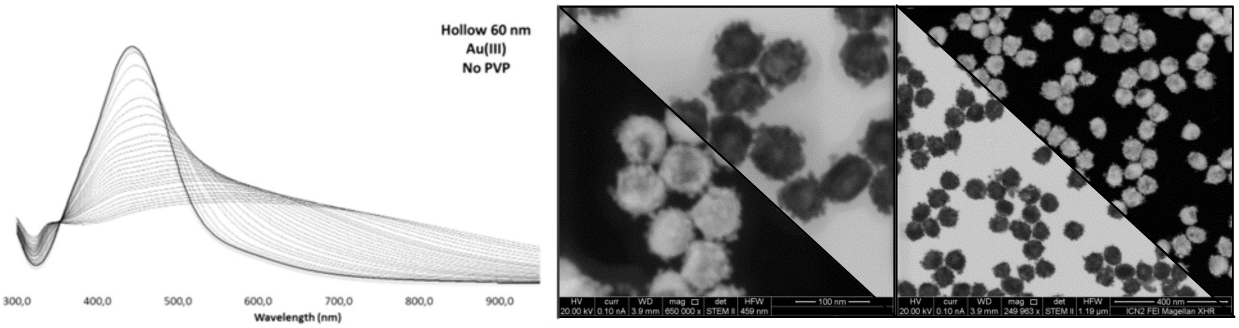

Figure S2 – GRR carried out in absence of PVP. UV-Vis spectra evolution end up in a black solution with flat absorbance profile (left). TEM bright and dark field images (*right*) show particles with uneven hollowing degree and a rough granular surface.

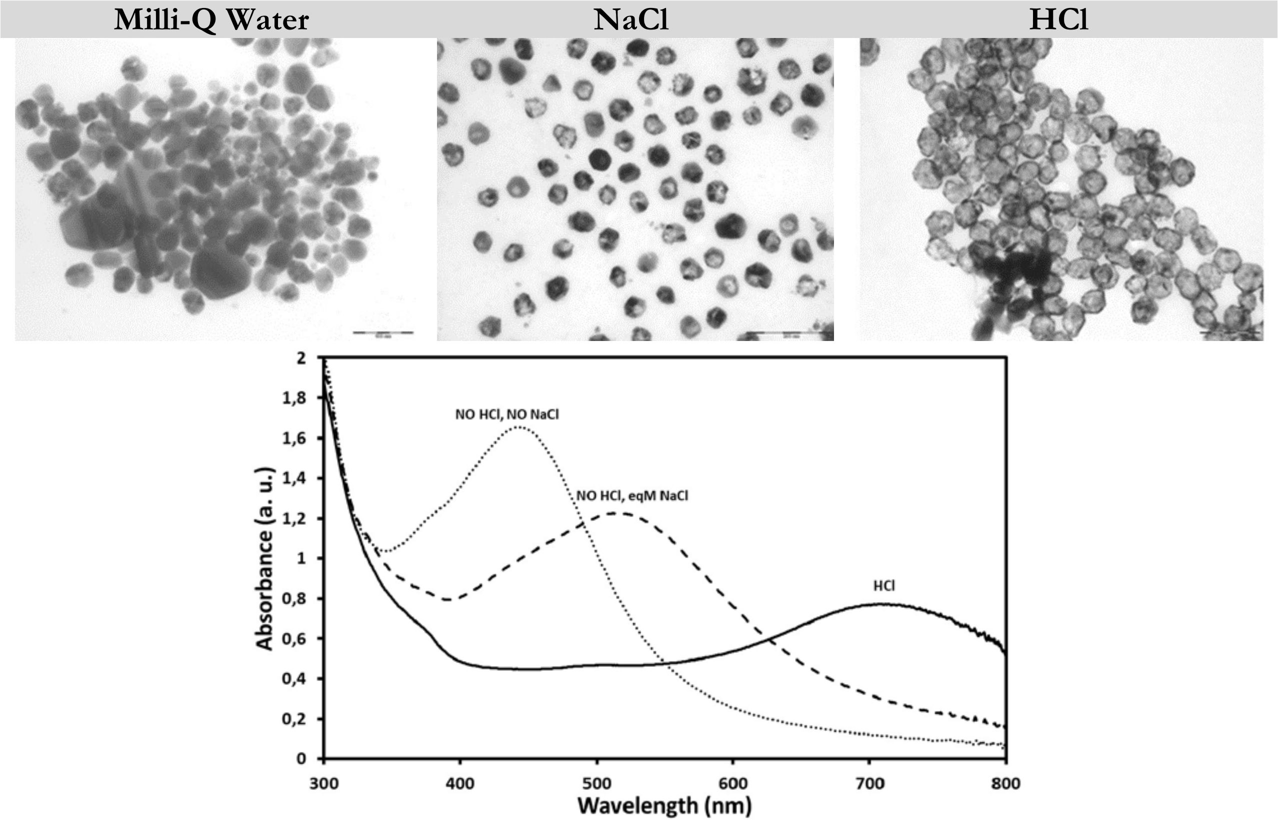

Figure S3 – Final morphology (*above*) and UV-Vis spectra (*below*) obtained when carrying out GRR in Milli-Q water, 10 mM NaCl and 10 mM HCl respectively. When both chlorides and proton are present, a hollow final morphology characterized by thin shell and large void is observed. When using an equinormal NaCl solution instead, that is with the same amount of chlorides as protons in the previous case, the degree of hollowing of the forming structure is decreased strongly. In these conditions only chlorides and Au^{III} compete for the oxidative etching of Ag form the particles core, making the hollow morphology still recognizable at the final stages of GRR but with a smaller void. Carrying out the reaction in absence of both co-etchers lowers the reaction rate so significantly that, for equivalent $HAuCl_4$ volumes added, no relevant shift in LSPR is observed.

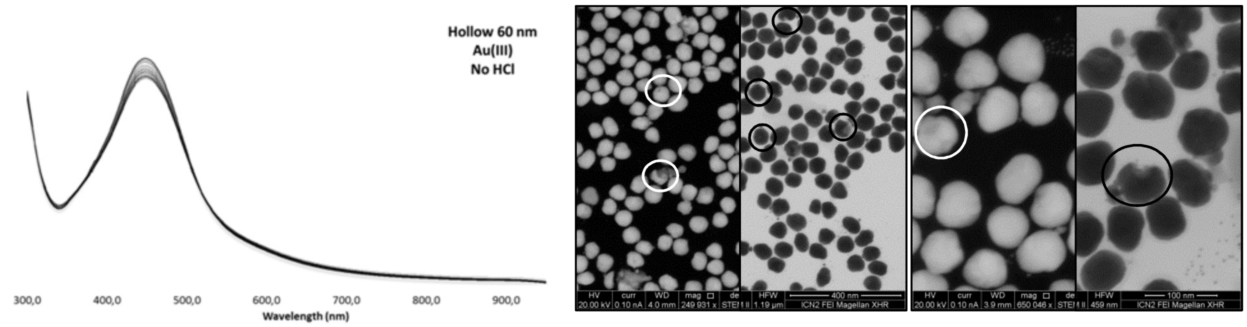

Figure S4 – GRR carried out in absence of HCl. UV-Vis spectra evolution reveals a significant delay in GRR initiation (*left*). TEM bright and dark field images show particles with random pitting corrosion events (*right*).

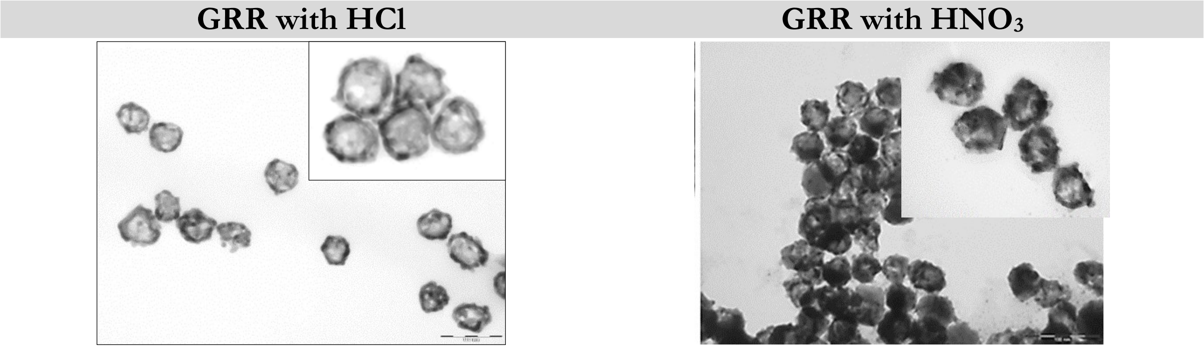

Figure S5 – GRR carried out with different co-etchers: with HCl (*left*) a smoother surface and larger void are obtained; with HNO_3 (*right*) rough, granular Au deposition on the templates surface is observed, while the degree of hollowing is significantly lower.

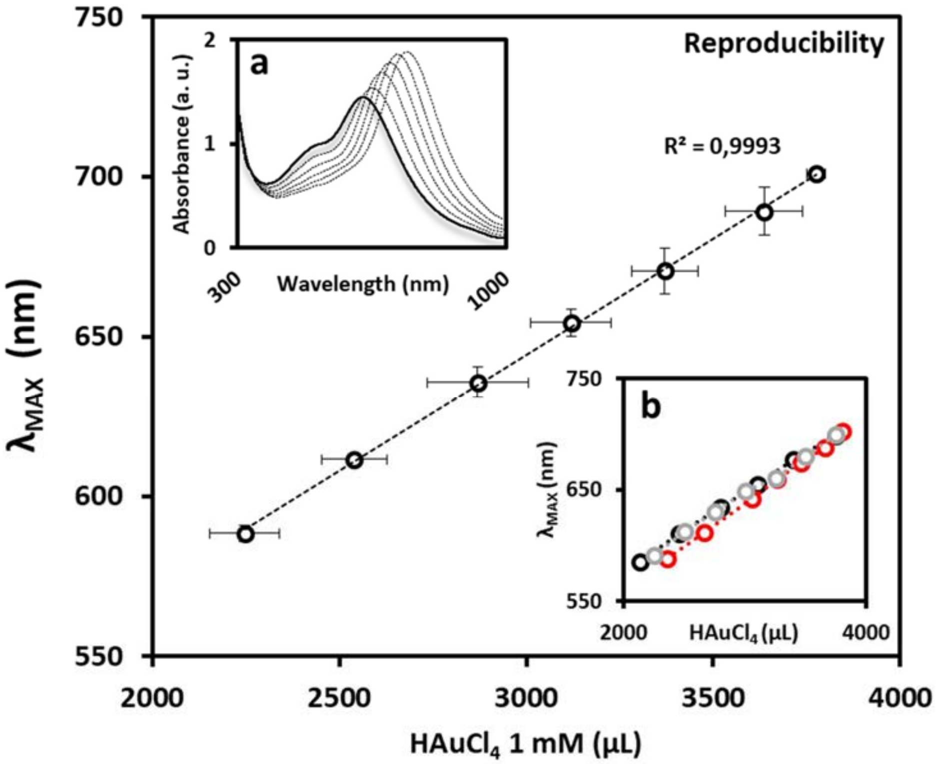

Figure S6 – Study of the reproducibility of the optimized GRR for the selective synthesis of hollow AuAg NSs with large voids and thin, smooth shells. Three different AuAg NSs syntheses were compared by monitoring the LSPR band shift of three solutions of monodisperse Ag NCs (d = 80 nm) titrated with HAuCl$_4$ 1 mM during the last GRR phase (total templates volume used = 25 mL). **Inset a** shows the time-dependent absorbance spectra of a 80 nm-sized solution of Ag NCs titrated with increasing volumes of HAuCl$_4$, each absorption spectrum corresponding to 25 µL of a 1 mM HAuCl$_4$ aqueous solution injected at 10 µL/min (spectra for earlier GRR are not shown for clarity). **Inset b** reports the LSPR maximum wavelength position during the titration, three different syntheses (*black, red and grey curves*) are compared and their average plotted against their corresponding HAuCl$_4$ volume added (vertical error bars represent standard deviation for LSPR maximum wavelength; horizontal error bars represent standard deviation for volume of HAuCl$_4$ solution added; N = 3). For all the cases (*main plot*), the same linear trend between the amount of Au^{III} added and the LSPR position was observed revealing an almost complete reproducibility (R^2 = 0.9993 or linear trend). Each synthesis was carried out onto a different Ag NCs solution, whose slight variability in templates concentration is responsible for the relatively small differences between each GRR.

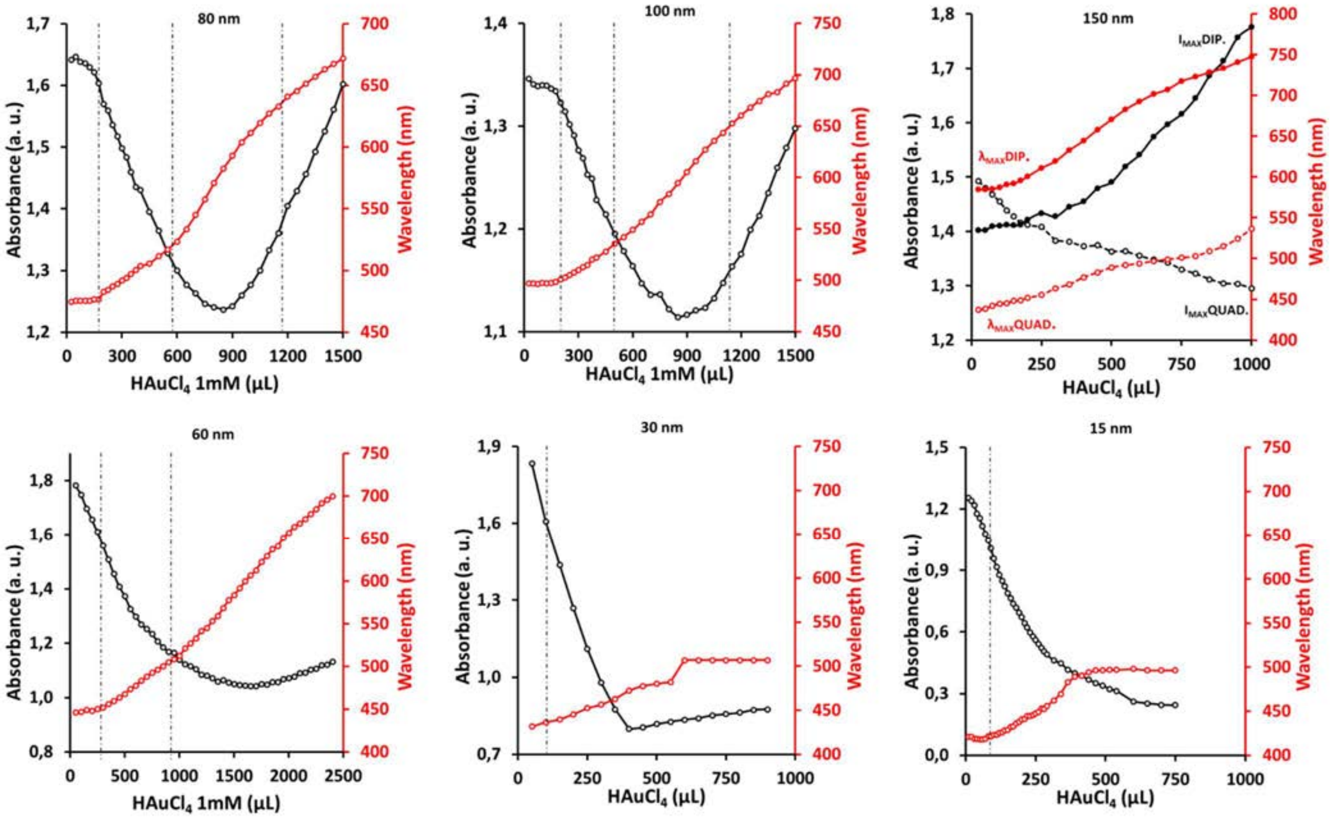

Figure S7 – Time-resolved evolution of maximum LSPR wavelength (*red*) and intensity (*black*) of Ag templates solutions of different sizes titrated with increasing volumes of $HAuCl_4$ (each absorption spectrum corresponding to 25 µL of a 1 mM $HAuCl_4$ aqueous solution upon titration at 10 µL/min). Four optical regimes are identified for bigger particles (150, 100 and 80 nm) while for smaller ones the hollow structure collapses at earlier stages. Differences in total HAuCl4 volumes added are probably caused by slight variation in templates concentration due to their synthetic protocol. (Bastús, N.G., Merkoçi, F., Piella, J., Puntes, V.F., **2014**. Synthesis of Highly Monodisperse Citrate-Stabilized Silver Nanoparticles of up to 200 nm: Kinetic Control and Catalytic Properties. *Chem. Mater. 26*, 2836–2846.) In addition to the dipole mode, particles larger than 60 nm exhibited quadrupole plasmon resonance modes, found at 400, 410 and 425 nm for 80, 100 and 150 nm-sized particles respectively. The quadrupole and dipole peaks both shifted to longer wavelengths with increased Au content in AuAg NSs, the extent of this shift depending on the interplay between the thickness of the Au shell and the internal void size. While this quadrupole has been previously reported in solid Ag NCs, its observation after GRR with Au^{III} species is challenging because of the relatively weaker optical activity of Au. However, the extent of the quadrupole peak shift ($\Delta\lambda_{MAX} \approx 100$ nm) is less than that of the dipole peak shift ($\Delta\lambda_{MAX} \approx 250$ nm). Considering that a quadrupole peak can be observed on single metal Ag NCs of 80 nm size but cannot be found on Au NCs of the same size, we conclude that the quadrupole peak originated from the formation of hollow AuAg NSs is a further indicator of the presence of Ag in the hollow NSs, since the phase retardation of oscillating surface electrons needs to be established in order to observe a higher order surface plasmon resonance band. The Ag component in Au matrix and the free electrons on the hollow shell may induce effectively such retardation in hollow AuAg NSs.

<table>
<tr><th>AuIII</th><th>AuI</th></tr>
<tr><td>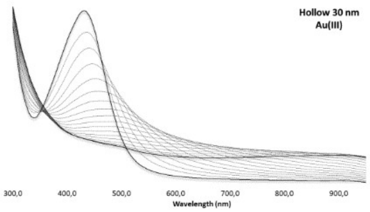 </td><td>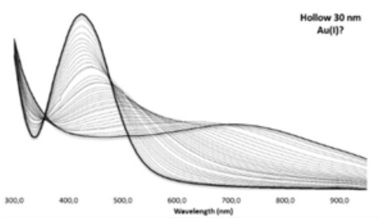 </td></tr>
<tr><td colspan="2">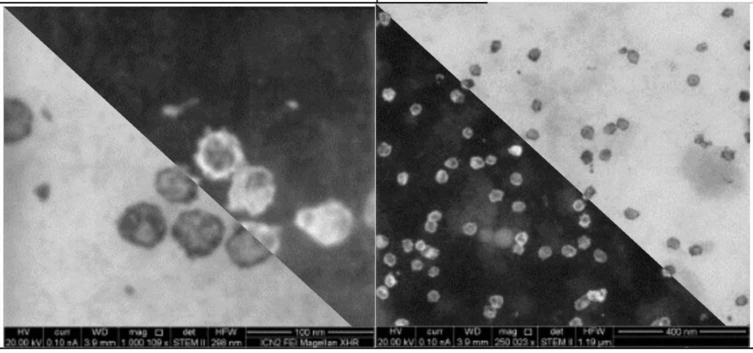 </td></tr>
</table>

Figure S8 – GRR carried out onto 30 nm silver templates: only when Au^{I} precursor is used (*above right, below*) the hollow morphology is reached, even if slightly incomplete. When using instead the normal Au^{III} precursor the hollow morphology collapses before reaching completion.

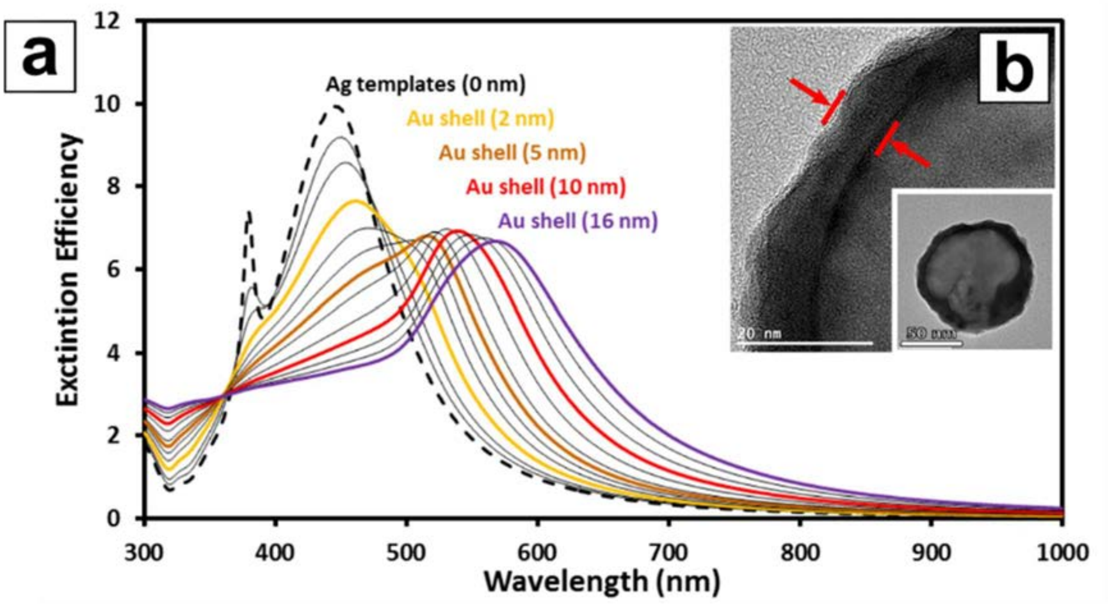

Figure S9 – a) Calculated extinction efficiency for 80 nm Ag spheres surrounded by a thin Au shell of growing diameter. **b)** HRTEM image of AuAg NS at its last GRR stage, displaying a thin outer shell of about 10 nm. **Figure 6 – a)** represents the calculated spectra evolution for 80 nm Ag templates with the initial deposition of a thin growing Au shell, modelled by adding a second Au layer of varying thickness onto the initial Ag core. The calculated spectrum for the analogous Ag NC exhibited a dipole mode at ca. 430 and a quadrupole mode at ca. 380 nm, showing the good agreement with the experiment (dipole and the quadrupole modes found at ca. 440 and 400 nm, respectively in **Figure 1 – A**). In accordance with experimental results previously described, the calculated spectra reveal how the presence of this Au layer is translated into a red-shift of the position of the LSPRs of the Ag templates from 446 nm (Ag NC templates) to 460 nm (2 nm thickness), 517 nm (5 nm thickness), 537 nm (10 nm thickness) and 568 nm (16 nm thickness). Remarkably, the quadrupolar peak of Ag NCs templates rapidly attenuate and vanishes as the thickness of the Au shell increases. The second stage involves the voiding of the core/shell AgAu NC, modelled by adding an inner H_2O sphere of varying diameter surrounded by two shells: one of Ag, which corresponds to the original Ag template not dissolved, and one of Au corresponding to initial deposition already described (**Figure 6 – a)**)

Chapter 4

SERS Detection of Myxovirus Resistance Protein A in Paper-based Immunoassays with AgAu Nanoshells

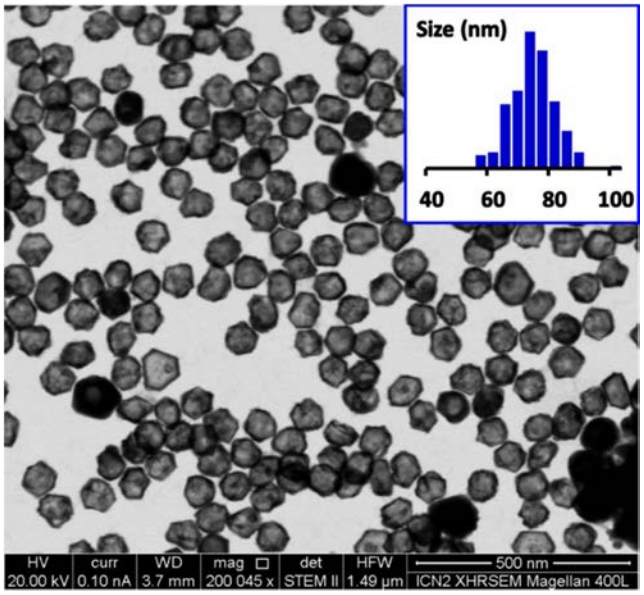

Figure S1 - TEM bright field micrograph of monodisperse hollow AuAg NSs with a mean diameter of 75 nm ± 7 nm.

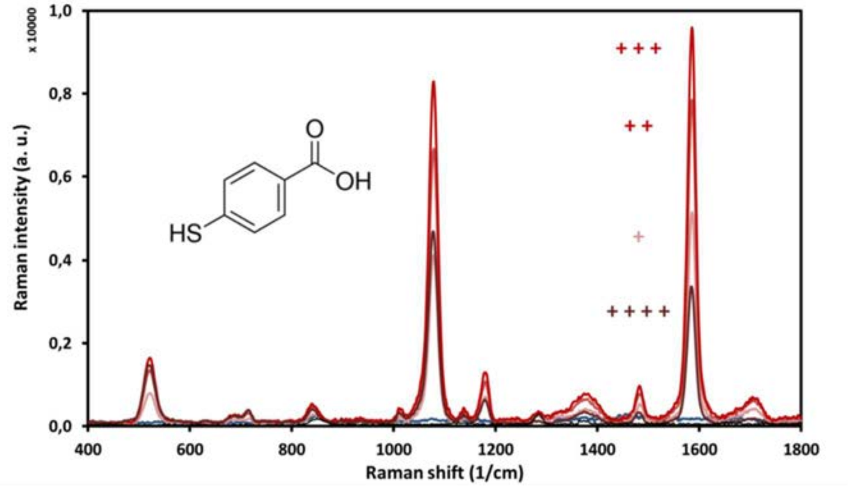

Figure S2 - SERS spectra of 4-MBA-coated AuAg NSs recorded at different concentrations of immobilized Raman reporter (red curves). In absence of either 4-MBA (grey curve) or AuAg NSs (blue curve) no signal is observed.

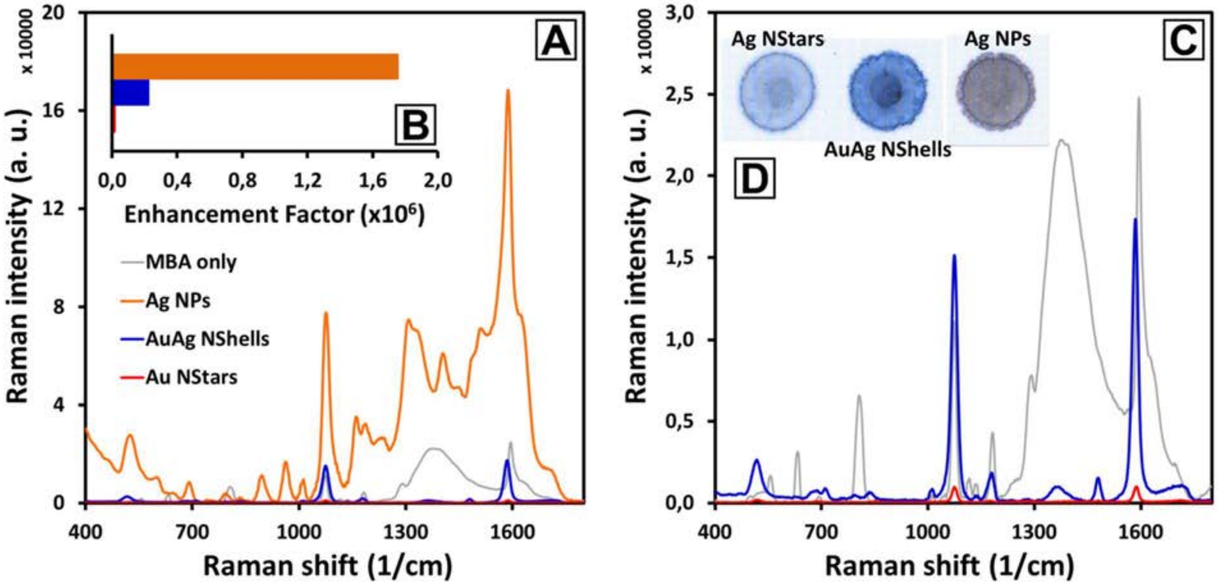

Figure S3 – Comparison SERS signal enhancements between the different reporter-encoded nanotags. **A:** Raman spectral intensities of plain reporter molecules (grey line) were compared to intensities of the Ag NPs (orange), AuAg NShells (blue) and Au NStars (red) under the same measuring conditions (laser excitation at 785 nm, 2 coadditions of 5 sec each). B: Enhancement factor calculated for the three reporter-encoded nanotags using the following equation:

$$\boldsymbol{EF = \frac{I_{SERS}}{I_{Raman}} \times \frac{N_{Raman}}{N_{SERS}} \times \frac{P_{Raman}}{P_{SERS}} \times \frac{t_{Raman}}{t_{SERS}}}$$

where $\boldsymbol{I}$ is the peak intensity, $\boldsymbol{N}$ is the number of contributing reporter molecules, $\boldsymbol{P}$ is the laser power, $\boldsymbol{t}$ is the integration time, and subscripts ***Raman*** and ***SERS*** stand for measurements performed on the reporter molecule or on the nanotag, respectively. **C:** Re-scale of **A** for better comparison of AuAg NShells (blue) and Au NStars (red) SERS enhancement (Raman spectral intensities of plain 4-MBA molecules (grey line) are shown for reference). **D:** Bright field images of the measured area for Ag NPs, AuAg NShells and Au NStars drop-casted onto nitrocellulose.

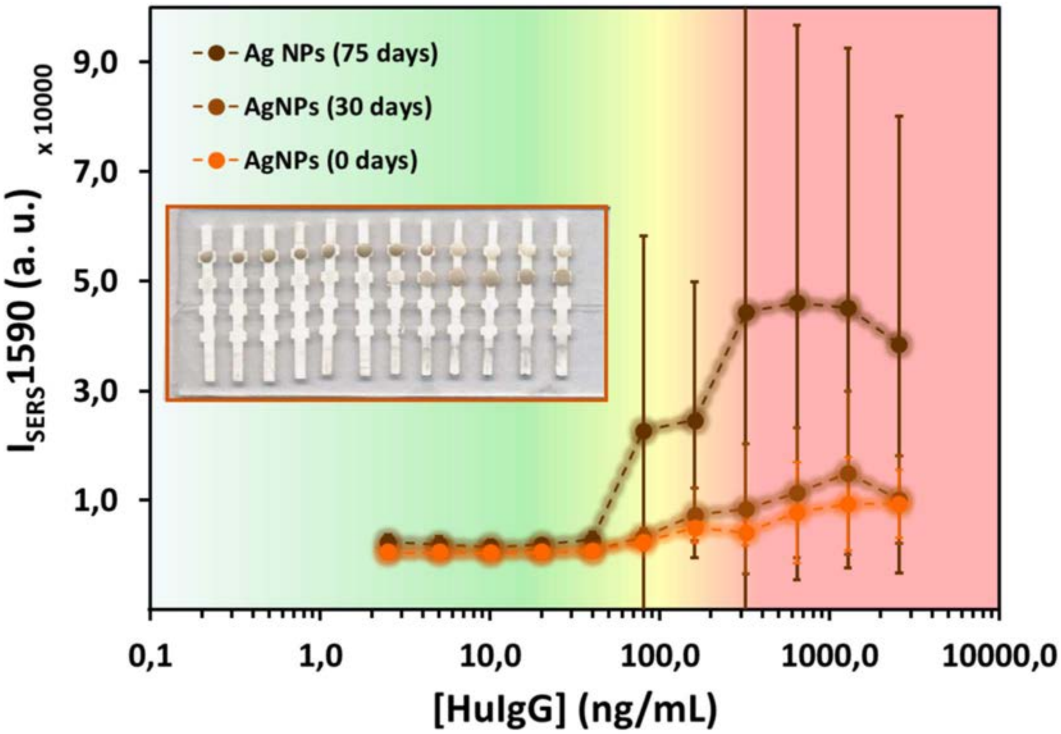

Figure S4 – HuIgG LFA using Ag NPs as labelled SERS nanotag. Ag NPs of ≈ 75 nm coated with 4-MBA (0.04 mM) and functionalized with anti-HuIgG (40 µg/mL) were used in the immunoassay strip against HuIgG (concentrations ranging from 2.5 ng/mL to 2.5 µg/mL). SERS read-out of the test-line was performed inmediatly after the test was run (orange), 30 (light brown) and 75 days (dark brown).

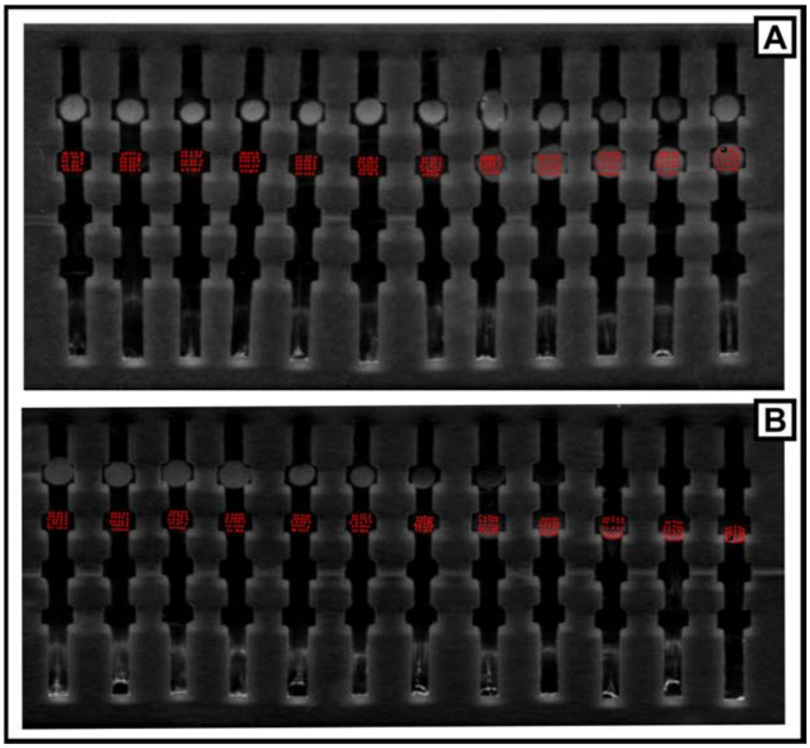

Figure S3 S54 - Dark field image of LFA strips used for the detection of A: HuIgG and B: MxA. The visual detection of the analyte was quantified using the free software "ImageJ" by measuring 25 spots on the Test Line area of each strip (red dots). Each spot was obtained by tracing a circular area with area = 1.

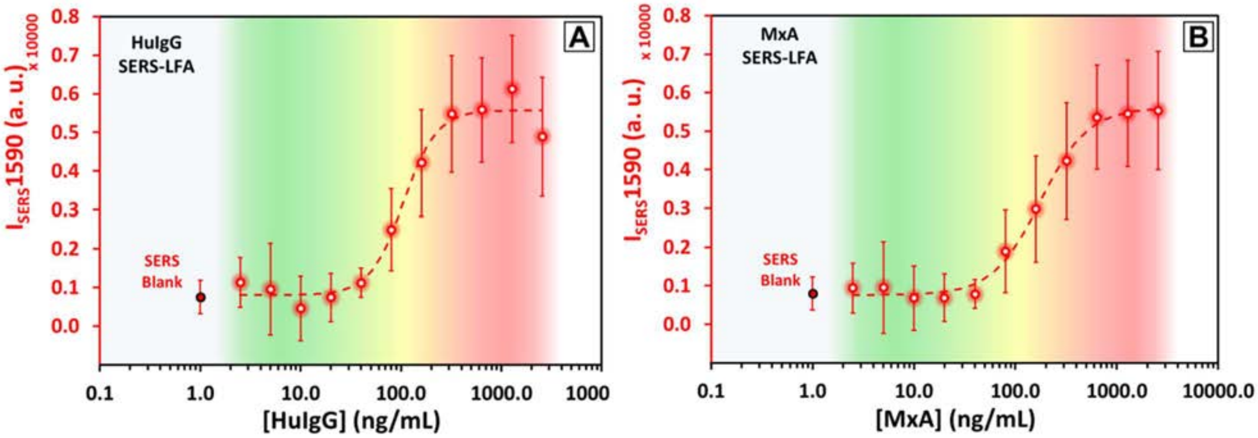

Figure S6: SERS detection of **A:** HuIgG and **B:** MxA with LFA (antigen concentrations ranging from 2.5 ng/ml to 2.5 µg/ml; "Hill" fitting curves (HuIgG: $R^2 = 0.97$, $K_d = 105.4$ nM; calculated LOD = 70.1 ng/ml. MxA: $R^2 = 0.99$, $K_d = 64.2$ nM; calculated LOD = 118.4 ng/ml).

Chapter 4

A low-cost strategy for the development of a rapid electrochemical assay for bacteria detection based on AuAg nanoshells

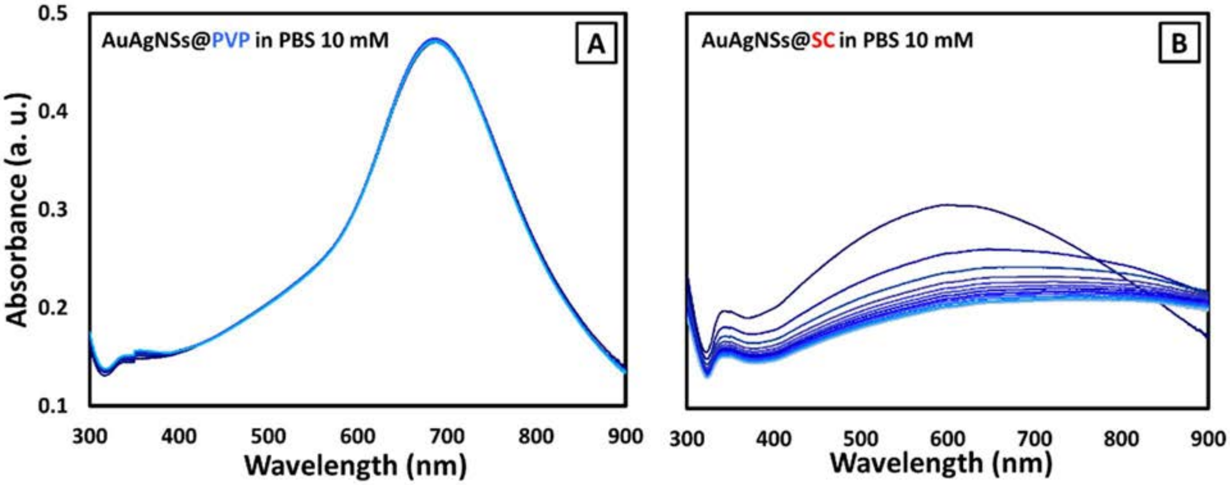

Figure S1. Study of AuAg NSs aggregation in PBS 10 mM (NaCl 137 mM) comparing different capping agents (spectra recorded during time, each curve corresponding to 5 minutes). The presence of PVP adsorbed on AuAg NSs surfaces provides the hollow nanocrystals with high colloidal stability through steric stabilization. As shown in **Figure S1 – A**, when AuAgNSs@PVP are suspended into the relatively high saline phosphate buffer, no significant LSPR band shift is observed, confirming how the charge screening caused by the elevate ionic strength do not affect their colloidal stability. On the contrary, when sodium citrate (SC)-coated AuAgNSs are suspended in the same buffer (**Figure S1 – B**), almost instantaneous aggregation takes place, and a fast quenching of the LSPR band together with a strong *red-shift* is observed.

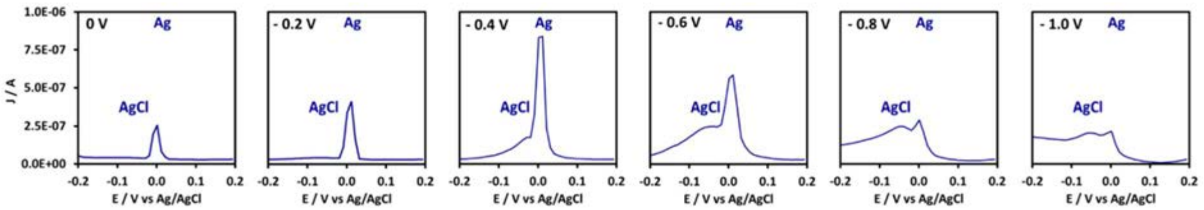

Figure S2. Study of the effect of DPV applied deposition potential on the stability of Ag/AgCl pseudo-reference electrode on SPCEs in PBS 10 mM pH 7.5. In presence of relatively high concentrations of chloride anions in the electrolyte, the stability of the pseudo-reference electrode is strongly influenced by the deposition potential applied. For low reduction potentials (0.0 and -0.2 V vs Ag/AgCl) no apparent effect on the reference peak is observed and only one peak is recorded (≈0.0 V vs Ag/AgCl, corresponding to Ag^+ formation from Ag paste on SPCEs). Increasing the deposition potential causing the appearance of a side peak at slightly lower potentials, probably corresponding to AgCl formation, due to a higher deposition rate of Ag^+ during the deposition step. This peak seems to "drain" oxidation current from the reference one, causing the loss of stability during the measurement.

pH	ζ (mV)	SD
6.5	-24.5	0.31
7.5	-25.9	0.17
8.5	-29.6	0.39

Table S3. Z-potential (ζ) of AuAg NSs measured at different pH. The relatively negative surface charge depends on the ionisable carboxylic groups of sodium citrate found on the particles surface (residue of the synthetic methodology). As expected, at lower pHs the particles possess a slightly higher surface charge due to the higher degree of ionization of the citrate moieties (sodium citrate pKas: pK_1=3.13; pK_2=4.66-4.76; pK_3 = 6.40).

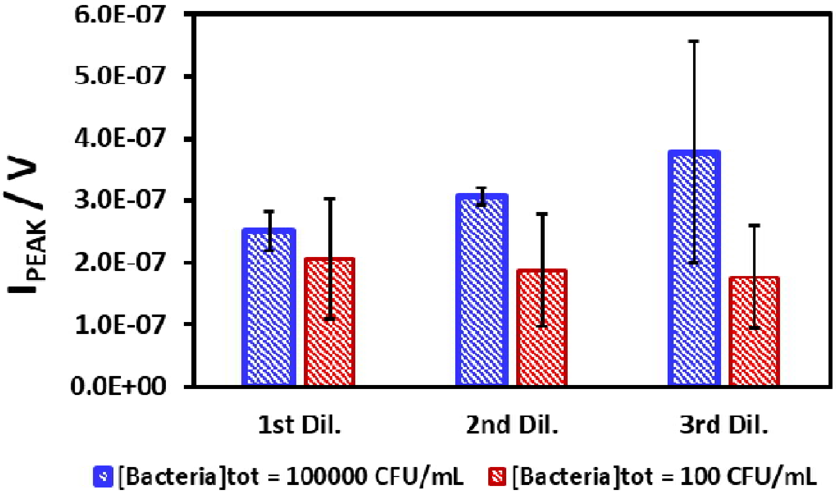

Figure S4 – Discrimination between samples displaying the same current but bearing different bacteria concentrations was demonstrated through a serial dilution experiment. Samples containing 10^2 and 10^6 CFU/mL respectively were chosen since, as shown in **Figure 3 – A**, these two concentrations both correspond to a peak current of c.a 2.3×10^{-7} A. By diluting twice each of these samples of a factor 1:10, and performing the electrochemical assay each dilution step in duplicates, we observed 2 different trends. For the sample containing 10^2 CFU/mL, the average current recorded was slightly decreasing with each dilution, even though the variation was negligible. Instead, when performing the same experiment on a sample containing 10^6 CFU/mL, we observed a clearer increase on the average peak current. These two opposite trends, although still optimizable, follow exactly the tendency described in the manuscript (**Figure 3 – A**). With this extremely simple procedure it is possible to solve the issue of non-univocal current responses.

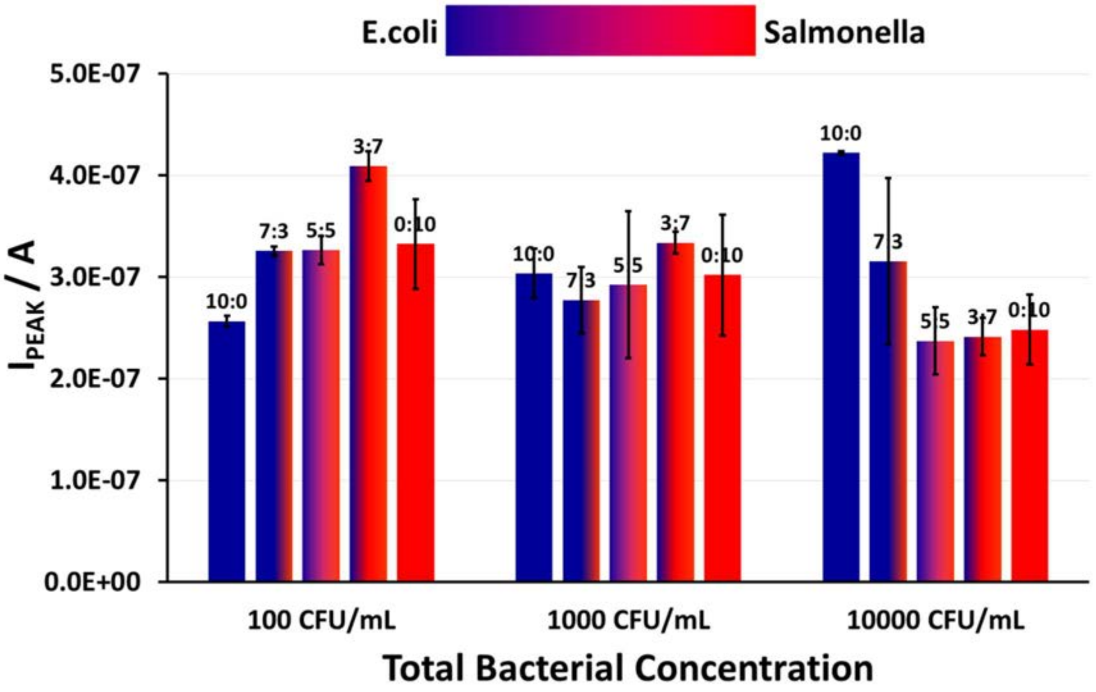

Figure S5 – For testing the capability of this assay to distinguish and quantify different bacterial strains in complex mixtures, a set of duplicate experiments on samples containing both E.coli and Salmonella at 3 different total bacterial concentrations, namely 10^2, 10^3 and 10^4 CFU/mL were run. For each total bacteria concentration, five "E.coli:Salmonella" compositions were tried, namely 10:0. 7:3, 5:5, 3:7 and 0:10, in duplicates. The results, reported in **Figure S5**, show clearly that the assay in its current format is not able to distinguish univocally between different compositions of the two model bacterial strains, as the peak currents recorded do not highlight an evident trend. This is especially true for samples with a total bacteria concentration of 10^3 CFU/mL, being this concentration the one corresponding to $3.0\text{x}10^{-7}$ A for mono-component suspensions of both bacterial strain (**Figure 4 – A**). Nevertheless, it seems that the influence of Salmonella on the current generation mechanism, that is the capture of AuAg NSs in solution through their non-specific adsorption onto bacterial cells, is stronger than the E.coli one. For samples containing 10^4 CFU/mL total bacteria concentration, that is corresponding to the highest signal for E.coli (**Figure 4 – A**), the gradual increase of Salmonella composition "quenches" the signal thanks to its higher affinity for AuAg NSs, therefore bringing the peak current value closer to a "pure"(0:10) Salmonella sample. A similar effect is also observed at the lower total bacteria concentration of 10^2 CFU/mL, which corresponds to the maximum in current intensity for the E.coli calibration curve (**Figure 3 – A** and **Figure 4 – A**). In this case the current recorded for "pure" E.coli (10:0) increases with the increasing Salmonella composition of the sample, again bringing it towards the "pure" Salmonella sample value. This behaviour gives additional clues about the different affinities of bacterial cell walls for AuAg NSs and could be used to further tune the hydrophobicity of the coating polymer towards a better selectivity of the assay.

Annex 3 – List of Abbreviations

Abbreviation	Explanation
4-MBA	4-Mercaptobenzioc Acid
Ab	Antibody
ABTS	2,2'-azino-bis(3-ethylbenzothiazoline-6-sulphonic Acid)
AR	Aspect-Ratio
BEM	Boundary Element Method
BSA	Bovine Serum Albumin
CCM	Cell Culture Media
CD	Circular Dichroism
CFU	Colony-Forming Units
CRP	C-Reactive Protein
CTCs	Cancer Circulating Cells
CV	Cyclic Voltammetry
DLS	Dynamic Light Scattering
DNA	*Desossi Ribonucleic Acids*
DPV	Differential Pulsed Voltammetry
E.coli	*Escherichia coli*
EDS/EDX	Energy-Dispersive X-ray Spectroscopy
EELS	Electron Energy Loss Spectroscopy
ELISA	Enzyme-Linked Immunosorbent Assay
FBS	Fetal Bovine Serum

FDTD	Finite Difference Time Domain
FTO	Fluorine-doped Tin Oxide
GDH	Glucose Dehydrogenase
GOx	Glucose Oxidase
GRR	Galvanic Replacement Reaction
HA	Humic Acid
HAADF	High-Angle Annular Dark Field
HAS	Human Serum Albumin
HER	Hydrogen Evolution Reaction
HRP	Horseradish Peroxidase
HRTEM	High Resolution Transmission Electron Microscopy
HS	Human Serum
IFN	Interferon
IgG	Immuno Globulin G
INPs	Inorganic Nanoparticles
IVD	*In vitro* Diagnostics
LFA	Lateral Flow Assay
LOD	Limit of Detection
LSPR	Localized Surface Plasmon Resonance
MNPs	Metallic Nanoparticles
MxA	Human Myxovirus Resistance Protein A
NCs	Nanocrystals
NIR	Near Infrared
NPs	Nanoparticles

NRs	Nanorods
NS 1	Dengue Non-Structural Protein 1
NSs	Nanoshells
NWs	Nanowires
OTA	Ochratoxin
PB	Phosphate Buffer
PBS	Phosphate Buffer Saline
PC	Protein Corona
PCR	Polymerase Chain Reaction
PoC	Point-of-Care
PSA	Prostate-Specific Antigen
PVP	Polyvinyl Pyrrolidone
QDs	Quantum Dots
QY	Quantum Yield
RHE	Reversible Hydrogen Electrode
ROS	Reactive Oxygen Species
RT	Room Temperature
Salmonella	*Salmonella typhimurium*
SAM	Self-Assembled Monolayer
SC	Sodium Citrate
SEM	Scanning Electron Microscopy
SERS	Surface-Enhanced Raman Spectroscopy
SOD	Super Oxide Dismutase
SPCEs	Screen-Printed Carbon Electrodes

STEM	Scanning Transmission Electron Microscopy
TEM	Transmission Electron Microscopy
TMB	3,3',5,5'-tetramethylbenzidine
TOC	Total Organic Carbon
UCNPs	Up-Converting Nanoparticles
UPD	Under-Potential Deposition
UV	Ultra Violet
VOC	Volatile Organic Compound
WHO	World Health Organization

Annex 4 – Publications

CHEMISTRY OF MATERIALS
Article
Cite This: *Chem. Mater.* 2018, 30, 5098−5107
pubs.acs.org/cm

Time- and Size-Resolved Plasmonic Evolution with nm Resolution of Galvanic Replacement Reaction in AuAg Nanoshells Synthesis

Lorenzo Russo,[†,‡] Florind Merkoçi,[†] Javier Patarroyo,[†,‡] Jordi Piella,[†,‡] Arben Merkoçi,[†,∥] Neus G. Bastús,[†] and Victor Puntes*[,†,§,∥]

[†]Catalan Institute of Nanoscience and Nanotechnology (ICN2), CSIC and BIST, Campus UAB, Bellaterra, 08193 Barcelona, Spain
[‡]Universitat Autònoma de Barcelona (UAB), Campus UAB, 08193, Bellaterra, Barcelona, Spain
[§]Vall d'Hebron Institut de Recerca (VHIR), 08035, Barcelona, Spain
[∥]Institució Catalana de Recerca i Estudis Avançats (ICREA), P. Lluís Companys 23, 08010 Barcelona, Spain

Supporting Information

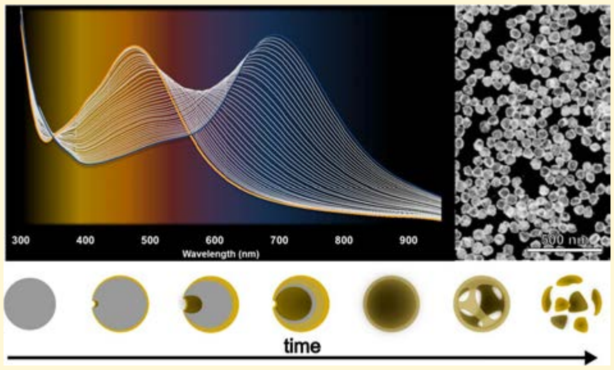

ABSTRACT: The rational design of advanced nanomaterials with enhanced optical properties can be reached only with the profound thermodynamic and kinetic understanding of their synthetic processes. In this work, the synthesis of monodisperse AuAg nanoshells with thin shells and large voids is achieved through the development of a highly reproducible and robust methodology based on the galvanic replacement reaction. This is obtained thanks to the systematic identification of the role played by the different synthetic parameters involved in the process (such as surfactants, co-oxidizers, complexing agents, time, and temperature), providing an unprecedented control over the material's morphological and optical properties. Thus, the time- and size-resolved evolution of AuAg nanoshells surface plasmon resonance band is described for 15, 30, 60, 80, 100, and 150 nm-sized particles spanning almost through the entire visible spectrum. Its analysis reveals a four-phase mechanism coherent with the material's morphological transformation. Simulations based on Mie's theory confirm the observed optical behavior in AuAg nanoshells formation and provide insights into the influence of the Au/Ag ratio on their plasmonic properties. The high degree of morphological control provided by this methodology represents a transferable and scalable strategy for the development of advanced-generation plasmonic nanomaterials.

INTRODUCTION

The emerging physical and chemical properties materials display when down-sized to the nanoscale surpass those of their macroscale counterparts and give them unique behavior, otherwise unreachable with more traditional ones. Achieving the highest degree of control and understanding of the processes employed in their crafting is key for obtaining the best performances and highest added value from the technologies in which they find application, such as highly sensitive (bio)diagnostics and imaging as well as efficient and selective catalysis.[1−6]

In this context, the process of galvanic replacement reaction (GRR) represents an extremely versatile chemical tool for designing and producing high-quality materials with customized features, combining the effect of both chemical conversion and structural transformation to obtain enhanced optical and catalytic properties.[7] GRR is a heterogeneous redox reaction which happens at the solid−liquid interface between a solid metal and a cation of a nobler one in solution. This process, very well-known at the macro- and microscale for its numerous applications in metallurgy and engineering, is used at the nanoscale as a very convenient and flexible synthetic tool for obtaining complex hollow morphologies, which represent a new class of materials with enhanced properties in the fields of catalysis,[8,9] drug delivery,[10] and optics.[11] In a typical reaction, the surface atoms of a colloidal suspension of presynthesized metal nanocrystals (NCs) (typically Ag[12] but also Cu and Co[13]) are used as sacrificial templates and undergo oxidative dissolution caused by the redox reaction with a more noble metal ion in solution (mainly Au and Pt).[14]

Despite all these advantages, few are the examples found in the literature providing reproducible and reliable methods for synthesizing hollow nanomaterials through GRR with highly controlled reproducibility, morphologies, and properties.[12,15−17] The majority of studies provide instead spurious and limited recipes whose lack of reproducibility has been attributed to a poor understanding of the reaction mechanism.[18−21] Given the fundamental importance of correlating

Received: April 11, 2018
Revised: July 10, 2018
Published: July 12, 2018

DOI: 10.1021/acs.chemmater.8b01488

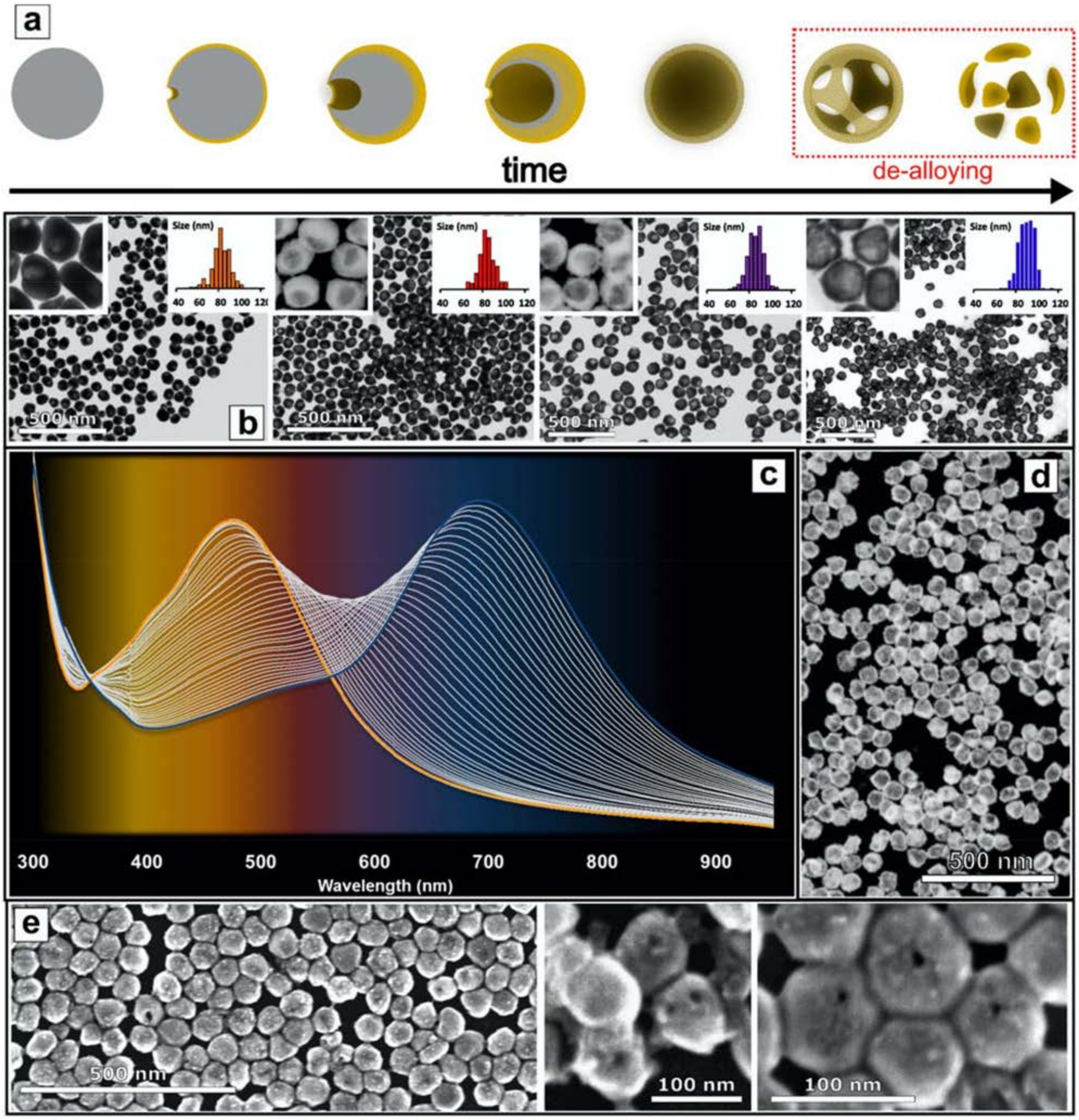

Figure 1. (a) Schematic representation of the structural evolution of AuAg nanostructures during GRR upon addition of $HAuCl_4$. (b) TEM and HAADF-STEM micrographs showing four different phases of GRR (from left to right, images corresponding to the addition of ca 100, 550, 900, and 1500 uL of $HAuCl_4$ 1 mM, corresponding at 10 min, 55 min, 1 h 30 min, and 2 h 30 min of GRR, respectively): the morphological transformation starts with a small cavity which grows together with the thickening of the outer shell, resulting in a hollow structure. This modification affects slightly the monodispersity of the initial templates. (c) Time-resolved absorption spectra evolution of 80 nm-sized solution of Ag NCs titrated with increasing volumes of $HAuCl_4$ (each absorption spectrum corresponding to 25 μL of a 1 mM $HAuCl_4$ aqueous solution upon titration at 10 μL/min): LSPR shifts gradually through the whole visible spectrum toward NIR wavelengths (background color corresponding to the color of the solution). (d) HAADF-STEM micrographs of highly monodisperse 80 nm AuAg NSs. (e) SEM micrographs of PVP-coated AuAg NSs with a clearly visible single pinhole (depending on the orientation).

synthesis recipes and NCs atomic distribution with the strict determination of the material properties, it is crucial to deeply understand the role of each governing parameter of the hollowing process. With this strategy, it is possible to produce a larger palette of materials whose properties are precisely tailored for the specific application for which they are required. In addition, the variation in the optical properties of the material, while often considered merely as a secondary effect of the reaction, has to be considered instead a direct projection of the undergoing modification in its structure and composition.

Thus, in this work, we report the time- and size-resolved plasmonic evolution of the synthesis of AuAg hollow nanoshells (NSs) through GRR at room temperature (RT). We focus our efforts in achieving a precise morphology among all the thermodynamically possible ones,[22] composed by a thin gold shell with homogeneous and smooth surface and a large internal void. These features have been shown to possess the most desirable enhanced optical properties for application in plasmonic sensing thanks to the resonant cavity effect,[11] the possibility to tune their absorption spectra into NIR wavelength in order to take advantage of the biological window,[23] and an improved stability toward corrosion of alloyed Ag given by the "nobleing" effect of gold.[24] This improved and extremely reproducible synthetic process allows the quantitative production of large amounts of monodisperse, high-quality AuAg NSs of different sizes and degrees of conversion of Ag to Au, while working at RT permits the easy monitoring of the process and avoids temperature gradients, adding the possibility to scale up the methodology toward its use in real-world applications.

■ MATERIALS AND METHODS

Silver nitrate ($AgNO_3$), trisodium citrate ($Na_3C_6H_5O_7$), tannic acid ($C_{76}H_{52}O_{46}$), $HAuCl_4 \cdot 3H_2O$ (99%), and polyvinylpyrrolidone (PVP) $(C_6H_9NO)_n$ Mw ≈ 55 000 were purchased from Sigma-Aldrich. All chemicals were used as received without further purification. Distilled water passed through a Millipore system ($\rho = 18.2$ MΩ) was used in all experiments. All glassware was first rinsed with acetone and then with Millipore water before use. Ag NCs of the desired size used as sacrificial templates for GRR were synthesized following a method developed by our group.[25] 10 mL of the prepared colloidal solution was centrifuged (8000−12000 rcf depending on particle size), the supernatant removed and the pellet resuspended with 10 mL of a 5 mM (repeating unit) aqueous solution of PVP. The templates were then left conjugating with the polymer for about 1 h. A syringe pump (Pump 11 Elite; Harvard Apparatus, U.S.A.) equipped with a plastic syringe (BD plastic, 5 mL) and a microfluidic silicon tube of 500 μm ending with a 0.1−10 μL plastic pipet tip was used to dose a $HAuCl_4$ 1 mM aqueous solution freshly prepared (10 μL/min). The approximate inner orifice diameter of the plastic pipet tip is 0.31 mm which corresponds to a needle of 24G. A 50 mL glass beaker containing Milli-Q water (10 mL), PVP 5 mM aqueous solution (20 mL) and 10 mL of the previously conjugated templates was prepared under vigorous stirring. The stirring rate was kept high enough (400/600 rpm) to ensure the homogeneity of the solution during the reaction, particularly to avoid mass gradients that often lead to the lack of control of the final NCs. Once homogenized, HCl 10 mM (10 mL) was added at once and let reacting with the mixture for 60 s. Immediately after, the syringe pump injection was started and the reaction covered with *parafilm* in order to avoid volume variations due to evaporation. When aliquots were collected to perform UV−vis spectra, the injection was stopped, the sample measured quickly without any purification and readded to the reaction mixture. Once the desired degree of conversion was reached, the reaction mixture was divided into 10 mL aliquots and transferred into 50 mL Falcon tubes, diluted with 10 mL Milli-Q water each and then centrifuged at 8000 rcf for 10 min. The supernatant was removed and the pellet resuspended in Milli-Q water (20 mL each aliquot), then sonicated for 5−10 min. This washing step was repeated for a total of 3 times and the last resuspension in Milli-Q water was performed into a total final volume of 10 mL, so to obtain the original particles concentration. All samples were characterized by UV−vis spectroscopy (PerkinElmer "Lambda25"), Dynamic Light Scattering (DLS) Malvern Zetasizer, Transmission Electron Microscopy (TEM) and Scanning Electron Microscopy (SEM) with FEI Magellan XHR SEM, in transmission mode operated at 20 kV. HRTEM and HAADF-STEM micrographs and elemental distribution analysis by EDS line scan were obtained using a FEI Tecnai F20 field-emission gun microscope with a 0.19 nm point-to-point resolution operated at 200 keV. Localized Surface Plasmon Resonance (LSPR) extinction spectra of void/shell/shell NCs was modeled using the online platform "Extinction, Scattering and Absorption efficiencies of single and multilayer nanoparticles" based on the standard Mie theory.[26] Series of void/shell/shell NCs of varied core sizes, shell thicknesses and compositions, embedded in water at 25 °C were modeled. In all cases, the mean size measured by TEM was used for the calculations. Input parameters chosen were: the original Ag template's size, the core (void) diameter, and the shell thickness. As a result, the extinction (Q_{ext}) efficiency was obtained and plotted using Origin software.

■ RESULTS AND DISCUSSION

The synthesis of AuAg NSs through GRR consists in mixing a solution of silver NCs in a variety of conditions with a solution of a gold salt in a controlled reacting medium: thanks to the difference in reduction potentials between the two noble metals (standard reduction potentials of Ag^+ and Au^{III} are 0.7996 and 1.498 V, respectively[27,28]), Au^{III} cations oxidize Ag atoms from the bulk of the particle and get reduced at the particle surface, resulting in a hollow shell of a varying degree of AuAg alloy. Initially, the reduction of Au causes the passivation of the Ag templates surface through the formation of a thin metallic shell, forcing the oxidation of the bulk NC atoms to take place through a pinhole, kept unclogged thanks to the continuous cations outflow from its interior (Figure 1a).[14] This process establishes a galvanic pair where, as the deposited metal protects the template, the surface ratio between the galvanic electrodes increases, directing the flow of electrons through the NC body and favoring the interdiffusion and alloying of the two metals at their interface.[29] Figure 1b shows the morphological evolution of nearly monodispersed 80 nm-sized quasi-spherical Ag NCs upon titration with $HAuCl_4$ (thorough templates characterization is reported in Figure S1). We use spheres instead of the commonly used nanocubes to avoid surface atomic heterogeneity (flat surface, edges, and corners), which improved homogeneity and reproducibility. At short reaction times, a tiny cavity appears in the body of the Ag templates at the initial stages of GRR, caused by Ag oxidation and dissolution, which grows progressively as Au deposition proceeds. This chemical and structural transformation, which occurs without significant loss in monodispersity, as shown by histograms, ends up in the formation of a hollow structure enclosed by a metal alloy outer shell (Figure 1d), which can further evolve into a porous one with the dealloying of its less noble component.[7] Conversely, the pinhole ends up closed when oxidizers are the limiting reagents in the reaction, as it is clearly visible from SEM micrographs of final GRR stages (Figure 1e), where only a few hollow NCs still display a hole in their surfaces. Following the change in morphology, a radical transformation in the material's optical properties takes place, visibly indicated by clear color changes as the localized surface plasmon resonance (LSPR) band shifts through the whole visible spectrum (Figure 1c, *spectra not shown for the late dealloying phase*). In order to study the time-dependent evolution of Ag NCs into hollow AuAg NSs by stopping the reaction at different times, different precursor amounts were carefully dosed using a syringe pump.

After the addition of 100−150 μL of the $HAuCl_4$ aqueous solution, the typical dipole plasmon resonance mode of 80 nm Ag templates ($\lambda_{MAX} \approx 450$ nm) starts decreasing in absorbance intensity together with a slow but constant red-shift, indicating the progressive Ag plasmon suppression operated by the deposited Au thin shell. This trend continues throughout the wavelengths range typical of AuAg alloy NCs,[24,30] until reaching an absorbance minimum ($\lambda_{MAX} \approx 570$ nm). Then, as the process advances, a larger red-shift is accompanied by a steep increase in absorbance intensity: a plasmonic enhancement typical of hollow nanostructures caused by plasmon

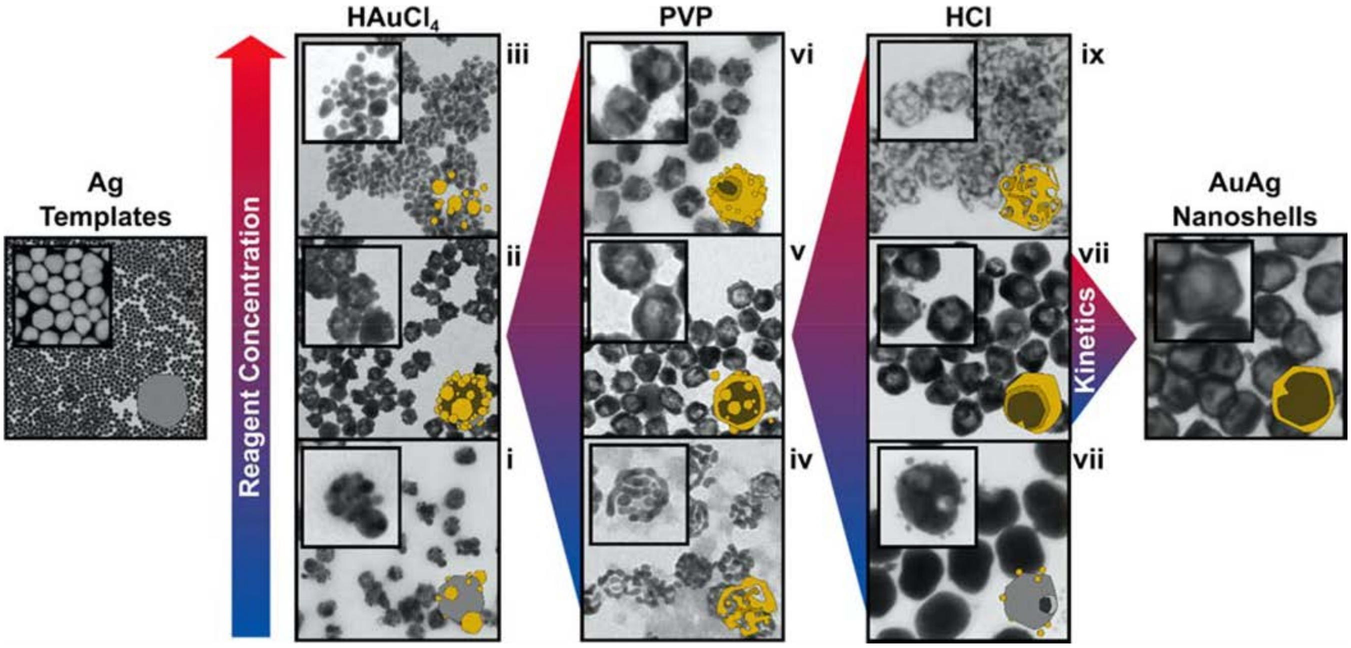

Figure 2. Rational synthetic design of the hollow AuAg NSs morphology starting from nearly monodisperse 80 nm-sized Ag NCs (TEM micrographs recorded at different magnifications). The effect of each coreagent (HAuCl$_4$, PVP, and HCl) is explored and balanced in order to define the optimal synthetic strategy. Once the best synthetic conditions are found, a further kinetic optimization allows focusing the synthetic control on the precise and unique morphology (i.e., thin, smooth shells, and large voids).

"hybridization",[31] in which the presence of cavities allows the dipole plasmon mode to extend up to the beginning of the near-infrared (NIR) range ($\lambda_{MAX} \approx 700$ nm).[11] During this process, the entire added gold precursor was converted into gold hollow NCs.

Since GRR can also be described as a progressive corrosion of the silver scaffold, which will be sacrificed as a source of electrons for the Au deposition, the two half-reactions can be to some extent independently controlled by introducing surfactants, coetchers, halides, and species able to modify the reactivity of the template surfaces and the intermediates stability.[18] In order to control the production of high-quality AuAg NSs, the systematic identification of the role played by the different synthetic parameters involved in the process (such as template polydispersity, surfactants, co-oxidizers, complexing agents, time, and temperature) has to be investigated.

The key feature for obtaining this smooth evolution of AuAg NSs optical properties relies, among others, on the use of highly monodisperse quasi-spherical Ag NCs, obtained following a recently developed synthetic methodology (Figure S1),[25] as colloidal scaffolds onto which gold will be deposited and from which the resulting material will inherit its shape. Otherwise, templates of different sizes, that is with a dissimilar chemical potential, will introduce polydispersity in the hollowing process.[32] Additionally, due to the high difference in reduction potentials of the Au^{III}−Ag^0 redox couple, the process often results extremely fast, meaning that surface nucleation and growth of the Au shell are limited only by thermodynamics, allowing only a poor control over morphology. Thus, the passivation of the Ag NCs surface plays a critical role in controlling the kinetics of the heterogeneous redox process. Furthermore, the molar ratio of Au^{III} precursor with respect to Ag^0 content in the templates solution (Au/Ag ratio from now on) is known to affect strongly the final morphology of the material.[27] As shown in Figure 2i, the initial nucleation of small Au domains in correspondence of the template's surface defects is observed when low concentrations of HAuCl$_4$ are used, not providing the system with enough material to build a complete and stable gold shell; an excess of metal precursor instead leads first to the depletion of the bulk silver reservoir in the particle core, then triggering an energetically less convenient dealloying process (the selective removal of the less noble metal from a binary alloy), and in the end to the formation of a porous frame or to the complete breakdown of the nanostructure into smaller (<5 nm) Au NCs (Figure 2iii). Unfortunately, Au/Ag ratio sole adjustment does not provide the desired control on shell thickness, void size, and surface porosity of the AuAg NSs. Indeed, irregular, half broken structures presenting granular and rough surfaces are obtained even when the Au/Ag ratio seems to be the optimal one (Figure 2ii).

Thus, carrying out the reaction in the presence of a high concentration of polyvinylpyrrolidone (PVP) protects the Ag templates surface, lowering the reaction rate, while at the same time forming a complex with Au^{III}, decreasing its reactivity and reducing it to Au^{I} (as control experiments did show[29]), whose deposition has been shown to produce smoother and more uniform surface morphologies.[33,18,20] Thus, gradually augmenting the amount of PVP leads to an increasingly recognizable hollow morphology with more integral shells (Figure 2iv,v,vi), while in its absence a loss in monodispersity with broader ranges of void sizes and shell thicknesses is observed, which in turn leads to a flat absorbance spectrum of a black colored particles solution (Figure S2). Besides, the introduction of coetchers such as HCl increases the oxidizing character of the reaction media, making protons compete with Au^{III} for the oxidative etching of silver atoms from the core of the particle and therefore participate in determining the extent of wavelength shift for equivalent Au/Ag ratios (Figure 2vii,vii,ix; Figure S3).

DOI: 10.1021/acs.chemmater.8b01488
Chem. Mater. 2018, 30, 5098−5107

Remarkably, the addition of protons to the system appears to be crucial for speeding up the GRR: TEM micrographs of morphologies resulting from GRR without HCl show that in these conditions the process initiation appears greatly delayed (1−2 h of reaction compared to few minutes), since only untouched or slightly "bitten" templates by "soft-etching" of the surface low coordination atoms are observed (Figure S4). The plasmonic band does not change significantly either, apart from a relatively small quenching of the plasmon intensity due to some minor gold deposition on the surface of the template. Interestingly, chlorides well-known affinity for Ag atoms[34] seems to lower templates surface energy by removing some degree of passivation due to the presence of a native Ag_2O layer, favoring Au epitaxial deposition.[12] Indeed, when GRR was carried out with HNO_3 instead of HCl (Figure S5), that is, in the presence of protons but the absence of halides, small gold domains where observed on the surface of the hollow structure, indicating a poorer surface homogeneity.[15,18] Finally, the precise, diffusion-controlled dosage obtained using a syringe-pump helps slowing down Au^{III} deposition rate, allowing a better NC surface reorganization through interdiffusion and alloying of the two metals (whose typical diffusion rates at the nanoscale are about 10^{-11} cm^2 s^{-1}),[35] kinetically favoring its heteronucleation onto Ag surface[22] without compromising the thin shell stability. Thus, through the concerted interplay of all the synthetic parameters, it is possible to selectively reach the desired particles morphology of a thin gold shell with homogeneous and smooth surfaces and large internal voids.

The time-dependent evolution of GRR can be precisely followed by monitoring the optical properties of the system. The evolution of both LSPR maximum wavelength and intensity of a solution of 80 nm-sized Ag NCs was analyzed upon titration with 1 mM $HAuCl_4$ at a constant flux of 10 μL/min (Figure 3b). Remarkably, the process is highly reproducible as shown in Figure S6, where the evolution of the LSPR position after the addition of controlled volumes of $HAuCl_4$ is plotted for three independent syntheses.

The study of the kinetics of AuAg NSs structural and chemical conversion through GRR, associated with the elemental distribution analysis and EDS line scan (Figure 4a,b,c), led to the proposal of a general GRR mechanism divided into four phases, corresponding to the four different plasmonic regimes observed. In the first GRR phase, Au^{III} reaches the particle's surface, is reduced by reacting with Ag surface atoms, and it is then deposited on the nearby surface while the oxidized silver ions are transferred into solution (eventually precipitating as insoluble AgCl and resuspended by PVP[14]) (Figure 4a, phase I). At this early GRR stage, almost no red-shift of the LSPR band is observed (Figure 3b, phase I), which may indicate the amount of Au deposited does not have a detectable impact in the optical properties of the Ag templates. This induction time could correspond to the critical size needed by the vacancies created with the pitting corrosion to coalesce and form the pinhole, together with the formation of a continuous Au shell. Interestingly, TEM and SEM micrographs show that AuAg NSs present always a single pinhole (Figure 1d), even though pitting corrosion should start at the multiple asperities and defects at the NCs surfaces.

It is important to note that in the many examples reported in the literature of GRR with silver cubes,[12,15,27,36] the initial Au^{III} pitting corrosion is directed only to particular facets {110} and {100} as well as highly reactive corners or edges because of differences in their surface energies. Thus, the final morphology of hollow nanocages with multiple cavities results from the initial distribution of etching locations. It appears then that for spherical templates though, the multiple surface vacancies created through heterogeneous electron transfers between surface Ag atoms and molecular Au^{III} ions in solution rapidly coalesce through surface reorganization, reaching a critical size (or better, critical internal surface) able to act as the anode for the half redox reaction of oxidation; synergistically, the gold domains deposited will eventually join and achieve a sufficient extension to stand the other half of the redox reaction and become the cathode (Figure 4a, phase I). The conductive nature of the core of the particle, characterized by a lower resistance compared to the electrolyte, becomes, therefore, a more convenient channel for the flux of electrons generated at the anode to move freely to the cathode.[7]

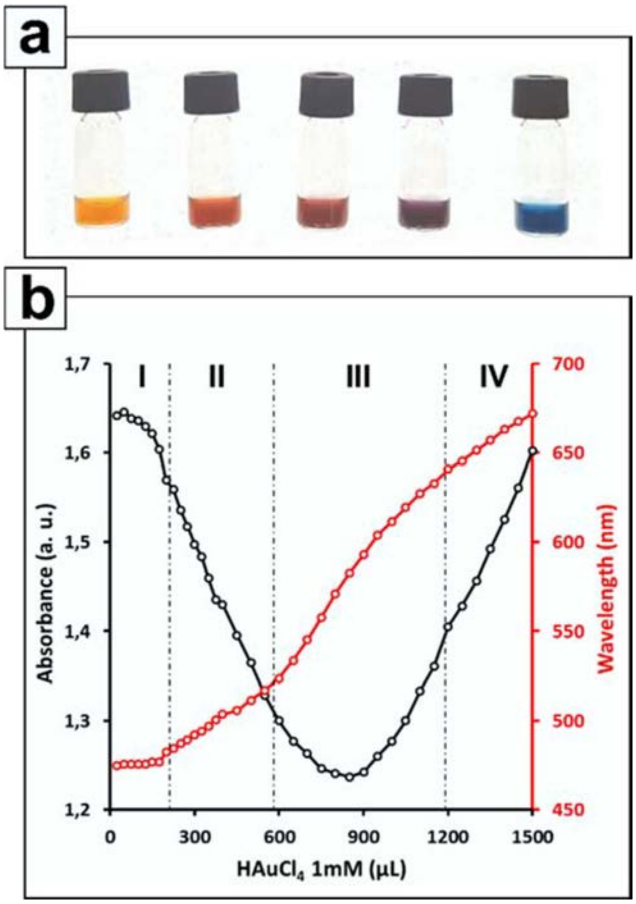

Figure 3. (a) AuAg NSs solution color change during GRR. (b) Maximum LSPR wavelength (red) and intensity (black) vary with increasing amount of Au^{III} added (at a constant flux): four rates of variation in both features are observed in all GRR, accompanying the color transformation (above).

While this kinetic barrier, described also by Smith et al.,[37] is easily overcome in the presence of HCl, GRR ignition significantly slows down without the catalysis of a small excess of protons, which enhance the templates' initial pit corrosion and favors a faster pinhole formation (Figure S4). With the completion of a thin Au shell and the formation of a single pinhole begins the second GRR phase (Figure 3b, phase II), dominated by a red-shift restricted between 400 and 520 nm, typical of Au−Ag alloy NCs.[24,30] At the same time, the two noble metals initiate their alloying by interdiffusing at their

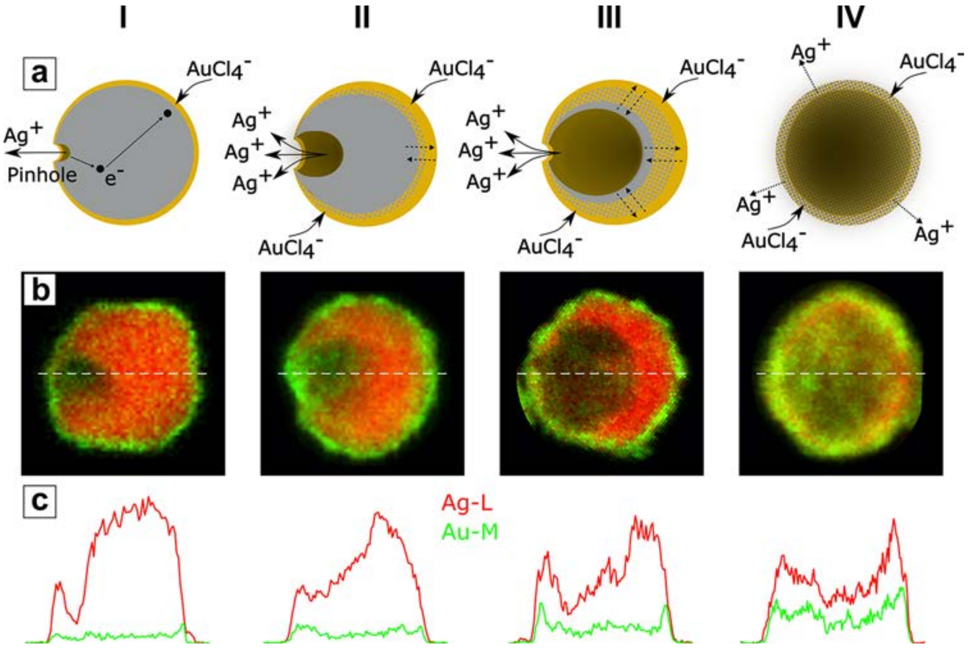

Figure 4. (a) GRR mechanism hypothesis with four phases, modeled correspondingly to the four different plasmonic regimes observed; (b,c) HAADF-STEM elemental distribution micrographs and EDS line scan elemental analysis of individual AuAg NSs corresponding to each GRR phase, confirming the proposed mechanism.

interface, thermodynamically driven by their bonding stabilization (Au–Au (226 kJmol^{-1}) vs Au–Ag (229 kJmol^{-1})).[27] The gradual LSPR wavelength increase accompanied by a steep decrease in absorbance, which suggests a probable overlap in time and stoichiometry of gold deposition and alloy formation, marks a radical change compared to the previous phase. This transformation can be readily followed both with the increasing Au/Ag ratio (reported in Table 1), showing good agreement between calculated and experimental data) as well as the rapidly evolving elemental profile displayed in the EDS line scan (Figure 4c). The third GRR phase is characterized by a minimum in absorbance followed by a steepening in the LSPR wavelength red-shift and an increase of the absorbance intensity (Figure 3b, phase III). This new plasmonic regime is determined not only by an enrichment in Au composition, provided with its continued deposition on the surface but also by the appearance of a plasmonic void as the Ag core is emptied. The growth of the alloy interface causes the Ag outward migration and the accumulation of vacancies in the core, which eventually coalesce and add up to the internal void.[27,38] The impact of the void on the optical properties of the system, well-described by El-Sayed et al.,[39] starts with the absorbance minimum and is translated into the attenuation of the NCs scattering contribution. When the AuAg NSs aspect-ratio reaches certain threshold values (Table 1) the contribution of the void starts to be dominant which results into a further red-shift of the SPR position toward the NIR region characteristic of thin NSs.[40] Finally, in the last proposed GRR phase the further LSPR band red-shift at NIR wavelengths and the absorbance increase corresponding to the construction of a smooth and thin AuAg shell and a large internal void (Figure 4a,b, phase IV). At this point, the continuation of the reaction would cause the nearly complete depletion of the core Ag, forcing its migration toward the outer shell and its oxidative dealloying forming porous structures.[24,28] Indeed, in order to balance the solidity loss of the Au-rich scaffold with the lattice tension and surface curvature, the hollow morphology undergoes a structural reorganization that opens large pores through the AuAg shell (Figure 2iv,ix), a commonly observed behavior also in nanoporous gold.[41]

Table 1. Evolution of Morphological Parameters and Experimental (EDS) Au/Ag Ratios during GRR

phase (80 nm)	Au/Ag $_{\text{EDS}}$ (%)	void size (nm)	shell thickness (nm)	aspect ratio (nm)
I	1.01 ± 0.08	23.0 ± 6.1	20.8 ± 4.1	**1.0** ± 0.4
II	3.38 ± 0.16	31.5 ± 6.0	16.4 ± 3.3	**0.5** ± 0.2
III	5.89 ± 0.35	39.9 ± 5.8	14.5 ± 2.8	**0.4** ± 0.1
IV	5.61 ± 0.31	63.8 ± 7.5	12.4 ± 2.6	**0.2** ± 0.1

We extended the analysis of the time-dependent plasmonic evolution of GRR onto Ag templates solutions of different sizes (namely: 15, 30, 60, 80, 100, 150 nm, Figure 5a), Figure S7). To the extent of our knowledge, a systematic study of the effect of Ag templates size in GRR has not been reported in the literature yet, probably due to the intrinsic difficulty in preparing highly monodisperse Ag NCs with controlled size.[25] By following the dipole plasmon resonance mode of all sizes, it appears clear that an analogous trend is followed both by the LSPR maximum wavelength and intensity, as shown in Figure 5a and Figure S7.

For GRR carried out onto templates of 60, 80, 100, and 150 nm, the presence of an initial induction time is clearly evidenced (for smaller templates (15, 30, and 60 nm) this stage is too fast to be observed spectroscopically). Later during the process, an intensity minimum is reached, followed by a gradual and constant increase caused by the cavity effect, a common feature for AuAg NSs of 60, 80, 100, and 150 nm which appears to be related to a common aspect ratio (Table 2).[32] In addition to the dipole mode, particles larger than 60 nm exhibited quadrupole plasmon resonance modes. The quadrupole and dipole peaks both shifted to longer wave-

DOI: 10.1021/acs.chemmater.8b01488
Chem. Mater. 2018, 30, 5098–5107

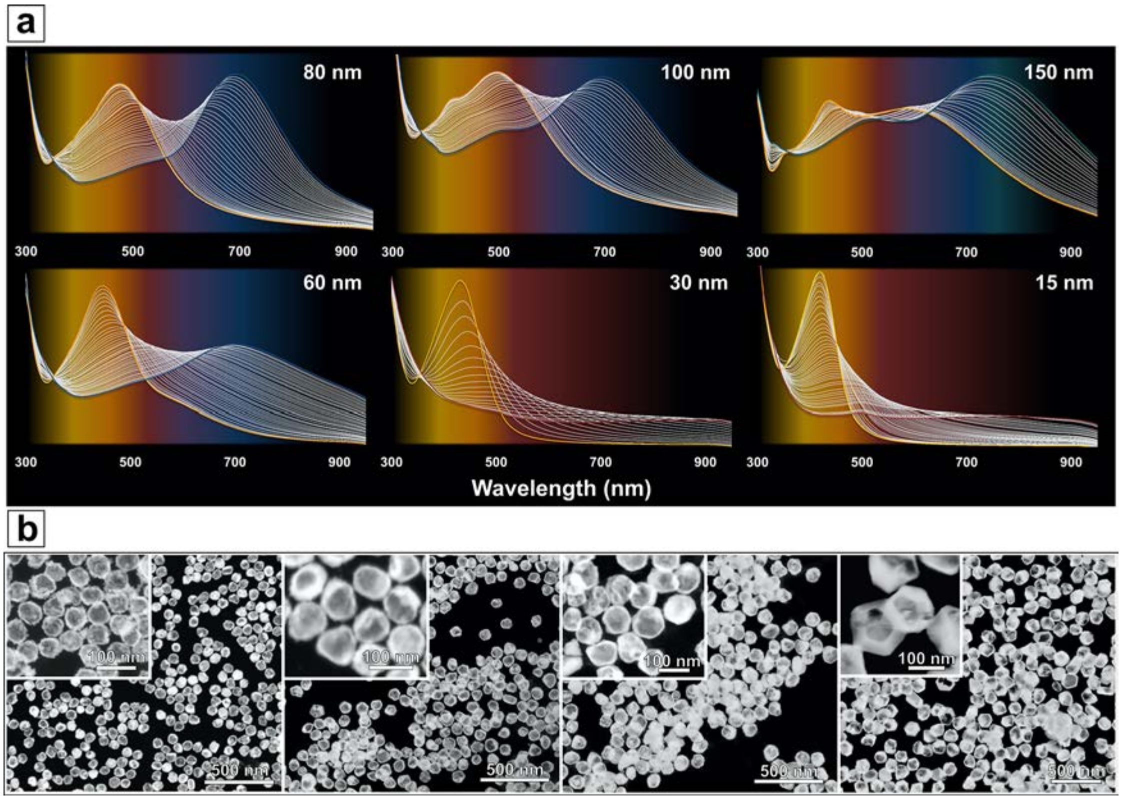

Figure 5. (a) Time-resolved absorption spectra evolution of Ag templates solutions of different sizes titrated with increasing volumes of $HAuCl_4$ (each absorption spectrum corresponding to 25 μL of a 1 mM $HAuCl_4$ aqueous solution upon titration at 10 μL/min). Starting from ca. 60 nm, the Au−Ag stoichiometry allows to obtain the hollow morphology and to reach NIR wavelengths. (b) HAADF-STEM micrographs of AuAg NSs with thin shells and large voids (aspect ratio ≈0.2) of different diameters: from the left, 60, 80, 100, 150 nm.

Table 2. AuAg NSs Plasmonic Properties Are Strongly Influenced by Experimental Au/Ag Ratios (from EDS Mapping), Void Size and Shell Thickness[a]

size (nm)	concentration (NCs/mL)	Au/Ag $_{EDX}$ (%)	void size (nm)	shell thickness (nm)	aspect ratio (nm)
60	2.5×10^{11}	22.91 ± 0.20	41.6 ± 5.4	9.1 ± 1.6	**0.1** ± 0.0
80	1.0×10^{11}	18.96 ± 0.20	63.8 ± 7.5	12.4 ± 2.6	**0.2** ± 0.1
100	5.2×10^{10}	14.14 ± 0.13	68.2 ± 9.3	16.1 ± 5.2	**0.2** ± 0.1
150	2.1×10^{10}	10.13 ± 0.12	98.9 ± 16.5	24.1 ± 8.8	**0.3** ± 0.1

[a] Aspect ratio calculated as $(D - d)/d$, with D the outer and d the inner diameter, respectively.

lengths with increased Au content in AuAg NSs. Experimental (from EDS) Au/Ag ratios, void size, and shell thickness distributions and aspect ratio (calculated as $(D - d)/d$), reported in Table 2 for four different sizes, show how the elemental composition and morphology are the two main parameters governing the evolution of AuAg NSs plasmonic properties, and that a crucial feature needed for reaching absorption in NIR wavelength seems to be a precise aspect-ratio.

When using smaller templates (15, 30 nm), keeping constant the $(Au^{III} + H^{+})/Ag$ ratio used for bigger ones does not apparently allow observing either the formation of the hollow morphology or an analogous plasmonic progression toward NIR wavelengths. Rather, Figure 5a and Figure S6 show that in these cases the LSPR shift stops in correspondence with the typical Au NCs peak (ca. 500 nm), indicating the complete templates corrosion and conversion into Au NCs. The higher surface atoms mobility as well as lower atomic coordination at the surface of small NCs, given by their increased curvature, impede the formation of a stable homogeneous shell and favor the segregation of gold atoms into discrete domains. This behavior, together with the limited silver content, leads to the collapse of the forming structure and the conversion of the shell into a porous, ligamented Au-rich structure and, eventually, its fragmentation into small Au NCs, and it establishes a minimum size for hollow NCs. In the attempt to lower this limit, we also compared the use of $HAuCl_4$ as a gold precursor with a reduced Au^{I} salt in the GRR of 30 nm-sized Ag templates (Figure S7) in order to highlight the stoichiometric limit imposed by the amount of Ag atoms in small templates, modifying an existing protocol described elsewhere.[16,38] Only in the latter case is the hollow morphology achieved, conferring a pale blue color to the solution, while in the former the structure inevitably collapses into small Au NCs agglomerates. These are, to the extent of our knowledge, among the smallest ever reported AuAg NSs.[43]

When bigger particles are used instead, a higher amount of Au can be deposited thanks to the more relaxed crystal and a larger silver reservoir, and more robust shells with a higher degree of alloy are obtained (Figure 5b). Indeed, the surface morphology comparison of AuAg NSs obtained using templates of bigger sizes present a gradual increase in smoothness and disappearance of pores/fractures. In these cases (60, 80, 100, and 150 nm), the dipole plasmon peak follows the stoichiometric-dependent evolution described before, confirming the undergoing morphological and chemical transformation (Figure S6).

In order to confirm the experimental observations, we carried out theoretical calculations based on the standard Mie theory of spherical particles.[42] The model system used in our calculations is based on a core/shell/shell structure. Morphological parameters that describe our system are the diameter of the original Ag template used, the core (void) size and the thickness of the shell layer (Figure 6b, Figure S9).

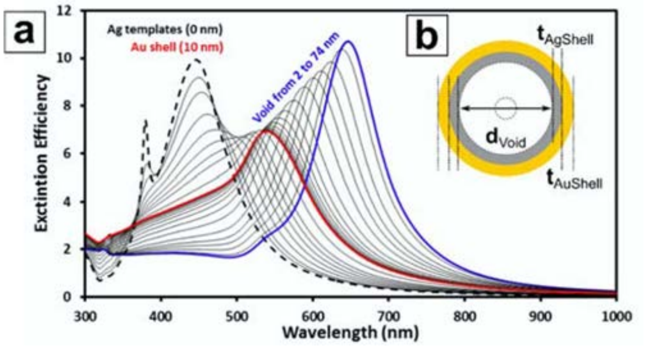

Figure 6. (a) Calculated extinction efficiency for 80 nm Ag spheres surrounded by a 10 nm-thick Au shell enclosing a void of growing diameter. (b) Scheme of the morphological parameters used to model the LSPR response of hollow AuAg systems (void/shell/shell configuration), including core-void- diameter (d_{Void}), Ag shell thickness ($t_{AgShell}$), Au shell thickness ($t_{AuShell}$). The NCs are dispersed in an aqueous medium and coated with a ligand shell that was not accounted for in the models.

For each NC system, the outer and inner diameters were measured from TEM micrographs obtained from the sample shown in Figure 1c, and the measured values were used for the calculations. Figure 6a represents the calculated spectra evolution for 80 nm AuAg NSs composed by an inner H_2O sphere of varying diameter surrounded by two shells: one of Ag, which corresponds to the original Ag template not dissolved, and one 10 nm-thick of Au, corresponding to the deposited outer shell. In general, although there is a slight mismatch in the peak positions, a good agreement with the experimental observation is obtained, allowing to estimate the dimensions of the Au shell deposited and therefore to develop a computational tool for precisely define the morphological architecture of plasmonic nanomaterials with tailored optical properties.

■ CONCLUSIONS

We report herein a robust, highly reproducible and quantitative synthetic method for the high yield production of monodisperse AuAg NSs at RT with extended control over surface morphology, wall thickness, void size, and elemental composition. The process described allows to finely modulate the optical and structural properties of the material almost at will, enabling its employment in a variety of real-world applications. This unique optical tunability, resulting from the synergy between both the change in the outer shell chemical composition and the formation of the hollow architecture, is achieved through the reasoned and dosed use of halide coetchers and complexing surfactants, which can change drastically not only stoichiometry but also both the precursor surface chemical potential and the diffusion of dissolved species toward it. We also propose a detailed mechanism for the GRR of silver quasi-spherical templates and $HAuCl_4$ composed of four phases as an attempt to better describe this versatile synthetic strategy and increase the resolution of its underlying mechanism, richly corroborated by computational simulations displaying extremely good correspondence with experimental data. Remarkably, this process can be easily scaled up to thanks to the absence of temperature gradients (RT synthesis) and the slow precursor addition that avoids complicated mass gradients, both conditions necessary for an easy scale-up of the reaction.

■ ASSOCIATED CONTENT

Ⓢ Supporting Information

The Supporting Information is available free of charge on the ACS Publications website at DOI: 10.1021/acs.chemmater.8b01488.

> Characterization of Ag templates, study of the effect of coetchers and surfactants on morphology, study of reproducibility, simulations (PDF)

■ AUTHOR INFORMATION

Corresponding Author

*E-mail: victor.puntes@icn2.cat.

ORCID

Lorenzo Russo: 0000-0001-7215-6600
Javier Patarroyo: 0000-0002-3703-666X
Arben Merkoçi: 0000-0003-2486-8085
Neus G. Bastús: 0000-0002-3144-7986

Author Contributions

L.R. performed the experiments with the assistance from F.M., J.Pa., and J.Pi.; A.M., N.G.B, and V.P. supervised the project; and L.R., N.G.B., and V.P. wrote the manuscript.

Notes

The authors declare no competing financial interest.

■ ACKNOWLEDGMENTS

This work was carried out within the “Doctorat en Química” Ph.D. programme of Universitat Autònoma de Barcelona, supported by the Spanish MINECO (MAT2015-70725-R) and from the Catalan Agència de Gestió d’Ajuts Universitaris i de Recerca (AGAUR) (2017-SGR-143). Financial support from the HISENTS (685817) Project financed by the European Community under H20202 Capacities Programme is gratefully acknowledged. N.G.B. acknowledges financial support by MINECO through the Ramon y Cajal program (RYC-2012-10991). It was also funded by the CERCA Program/Generalitat de Catalunya. ICN2 acknowledges the support of the Spanish MINECO through the Severo Ochoa Centers of Excellence Program under Grant SEV-2013-0295.

■ REFERENCES

(1) Qiu, H.-J.; Li, X.; Xu, H.-T.; Zhang, H.-J.; Wang, Y. Nanoporous Metal as a Platform for Electrochemical and Optical Sensing. *J. Mater. Chem. C* **2014**, *2*, 9788−9799.

(2) Prieto, G.; Tüysüz, H.; Duyckaerts, N.; Knossalla, J.; Wang, G. H.; Schüth, F. Hollow Nano- and Microstructures as Catalysts. *Chem. Rev.* **2016**, *116*, 14056−14119.

(3) Hembury, M.; Chiappini, C.; Bertazzo, S.; Kalber, T. L.; Drisko, G. L.; Ogunlade, O.; Walker-Samuel, S.; Krishna, K. S.; Jumeaux, C.; Beard, P.; et al. Gold-Silica Quantum Rattles for Multimodal Imaging and Therapy. *Proc. Natl. Acad. Sci. U. S. A.* **2015**, *112*, 1959−1964.

(4) Yang, X. F.; Yang, J. H.; Zhong, Y. L.; Gariepy, V.; Trudeau, M. L.; Zaghib, K.; Ying, J. Y. Hollow Melon-Seed-Shaped Lithium Iron Phosphate Micro- and Sub-Micrometer Plates for Lithium-Ion Batteries. *ChemSusChem* **2014**, *7*, 1618−1622.

(5) Santos, L.; Neto, J. P.; Crespo, A.; Nunes, D.; Costa, N.; Fonseca, I. M.; Barquinha, P.; Pereira, L.; Silva, J.; Martins, R.; et al. WO3 Nanoparticle-Based Conformable pH Sensor. *ACS Appl. Mater. Interfaces* **2014**, *6*, 12226−12234.

(6) Yazdi, A.; Merkoçi, F.; Bastús, N. G.; Imaz, I.; Puntes, V. F.; Maspoch, D. The Influence of the MOF Shell Thickness on the Catalytic Performance of Composites Made of Inorganic (Hollow) Nanoparticles Encapsulated into MOFs. *Catal. Sci. Technol.* **2016**, *6*, 8388−8391.

(7) Cobley, C. M.; Xia, Y. Engineering the Properties of Metal Nanostructures via Galvanic Replacement Reactions. *Mater. Sci. Eng., R* **2010**, *70*, 44−62.

(8) Nafria, R.; Genç, A.; Ibáñez, M.; Arbiol, J.; Ramírez De La Piscina, P.; Homs, N.; Cabot, A. Co-Cu Nanoparticles: Synthesis by Galvanic Replacement and Phase Rearrangement during Catalytic Activation. *Langmuir* **2016**, *32*, 2267−2276.

(9) Liu, R.; Guo, J.; Ma, G.; Jiang, P.; Zhang, D.; Li, D.; Chen, L.; Guo, Y.; Ge, G. Alloyed Crystalline Au−Ag Hollow Nanostructures with High Chemical Stability and Catalytic Performance. *ACS Appl. Mater. Interfaces* **2016**, *8*, 16833−16844.

(10) Yavuz, M. S.; Cheng, Y.; Chen, J.; Cobley, C. M.; Zhang, Q.; Rycenga, M.; Xie, J.; Kim, C.; Song, K. H.; Schwartz, A. G.; et al. Gold Nanocages Covered by Smart Polymers for Controlled Release with near-Infrared Light. *Nat. Mater.* **2009**, *8*, 935−939.

(11) Genç, A.; Patarroyo, J.; Sancho-Parramon, J.; Bastús, N. G.; Puntes, V. F.; Arbiol, J. Hollow Metal Nanostructures for Enhanced Plasmonics: Synthesis, Local Plasmonic Properties and Applications. *Nanophotonics* **2017**, *6*, 193−213.

(12) Sun, X.; Kim, J.; Gilroy, K. D.; Liu, J.; König, T. A. F.; Qin, D. Gold-Based Cubic Nanoboxes with Well-Defined Openings at the Corners and Ultrathin Walls Less Than Two Nanometers Thick. *ACS Nano* **2016**, *10*, 8019−8025.

(13) Gilroy, K. D.; Farzinpour, P.; Sundar, A.; Hughes, R. A.; Neretina, S. Sacrificial Templates for Galvanic Replacement Reactions: Design Criteria for the Synthesis of Pure Pt Nanoshells with a Smooth Surface Morphology. *Chem. Mater.* **2014**, *26*, 3340−3347.

(14) Gonzalez, E.; Arbiol, J.; Puntes, V. F. Carving at the Nanoscale: Sequential Galvanic Exchange and Kirkendall Growth at Room Temperature. *Science (Washington, DC, U. S.)* **2011**, *334*, 1377−1380.

(15) Jing, H.; Wang, H. Structural Evolution of Ag−Pd Bimetallic Nanoparticles through Controlled Galvanic Replacement: Effects of Mild Reducing Agents. *Chem. Mater.* **2015**, *27*, 2172−2180.

(16) Bai, T.; Tan, Y.; Zou, J.; Nie, M.; Guo, Z.; Lu, X.; Gu, N. AuBr 2 − -Engaged Galvanic Replacement for Citrate-Capped Au−Ag Alloy Nanostructures and Their Solution-Based Surface-Enhanced Raman Scattering Activity. *J. Phys. Chem. C* **2015**, *119*, 28597−28604.

(17) Wan, D.; Xia, X.; Wang, Y.; Xia, Y. Robust Synthesis of Gold Cubic Nanoframes through a Combination of Galvanic Replacement, Gold Deposition, and Silver Dealloying. *Small* **2013**, *9*, 3111−3117.

(18) Zhang, W.; Yang, J.; Lu, X. Tailoring Galvanic Replacement Reaction for the Preparation of Pt/Ag Bimetallic Hollow Nanostructures with Controlled Number of Voids. *ACS Nano* **2012**, *6*, 7397−7405.

(19) Xie, H.; Larmour, I. a; Chen, Y.-C.; Wark, A. W.; Tileli, V.; McComb, D. W.; Faulds, K.; Graham, D. Synthesis and NIR Optical Properties of Hollow Gold Nanospheres with LSPR Greater than One Micrometer. *Nanoscale* **2013**, *5*, 765−771.

(20) Preciado-Flores, S.; Wang, D.; Wheeler, D. a.; Newhouse, R.; Hensel, J. K.; Schwartzberg, A.; Wang, L.; Zhu, J.; Barboza-Flores, M.; Zhang, J. Z. Highly Reproducible Synthesis of Hollow Gold Nanospheres with near Infrared Surface Plasmon Absorption Using PVP as Stabilizing Agent. *J. Mater. Chem.* **2011**, *21*, 2344−2350.

(21) Jang, H.; Min, D. H. Spherically-Clustered Porous Au-Ag Alloy Nanoparticle Prepared by Partial Inhibition of Galvanic Replacement and Its Application for Efficient Multimodal Therapy. *ACS Nano* **2015**, *9*, 2696−2703.

(22) Wang, Y.; He, J.; Liu, C.; Chong, W. H.; Chen, H. Thermodynamics versus Kinetics in Nanosynthesis. *Angew. Chem., Int. Ed.* **2015**, *54*, 2022−2051.

(23) Pansare, V. J.; Hejazi, S.; Faenza, W. J.; Prud'Homme, R. K. Review of Long-Wavelength Optical and NIR Imaging Materials: Contrast Agents, Fluorophores, and Multifunctional Nano Carriers. *Chem. Mater.* **2012**, *24*, 812−827.

(24) Gomes, J. F.; Garcia, A. C.; Pires, C.; Ferreira, E. B.; Albuquerque, R. Q.; Tremiliosi-Filho, G.; Gasparotto, L. H. S. Impact of the AuAg NPs Composition on Their Structure and Properties: A Theoretical and Experimental Investigation. *J. Phys. Chem. C* **2014**, *118*, 28868−28875.

(25) Bastús, N. G.; Merkoçi, F.; Piella, J.; Puntes, V. F. Synthesis of Highly Monodisperse Citrate-Stabilized Silver Nanoparticles of up to 200 Nm: Kinetic Control and Catalytic Properties. *Chem. Mater.* **2014**, *26*, 2836−2846.

(26) Juluri, B. K.; Huang, J.; Jensen, L. *NanoHUB: Extinction, Scattering and Absorption Efficiencies of Single and Multilayer Nanoparticles.* https://nanohub.org/resources/nmie (accessed 06/16/2018).

(27) Xia, X.; Wang, Y.; Ruditskiy, A.; Xia, Y. 25Th Anniversary Article: Galvanic Replacement: A Simple and Versatile Route To Hollow Nanostructures With Tunable and Well-Controlled Properties. *Adv. Mater.* **2013**, *25*, 6313−6333.

(28) Lewis, E. a.; Slater, T. J. a.; Prestat, E.; Macedo, A.; O'Brien, P.; Camargo, P. H. C.; Haigh, S. J. Real-Time Imaging and Elemental Mapping of AgAu Nanoparticle Transformations. *Nanoscale* **2014**, *6*, 13598−13605.

(29) González, E.; Merkoçi, F.; Arenal, R.; Arbiol, J.; Esteve, J.; Bastús, N. G.; Puntes, V. F. Enhanced Reactivity of High-Index Surface Platinum Hollow Nanocrystals. *J. Mater. Chem. A* **2016**, *4*, 200−208.

(30) Link, S.; Wang, Z. L.; El-Sayed, M. a. Alloy Formation of Gold-Silver Nanoparticles and the Dependence of the Plasmon Absorption on Their Composition. *J. Phys. Chem. B* **1999**, *103*, 3529−3533.

(31) Prodan, E. A Hybridization Model for the Plasmon Response of Complex Nanostructures. *Science* **2003**, *302*, 419−422.

(32) Varón, M.; Ojea-Jimenez, I.; Arbiol, J.; Balcells, L.; Martínez, B.; Puntes, V. F. Spontaneous Formation of Hollow Cobalt Oxide Nanoparticles by the Kirkendall Effect at Room Temperature at the Water−air Interface. *Nanoscale* **2013**, *5*, 2429−2436.

(33) Nakazato, Y.; Taniguchi, K.; Ono, S.; Eitoku, T.; Katayama, K. Formation Dynamics of Gold Nanoparticles in Poly(vinylpyrrolidone) and Other Protective Agent Solutions. *Phys. Chem. Chem. Phys.* **2009**, *11*, 10064−10072.

(34) Zelyanskii, A. V.; Zhukova, L. V.; Kitaev, G. A. Solubility of AgCl and AgBr in HCl and HBr. *Inorg. Mater.* **2001**, *37*, 523−526.

(35) Hodak, J. H.; Henglein, A.; Giersig, M.; Hartland, G. V. Laser-Induced Inter-Diffusion in AuAg Core-Shell Nanoparticles. *J. Phys. Chem. B* **2000**, *104*, 11708−11718.

(36) Sutter, E.; Sutter, P. In-Situ Liquid Cell Electron Microscopy of Ag-Au Galvanic Replacement Reactions. *Nanoscale* **2017**, *9*, 1271−1278.

(37) Smith, J. G.; Yang, Q.; Jain, P. K. Identification of a Critical Intermediate in Galvanic Exchange Reactions by Single-Nanoparticle-Resolved Kinetics. *Angew. Chem., Int. Ed.* **2014**, *53*, 2867−2872.

(38) Au, L.; Lu, X.; Xia, Y. A Comparative Study of Galvanic Replacement Reactions Involving Ag Nanocubes and $AuCl^{2-}$ or $AuCl^{4-}$. *Adv. Mater.* **2008**, *20*, 2517−2522.

(39) Jain, P. K.; Lee, K. S.; El-Sayed, I. H.; El-Sayed, M. A. Calculated Absorption and Scattering Properties of Gold Nanoparticles of Different Size, Shape, and Composition: Applications in Biological Imaging and Biomedicine. *J. Phys. Chem. B* **2006**, *110*, 7238−7248.

(40) Genç, A.; Patarroyo, J.; Sancho-Parramon, J.; Arenal, R.; Duchamp, M.; González, E. E.; Henrard, L.; Bastús, N. G.; Dunin-Borkowski, R. E.; Puntes, V. F.; et al. Tuning the Plasmonic Response up: Hollow Cuboid Metal Nanostructures. *ACS Photonics* **2016**, *3*, 770−779.

(41) Erlebacher, J.; Aziz, M. J.; Karma, a; Dimitrov, N.; Sieradzki, K. Evolution of Nanoporosity in Dealloying. *Nature* **2001**, *410*, 450−453.

(42) Bastús, N. G.; Piella, J.; Puntes, V. F. Quantifying the Sensitivity of Multipolar (Dipolar, Quadrupolar, and Octapolar) Surface Plasmon Resonances in Silver Nanoparticles: The Effect of Size, Composition, and Surface Coating. *Langmuir* **2016**, *32*, 290−300.

(43) Kim, M. H.; Lu, X.; Wiley, B.; Lee, E. P.; Xia, Y. Morphological Evolution of Single-Crystal Ag Nanospheres during the Galvanic Replacement Reaction with $HAuCl_4$. *J. Phys. Chem. C* **2008**, *112*, 7872−7876.

Nano Research
https://doi.org/10.1007/s12274-018-2157-y
Research Article

ISSN 1998-0124
CN 11-5974/O4

Tunable electrochemistry of gold-silver alloy nanoshells

Lorenzo Russo[1,2], Victor Puntes[1,3,4], and Arben Merkoçi[1,4] (✉)

[1] *Catalan Institute of Nanoscience and Nanotechnology (ICN2), CSIC and BIST, Campus UAB, Bellaterra, 08193 Barcelona, Spain*
[2] *Universitat Autònoma de Barcelona (UAB), Campus UAB, Bellaterra, 08193 Barcelona, Spain*
[3] *Vall d'Hebron Institut de Recerca (VHIR), 08035 Barcelona, Spain*
[4] *Institució Catalana de Recerca i Estudis Avançats (ICREA), P. Lluís Companys 23, 08010 Barcelona, Spain*

Received: 27 May 2018
Revised: 4 July 2018
Accepted: 27 July 2018

KEYWORDS

Au nanoshells,
nanoparticles,
surface chemistry,
underpotential deposition

ABSTRACT

The widespread and increasing interest in enhancing biosensing technologies by increasing their sensitivities and lowering their costs has led to the exploration and application of complex nanomaterials as signal transducers and enhancers. In this work, the electrochemical properties of monodispersed AuAg alloy nanoshells (NSs) with finely tunable morphology, composition, and size are studied to assess their potential as electroactive labels. The controlled corrosion of their silver content, caused by the oxidizing character of dissolved oxygen and chlorides of the electrolyte, allows the generation of a reproducible electrochemical signal that is easily measurable through voltammetric techniques. Remarkably, the underpotential deposition of dissolved Ag^+ catalyzed on AuAg NS surfaces is observed and its dependence on the nanoparticle morphology, size, and elemental composition is studied, revealing a strong correlation between the relative amounts of the two metals. The highest catalytic activity is found at Au/Ag ratios higher than ≈ 10, showing how the synergy between both metals is necessary to trigger the enhancement of Ag^+ reduction. The ability of AuAg NSs to generate an electrocatalytic current without the need for any strong acid makes them an extremely promising material for biosensing applications.

1 Introduction

The rational design of advanced metallic nanoparticles (MNPs) with unique properties and functionalities has proven to be an extremely successful strategy for devising innovative and advantageous solutions to overcoming the conventional intrinsic limitations of macro/micro size materials applied in *in vitro* diagnostic technologies [1, 2], among other industrial uses. In particular, the profound understanding of the relationship between noble MNPs' localized surface plasmon resonance (LSPR) and their atomic structure, morphology, and composition has led to the successful development of a number of optical biosensors, whose enhanced sensitivities and flexibilities outperform those of their more conventional predecessors [3]. Despite

---

Address correspondence to arben.merkoci@icn2.cat

this, a comparable ability to predict and design MNPs' electrochemical properties through their controlled synthesis has not yet been achieved (with only a few exceptions available in Ref. [4]), probably owing to a lack of reliable and reproducible synthetic methodologies for complex nanomaterials. Interestingly, however, the introduction of electroactive MNPs as signal amplification carriers or direct signal generating elements has provided increased sensitivities and enhanced performances in many biosensing applications, thanks to their unique redox and electrocatalytic properties [5–7], which in turn emerge from their shape, surface morphology, and chemical composition [4, 8, 9]. Indeed, electroactive MNPs represent a promising alternative to redox enzymes as electrochemical transducers, as they are significantly more affordable in terms of production and engineering, while their robustness allows for easy storage (i.e., temperature and pH) and longer half-lives [10].

Gold and silver nanoparticles (Au and Ag NPs) are probably the most widely studied and applied nanomaterials in sensing, owing to a well-established understanding of their optical properties; the fact that they are highly susceptible to their chemical environment and easily tunable by controlling their shape, morphology, and composition; and the electrochemical behavior they exhibit under certain working conditions [11, 12]. Unfortunately, monometallic Ag NPs have found limited practical use, because of a severe susceptibility to oxidation [13], resulting in a low durability and reproducibility in many bio-related applications. On the other hand, obtaining a direct electrochemical response from monometallic Au NPs requires secondary reagents or strong oxidizers that are able to activate catalytic effects or generate redox active species, making it extremely impractical to translate the use of this nanomaterial into electrochemical diagnostic platforms for commercial use [8]. As a result, significant effort has been put into combining Au and Ag into a single functional nanoprobe, possessing both the former's high biocompatibility and stability to oxidation and the readily accessible electrochemical activity of the latter [11, 14]. In this context, the two most explored morphologies, namely core shell Au@Ag NPs and AuAg alloy NPs, both exhibit an enhanced resistance to Ag oxidation, thanks to an electronic density redistribution between the two noble metals that enriches Ag orbitals with d-charge from Au [15, 16]. However, no previous studies have focused on controlling the extent of this effect in order to trigger the electrochemical activity of silver without compromising the structural integrity of the system. This is in part on account of the inherent immiscibility of Au and Ag at the nanoscale which, despite their perfect bulk miscibility, promotes the spontaneous segregation of the latter in polycrystalline heterogeneous mixtures, given its higher surface energy [17].

Herein, hollow AuAg nanoshells (NSs) are proposed as a novel class of electroactive nanomaterial with highly promising applicability and flexibility as electrochemical labels. Their electrochemical characterization reveals the features of catalytic Ag underpotential deposition (UPD) at their surface, which has been found to depend directly on the combination of their morphology and relative chemical composition. This work provides a basis for a better understanding of the electrochemistry of hollow AuAg NSs, as well as a successful example of how the rational design of nanomaterials with controlled properties can provide suitable tools for electrochemical sensing.

2 Experimental

Silver nitrate ($AgNO_3$), trisodium citrate ($Na_3C_6H_5O_7$), tannic acid ($C_{76}H_{52}O_{46}$), $HAuCl_4 \cdot 3H_2O$ (99%), and polyvinyl pyrrolidone ($(C_6H_9NO)_n$, $M_W \approx 55{,}000$ (PVP)) were purchased from Sigma-Aldrich. All chemicals were used as received, without further purification. Distilled water that was passed through a Millipore system ($\rho = 18.2$ MΩ) was used in all experiments. All glassware was first rinsed with acetone and then with Millipore water before use. Buffer solutions were prepared in Milli-Q water obtained from a Millipore system vent filter MPK01. The two buffers, phosphate buffer (PB) and phosphate buffer saline (PBS), were prepared at a concentration of 0.01 M and at pH 7.4. PB was prepared by mixing sodium-phosphate monobasic hydrogen with sodium-phosphate dibasic hydrogen in the desired proportion, and PBS was purchased from Sigma-Aldrich in tablet form. Screen printed carbon electrodes (SPCEs) were fabricated using a semi-automatic screen-printing machine DEK248 (DEK International, Switzerland). Electrodes were printed over Autostat HT5 polyester sheets (McDermid Autotype, UK) using carbon sensor paste C2030519P4 for the working (WE) and counter (CE) electrodes, grey dielectric paste D2070423P5 (Gwent, The Netherlands) to insulate the contacts and define the sample interaction area, and silver/silver chloride ink for the reference electrode (RE) EDAG 6037E SS (Loctite).

All nanoparticles were characterized by UV–vis spectroscopy (Perkin-Elmer "Lambda25" Spectrophotometer), dynamic light scattering (DLS) (Malvern Zetasizer), transmission electron microscopy (TEM), and scanning electron microscopy (SEM) (FEI Magellan 400L). High-resolution TEM (HRTEM) images were obtained using an FEI Tecnai F20 field-emission gun microscope with a 0.19 nm point-to-point resolution, operated at 200 keV. The electrochemical experiments were performed by an AUTOLAB PGSTAT302N (Echo Chemie, The Netherlands) potentiostat/galvanostat, which was connected to a computer and monitored by Autolab GPES software. All experiments were performed at room temperature. The SCPEs were connected to the potentiostat through a homemade connector. The general protocol for the electrochemical measurements of AuAg NSs is as follows: 10 μL of AuAg NSs solution (1.6×10^{11} NPs/mL) was transferred into a plastic 1.5 mL Eppendorf tube containing 50 μL of a PBS 10 mM pH 7.4. After incubation for a given time in the saline matrix and stirring at 600 rpm in a thermoshaker at 25 °C, 50 μL of the mixture were dropped onto the SPCE to cover the three electrodes. Differential pulsed voltammetry (DPV) was performed. Here, after applying a fixed deposition negative potential for 60 s, the voltage was scanned between +0.6 and +1.04 V vs. RHE with 0.01 V step potential. Cyclic voltammetries (CVs) were recorded under the same conditions scanning from –0.16 to +0.94 V vs. RHE at a 100 mV/s scan rate with a 0.005 V step potential.

3 Results and discussion

3.1 Synthesis of hollow AuAg nanoshells

Hollow AuAg nanoshells were synthetized according to a protocol developed recently by our group [18]. Briefly, starting from an aqueous 5 mM PVP solution containing Ag NPs of the desired size, a galvanic replacement reaction (GRR) was carried out by gradually adding a 1 mM $HAuCl_4$ solution through a syringe pump. Thanks to the difference in reduction potentials of the two noble metals (the standard reduction potentials of Ag^+ and Au^{3+} are 0.7996 and 1.498 V, respectively [19]), Au^{III} is progressively reduced onto the silver sacrificial template surface while metallic Ag is oxidized, forming a gold shell that encloses a growing inner cavity. Figure 1(a) presents the TEM micrograph for the final stage of the reaction, displaying highly monodisperse hollow AuAg NSs of ca. 60 nm in diameter, with a thin and smooth outer shell of ca. 10 nm in thickness. The presence of PVP in the reaction mixture is crucial for slowing down the reaction kinetics and obtaining thin and smooth surfaces, while at the same time providing an increased stability towards aggregation [20].

During GRR, the difference in interdiffusion rates between the two noble metals favors the formation of a stable alloy at the interface between the particle's dissolving Ag core and the forming Au-rich shell [21]. Figure 1(b) shows the elemental distribution of hollow AuAg NSs by energy-dispersive X-ray spectroscopy (EDS) mapping: while Au (green) is located only in the outer particle surface together with alloyed Ag (red), some "bulk" silver remaining from the original core is still present at the interface. Indeed, co-etchers, such as HCl, are required during the hollowing process in order to vary the internal void size by corroding the "bulk" non-alloyed core Ag remaining during the reaction. Thin hollow AuAg NSs with smooth integral surfaces are then obtained in high conversion yields with precisely controlled morphologies and chemical composition (Fig. 1(c)), also thanks to the high monodispersity of the template solution [22].

3.2 Electrochemistry of AuAg NSs

The exposure of metallic silver to the ambient atmosphere as well as nucleophilic species (such as halide anions) at a pH lower than 8 is known to lead to its oxidative dissolution [15, 23]. In order to generate the necessary electrochemical signal for AuAg NSs to be employed as redox reporters, the controlled

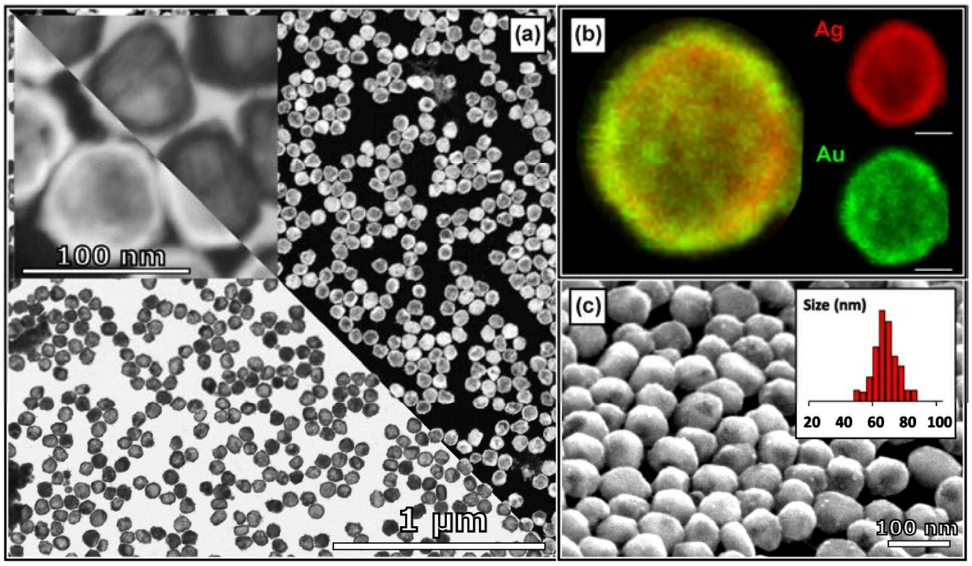

Figure 1 (a) TEM and high-angle annular dark-field scanning TEM (HAADF-STEM) micrographs of highly monodispersed 60.0 ± 4.4 nm AuAg NSs composed of a thin (≈ 10 nm) shell with a smooth surface and a large (≈ 40 nm) internal void. (b) HAADF-STEM elemental distribution micrographs of a single AuAg NS (white bar corresponds to 20 nm). At the final stage of GRR, Ag is found in both the Au-rich alloy thin outer shell and the inner particle surface in its metallic form. (c) SEM AuAg NSs surface characterization and size distribution.

corrosion of their "bulk" Ag core must be achieved through the use of a suitable medium [24]. Therefore, PBS at a pH of 7.4 was chosen as an electrolyte not only to provide this necessary oxidizing character, given by its relatively high chloride concentration, but also to better reproduce the typical pH and salinity of biological matrixes. Figures 2(a) and 2(b) show the DPVs of AuAg NSs performed on SPCEs in PBS 10 mM pH 7.5. When performing DPVs of PVP-coated AuAg NSs (Fig. 2(a), "AuAgNSs@PVP"), two well-defined anodic current peaks were observed: The first and more intense one (+0.8 V vs. RHE, red curve segment), corresponding to oxidation of the metallic "bulk" silver contained in the partially emptied particle core, is accompanied by a weaker signal at higher oxidation potentials (+0.9 V vs. RHE, green curve segment), produced by the "more noble" alloyed silver. It is known that the driving force for the formation of energetically favorable alloys, such as the gold-silver one, is the thermodynamic gain obtained by the interdiffusion of the two metals favored by the rather small difference observed in the lattice parameters of both (408.53 pm for Ag and 407.82 pm for Au) [19]. Compared to metallic silver, the Ag atoms composing the alloy possess a higher stability towards oxidation, thanks to the proximity effect [14–16], causing their characteristic anodic stripping peak to be observed at higher oxidation potentials. This behavior is consistent with the unique electronic configuration of bimetallic AuAg systems, also described by Nishimura et al., where a unique charge transfer between the Au 4f and 5d levels increases the electron density within the Ag d-levels, yielding a negative Ag oxidation state that suppresses its chemical oxidation when exposed to surrounding environments [15, 16, 25]. This description of the system is further corroborated when sodium citrate (SC)-coated hollow AuAg NSs are characterized (Fig. 2(b), "AuAgNSs@SC"). In this case, the material does not have any polymeric coating preventing direct contact between the thin alloy shell and the electrode surface [26], and even if an analogous current profile is observed in terms of the peak potentials, their relative intensities change. In particular, the signal of the alloyed Ag, localized only in the 10 nm thick AuAg shell, correspondingly increases thanks to better contact with the electrode. Figure 2(c) presents a schematization of the electrochemical signal's generation mechanism for AuAg NSs with each type of coating. Moreover, the same measurement performed on a PVP-coated monometallic Ag NPs solution (Fig. S1

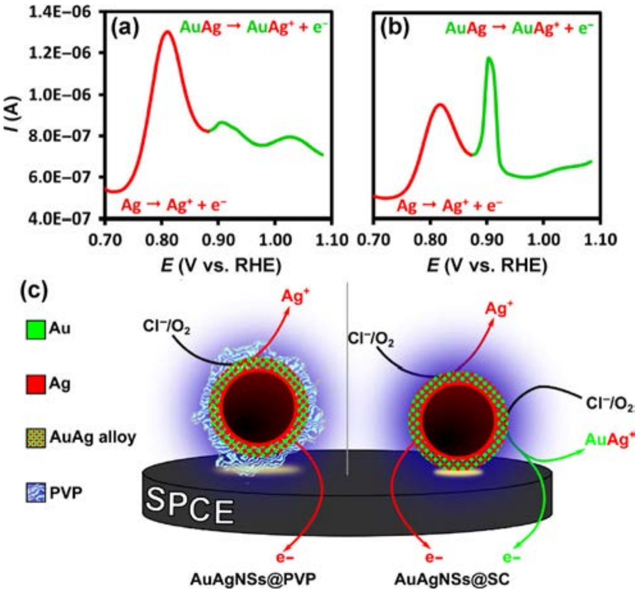

Figure 2 (a) and (b) DPVs in PBS 10 mM pH 7.5 of AuAg NSs coated with PVP and SC, respectively. The analytical peak, observed at +0.8 vs. RHE, corresponds to the stripping oxidation of metallic silver, while the secondary one recorded at +0.9 vs. RHE is derived from the concurrent oxidation of the alloyed silver. (c) proposed electrochemical mechanism for the AuAg NSs voltammetric profile. Left: PVP-coated AuAg NSs. The presence of chlorides and dissolved oxygen promotes the partial corrosion of metallic Ag from the particle's core, allowing for its detection through anodic stripping voltammetry. Only a weak signal for the oxidation of alloyed silver is observed. Right: SC-coated AuAg NSs. No insulating layer prevents the particle from directly contacting the electrode surface, resulting in an increased current intensity in correspondence with the anodic stripping peak of alloyed silver.

in the Electronic Supplementary Material (ESM)) demonstrates the correspondence between the $Ag^0 \rightarrow Ag^+$ oxidation peaks at +0.80 – +0.82 vs. RHE [23] for the three considered kinds of NP (only sodium citrate-coated Ag NPs (Fig. S1 in the ESM) cannot be measured, owing to their instant aggregation in PBS [27]). Interestingly, no electrochemical signal appears when using equimolar PB instead of its saline formulation (Fig. S1 in the ESM). As expected, in the absence of chlorides no Ag^+ ions are generated from the particles' residual silver core in its cathodic reduction during the initial DPV deposition step, and therefore no anodic stripping current can be observed, showing how crucial the presence of the corroding O_2/Cl^- solvated couple is in promoting silver oxidation. This aspect is of notable importance, because conventionally the use of metal and semiconductor NPs for electrochemical labels requires strong acids in order to generate the corresponding cations through particles corrosion [2]. The need for these impractical but necessary components completely precludes the possibility of the commercialization of such a system or its application in biological environments. Exploiting the mild oxidizing character of biological matrixes instead as the only trigger for activating the electrochemical properties of AuAg NSs represents a game-changing step forward in the development of electrochemical transducers for real-world diagnostic applications.

3.3 Au electrocatalytic effect

As is widely known and reported, the elemental composition of AuAg NSs, together with their aspect-ratio (understood as the ratio between the shell thickness and void radius), determines the LSPR band position [18]. These two parameters depend on the extent of GRR and can be controlled by tuning the amount of Au^{III} added to the reaction mixture. Depending on the stoichiometry of the process, the silver core of the particle is progressively depleted by both the redox reaction driven by the difference in reduction potentials between the two noble metals, and by the alloying process, which "extracts" metallic silver from the particle core and favors its migration towards the surface [17]. In addition, core Ag is dissolved by the combined action of protons, dissolved oxygen, and nucleophiles present in the solution [18]. Figure 3(a) presents the high magnification TEM micrographs of the different phases of the GRR, where 60 nm-sized Ag NPs are progressively converted into hollow NSs through the formation of a thin Au shell on their surface, while an expanding inner void is corroded from their core. During this process, the ratio between the two noble metals (Au/Ag ratio) increases accordingly. Table 1 reports the calculated and experimental values of the Au/Ag ratio for different phases of GRR, which are in good agreement with each other. Less often reported is the effect of the nanoalloys' composition on their electrochemical behavior. To our knowledge, this has only been explored for "bulk" AuAg NPs [28, 29] and macroscopic AuAg micro/nanoporous electrodes [30, 31]. Thus, CVs of AuAg NSs at different degrees of galvanic replacement conversion

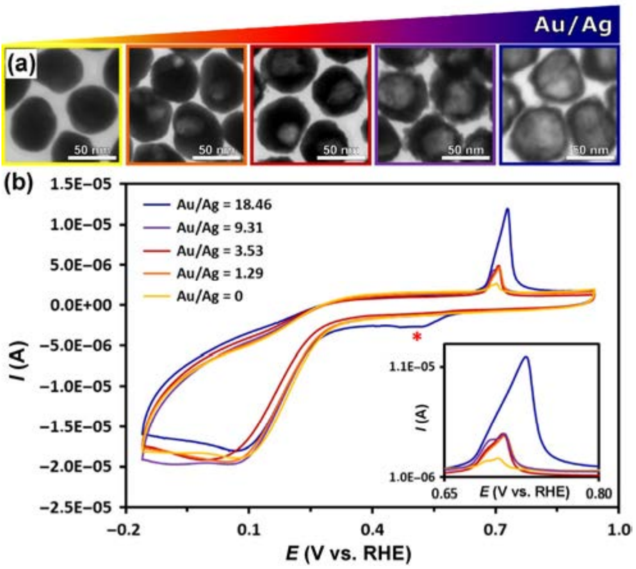

Figure 3 (a) TEM images showing the morphological evolution of silver templates during GRR. Starting from ≈ 60 nm monodispersed Ag NPs (left), titration with $HAuCl_4$ triggers a structural and chemical transformation leading gradually to the formation of a thin AuAg alloy shell enclosing an empty internal cavity (right). (b) CVs of AuAg NSs at different GRR stages (inset showing peak currents for Ag oxidation at ≈ +0.76 vs. RHE normalized over concentration). While the voltammetric profile maintains the same features in terms of peak positions and shapes, the current intensity increases once the GRR is initiated. At the latest phase, corresponding to a thin Au-rich shell enclosing a large void (right), the electrocatalytic $Ag^+ + e^- \rightarrow Ag^0$ reduction peak appears at +0.44 V vs. RHE (*).

Table 1 Calculated and experimental values of Au/Ag ratio for the different phases of GRR and their corresponding anodic current. For low Au/Ag ratios, only a slight increase in peak current is observed, compared with the sacrificial Ag NPs (Au/Ag = 0). At the latest stages of GRR, corresponding to the higher amount of deposited Au (Au/Ag ≈ 20), a greater signal enhancement appears

Peak current (μA)[a]	Au/Ag (%) (theor.)	Au/Ag (%) (EDS)
0.66 ± 0.5	0.00	0.00
2.88 ± 0.5	1.87	1.29
2.92 ± 0.1	3.38	3.53
3.25 ± 0.2	10.77	9.31
7.76 ± 0.4	22.91	18.46

[a] Anodic current measured at +0.12 mV vs. Ag/AgCl.

were performed (Fig. 3(b)), revealing an increasing trend in the Ag oxidation current intensity. At the initial and intermediate stages of GRR (Fig. 3(b), yellow, orange, red, and purple curves), characterized by a relatively low Au/Ag ratio, a small void, and an incomplete Au shell, the hollow nanocrystals display a weak anodic signal, with peak currents not above the ≈ 3 μA value (Fig. 2(b), inset; Table 1). The higher amount of Au deposited at the later GRR stages, together with the continued enlargement of the internal cavity, considerably enhances the oxidation current intensity, reaching a maximum for particles with Au-rich alloyed outer shells and large internal voids (Fig. 3(b), blue curve, Table 1). The reason for this electrochemical signal amplification probably resides in two synergic effects caused by the transformations in AuAg NSs morphology and chemical composition. First, the increased surface-to-volume ratio obtained from the void enlargement (Fig. 3(a)) would correspond to a higher degree of chloride corrosion, and therefore a larger amount of Ag^+ generated at the electrode surface, which in turn introduces higher oxidation currents. Second, when analyzing the CVs of the different GRR phases, a weak but clearly defined reduction peak appears at +0.44 vs. RHE only in the case of the latest GRR stages (Fig. 3(b), blue curve). This well-known and widely studied feature corresponds to the UPD of Ag^+ ions on the NSs' surface [32, 33] exploited successfully in the electrochemical silver-enhanced method with Au NPs [34–36]. The metal cation electrodeposition mechanism on other metallic surfaces has been largely investigated at the macro-scale, while few examples of metal UPD over MNPs are found in Refs. [37, 38]. During the UPD process, metal ions in solution can adsorb onto the MNP surface, altering the local surface charge density of the metal. Upon application of a cathodic potential, the ad-atoms undergo a partial discharge, which corresponds to a negative partial charge transfer from the excess electron density of the NPs. This cathodic current is observed for reducing potentials that are less negative than the metal's standard reduction potential. As shown by the CVs of hollow AuAg NSs bearing an Au-rich outer shell and a large internal void (Fig. 3(b), blue curve), during the cathodic scan the peak observed at –0.2 V vs. Ag/AgCl represents the first deposition stage, attributed to the partial discharge of solvated Ag^+ ad-atoms, followed by bulk deposition of Ag only at –0.16 V vs. RHE (the broad nature of the UPD peak compared to macroscale metal surfaces is attributed to the small sizes and faceted surfaces of AuAg NSs). This catalytic effect is only observed for AuAg NSs obtained at the final stages of the GRR, suggesting a correlation between the morphology, surface chemical composition, and Ag UPD reaction. Indeed, variations in the morphology and degree of alloying in bimetallic systems are known to influence their catalytic activity through a modulation of the electronic structure of the constituent metals [12, 14, 39, 40]. Hollow AuAg NSs at the latest GRR stages possess the highest content of Au atoms (Table 1), which are concentrated in the thin outer shell owing to their synthesis mechanism [18]. As previously explained, the injection of Au d-charge into the Ag electronic levels results in an increased electron density localized on the particle surface [16]. Therefore, hollow AuAg NSs will display higher surface potentials, given their direct dependence on the metal surface excess charge [41], causing the adsorbed Ag ions to interact with a more intense generated electromagnetic field. As a consequence, Au-rich NSs will then catalyze the reduction of Ag^+ produced by PBS, generating a more intense anodic stripping current.

Following a different but consistent description of the catalytic mechanism, hollow nanostructures are known to display better plasmonic properties than their solid counterparts, thanks to the plasmon hybridization mechanism, in which the presence of cavities induces an enhancement and a more homogeneous distribution of the generated electromagnetic fields [42, 43]. The adsorption and partial discharge of metal ions during the UPD, which takes place at the closest proximity to the MNP surface, will therefore be affected by the enhanced field intensities exhibited by the hollowed particles, resulting in an increased Ag catalytic reduction.

We extended the study of the electronic effect on AuAg NSs electrocatalytic UPD to hollow nanoalloys of different sizes (namely 60, 80, 100, and 150 nm), all with a common final SPR maximum wavelength, found at 700 nm. As it is extremely difficult to synthetically control the final relative amount of Au and Ag precisely using templates, whose silver content and total surface area vary with size at different proportionalities, fixing a common final wavelength provides a direct correlation between both the Au/Ag composition and the relative morphological aspect ratio [18]. Figure 4(a) shows low and high magnification TEM dark field micrographs of 60, 80, 100, and 150 nm AuAg NSs (from top-left, clockwise), all possessing the common hollow morphology characterized by a relatively thin outer shell and a large internal void, as summarized in Table 2. The EDS elemental mappings of these particles (Fig. 4(b)) reveal that while the

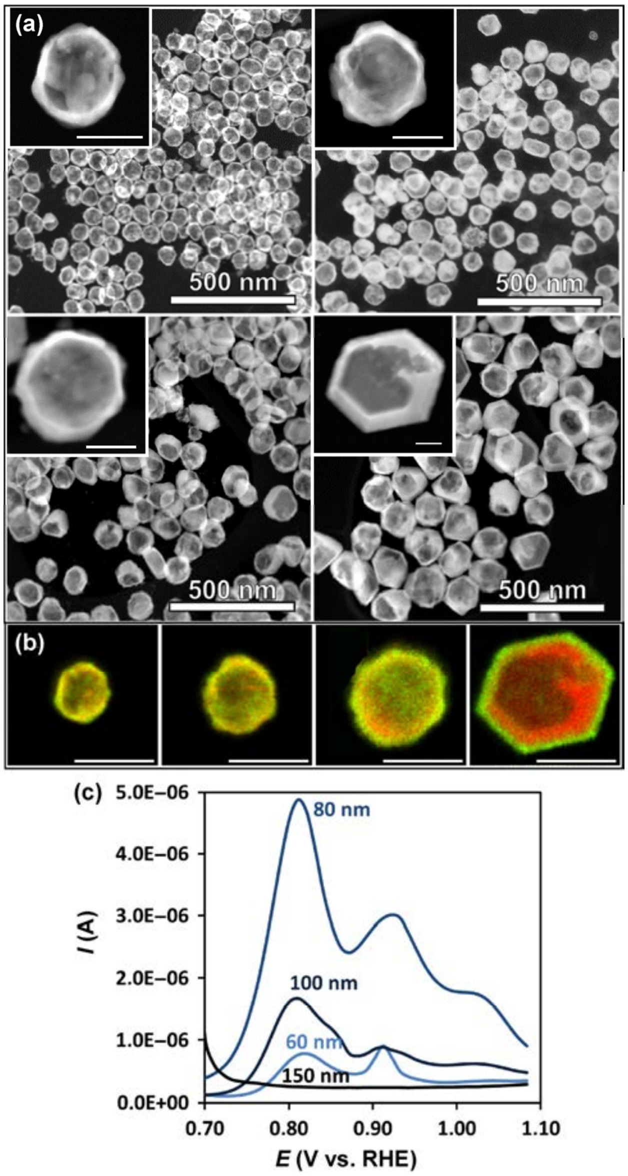

Figure 4 (a) Dark field TEM micrographs and HRTEM images (insets) of highly monodispersed AuAg NSs of different sizes (form top-left, clockwise: 60, 80, 100, and 150 nm). (b) HAADF-STEM elemental distribution micrographs of individual AuAg NSs (white bar corresponds to 100 nm). (c) DPVs of AuAg NSs of different sizes (60, 80, 100, and 150 nm). Depending on the chemical composition and morphological structure, different electrochemical profiles are displayed.

topological distribution of Au (green) and Ag (red) is analogous among all the different sizes, their relative amount differs from size to size. The calculated and experimental Au/Ag ratios for all sizes, reported with significantly good agreement in Table 2, show that bigger hollow AuAg NCs possess a higher Ag content compared to smaller ones, regardless of the fairly constant aspect ratio between the shell thickness and void size. As shown in Fig. 4(c), DPVs of AuAg NSs of different sizes exhibit large current intensity variations depending on their relative noble metal content. The most intense oxidation current is observed for 80 nm NSs, which seem to provide a higher signal enhancement. Both 60 and 100 nm AuAg NSs display lower current amplifications, while for 150 nm hollow nanocrystals no peak appears. By comparing these results with the Au/Ag content of each case (Table 2), it is clearly visible that 80 nm AuAg NSs possess a sufficiently high Au content to trigger the electrocatalytic silver reduction through the mechanism described above. In contrast, larger particles do not possess a sufficiently high Au content, because their alloy composition is still too rich in silver (an effect that cannot be explained by the morphological aspect ratio alone). Interestingly, even though 60 nm particles possess a sufficient Au/Ag ratio for triggering the catalyzed Ag UPD, their lower anodic current intensity is a consequence of the almost complete depletion of the core metallic silver, which is responsible for generating the actual electrochemical signal.

Table 2 Au/Ag ratio calculated and measured by EDS, morphological features, and aspect ratio of AuAg NSs of different sizes (60, 80, 100, and 150 nm). A gold-rich alloy shell, together with a low aspect ratio, is necessary in order to obtain a strong oxidation signal

Size (nm)	60	80	100	150
Au/Ag (%) (theor.)	18.46	17.17	16.73	9.74
Au/Ag (%) (EDS)	22.91 ± 0.20	18.96 ± 0.20	14.14 ± 0.13	10.13 ± 0.12
Void size (nm)	41.6 ± 5.4	63.8 ± 7.5	68.2 ± 9.3	98.9 ± 16.5
Shell thick (nm)	9.1 ± 1.6	12.4 ± 2.6	16.1 ± 5.2	24.1 ± 8.8
Aspect ratio[a]	0.1 ± 0.0	0.2 ± 0.1	0.2 ± 0.1	0.3 ± 0.1

[a] Aspect ratio calculated as $(D - d)/d$, with D being the outer and d the inner diameter.

4 Conclusions

Hollow AuAg NSs are presented as promising electroactive nanomaterials demonstrating high potential and flexibility for future use as electrochemical labels for diagnostics (biosensing), besides other applications. AuAg surface-catalyzed Ag underpotential deposition is observed, and its mechanism is described in detail. Thanks to this, DPV anodic oxidation signals are enhanced up to almost one order of magnitude compared to Ag NPs, depending on the AuAg NS morphologies and relative chemical composition. This behavior, previously unreported for AuAg NSs, is likely to be connected to the increase in surface charge density obtained from the Au enrichment of the outer shell, which appears to favor Ag^+ UPD. A precise modulation of this electrocatalytic effect can be achieved by carefully designing and controlling the synthesis of these advanced materials, allowing the construction of efficient and robust electrochemical transducers that are ready for substituting enzymes in electrochemical diagnostic technologies, besides other uses. This approach could be extended to other types of multimetallic nanomaterials whose diverse and selective electrocatalytic properties could be exploited as labels in immune- and enzymatic assays.

Acknowledgements

This work was carried out within the “Doctorat en Quìmica” PhD programme of Universitat Autònoma de Barcelona, supported by the Spanish MINECO (No. MAT2015-70725-R) and from the Catalan Agència de Gestió d’Ajuts Universitaris i de Recerca (AGAUR) (No. 2017-SGR-143). Financial support from the HISENTS (685817) Project financed by the European Community under H20202 Capacities Programme is gratefully acknowledged. It was also funded by the CERCA Program/Generalitat de Catalunya. ICN2 acknowledges the support of the Spanish MINECO through the Severo Ochoa Centers of Excellence Program under Grant SEV2201320295.

Electronic Supplementary Material: Supplementary material (further details of the electrochemical characterization of AuAg NSs) is available in the online version of this article at https://doi.org/10.1007/s12274-018-2157-y.

References

[1] Genç, A.; Patarroyo, J.; Sancho-Parramon, J.; Bastús, N. G.; Puntes, V. F.; Arbiol, J. Hollow metal nanostructures for enhanced plasmonics: Synthesis, local plasmonic properties and applications. *Nanophotonics* **2017**, *6*, 193–213.

[2] Merkoçi, A. Nanoparticles-based strategies for DNA, protein and cell sensors. *Biosens. Bioelectron.* **2010**, *26*, 1164–1177.

[3] Kumar, A.; Kim, S.; Nam, J. M. Plasmonically engineered nanoprobes for biomedical applications. *J. Am. Chem. Soc.* **2016**, *138*, 14509–14525.

[4] Qiu, H.-J.; Li, X.; Xu, H.-T.; Zhang, H.-J.; Wang, Y. Nanoporous metal as a platform for electrochemical and optical sensing. *J. Mater. Chem. C* **2014**, *2*, 9788–9799.

[5] Maltez-da Costa, M.; de la Escosura-Muñiz, A.; Nogués, C.; Barrios, L.; Ibáñez, E.; Merkoçi, A. Simple monitoring of cancer cells using nanoparticles. *Nano Lett.* **2012**, *12*, 4164–4171.

[6] Perfézou, M.; Turner, A.; Merkoçi, A. Cancer detection using nanoparticle-based sensors. *Chem. Soc. Rev.* **2012**, *41*, 2606–2622.

[7] Merkoçi, A. Nanoparticles based electroanalysis in diagnostics applications. *Electroanalysis* **2013**, *25*, 15–27.

[8] de la Escosura-Muñiz, A.; Ambrosi, A.; Merkoçi, A. Electrochemical analysis with nanoparticle-based biosystems. *TrAC Trends Anal. Chem.* **2008**, *27*, 568–584.

[9] Kelley, S. O.; Mirkin, C. A.; Walt, D. R.; Ismagilov, R. F.; Toner, M.; Sargent, E. H. Advancing the speed, sensitivity and accuracy of biomolecular detection using multi-length-scale engineering. *Nat. Nanotechnol.* **2014**, *9*, 969–980.

[10] Wang, X. Y.; Hu, Y. H.; Wei, H. Nanozymes in bionanotechnology: From sensing to therapeutics and beyond. *Inorg. Chem. Front.* **2016**, *3*, 41–60.

[11] Byers, C. P.; Zhang, H.; Swearer, D. F.; Yorulmaz, M.; Hoener, B. S.; Huang, D.; Hoggard, A.; Chang, W.-S.; Mulvaney, P.; Ringe, E. et al. From tunable core-shell nanoparticles to plasmonic drawbridges: Active control of nanoparticle optical properties. *Sci. Adv.* **2015**, *1*, e1500988.

[12] Zugic, B.; Wang, L.; Heine, C.; Zakharov, D. N.; Lechner, B. A. J.; Stach, E. A.; Biener, J.; Salmeron, M.; Madix, R. J.; Friend, C. M. Dynamic restructuring drives catalytic activity on nanoporous gold-silver alloy catalysts. *Nat. Mater.* **2017**, *16*, 558–564.

[13] Zheng, Y. Q.; Zeng, J.; Ruditskiy, A.; Liu, M. C.; Xia, Y. N. Oxidative etching and its role in manipulating the nucleation and growth of noble-metal nanocrystals. *Chem. Mater.* **2014**, *26*, 22–33.

[14] Slater, T. J. A.; Macedo, A.; Schroeder, S. L. M.; Burke, M. G.; O'Brien, P.; Camargo, P. H. C.; Haigh, S. J. Correlating catalytic activity of Ag-Au nanoparticles with 3D compositional variations. *Nano Lett.* **2014**, *14*, 1921–1926.

[15] Shankar, C.; Dao, A. T. N.; Singh, P.; Higashimine, K.; Mott, D. M.; Maenosono, S. Chemical stabilization of gold coated by silver core-shell nanoparticles via electron transfer. *Nanotechnology* **2012**, *23*, 245704.

[16] Nishimura, S.; Dao, A. T. N.; Mott, D.; Ebitani, K.; Maenosono, S. X-ray absorption near-edge structure and X-ray photoelectron spectroscopy studies of interfacial charge transfer in gold–silver–gold double-shell nanoparticles. *J. Phys. Chem. C* **2012**, *116*, 4511–4516.

[17] Lewis, E. A.; Slater, T. J. A.; Prestat, E.; Macedo, A.; O'Brien, P.; Camargo, P. H. C.; Haigh, S. J. Real-time imaging and elemental mapping of AgAu nanoparticle transformations. *Nanoscale* **2014**, *6*, 13598–13605.

[18] Russo, L.; Merkoçi, F.; Patarroyo, J.; Piella, J.; Merkoçi, A.; Bastús, N. G.; Puntes, V. F. Time- and size-resolved plasmonic evolution with nm resolution of galvanic replacement reaction in AuAg nanoshells synthesis. *Chem. Mater.*, in press, DOI: 10.1021/acs.chemmater.8b01488.

[19] Xia, X. H.; Wang, Y.; Ruditskiy, A.; Xia, Y. N. 25th anniversary article: Galvanic replacement: A simple and versatile route to hollow nanostructures with tunable and well-controlled properties. *Adv. Mater.* **2013**, *25*, 6313–6333.

[20] González, E.; Arbiol, J.; Puntes, V. F. Carving at the nanoscale: Sequential galvanic exchange and kirkendall growth at room temperature. *Science* **2011**, *334*, 1377–1380.

[21] Cobley, C. M.; Xia, Y. N. Engineering the properties of metal nanostructures via galvanic replacement reactions. *Mater. Sci. Eng. R: Reports* **2010**, *70*, 44–62.

[22] Bastús, N. G.; Merkoçi, F.; Piella, J.; Puntes, V. F. Synthesis of highly monodisperse citrate-stabilized silver nanoparticles of up to 200 nm: Kinetic control and catalytic properties. *Chem. Mater.* **2014**, *26*, 2836–2846.

[23] Toh, H. S.; Batchelor-McAuley, C.; Tschulik, K.; Compton, R. G. Electrochemical detection of chloride levels in sweat using silver nanoparticles: A basis for the preliminary screening for cystic fibrosis. *Analyst* **2013**, *138*, 4292–4297.

[24] Tschulik, K.; Batchelor-McAuley, C.; Toh, H.-S.; Stuart, E. J. E.; Compton, R. G. Electrochemical studies of silver nanoparticles: A guide for experimentalists and a perspective. *Phys. Chem. Chem. Phys.* **2014**, *16*, 616–623.

[25] Liu, R. X.; Guo, J. H.; Ma, G.; Jiang, P.; Zhang, D. H.; Li, D. X.; Chen, L.; Guo, Y. T.; Ge, G. L. Alloyed crystalline Au–Ag hollow nanostructures with high chemical stability and catalytic performance. *ACS Appl. Mater. Interfaces* **2016**, *8*, 16833–16844.

[26] Kleijn, S. E. F.; Lai, S. C. S.; Koper, M. T. M.; Unwin, P. R. Electrochemistry of nanoparticles. *Angew. Chem., Int. Ed.* **2014**, *53*, 3558–3586.

[27] Cloake, S. J.; Toh, H. S.; Lee, P. T.; Salter, C.; Johnston, C.; Compton, R. G. Anodic stripping voltammetry of silver nanoparticles: Aggregation leads to incomplete stripping. *ChemistryOpen* **2015**, *4*, 22–26.

[28] Holt, L. R.; Plowman, B. J.; Young, N. P.; Tschulik, K.; Compton, R. G. The electrochemical characterization of single core-shell nanoparticles. *Angew. Chem., Int. Ed.* **2016**, *55*, 397–400.

[29] Saw, E. N.; Grasmik, V.; Rurainsky, C.; Epple, M.; Tschulik, K. Electrochemistry at single bimetallic nanoparticles—Using nano impacts for sizing and compositional analysis of individual AgAu alloy nanoparticles. *Faraday Discuss.* **2016**, *193*, 327–338.

[30] Liu, Z. N.; Huang, L. H.; Zhang, L. L.; Ma, H. Y.; Ding, Y. Electrocatalytic oxidation of D-glucose at nanoporous Au and Au-Ag alloy electrodes in alkaline aqueous solutions. *Electrochim. Acta* **2009**, *54*, 7286–7293.

[31] Xu, C. X.; Su, J. X.; Xu, X. H.; Liu, P. P.; Zhao, H. J.; Tian, F.; Ding, Y. Low temperature CO oxidation over unsupported nanoporous gold. *J. Am. Chem. Soc.* **2007**, *129*, 42–43.

[32] Herrero, E.; Buller, L. J.; Abruña, H. D. Underpotential deposition at single crystal surfaces of Au, Pt, Ag and other materials. *Chem. Rev.* **2001**, *101*, 1897–1930.

[33] Rogers, L. B.; Krause, J. C.; Griess, J. C.; Ehrlinger, D. B. The electrodeposition behavior of traces of silver. *J. Electrochem. Soc.* **1949**, *95*, 33–46.

[34] Lai, G. S.; Wang, L. L.; Wu, J.; Ju, H. X.; Yan, F. Electrochemical stripping analysis of nanogold label-induced silver deposition for ultrasensitive multiplexed detection of tumor markers. *Anal. Chim. Acta* **2012**, *721*, 1–6.

[35] Chu, X.; Xiang, Z. F.; Fu, X.; Wang, S. P.; Shen, G. L.; Yu, R. Q. Silver-enhanced colloidal gold metalloimmunoassay for *Schistosoma japonicum* antibody detection. *J. Immunol. Methods* **2005**, *301*, 77–88.

[36] Zhang, J.; Xiong, Z. B.; Chen, Z. D. Ultrasensitive electrochemical microcystin-LR immunosensor using gold nanoparticle functional polypyrrole microsphere catalyzed silver deposition for signal amplification. *Sensors Actuators B: Chem.* **2017**, *246*, 623–630.

[37] Price, S. W. T.; Speed, J. D.; Kannan, P.; Russell, A. E. Exploring the first steps in core–shell electrocatalyst preparation: *In situ* characterization of the underpotential deposition of Cu on supported Au nanoparticles. *J. Am. Chem. Soc.* **2011**, *133*, 19448–19458.

[38] Mulvaney, P.; Linnert, T.; Henglein, A. Surface chemistry of colloidal silver in aqueous solution: Observations on chemisorption and reactivity. *J. Phys. Chem.* **1991**, *95*, 7843–7846.

[39] He, W. W.; Wu, X. C.; Liu, J. B.; Hu, X. N.; Zhang, K.; Hou, S.; Zhou, W. Y.; Xie, S. S. Design of AgM bimetallic alloy nanostructures (M = Au, Pd, Pt) with tunable morphology and peroxidase-like activity. *Chem. Mater.* **2010**, *22*, 2988–2994.

[40] Tominaga, M.; Shimazoe, T.; Nagashima, M.; Kusuda, H.; Kubo, A.; Kuwahara, Y.; Taniguchi, I. Electrocatalytic oxidation of glucose at gold-silver alloy, silver and gold nanoparticles in an alkaline solution. *J. Electroanal. Chem.* **2006**, *590*, 37–46.

[41] Scanlon, M. D.; Peljo, P.; Méndez, M. A.; Smirnov, E.; Girault, H. H. Charging and discharging at the nanoscale: Fermi level equilibration of metallic nanoparticles. *Chem. Sci.* **2015**, *6*, 2705–2720.

[42] Prodan, E.; Nordlander, P. Plasmon hybridization in spherical nanoparticles. *J. Chem. Phys.* **2004**, *120*, 5444–5454.

[43] Mahmoud, M. A.; El-Sayed, M. A. Gold nanoframes: Very high surface plasmon fields and excellent near-infrared sensors. *J. Am. Chem. Soc.* **2010**, *132*, 12704–12710.